Karlsruhe Institute of Technology

Integrity of the bentonite barrier for the retention of radionuclides in crystalline host rocks - experiments and modeling

(Project KOLLORADO-e2; Final Report)

by Ulrich Noseck[2], Thorsten Schäfer[1] (Eds.)

KIT SCIENTIFIC WORKING PAPERS 140

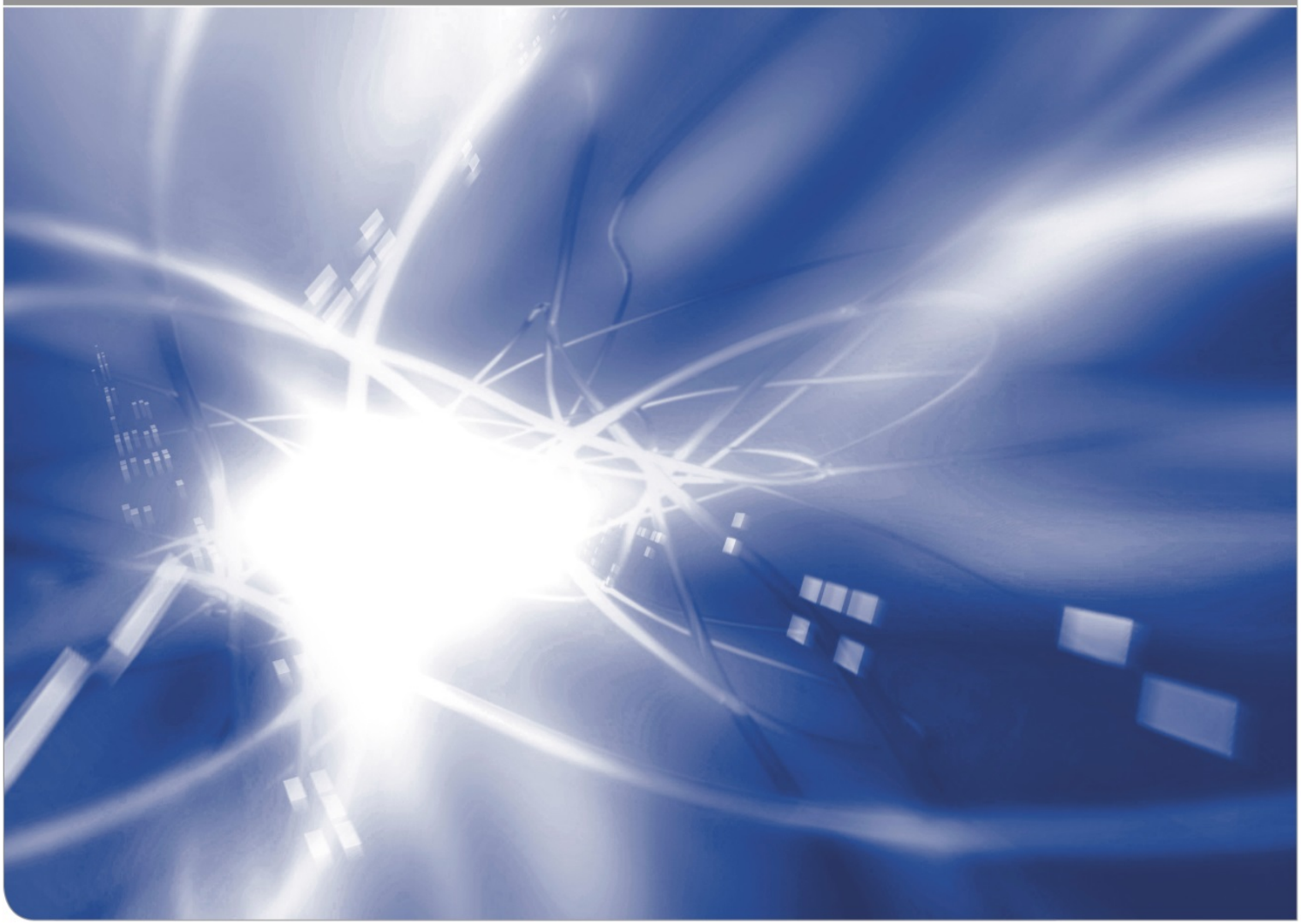

(1) Information on affiliation as follows:

[1] Institut für Nukleare Entsorgung (INE)
[2] Gesellschaft für Anlagen- und Reaktorsicherheit (GRS) gGmbH

(2) The authors of this report are:

Susan Britz[2], Judith Flügge[2], Carmen Garcia-Perez[1], Robert Götz[1], Stephanie Heck[1], Fabian Holl[1], Florian Huber[1], Felix Mattick[1], Vanessa Montoya[1], Ulrich Noseck[2], Francesca Quinto[1], Tatiana Reiche[2], Franz Rinderknecht[1], Thorsten Schäfer[1], Madeleine Stoll[1]

(3) The work described in this report was funded by the Federal Ministry for Economic Affairs and Energy (BMWi) under grant number 02 E 11456A & 02 E 11456B. The authors alone are responsible for the content of this publication.

Impressum

Karlsruher Institut für Technologie (KIT)
www.kit.edu

2020

ISSN: 2194-1629

Integrität der Bentonitbarriere zur Rückhaltung von Radionukliden in kristallinen Wirtsgesteinen– Experimente und Modellierung

(Project KOLLORADO-e^2; Final Report)

Editors:
Ulrich Noseck[2]
Thorsten Schäfer[1]

Authors:
Susan Britz[2]
Judith Flügge[2]
Carmen Garcia-Perez[1]
Robert Götz[1]
Stephanie Heck[1]
Fabian Holl[1]
Florian Huber[1]
Felix Mattick[1]
Vanessa Montoya[1]
Ulrich Noseck[2]
Francesca Quinto[1]
Tatiana Reiche[2]
Franz Rinderknecht[1]
Thorsten Schäfer[1]
Madeleine Stoll[1]

[1]Karlsruhe Institut für Technologie (KIT), Institut für Nukleare Entsorgung (INE)

[2]Gesellschaft für Anlagen- und Reaktorsicherheit (GRS) gGmbH

ANMERKUNG:

Die diesem Bericht zugrundeliegenden Arbeiten wurden mit Mitteln des Bundesministeriums für Wirtschaft und Energie (BMWi) unter den Förderkennzeichen 02 E 11456A & 02 E 11456B gefördert. Die Verantwortung für den Inhalt dieser Veröffentlichung liegt alleine bei den Autoren.

Content

1. Introduction 1
1.1 Scope of the work 1
1.2 State of the art 1
1.3 Aims and approach 4
1.3.1 Laboratory program 4
1.3.2 Modelling 5
1.4 List of publications within KOLLORADO-e^2 6
2. Experimental 9
2.1 Laboratory program 9
2.1.1 RN-sorption reversibility on Fracture Filling (FG) with competing surface 9
2.1.1.1 Materials and methods 9
2.1.1.3 Experimental layout 13
2.1.1.4 Results 14
2.1.2 LIT mock-up: RN release, resin selection and overcoring test 29
2.1.2.1 Mock-up status 29
2.1.2.2 Resin selection 31
2.1.2.3 Mock-up test overcoring 35
2.2 Field experiments 38
2.2.1 AMS analysis of samples from the CFM 13-05 in situ radionuclide tracer test 38
2.2.2 REMO tests 41
2.2.1.1 AMS analysis 44
2.2.2 Long-term In-situ test 46
2.2.2.1 Experimental Layout 46
2.2.2.2 Bentonite sample and tracer composition 48
2.2.2.3 Background monitoring 49
2.2.2.4 LIT online monitoring 49
2.2.2.5 LIT sample analysis 52
2.2.3 Reaction of MI shear zone on ISC activities: LIBD versus hydraulic results 60
3. Modelling 63
3.1 Thermodynamic benchmark calculations 63
3.1.1 Benchmark description 63
3.1.2 Benchmark results 65
3.1.3 Benchmark conclusions and outlook 72
3.2 Transport calculations with COFRAME 73
3.2.1 Screening calculations for radionuclide remobilization tests 75
3.2.2 Screening calculations for a field experiment to further investigate the desorption mechanism 81
3.2.3 Screening calculations for a field experiment on U and Np reduction 86
3.2.4 Simulation of long-term tailing in CFM RUN 13-05 87
3.2.5 Simulation of redox reactions of Np and U 89

3.3 Simulation of radionuclide diffusion in the bentonite source of the LIT with CLAYPOS 96
3.3.2 Transport Code CLAYPOS 97
3.3.3 Diffusion and porosity in bentonite 98
3.3.4 Modelling data 98
3.3.5 Results 100
3.3.6 Conclusions on radionuclide diffusion 103
3.4 The role of fracture geometry and orientation on transport properties and bentonite erosion 104
4. Conclusions 107
5. Outlook 111
6. References 113

List of figures

Figure 1: ESEM images of the 250-500 µm grain size fraction of FG. EDX verifies quartz, feldspars and phyllosilicates. 10

Figure 2: Scheme of the experimental procedure concerning the FG sorption reversibility experiment (Me = Metal ion). Step 2 is triggered by water exchange which can be seen as a disurbance of the sorption equilibrium. 14

Figure 3: Schematic overview of the sorption reversibility studies. Sorption and desorption experiments are performed successively during the first 232 days of the experiment. Ni-mnt colloids are introduced as competing ligand at a run-time of 400 days (ternary system)..... 14

Figure 4: (a) pH evolution for the sorption experiments (symbols), desorption in the binary system (light grey area) and desorption in the ternary system (dark grey area), respectively. (b) Eh_{SHE} evolution for the sorption (symbols) binary (grey area) and ternary desorption (symbols) experiments, respectively..... 16

Figure 5: (left) Predominance diagram for ^{99}Tc under the given conditions. The region of interest is marked with the light grey area and (right) thermodynamic speciation calculation. 17

Figure 6: (left) Predominance diagram for ^{233}U under the given conditions. The region of interest is marked with the light grey area and (right) thermodynamic speciation calculation. There is no change in the oxidation state but it is obvious that calcium complexes which are not shown in the pre-dominance diagram cannot be neglected. 17

Figure 7: (left) Predominance diagram for ^{237}Np under the given conditions. The region of interest is marked with the light grey area and (right) thermodynamic speciation calculation. 18

Figure 8: (left) Predominance diagram for ^{242}Pu under the given conditions. The region of interest is marked with the light grey area and (right) thermodynamic speciation calculation. 18

Figure 9: (left) Predominance diagram for ^{243}Am under the given conditions. The region of interest is marked with the light grey area and (right) thermodynamic speciation calculation. 18

Figure 10: Results of (a) ^{99}Tc, (b) ^{233}U and (c) ^{237}Np batch sorption kinetic experiments. 20

Figure 11: Results of ^{242}Pu (a) and ^{243}Am (b) batch kinetic sorption experiments**.** 20

Figure 12: Results of (a) ^{99}Tc and (b) ^{233}U batch kinetic desorption experiments. 22

Figure 13: Results of (a) ^{237}Np single radionuclide and (b) ^{237}Np cocktail kinetic desorption experiments, respectively. 23

Figure 14: Results of (a) ^{242}Pu single radionuclide, (b) ^{242}Pu cocktail and (c) ^{243}Am single radionuclide kinetic desorption experiments, respectively. The legend in (a) is valid for all diagrams..... 24

Figure 15: Results of ^{99}Tc (a), ^{233}U (b) and ^{237}Np (c) desorption experiments of the radionuclide cocktail sample series. A combination of the desorption in the binary (open symbols) and the ternary system (filled symbols) over the desorption time only. The legend in (a) is valid for all diagrams. 27

Figure 16: Results of ^{242}Pu (cocktail (a) and single nuclide (b)) and ^{243}Am (single nuclide (c)) desorption experiments. A combination of the desorption in the binary (open symbols) and the ternary system (filled symbols) over the desorption time only. The description in (a) is valid for all diagrams. 28

Figure 17: Release of Tc-99, U-233 and Np-237 and the conservative tracer Amino-G (AGA) in the Mock-up experiment under Argon atmosphere. 30

Figure 18: (left) Schematic arrangement of the bentonite erosion experiment and (right) bentonite erosion experiment set-up as installed in the lab. Pressure monitoring sensor on top (white cable). 31

Figure 19: Flow velocity distribution in the 1mm artificial fracture erosion experiments calculated with COMSOL Multiphysics for the initial condition before swelling into the fracture 32

Figure 20: FFM after different pre-treatment and in contact with LR white, Sika-52 and Araldite resin (from left to right, respectively) after hardening at 12 °C. 32

Figure 21: FFM Resin impregnation after washing with 90/10, 80/20, 70/30, 50/50% MeOH/GGW mixture (from left to right). Sika-52 samples are shown in the left and Araldite samples in the right picture 33

Figure 22: Experimental procedure for Febex bentonite impregnation 34

Figure 23: Araldite impregnated Febex samples; #2, 4, 6, 8, 10, 12 from left to right 34

Figure 24: Bentonite erosion experiment used for LIT mock-up overcoring 36

Figure 25: Test cell orientation in a tempered water bath during resin injection and curing 36

Figure 26: LIT mock-up after first (upper left) and second (upper right) resin injection. The blue color indicates regions with higher EtOH ratios. Prepa-ration for the overcoring (lower left) and water pressure during mack-up test overcoring (lower right). 37

Figure 27: ^{233}U concentration (ppq) determined with AMS in chosen samples of the CFM run 13-05 39

Figure 28: ^{237}Np concentration (ppq) determined with AMS in chosen samples of the CFM run 13-05 39

Figure 29: ^{242}Pu and ^{244}Pu concentration (ppq) determined with AMS in chosen samples of the CFM run 13-05 40

Figure 30: ^{243}Am and ^{241}Am concentration (ppq) determined with AMS in chosen samples of the CFM run 13-05. 40

Figure 31: (left) colloid concentration (ppb) determined with LIBD before the start of the experiment showing the disturbance through the experimental setup reaching a plateau value, (right) In-line colloid monitoring through turbidity measurements (NTU) and direct measurements using in-line LIBD. Samples 02-5 to 02-7 also shown for comparison. . 42

Figure 32: Colloid concentration (ppm) and calculated recovery during the push/pull experiment in observation borehole CRR 99.002-i2. 43

Figure 33: Colloid concentration (ppm) and calculated recovery during monitored at the Pinkel surface packer during the REMO 2 experiment with the comparison of the colloid detection of the push/pull experiment in observation borehole CRR 99.002-i2. 44

Figure 34: ^{233}U concentration (ppq) determined with AMS in chosen samples of the REMO and REMO II tests. 45

Figure 35: ^{237}Np concentration (ppq) determined with AMS in chosen samples of the REMO and REMO II tests. 45

Figure 36: Actinide concentrations (ppt) in comparison to the conservative data monitored at the Pinkel surface packer of REMO 2. 45

Figure 37: LIT experimental layout (www.grimsel.com). LIT enables bentonite erosion and colloid generation directly from compacted bentonite and can be seen as enhancement in comparison to past experiments that focused on injection of colloid suspensions under realistic flow conditions. 47

Figure 38: Arrangement of the boreholes relevant for LIT. A schematic overview (left) and a picture of the installation site during the experiment (right). The bentonite source is located in the central borehole and the surrounding boreholes (CFM 11.00X) are used for near-field observation and resin-injection prior overcoring of the bentonite source. 47

Figure 39: Conceptual design of the emplacement packer system and location in the borehole CFM 06.002 (NAB 14-092). Observation boreholes are not shown. The source is sealed with two hydro-mechanical packers (P1 and P2) and the hydraulic packer (P3) is located close to the tunnel wall. Drawing not to scale. 48

Figure 40: Photograph of the geochemistry cabinet at GTS (left) and schematic overview of the surface equipment setup for nearfield monitoring and sample collection (right). 50

Figure 41: Swelling pressure evolution within the LIT bentonite source. 51

Figure 42: Amino G concentration as a function of sampling flow velocity and extraction point as indicated by the color-coding. Cumulative extracted Amino-G mass is summed up from all monitoring boreholes 53

Figure 40: LIT - Geochemical evolution, data from Pinkel is colored in magenta. The color code of the near-field monitoring boreholes is shown in the borehole scheme. 53

Figure 44: pH and conservative tracer evolution. 55

Figure 45: (top) Magnesium, aluminum and zinc evolution in comparison to the respective background value of Pinkel and (bottom) calcium and sulfate molar concentrations. The respective background concentrations (0.09 mM Ca and 0.06 mM SO_4 from Pinkel, n=21) are subtracted to compare the molar ratios regarding the dissolution of gypsum. 56

Figure 46: (top) Colloid concentrations and (bottom) mean sizes derived by LIBD with optical data acquisition. 57

Figure 47: Nucleon number 99 release from LIT sampled from GTS borehole CFM11.002 59

Figure 48: ^{99}Tc concentration (ppq) determined with AMS in chosen samples of LIT. 60

Figure 48: Monitoring data by LIBD and pressure heads (08.02.2017, 09.02.2017, 10.02.2017, 13.02.2017, 14.02.2017 & 15.02.2017); respective date is indicated in the figure. 62

Figure 50: PH-Eh diagram calculated with (KIT-INE, left) and without (JAERI, right) consideration of ternary calcium UO_2 carbonate complexes for GGW; [U] = $4 \cdot 10^{-10}$ mol/l 69

Figure 51: Transport code COFRAME for colloid facilitated radionuclide transport in fractured media. 74

Figure 52: Exchange processes between the components that represent radionuclides and colloids in the modelling system. 75

Figure 53: Cross section of the shear zone with transmissivities and location of boreholes. The red arrows indicate the dipoles used for the field tests in the CFM project: dipole 1 with injection borehole CFM06.002 and outflow at tunnel surface Pinkel and dipole 2 located between BOCR 99.002 and BOMI 87.010. See text for more explanation. 77

Figure 54: Total concentration and concentration of the free (C_{fr}) and colloid-bound (C_{cr}) radionuclide fraction for Am-243 and Pu-242 applying a colloid concentration pulse with 1000 mg/l for 5 days (top). For better visibility the total concentration is not shown (bottom). 79

Figure 55: Total concentration and concentration of the free (C_{fr}) and colloid-bound (C_{cr}) radionuclide fraction for Am-243 and Pu-242 applying a colloid concentration pulse with 100 mg/l for 5 days. 80

Figure 56: Total concentration and concentration of the free (C_{fr}) and colloid-bound (C_{cr}) radionuclide fraction for Am-243 and Pu-242 applying a colloid concentration pulse with 1000 mg/l for 2.5 days. 80

Figure 57: Desorption rates of tetravalent Th (squares), Hf (rhomb) and Pu (triangles) – see top – and desorption rates of trivalent Eu (squares), Tb (rhomb) and Am (triangles) – see bottom – from colloids as a function of travel time as derived from model simulations with the codes RELAP (green), r^3t (red) and COFRAME (blue). The dotted black line indicates values determined in batch experiments. 81

Figure 58: Predicted difference in desorption rates of trivalent radionuclides from colloids between previous experiments (reference desorption rate) and the proposed new experiment (desorption rate: strong site) for an envisaged travel time of ten hours. 82

Figure 59 Transport time vs. outflow rates for the field experiments in the CFM (blue rhombs) and CRR dipole (red open squares). 83

Figure 60 Simulated breakthrough curves for Aga, colloids and Am-243 for case 1, 2, 3 and ref a. 84

Figure 61 Simulated breakthrough curves for non-sorbing tracer Aga, colloids and Pu-242 for case 1, 2, 3 and ref a. 85

Figure 62 Simulated breakthrough curves for non-sorbing tracer Aga, U-233 and Np-237 assuming a reduction and subsequent immobilization of U(VI) and Np(V). The reaction rates are taken from Tab. 36. 86

Figure 63 Measured and simulated breakthrough curves with long-term tailings for Run 12-02 (top), Run 13-05 (bottom), for explanations see text. 88

Figure 64 Development of concentrations for Am-243 and Pu-242 after run CRR #31 in the very long term based on an exemplary model simulation, explanation see text. 89

Figure 65 Breakthrough curve for CFM RUN 13-05, linear scale: Experimental data and simulation results for non-sorbing tracer (AGA), U-233 and Np-237. 92

Figure 66 Breakthrough curve for CFM RUN 13-05, log scale: Experimental data and simulation results for non-sorbing tracer (AGA), U-233 and Np-237. 92

Figure 67 Breakthrough curve for CRR #32: Experimental data and simulation results for non-sorbing tracer (I-131), U-233 and Np-237. Rectangular input function. 93

Figure 68 Breakthrough curve for CRR #32: Experimental data and simulation results for non-sorbing tracer (I-131), U-233 and Np-237. Two step input function. 94

Figure 69 Breakthrough curve for U-233 and Np-237, experimental data and model calculations; top: linear scale; bottom: log scale. 95

Figure 70 Breakthrough curve for non-sorbing tracer AGA in CFM RUN 13-05: Experimental values and simulation results from fit (no matrix diffusion) and calculation with matrix diffusion parameters applied in CRR RUN #32 U-233, see text 96

Figure 71 Schematic cross section of a bentonite ring with radionuclide containing glass vials as used in the LIT experiment and the models applied for radionuclide diffusion. 98

Figure 72 Illustrations of the bentonite structure and porosity types (Appello, 2013). 99

Figure 73: Effect of ionic strength on the anion diffusion accessible porosity in bentonite compacted at different dry densities (Van Loon, et al., 2007). 99

Figure 74: Spatial distribution of Am (left) and U(VI) and U(IV) calculated for plane and radial diffusion after 4.5 years transport time. 101

Figure 75: Spatial distribution of Np(V) and Np(IV)(left) and Pu(IV) and Pu(III) calculated for plane and radial diffusion after 4.5 years transport time. 101

Figure 76: Spatial distribution of Tc(IV) calculated for plane and radial diffusion after 4.5 years transport time. 102

Figure 77: Breakthrough curves for Np(V) (top), Tc(VII) (middle) and Se (VI) (bottom) calculated for plane and radial diffusion. 102

Figure 78: Breakthrough curves for ^{137}Cs and ^{45}Ca (bottom) calculated for plane and radial diffusion. 102

List of tables

Table 1: Results of XRF analysis, the main components are given in weight-% of the respective oxides. 11

Table 2: Specific surface area of the FG material used in the batch experiments. 11

Table 3: Concentration and mean size of synthetic Ni labelled montmorillonite colloids. ICP-OES derived concentrations are calculated over the elemental composition. The respective element is given below the values..... 12

Table 4: GGW composition. 12

Table 5: Concentration of the radionuclides and stock solutions used in the different batch experiments , combined with the respective solubility in GGW (Möri et al., 2003)..... 13

Table 6: Maximum sorption values and distribution coefficients of the RN sorption samples. Duplicates have been prepared and a value for each sample is given..... 21

Table 7: Radionuclide sorption rates fitted to the batch sorption experiment results. 22

Table 8: Overview of the fitted desorption rates and measured radionuclide recoveries. Recovery denotes the radionuclide fraction found in solution after the desired contact time of desorption..... 25

Table 9: Results of ^{242}Pu (cocktail (a) and single nuclide (b)) and ^{243}Am (single nuclide (c)) desorption experiments. A combination of the desorption in the binary (open symbols) and the ternary system (filled symbols) over the desorption time only. The description in (a) is valid for all diagrams. 28

Table 10: Sample list and details for Febex bentonite impregnation. 34

Table 11: Selected list of samples taken from CRR 99.002-i2..... 42

Table 12: Within LIT emplaced activity and license limits. 50

Table 13: Elemental composition of the bentonite rings emplaced within LIT. 58

Table 14: Log p_{CO2}, pH-value, Eh-value and concentration of dissolved elements in [M] in bentonite porewaters (Fernandez et al., 2004) and Grimsel groundwater (Duro, et al., 2006)..... 65

Table 15: Reference concentrations for the elements considered in the benchmark..... 65

Table 16:PH-value, Eh-value and concentration of dissolved elements in [M] in reducing and oxidizing mixed waters as calculated by GRS and KIT. 65

Table 17: Maximum concentration and dominating species calculated for selenium. 68

Table 18: Relevant stability constants logβ and solubility products logK for selenium contained in the databases of GRS and KIT. 68

Table 19: Maximum concentration and dominating species calculated for technetium. 68

Table 20: Relevant stability constants logβ and solubility products logK for technetium contained in the databases of GRS and KIT. 68

Table 21: Maximum concentration and dominating species calculated for uranium with modified value for the $Ca_2UO_2(CO_3)_3$ complex for GRS. 69

Table 22: Relevant stability constants logβ and solubility products logK for uranium contained in the databases of GRS and KIT. 69

Table 23: Maximum concentration and dominating species calculated for thorium. 70

Table 24: Relevant stability constants logβ and solubility products logK for thorium contained in the databases of GRS and KIT. 70

Table 25: Maximum concentration and dominating species calculated for neptunium. 70

Table 26: Relevant stability constants logβ and solubility products logK for neptunium contained in the databases of GRS and KIT. 71

Table 27: Maximum concentration and dominating species calculated for americium. 71

Table 28: Relevant stability constants logβ and solubility products logK for americium contained in the databases of GRS and KIT. 71

Table 29: Maximum concentration and dominating species calculated for plutonium. 72

Table 31: Relevant stability constants logβ and solubility products logK for plutonium contained in the databases of GRS and KIT. 72

Table 31: Transport parameters used in the predictive simulations for CFM-RUN 16-02. 83

Table 32: Interaction parameters for cases considered in the bounding calculations. 84

Table 33: Normalized maximum concentrations and recoveries for AGA, colloids, Am and Pu obtained in the different calculated cases. 86

Table 34: Normalized maximum concentrations and recoveries for AGA, U and Np obtained in the screening calculations, reference case, peak residence time (RD) 5 h and 15h, respectively. 87

Table 35: Interaction data for uranium and neptunium in CRR RUN #32 and CFM RUN 13-05. 91

Table 36: Hydraulic data for CRR RUN #32 and CFM RUN 13-05. 91

Table 37: Measured and calculated recoveries (after 800 h) for CRR RUN #32 and CFM RUN 13-05. 92

Table 39: Comparison of reference data for CRR #32 and data used to describe the tailing by matrix diffusion. 94

Table 39: Data applied for diffusion in bentonitediffusion. 100

Table 40: Compilation of radionuclide data; K_d values are taken from (Bradbury & Baeyens, 2010) if not marked otherwise; effective diffusion coefficients are taken from (Van Loon, 2014), see text. 101

1. Introduction

1.1 Scope of the work

In order to assess the relevance of colloidal influences on radionuclide transport for the longterm safety of a radioactive waste repository, the KOLLORADO-e^2 project integrates the results of in-vitro (geochemical), in-situ and in-silico (hydrogeological) studies. From the commonly considered set of necessary conditions (colloid presence/generation, their mobility and stability as well as the uptake of radionuclides and the irreversibility of this sorption process) required for a non-negligible impact of colloids on the pollutant propagation (Smith et al., 2008) the project focuses on the questions of

- colloid generation from compacted bentonite under low saline groundwater conditions (reference repository evolution in (SKB, 2006a; SKB, 2006b)),
- nanoparticle mobility and
- radionuclide uptake/sorption mechanisms and the appropriate implementation of relevant data into a transport code.

Our results provide feedback for the design of future experiments. In particular the Grimsel Test Site Phase VI Project CFM (**C**olloid **F**ormation and **M**igration) realizes low flow rates similar to repository post-closure conditions in order to capture the slow desorption dynamics of tri- and tetravalent actinides from bentonite colloids and to better simulate repository relevant conditions of low ionic strength groundwater contact to the geo-engineered barrier (http://www.Grimsel.com/gts-phase-vi/cfm-section/cfm-introduction). The concomitant extended durations and the higher overhead in general necessitate a careful choice of parameters. Reactive transport modelling allows assessing the impact of various scenarios, which are difficult or too expensive to realize under in-situ conditions.

Finally, yet importantly our results may serve as a basis for an appraisal of the implications of colloid presence in the vicinity of radioactive waste repositories in different deep geological host-rock formations.

1.2 State of the art

Generation of energy by nuclear fission leads to the production of radioactive waste, which contains uranium, plutonium, fission products and the so-called “minor actinides” such as neptunium, americium and curium. The safe disposal of this highly toxic and radioactive waste demands its isolation from the biosphere for several hundred thousand years. In the German Safety requirements for the disposal of heat generating radioactive waste a site-specific safety case covering a compliance period of one million years must be made to show the safety of the system (BMU, Version of Sept. 30. 2010). In this respect one important aspect is the issue of radionuclide behavior (mobilization, release and transport) in the repository system. It is the primary aim of nuclear waste disposal to immobilize and contain long-lived radionuclides (actinides, activation and fission products) over a geological timescale in the repository. It is an internationally agreed concept to dispose of high-level radioactive waste in deep geological repositories using a multi-barrier system fulfilling different safety functions (Alonso et al., 2006b; Yoshida, et al., 2005; NEA, 2013). The multi-barrier system is composed of the following:

- the waste matrix itself consisting of the spent fuel and its container (technical barrier)
- the geotechnical barrier consisting of the buffer and backfill material; this report focuses solely on compacted bentonite, and
- the geological barrier (e.g., salt, granite, clay; this report focuses on crystalline host rocks).

Considering various scenarios for each of these barriers those processes have to be examined and described which potentially lead to the mobilization or immobilization of radionuclides. Beside transport a variety of geochemical processes can take place in the individual barriers (e.g., redox reactions, hydrolysis, sorption/desorption, dissolution/precipitation, colloid formation) and each has to be evaluated. The aim is to determine rates for the immobilization and/or mobilization of the radionuclides during transport through the individual barriers. From this it is possible to derive source terms for radionuclide release out of the barriers. The combined source terms allow quantification of the potential release of long-lived radionuclides into the biosphere and hence provide a basis for a geochemically well-founded long-term safety analysis.

The engineered barrier system (EBS) of a deep geological repository for high-level nuclear waste foresees in most concepts (POSIVA, 2012; SKB, 2011) the use of bentonite as buffer and backfill material. Bentonite clay has been found to be an appropriate material for the geotechnical barrier due to its swelling properties (Pusch, 1983; Push, 1983; Sellin & Leupin, 2013) inhibiting groundwater access to the waste canister and retarding radionuclide transport in form of dissolved and colloidal phases (safety functions "sorb radionuclides" and "filter colloids", as defined by SKB (SKB, 2011) away from the repository near field (Liu & Neretnieks, 2006). However, depending on the physico-chemical conditions (e.g., gas and water pressure, groundwater flow velocity, composition of the groundwater) the bentonite barrier may also be eroded by colloid formation (Alonso et al., 2006b; Birgersson, et al., 2009; Gallé, 2000; Jansson, 2009; Moreno, et al., 2010; Robinson & Bath, 2011; Schäfer et al., 2012; Yoshida, et al., 2005; Apted et al., 2010) Bentonite colloid erosion has been reported to take place at the interface between the compacted bentonite buffer and granite (Baik, et al., 2007; Missana, et al., 2003) These results as well as laboratory bentonite erosion experiments (e.g. (Alonso, et al., 2007a)) show a dependency of the colloid source term on ionic strength, pH, bentonite compaction and flow velocity (Sellin, 2016). Under certain conditions, as e.g. imperfect backfilling, defects in plugs or fracturing radionuclide transport through the bentonite barrier may be rather quick. Speciation of radionuclides in the groundwater/pore water mixing zone might control in such worst-case scenarios the radionuclide mobility in the far-field (Kunze et al., 2008). The heavily discussed scenario of glacial water intrusion (Liu & Neretnieks, 2006) estimates a high erosion of bentonite buffer due to the contact with glacial water of high pH and low salinity favoring the release of bentonite colloids/particles. In the framework of the Grimsel Test Site (GTS) Phase VI the international Colloid Formation and Migration (CFM) project with partners from Japan (JAEA and NUMO), Switzerland (NAGRA), Finland (POSIVA), South Korea (KAERI), United Kingdom (RWM) and Germany (BMWi, KIT-INE, FSU, GRS) investigate processes related to this bentonite erosion and the possible formation of colloids. The migration of bentonite colloids and associated radionuclides in the shear zone under investigation in CFM has been demonstrated in earlier studies (Geckeis et al., 2004; Kretzschmar & Schäfer, 2005; Möri et al., 2003).

Beside the formation/erosion of colloidal material of smectite origin also the neo-formation of colloids due to the geochemical gradients and oversaturation of mixing waters has to be considered. Colloid formation in chemically disturbed environments has been documented in a couple of cases. Acid mine drainage waters show the formation of colloids and the mobility of heavy metals is strongly associated with this colloidal phases (Zänker et al., 2002; Zänker, et al., 2003) Studies with simulated tank waste solution (TWS) from the U.S. Department of Energy (DOE) Hanford Site (Washington State) showed that the maximum formation of mobile colloids occurred at the plume fronts with calcium carbonate as one of the dominant phases of the plume front colloids (Wan et al., 2004). The authors identified the cation exchange process during infiltration of the high-Na+ TWS solution, with complete replacement of exchangeable Ca^{2+}/Mg^{2+} from the sediment caused accumulation of these divalent cations at the moving plume front. Precipitation of supersaturated Ca^{2+}/Mg^{2+}- bearing minerals caused dramatic pH reduction at the plume front which triggered, in turn, precipitation of other minerals. Concerning the formation of aluminosilicate colloids laboratory studies have already demonstrated that these newly formed phases can have a significantly influence on the speciation of trivalent actinides (Kim, et al., 2005).

Colloids are known to be ubiquitous in natural groundwater and have been frequently discussed as potential carriers for radionuclides. Colloids show, in comparison with ionic species, a different migration behavior due to their comparatively larger size, charge and low diffusion coefficient the probability to penetrate into matrix pores of the host rock is lower and therefore they may be transported unretarded or in the fastest streamlines of the laminar flow field being faster than the average groundwater velocity monitored by dissolved conservative tracers. Thus, colloid bound contaminants such as ra-

dionuclides may interact to a lesser degree with the surface of the host rock minerals and can be transported over considerable distances. Transport of man-made nanoparticles as well as natural occurring radionuclides by colloids has been reported e.g. for the Nevada Test Site, USA (Buddemeier & Hunt, 1988; Kersting et al., 1999) and the Whiteshell Research Area, Canada (Vilks, et al., 1991)

However, colloids can also be retained by interaction with mineral surfaces or by agglomeration, sedimentation and filtration. All processes strongly depend on geochemical parameters, e.g., pH, ionic strength or colloid concentration. Therefore, the colloid stability is a key parameter for colloid facilitated transport. Dynamic light scattering (photon correlation spectroscopy; PCS) is frequently used to determine the coagulation rate and critical coagulation concentration (CCC) of various clay colloid suspensions (Kretzschmar, et al., 1998; Missana & Adell, 2000; Novich & Ring, 1984). Montmorillonite platelets are the major colloidal particles found to be mobilized from Febex bentonite. Due to their permanent negative face charge originating from isomorphous substitution and their pH dependent edge charge caused by broken tetrahedral and octahedral sheets exposing silanol and aluminol groups (Jasmund & Lagaly, 1993; Meunier, 2005) three different modes of interactions can be distinguished: edge-face (EF), edge-edge (EE) and face-face (FF). In order to be able to predict montmorillonite colloid stability based on extended DLVO-theory (Derjaguin & Landau, 1941; Verwey & Overbeek, 1948) the overall surface potential has to be separated into potentials and interaction modes associated with the edge and face geometry of the montmorillonite platelets and summing up hydration forces, born repulsion, electric double layer repulsion and London – van der Waals attraction. One suitable approach is the geometrical assumption made by (Mahmood, et al., 2001) to calculate the total interaction energy by using a half-cylinder with the radius equal to half the thickness of the montmorillonite platelet.

In the Colloid and Radionuclide Retardation (CRR) experiment carried out at the Grimsel Test Site (GTS), Phase V, the in situ migration behavior of selected radionuclides and chemical radionuclide homologues in the presence and absence of bentonite colloids in a water-conducting shear zone was studied (Geckeis et al., 2004; Möri et al., 2003). Under fast flow conditions (~36 m/d) recovery of injected bentonite colloids was in the range of 50-100 %. Related laboratory experiments in granodiorite bore cores from the same site using carboxylated polystyrene (latex) colloids showed colloid recoveries ranging from 10 to nearly 50 % (Schäfer, et al., 2004) under longer fracture residence times. Similarly, low colloid recoveries with increasing residence time were found by other investigators (Missana, et al., 2008). The authors conclude that even under geochemical conditions where colloids are highly stabilized (low salinity, high pH) adsorption/filtration onto mineral surfaces may occur. In the Colloid Formation and Migration (CFM) project the fluid travel times are enhanced by up to two orders of magnitude compared to CRR, enabling a further study of the colloid filtration process. Colloid recoveries are found in the range of 99 to 40 % showing a slight trend of decreasing filtration rates with increasing travel time (Noseck, et al., 2016; Huber et al., 2014). The extent of colloid adsorption on natural mineral surfaces may be influenced by, e.g., the chemical heterogeneity of the mineral surfaces, surface roughness, surface coatings, discrete surface charges (mineral edges and planes), mineral dissolution, the presence of dissolved ions or by matrix diffusion (Alonso, et al., 2007c; Bowen & Doneva, 2000; Johnson, et al., 1996; Patelli, et al., 2006; Stumpf, et al., 2008; Vakarelski, et al., 2000). Degueldre et al. (Degueldre, et al., 1996) carried out sorption experiments at pH 8 (I = 10-2 M $NaClO_4$) with clay colloids and several single minerals (muscovite, biotite, quartz, feldspar) comprising the Grimsel granodiorite and observed considerable colloid adsorption. (Alonso, et al., 2004) studied the interactions between gold colloids and a granite surface by μ-Particle Induced X-Ray Emission (μPIXE) to determine the amount of adsorbed colloids on different minerals under varying chemical conditions. These authors concluded that adsorption of colloids on rock surfaces is generally determined by electrostatic interactions. However, colloid adsorption was also detected under unfavorable (repulsive) colloid-fracture surface attachment conditions (e.g., alkaline pH). It was suggested that chemical effects may enhance colloid/rock interaction when favorable (attractive) electrostatic interaction does not exist. Furthermore, theoretical studies have been performed to calculate surface charge heterogeneity effects (e.g., (Velegol & Thwar, 2001). These effects have also been experimentally evaluated, e.g. for Cu ion adsorption onto silica (Taboada-Serrano, et al., 2005).

The issues mentioned above have been investigated in detail within the projects KOLLORADO-1, KOLLORADO-2 and KOLLORADO-e (Schäfer, 2010; Huber et al., 2014; Huber, et al., 2016), which give a good overview of the state-of-the-art as basis of the project for the partners KIT-INE, FSU and GRS.

1.3 Aims and approach

1.3.1 Laboratory program

The laboratory program conducted within the project KOLLORADO-e^2 aimed on deriving further knowledge and data on (i) mechanisms of the interaction between colloids, radionuclides and fracture filling material and (ii) on the colloid-facilitated radionuclide migration.

Concerning the interaction mechanisms between colloids, radionuclides and fracture filling material the following aspects are investigated in detail within the KOLLORADO-e^2 project:

- Evaluation of radionuclide speciation in groundwater and porewater: In order to evaluate the behavior of the radionuclides ^{232}Th, ^{233}U, ^{237}Np, $^{238/242/244}$Pu, $^{241/243}$Am in the reversibility experiments and in the LIT, it is necessary to know their speciation and solubility in bentonite porewater, Grimsel groundwater and in the mixing zone of both. Speciation calculations are performed particularly to identify understand the observations in the reversibility experiments. Besides that, a larger benchmark including partners from the CFM project is performed (see below).
- Bentonite erosion and colloid formation at the bentonite porewater interface: The focus of the investigations is on the feasibility of structurally marked (Zn, Ni) montmorillonite for quantification of the erosion rates accompanied by the determination of erosion rates of Febex bentonite in the mock-up tests under the geometrical conditions of the LIT experiment. Febex bentonite rings are brought into contact with an artificial fracture of 1 mm aperture to yield a realistic colloid source term for the LIT.
- Colloid stability and interaction with fracture filling material: The interaction of colloids of different size with fracture surfaces is systematically studied. Investigations are based on the effects of real surface roughness of granodiorite from Grimsel site and horizontal / vertical fracture orientations on the interaction energies of carboxylated latex particles. Experimental work is accompanied by 2D simulations with COMSOL Multiphysics®.
- Interaction of radionuclides, colloids and fracture filling material: One focus of the investigations in the KOLLORADO-e^2 project was still on the determination of data for the radionuclide reversibility kinetics, which are necessary to simulate the field and laboratory experiments and are directly used in the transport codes. After investigation of the radionuclide reversibility on Febex clay mineral colloids in batch experiments by addition of humic substances as competing ligand (Bouby, et al., 2011) and pre-processed granodiorite of different grain size (Huber, et al., 2011; Huber et al., 2015) data for ^{99}Tc, ^{237}Np, ^{242}Pu or ^{243}Am were still lacking. Reversibility investigations for these radionuclides are addressed for the ternary system radionuclide-colloid-fracture filling/fault gouge material within KOLLORADO-e^2. In this respect, some emphasis is put on the behavior of structurally marked (Ni, Zn) montmorillonite.

Concerning the colloid-facilitated radionuclide migration specific field experiments are performed. These are accompanied by selected laboratory experiments. In particular, the following aspects are highlighted:

- Mock-up tests: The series of mock-up tests for the long-term in situ test (LIT) at KIT-INE has been continued. Natural Febex bentonite or a mixture with synthetic montmorillonite and GGW were used for this type of experiments to keep it close to the expected scenario in LIT. Beside investigation of bentonite erosion and radionuclide mobilization one additional focus lies on a feasibility study aiming to find a suitable way to conserve the LIT sample during overcoring. Therefore, the mock-up experimental set-up is used to perform resin impregnation tests with subsequent investigation of the contact zones.
- In-situ experiments at GTS: The long-term in-situ test (LIT) has been started in 2014 to investigate in situ colloid formation and mobilization of radionuclides from a radionuclide-labelled bentonite plug (NAGRA, 2016). During the KOLLORADO-e^2 project samples from observation boreholes and Pinkel have continuously been taken, analyzed and evaluated until the experiment has been stopped and overcored end of 2018.
- The application and further development of Accelerator Mass Spectroscopy (AMS, (Quinto et al., 2015)) offered the opportunity to study the long-term mobility of radionuclides by sampling the tailing of the breakthrough curve over a period of six months and will provide additional details on the sorption/desorption processes/kinetics of the fracture

filling material. Further AMS data on the long-term tailing of CFM RUN 13-05 have been collected and evaluated. It allowed to identify for the first time traces of radionuclides, which were injected in CRR tracer tests more than 12 years before CFM RUN 13-05 in the same dipole.

- Additional field tests on the remobilization of radionuclides retained during RUN 13-05 called REMO 1 and REMO 2. The conceptual idea of REMO 1 was to remobilize colloids via flow reversal and hydraulic push retained in the near-field of the injection borehole CRR 99.002-i2 without disturbing the LIT experiment. The REMO 2 experiment was designed to force desorption of surface retained actinides through injection of a high concentration colloid suspension. Here, the initial idea to follow a push/pull strategy proved to be impossible within the hydraulic limits set by the LIT experiment and a colloid migration experiment with a breakthrough at the Pinkel surface packer was followed.
- During stimulation experiments within the In-situ Stimulation and Circulation (ISC) project in 2017 the MI shear zone was monitored to measure possible disturbances and colloid/nanoparticle mobilization due to permeability creation and induced seismicity in the vicinity of the MI shear zone.

The analysis of samples by HR-ICP-MS, LIBD/ s-curve LIBD, LSC, γ-spectrometry and AMS of the migration experiments and the LIT performed at GTS in the framework of the CFM project was almost exclusively performed by KIT-INE. This included analysis of several radionuclides (Cs, Na, Ba, Se, Tc, Am, Th, Pu, Np) and bentonite colloids. In addition, for the LIT the mobile LIBD system was transferred to the GTS for on-site colloid detection.

1.3.2 Modelling

One goal is to shed light on the multitude of different interaction forms and paths between radionuclides, colloids and the sediment matrix. Special interest was on (i) the speciation of radionuclides to better understand the speciation of homologues and radionuclides under the field conditions at GTS (ii) the consequences of kinetically controlled adsorption and desorption processes, (iii) the effect of fracture heterogeneity on bentonite erosion and (vi) the effect of fracture heterogeneity on flow and non-reactive tracer transport. The following approaches were used:

- benchmark calculations with thermodynamic speciation models and respective databases,
- macroscopic 1D/2D models using simplified geometry implementing sorption/desorption kinetics of colloids/radionuclides,
- extend an available 2D model on bentonite erosion to include heterogeneous flow fields based on random aperture distributions, and
- COMSOL Multiphysics® to simulate flow and transport of non-reactive tracers in single fractures with complex geometry.

Thermodynamic benchmark calculations are performed in order to better understand the speciation and therewith the transport and retardation effects of homologues and radionuclides under the evolving geochemical conditions in the field experiments at GTS, particularly the LIT. Since a recent benchmark performed in year 2000 (Bruno, et al., 2000) updates affecting radionuclide speciation calculations have been reported in the literature which are mainly related to new thermodynamic data and more detailed knowledge on ground- and pore- water compositions as well as redox conditions for the scenario of interest. Especially, the conditions at the interface between bentonite and crystalline rock have become more important for the current experiments and been included into the new benchmark.

For the computer simulations of the radionuclide transport in the project KOLLORADO-e^2 two transport codes from perfomance assessment were applied: (i) the 1D-transport COFRAME (Reiche, et al., 2016) which considers colloid facilitated radionuclide transport in fractured media by a double porosity approach and (ii) the transport code CLAYPOS, which simulates one-dimensional radionuclide transport in low-permeable media either in cylindrical or in planar geometry (Rübel, et al., 2007).

One type of simulations concerns predictive calculations in order to contribute to the design of potential field tests and to verify the assumption of the modelling approach. During this project phase, predictive calculations with COFRAME are performed for: (i) a remobilization test, where a defined pulse of Grimsel groundwater with a high amount of dissolved bentonite colloids is injected into the dipole in order remobilize radionuclides from the fracture filling material or the immobilized colloids by desorption and subsequent sorption to the injected, mobile bentonite colloids; (ii) a field migration experiment aiming to further investigate a postulated two-site desorption mechanism of colloid-bound radionuclides during transport in the shear zone.

One specific effect observed in the field tests CRR #32 and CFM-13-05 carried out in the same dipole with high and low velocity concerns the redox reaction of U and Np during transport through the shear zone. Both radionuclides are not or only to a neglectable amount bound to colloids. Nevertheless, their recovery decreases significantly from the short transport time in CRR #32 to the long transport time in CFM RUN 13-05. Simulations are performed in order to simulate their breakthrough curves in both experiments regarding a reduction of the mobile U(VI) and Np(V) into the rather immobile tetravalent forms.

During Kollorado-e project the application of the AMS (see above) provided for the first time data on the long-term tailing of the breakthrough curves of ^{243}Am, ^{242}Pu and ^{237}Np in CFM Run 12-02. Within this project, Kollorado-e^2, AMS data became available for CFM-RUN 13-05. The data identified traces of radionuclides still present from a previous CRR experiment (performed 12 years before CFM RUN 13-05). Although the data from CFM RUN 13-05 are to some extent biased by the CRR experiment, calculations with COFRAME are performed to identify whether the long-term concentration ranges for ^{243}Am and ^{242}Pu can be met with the same parameters as used in CFM RUN 12-02.

During the lifetime of the LIT experiment from May 2014 until November 2018 no radionuclides (except traces of Tc) have been observed in the observation boreholes. Therefore, the simulation was focused on the diffusion of the RN tracers injected in glass vials in the bentonite ring. The investigations aimed at the question of the radionuclide mobility in the bentonite, namely to estimate either how RNs are distributed in the bentonite or whether significant amounts of radionuclides are expected to have been released from the bentonite. This is of high interest, with regard to the currently running analyses of the overcoring material from the LIT experiment.

The geometry of the fracture at the bentonite fracture interface is essential for the evolving contact area and the extension of the swelling bentonite into the fracture. Systematic model calculations are performed to investigate the impact of the surface roughness of the fracture and the correlation length on the erosion rate (Huber, et al., 2020, in review). Further, the impact of fracture geometry and aperture distribution on fluid movement and on non-reactive solute transport is investigated experimentally and numerically in single fractures. For this purpose, a hydrothermally altered and an unaltered granite drill core with axial fractures are investigated. Using three injection and three extraction locations at top and bottom of the fractured cores, different dipole flow fields were examined. Fluid flow and tracer transport were simulated using COMSOL Multiphysics® (Stoll, 2018).

1.4 List of publications within KOLLORADO-e^2

PhD thesis**:**

- Rinderknecht, Franz (2017). *Bentonite erosion and colloid mediated transport of radionuclides in advection controlled systems*. Dissertation (Dr. rer. nat.), Karlsruhe Institut für Technologie (KIT).
- Stoll, Madeleine (2018): *Colloid mobility controlling processes in single fractures : a bot-tom-up approach*. Dissertation (Dr. rer. nat.), FSU Jena.

Peer reviewed publications in the framework of KOLLORADO-e^2:

Published:

- Noseck, U.; Flügge, J.; Reimus, P.; Cvetkovic, V.; Lanyon, G.W.; Schäfer, Th.; Blechschmidt, I.: Grimsel Test Site Investigation Phase VI. Colloid Formation and Migration Project: Modelling of tracer, colloid and radionuclide transport for dipole CFM 06.002 – Pinkel surface packer. NAGRA Technical Report ntb 16-06, December 2016.
- Drake, H., F. A. Mathurin, T. Zack, T. Schäfer, Incorporation of Trace Elements into Calcite Precipitated from Deep Anoxic Groundwater in Fractured Granitoid Rocks. Procedia Earth and Planetary Science, 17, 841-844, 2017.
- Huber, F. M., Y. Totskiy, R. Marsac, D. Schild, I. Pidchenko, T. Vitova, S. Kalmykov, H. Geckeis, T. Schäfer, Tc interaction with crystalline rock from Äspö (Sweden): Effect of in-situ rock redox capacity, Appl. Geochem., 80, 90-101, 2017.
- Quinto, F., et al., Multiactinide Analysis with Accelerator Mass Spectrometry for Ultratrace Determination in Small Samples: Application to an in Situ Radionuclide Tracer Test within the Colloid Formation and Migration Experiment at the Grimsel Test Site (Switzerland). Anal. Chem., 89(13), 7182-7189, 2017.
- Stoll, M., F. M. Huber, E. Schill, T. Schäfer, Parallel-plate fracture transport experiments of nanoparticulate illite in the ultra-trace concentration range investigated by Laser-Induced Breakdown Detection (LIBD). Colloids and Surfaces A, 529, 222-230, 2017.
- Drake, H., F. A. Mathurin, T. Zack, T. Schafer, N. M. W. Roberts, M. Whitehouse, A. Karlsson, C. Broman, M. E. Astrom, Incorporation of Metals into Calcite in a Deep Anoxic Granite Aquifer. Environ. Sci. Technol., 52(2), 493-502, 2018.
- Shelton, A., Sellin, P., Missana, T., Schäfer, T., Červinka, R., Koskinen, K., 2018. Synthesis report: Colloids and related issues in the long term safety case. SKB Technical report TR-17-17.
- Stoll, M., F. M. Huber, M. Trumm, F. Enzmann, D. Meinel, A. Wenka, E. Schill, T. Schäfer, Experimental and numerical investigations on the effect of fracture geometry and fracture aperture distribution on flow and solute transport in natural fractures. J. Contam. Hydrol. https://doi.org/10.1016/j.jconhyd.2018.11.008, 2019.
- Quinto, F., Busser, C., Faestermann, T., Hain, K., Koll, D., Korschinek, G., Kraft, S., Ludwig, P., Plaschke, M., Schäfer, T., Geckeis, H., Ultratrace Determination of ^{99}Tc in Small Natural Water Samples by Accelerator Mass Spectrometry with the Gas-Filled Analyzing Magnet System. Anal. Chem. 91, 4585-4591, **2019**.

Submitted/ in review:

- Huber, F.M., Leone, D., Trumm, M., Moreno, L., Neretnieks, I., Wenka, A., Schäfer, T., (in review). Impact of fracture geometry on bentonite erosion - a numerical study. International Journal of Rock Mechanics and Mining Sciences.
- Seher, H., Geckeis, H., Fanghänel, T., Schäfer, T., (submitted). Bentonite nanoparticle stability and effect of fulvic acids: experiments and modelling. Journal of Colloid and Interface Sciences.
- Montoya, V., Noseck, U., Mattick, F., Britz, S., Rinderknecht, F., Blechschmidt, I., Schäfer, Th. (submitted). Radionuclide solubility and speciation calculations for the Long-term In-situ Test (LIT) at Grimsel Test Site (GTS, Switzerland). Environ. Sci. Technol.

2. Experimental

2.1 Laboratory program

2.1.1 RN-sorption reversibility on Fracture Filling (FG) with competing surface[1]

One of the reference evolution scenarios of a high-level nuclear waste disposal in crystalline formations (e.g. granitic rock) in e.g. Sweden and Finland foresees the intrusion of low mineralized glacial melt water down to repository depth (~500m below surface) (SKB, 2006b). Under these hydro-geochemical conditions, erosion of the geotechnical barrier consisting of compacted bentonite may occur leading to the formation of bentonite colloids. Radionuclides sorbed to these colloids may be transported over longer distances than in the absence of a colloidal phase (SKB, 2011). Laboratory batch studies on the reversibility of the sorption process to the colloids leading to a decrease in transport distances have been carried out in the past years for the ternary system radionuclide-colloid-fracture filling/fault gouge material (e.g. (King, et al., 2010; Huber et al., 2015)). Moreover, field scale experiments on colloid facilitated radionuclide transport in the framework of the Colloid Formation and Migration project (CFM (www.grimsel.com) have been conducted corroborating the occurrence of sorption reversibility. Derived desorption rates out of the experimental datasets can be directly used in performance assessment codes like e.g. (Robinson & Bath, 2011) to simulate the effect of sorption reversibility on the long-term migration behavior. Surprisingly, up to now, only little data is available on the binary system radionuclide- fracture filling/fault gouge material under these low ionic strength meltwater conditions (Degueldre & Benedicto, 2012). Reliable distribution coefficients (Kd values) and kinetic rates for the binary system are needed to decrease the uncertainties in the transport simulations. To close the data gap, a new experimental program was initiated during Kollorado-e and was finalized within Kollorado-e[2]. This program is focusing on the following aspects:

- Determination of Kd values for ^{99}Tc, ^{233}U, ^{237}Np, ^{242}Pu and ^{243}Am on fault gouge material from Grimsel under Grimsel groundwater conditions
- Study potential sorption competition effects by comparison of single radionuclide batch experiments with radionuclide cocktail batch experiments
- Examine a possible impact of the initial sorption time on the desorption kinetic process
- Study the impact of a competing surface in form of a bentonite colloid flush on the desorption kinetic

2.1.1.1 Materials and methods

Fault Gouge material (FG):

The FG material was collected at the Grimsel Test Site (GTS), Switzerland. The main rock type in the Grimsel area is the so-called Grimsel granodiorite (Alonso, et al., 2006a). It consists of plagioclase, quartz, K-feldspar, biotite and accessory minerals like muscovite/sericite, apatite, sphene, epidote, zircon, calcite and opaque minerals (e.g. Fe-oxides like magnetite) (Schäfer et al., 2012). The material was extracted from an outcrop of the Colloid Formation and Migration (CFM) project MI shear zone at the AU tunnel wall outside the controlled area. FG was transferred to KIT-INE, crushed and separated under ambient conditions using sieves with meshes between 63 µm up to 5 mm. Thereby, FG in seven different grain sizes (< 63 µm (VII), 63-125 µm (VI), 125-250 µm (V), 250-500 µm (IV), 500-1000 µm (III), 1-2 mm (II) and 2-5

[1] This chapter is partly published in Rinderknecht, F., 2017. Bentonite erosion and colloid mediated transport of radionuclides in advection controlled systems (in English), Faculty of Chemistry and Biosciences. Karlsruhe Institute of Technology (KIT), Karlsruhe.

mm(I)) was generated. Only the size fraction IV was used for the radionuclide sorption and reversibility experiments. These fractions were washed and equilibrated using natural Grimsel groundwater (GGW) over a period of two weeks and exchanged regularly five times to remove any fines in the supernatant.

Environmental Scanning Electron Microscopy (ESEM, QUANTA 650 FEG) analysis of the size fraction was carried out. The FG material was dried at 60°C and transferred to the ESEM device. Results are shown in Figure 1 corroborating the sieved size fraction of 250µm - 500µm. By application of energy-dispersive X-ray spectroscopy (EDX) element analysis was possible and used to estimate the FG mineralogy yielding mainly feldspar, plagioclase, quartz and phyllosilicates. As expected, the artificially and freshly crushed grains show a very rough and irregular shape.

Powder X-ra y diffraction analysis was conducted to determine the mineralogical composition of the size fraction used. XRD spectra were recorded from 5° - 90° 2Θ with a Siemens D5000 powder diffractometer equipped with a scintillation detector and Cu Kα radiation. Results of the analysis yield mainly mineral phases like quartz, plagioclase, K-feldspar in line with literature data. Chemical composition of FG was quantified by XRF (MagiXPro, PANalytical B. V.) concerning the major and trace elemental composition of the FG material used (Table 1). In line with general granitic rock composition SiO_2, Al_2O_3, Na_2O, Fe_2O_3 and K_2O dominate reflecting the main minerals plagioclase, feldspar and quartz. The dominating Fe redox state is Fe(II) with 2.71% of 3.87% total Fe present in the sample as determined by photometric analysis.

The specific surface area of the FG was measured by classical 5 point BET N_2-adsorption. All samples were heated to 90°C and degassed for 18h. Using multi point analysis the BET isotherm was fitted to obtain the surface area. A total surface area of > 1 m^2 was used in all measurements. Results of the BET analysis is given in Table 2. Additionally, the geometrical surface area was calculated assuming a density of 2.7 g/cm^3 for the FG. Comparing the measured BET with the calculated specific surface area it is obvious that the FG material specific surface area is fully dominated by inner porosity in pores or cracks or surface roughness. In addition to the BET measurements, the ESEM pictures for the FG material grains shown in Figure 1 support this conclusion and allow the direct comparison of different size fractions in terms of mass based K_d values to similar experiments using the same type of FG material but with a different size fraction (1160 µm) (Alonso, et al., 2006a).

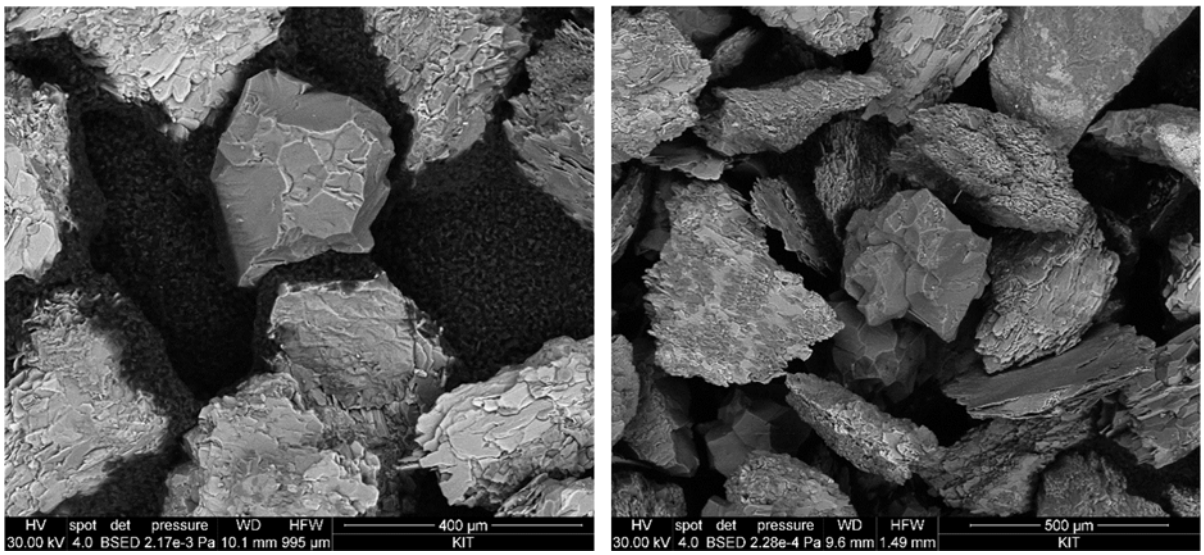

***Figure 1**: ESEM images of the 250-500 µm grain size fraction of FG. EDX verifies quartz, feldspars and phyllosilicates.*

Table 1: *Results of XRF analysis, the main components are given in weight-% of the respective oxides.*

Component	FG, 500 - 1000 µm grain size	FG, 250 - 500µm grain size
SiO2	65.3%	64.6%
Al2O3	15.8%	15.7%
Fe2O3	3.8%	3.9%
MgO	2.4%	2.4%
CaO	1.6%	1.7%
Na2O	4.7%	4.5%
K2O	3.7%	3.7%

Table 2: *Specific surface area of the FG material used in the batch experiments.*

FG grain size fraction (µm)	Specific surface area (m2/g)	
	BET	calculated (sphere)
250 - 500	22.8±1.1	8.8·10-3 (250µm) / 4.4·10-3 (500µm)

Natural granitic groundwater (GGW):

GGW from GTS is used for bentonite erosion experiments as well as for radionuclide sorption reversibility studies. The groundwater is a Na^{+}/Ca^{2+}-HCO_3^{-}-SO_4^{2-} groundwater type (Table 3) with a pH of 9.6 and an Eh_{SHE} below -200mV. Low salinity of 1.2 mM makes this groundwater comparable to expected glacial melting water that may in the Scandinavian scenario reach down to repository depth within the relevant time span of final disposal (Geckeis et al., 2004; Schäfer, et al., 2004).

The water was filled in 50 L Teflon coated Al- barrels which were cleaned and filled with Argon gas thoroughly before they were transported to the GTS for sampling. Sampling was performed under low flow rates (< 10mL/min) similar to the minimal-draw down procedure established by USEPA (Geckeis et al., 2004) in order to sample artifact-free the natural mobile colloid fraction. Once filled, the barrels remained for several days on the opened sampling line and the water was flushed through the barrels in order to exclude any interaction with oxygen or CO_2 that may still have been inside the barrels.

Synthetic Ni-montmorillonite derived colloids:

Synthetic Ni-bearing montmorillonite colloids in GGW have been produced from Ni-montmorillonite suspensions in a repeated four time cycles of suspending, centrifugation for 30 minutes at 4000 rpm (2.800 g) and re-suspending of the separated phase in GGW. The initial suspension contained 2 g montmorillonite in 200 mL GGW and was equilibrated prior the first centrifugation for 7 days. The final colloid containing supernatant was taken as colloid stock and diluted to the desired concentration of 35.9 mg/L according to ICP-OES data of the main elements (Si, Al and Ni). Element ratios of 24.8% (Si), 9.8% (Al) and 5.1% (Ni) are derived by the elemental composition $Na_{0.3}$ $[Al_{1.64}Ni_{0.39}\square_{0.97}]$-$[Si_{4.00}]O_{10}(OH_{1.95}*F_{0.05})*4H_2O$. A comparison between ICP-OES, LIBD and s-curve LIBD can be found in Table 3.

A thorough characterization of the separated colloids was reported by Huber et al. (Huber et al., 2015) including ICP-MS, PCS, AFM, AsFIFFF and LIBD.

***Table 3**: Concentration and mean size of synthetic Ni labelled montmorillonite colloids. ICP-OES derived concentrations are calculated over the elemental composition. The respective element is given below the values.*

	ICP-OES (N = 2)	**Optical LIBD (N = 3)**	**Stationary s-curve LIBD (N = 2)**	**Mobile s-curve LIBD (N = 1)**
Dilution	---	1000	100 - 1000	100
Colloid concentration [mg/L]	34.7 ± 0.7 (Si) 35.4 ± 1.0 (Al) 37.5 ± 0.7 (Ni)	17.0 ± 3.9	18.3 ± 6.8	5.2 ± 1.0
Mean colloid size [nm]	---	73 ± 6	44 ± 9	51 ± 10

***Table 4:** GGW composition.*

	Barrel 4-14	**Barrel 4-16**	**Literature [10]**
pH	9.33	9.18	9.67
EhSHE	201 mV	260 mV	
Ionic strength			1.2 mM
[Mg2+]	21.2 µg/L	34.5 µg/L	12.6 µg/L
[Ca2+]	7.5 mg/L	8.1 mg/L	5.3 mg/L
[Na+]	8 mg/L	12.4 mg/L	14.7 mg/L
[Al3+]	12.6 µg/L	-	42.9 µg/L
[Fe2+/3+]	-	-	< d. l.
[Sr2+]	210 µg/L	145 µg/L	182 µg/L
[Cl-]	0.9 mg/L	1.6 mg/L	6.7 mg/L
[SO42-]	5.9 mg/L	7.8 mg/L	5.8 mg/L
[F-]	4.5 mg/L	4.6 mg/L	6.3 mg/L
[Si]	4.2 mg/L	2.7 mg/L	5.6 mg/L
[HCO3-]	3.6 mg/L	4.0 mg/L	mg/L

Radionuclide cocktail characterization and speciation:

Two experimental series were prepared: (i) single radionuclide and (ii) radionuclide cocktail samples, respectively. The radionuclides used are listed in Table 5 in conjunction with their respective concentration and the oxidation states at the time of the addition. The concentrations are very similar in both sample series. ^{233}U was used in the cocktail experiments only. Radionuclide concentrations have been selected to not exceed the solubility limit under the geochemical conditions given therefore avoiding any precipitation which could bias the analysis of the experiments and the experimental results itself. Measurement of the radionuclide concentrations in the samples was done by either ICP-MS (THERMO X-Series II) or high-resolution (HR) ICP-MS (THERMO Element XR).

Radionuclide solubility data is given in Table 5. All RN, despite Pu(IV), are well below the solubility limit for the most stable oxidation state under GGW conditions, respectively. In case of Pu the limit is not strictly determined and ranges from $1 \cdot 10^{-10}$ M to $2 \cdot 10^{-9}$ M (Möri et al., 2003). In the case of an oversaturated Pu solution, precipitation is unlikely as Pu(IV) forms highly stable $Pu(OH)_4$ colloids that show similar sorption behavior as dissolved Pu(IV) (Bouby, et al., 2011).

2.1.1.3 Experimental layout

Both batch sorption and desorption (reversibility) experiments have been conducted in a glovebox under anaerobic conditions (Argon atmosphere) and room temperature (22°C). Separate samples have been prepared using HDPE 20 mL vials (ZINSSER) for each sampling time. This allows the use of the sorption samples subsequently as samples in the desorption experiments. A duplicate has been prepared for each sample to check for reproducibility. A scheme of the experimental procedure can be found in Figure 2.

Diluted stock solutions (RN-GGW) for each single radionuclide and for the cocktail sample series were prepared by mixing fresh GGW with the concentrated radionuclide stock solutions to reach the desired radionuclide concentrations. Afterwards pH of the RN-GGW solutions were re-adjusted to the original Grimsel pH of ~9.5. In each vial 1.5 g (dry weight) of the FG (250-500 µm size fraction) was brought in contact with 8.5 mL of the different RN-GGW solutions yielding a V/m ratio of 5.7 mL/g. The samples prepared were stored in the glove box during the whole experimental duration. Sampling times were as follows: 1 d, 3 d, 7 d, 14 d, 28 d, 100 d, 200 d and 300 d (Figure 26, step 1). After the desired contact time, pH and Eh_{SHE} have been monitored before taking an aliquot for further analysis. pH was measured in each sample using a semi-micro Ross electrode (81-03, Orion Co.) in combination with a digital pH meter (720A, Orion Co.) to check for any drift over the experimental duration. Calibration of the pH setup was carried out using at least five commercial buffer solutions (Merck). Eh measurements have been carried out with a Pt combined electrode (Metrohm) connected to the pH meter (Orion). Raw Eh data was corrected to a standard hydrogen electrode by addition of 207 mV. Eh_{SHE} was consistently monitored in the blank samples until a plateau value was reached within ~120 minutes. Afterwards, an aliquot of the sample was diluted in 2% HNO_3 and analyzed by (HR)-ICP-MS. After each sorption time, the remaining solution in each vial was discarded carefully and fresh RN free GGW was added (8.5 mL to keep the V/m ratio constant). A similar sampling schedule was chosen in the desorption experiments as used in the sorption experiments, namely 1 d, 3 d, 7 d, 14 d, 28 d, 100 d, 200 d and 300 d (Figure 26, step 2). That is, for the 7 d sorption sample for instance, after a desorption time of e.g. 1 d an aliquot was taken for RN analysis by (HR)-ICP-MS and pH of the sample was measured. Subsequently, the remaining solution was completely discarded from the sample vial and fresh GGW was added. After additional two days (that is 3 d desorption time in total), the same procedure of sampling, pH measurement and exchange of solution with fresh GGW was carried out. This procedure was repeated for all samples and desired desorption times. In other words, every sample out of the sorption series experiments was exchanged with fresh GGW 8 times (once for each desorption time) within the desorption experiment series. Subsequently to the desorption kinetics experiments under pure GGW conditions, the FG material containing sorbed RN (only for the single radionuclide series of Am, Pu and cocktail series samples, respectively) was brought in contact with 8.5 mL of synthetic Ni montmorillonite containing GGW colloid suspension (Huber et al., 2015; Reinholdt et al., 2013) to study a possible remobilization of RN due to the presence of an additional concurrence surface (Figure 2, steps 3&4). The colloid concentration in the sample was 35.9 mg/L. The samples were taken after 1 d, 5 d, 14 d, 28 d and 211 d and afterwards immediately prepared for elemental composition analysis.

Table 5*: Concentration of the radionuclides and stock solutions used in the different batch experiments , combined with the respective solubility in GGW (Möri et al., 2003).*

Nuclide	**C single radionuclide [M]**	**CRN-cocktail [M]**	**RN-solubility [M], (solid phase)**	**Stock solutions [M]**
^{99}Tc(VII)	$1.5\cdot10^{-7} \pm 4.5\cdot10^{-9}$	$1.5\cdot10^{-7} \pm 6.0\cdot10^{-9}$	$9.6\cdot10^{-4}$ ($TcO_2\cdot1.6\ H_2O$)	$1.0\cdot10^{-5}$
^{233}U(VI)	Not used	$8.2\cdot10^{-8} \pm 3.3\cdot10^{-10}$	$2\cdot10^{-4}$ ($UO_2(OH)_2$)	$1.5\cdot10^{-4}$
^{237}Np(V)	$5.5\cdot10^{-9} \pm 1.8\cdot10^{-10}$	$5.4\cdot10^{-9} \pm 2.1\cdot10^{-10}$	$2\cdot10^{-4}$ (NpO_2OH (am))	$1.6\cdot10^{-5}$
^{242}Pu(IV)	$5.9\cdot10^{-10} \pm 3.1\cdot10^{-11}$	$6.4\cdot10^{-10} \pm 2.6\cdot10^{-11}$	$1\cdot10^{-10}$ - $2\cdot10^{-9}$ ($PuOH_4$(am))	$4.4\cdot10^{-7}$
^{243}Am(III)	$4.2\cdot10^{-10} \pm 8.4\cdot10^{-12}$	$3.3\cdot10^{-10} \pm 1.3\cdot10^{-11}$	$1\cdot10^{-7}$ ($AmOHCO_3$(am))	$1.6\cdot10^{-4}$

The radionuclide sorption reversibility studies were divided in three phases (Figure 3):

1. Sorption of the RNs on FG took place during the first 232 days of the experiment. Thereby a sample duplicate was prepared for each sorption time step and for each RN solution. The sorption experiment ws divided in 6 sorption time steps varying between 1 day and 232 days.

2. Desorption in the binary system GGW-FG started as soon as the first sorption time step, which was one day of sorption, was over and lasted until a total experimental time of 400 days. The longer reacting sorption samples were added subsequently to the desorption experiment but desorption time was not extended accordingly. Therefore sorption and de-sorption in the binary system GGW-FG took place in parallel within the first 232 days of the experiment. A fraction of the RNs remained on the FG surface at the end of desorption in the binary system but did not change between the last samplings.

3. Desorption in the ternary system GGW-FG-Ni-mnt is the final phase of the sorption reversibility study. In order to remobilize part of the remaining FG-attached RNs, Ni-mnt colloids were added as competing surface. Only the strong sorbing RN samples (Pu and Am) and the RN cocktail containing samples were included in the final phase of the study. Desorption in the ternary system was investigated for the following 211 days, leading to a total experimental duration of 611 days.

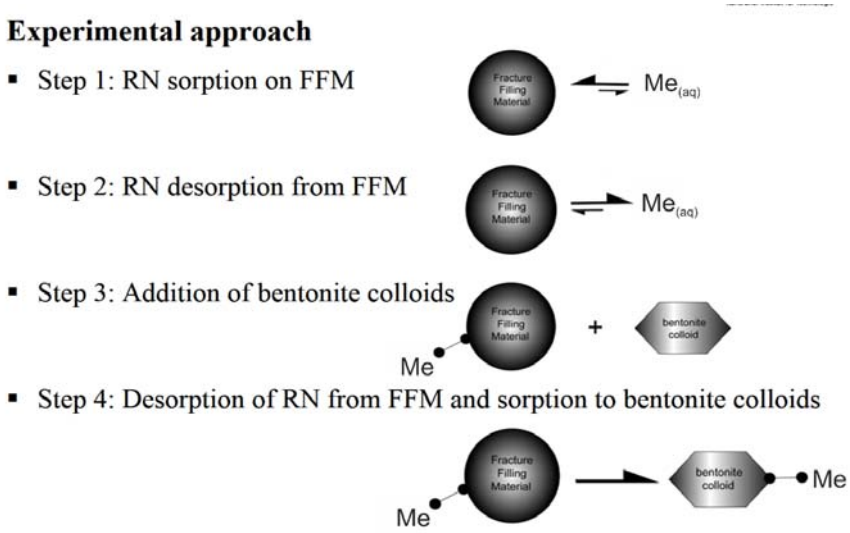

Figure 2: *Scheme of the experimental procedure concerning the FG sorption reversibility experiment (Me = Metal ion). Step 2 is triggered by water exchange which can be seen as a disurbance of the sorption equilibrium.*

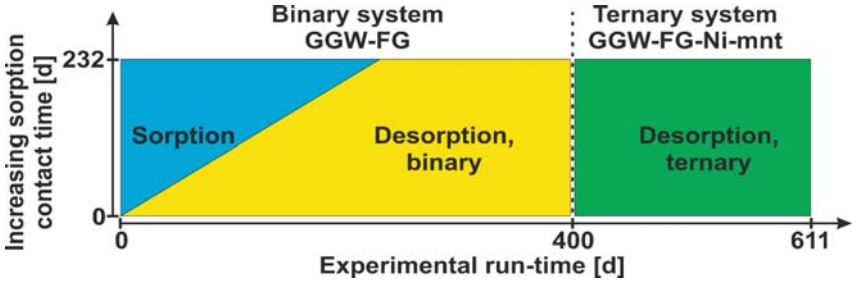

Figure 3: *Schematic overview of the sorption reversibility studies. Sorption and desorption experiments are performed successively during the first 232 days of the experiment. Ni-mnt colloids are introduced as competing ligand at a run-time of 400 days (ternary system).*

2.1.1.4 Results

Evolution of pH-Eh_{SHE} conditions:

pH evolution of both the sorption and desorption experiments are shown in Figure 4. In case of the sorption samples, each pH data point shown is an average of 34 single samples in total. Regarding the very small error bar (~0.1 pH unit) of the measured pH values for each time step, pH evolution is very reproducible. A constant pH was observed within the first 28 d contact time. Afterwards a drift from initially pH of ~9.3 down to pH of ~8.2 was detectable during the contact time of 232 d. This drift might be attributed to two possible reasons:

- a disequilibrium between the FG and the GGW inducing mineral dissolution and precipitation processes which consume OH^- ions shifting pH to lower values or
- intrusion of trace amounts of CO_2 (which could be present in the glove box Ar atmosphere) into the samples by diffusion.

The former explanation might be favored over the latter explanation when looking at the pH evolution during the desorption experiments. Here, the pH stayed very much constant (9.3 ± ~0.1 pH unit) over 600d despite having contact to the FG all the time. This effect can be explained by the sampling strategy of the desorption experiment. In contrast to the sorption experiment, which included duplicate samples for each sorption time step, contact times during desorption are short. The contact water is exchanged after each desorption time step and an equilibrium between the FG and the GGW cannot be established. Therefore, the disequilibrium cannot be resolved in the first desorption samples and aligned when it came to longer contact times. The pH during the desorption experiments in both the binary and the ternary system is shown in Figure 4 as greyish areas instead of single values. This was necessary since for each sorption time 14 pH values (7 samples with duplicates) have been measured for each desorption step for each single radionuclide and cocktail samples (5 RN series sums up to > 700 values).

The redox potential was measured in blank samples (GGW and FG only) in absence of RN to evaluate only the influence of the FG material on the Eh_{SHE} evolution and to avoid any leakage of the electrode inner filling electrolyte (3M KCl) into the sample solution during long measurement times. With respect to the sorption experiments, an initial drop from ~+250 mV down to ~+ 90 mV was detected within the first 7 d which stayed constant until 28 d. Afterwards Eh_{SHE} drifted to a value of ~+175 mV after 232 d. The drift for the long term samples might be explained by trace amounts of O_2 diffusing into the vials. Regarding the desorption experiments in the binary system, Eh_{SHE} was very constant over the whole experimental duration in line with the pH behavior. In case of the desorption experiment in the ternary system, higher $Eh_{(SHE)}$ values similar to the sorption experiments (~300 mV) are observed for the short contact times and converge to the values in the binary system within 28 d. Eh_{SHE} data for the latest sampling is missing because the electrode was not in use for a couple of months and needed a revision to give reliable results. This was not possible when sampling took place. The measured redox potentials of the GGW are much more positive than the in-situ Eh_{SHE} value measured in the field. Here values of around -300 mV have been measured by (Möri et al., 2003; Bouby, et al., 2012). Low redox potentials have also been measured within very similar laboratory batch experiments by (Huber et al., 2015). The discrepancies between the measured values in this study and reported values in the literature display the general high uncertainties in reliably measuring $Eh_{(SHE)}$ values in systems where only very small concentrations of redox active elements like e.g. Fe(II)/Fe(III) are present. For a thorough discussion on this topic the reader is referred to e.g. (Grenthe, et al., 1992) (Geckeis et al., 2013).

Radionuclide speciation

Predominance diagrams as well as speciation diagrams for the radionuclides used in the sorption reversibility experiments were calculated for the experimental conditions using the GGW composition given in Table 4 with the geochemical speciation code Hydra-Medusa (Guillaumont, et al., 2003). The applied radionuclide concentrations are given in Table 5. The relevant pH-Eh_{SHE} region is between pH 8.2 and pH 9.3 and Eh_{SHE} between +100 mV and +300 mV (Figure 4). The thermodynamic constants used are taken from the NEA database only (Guillaumont, et al., 2003) (except for U where two additional species were included (see discussion below)). In all speciation diagrams shown only species with a fraction of at least 10% are included.

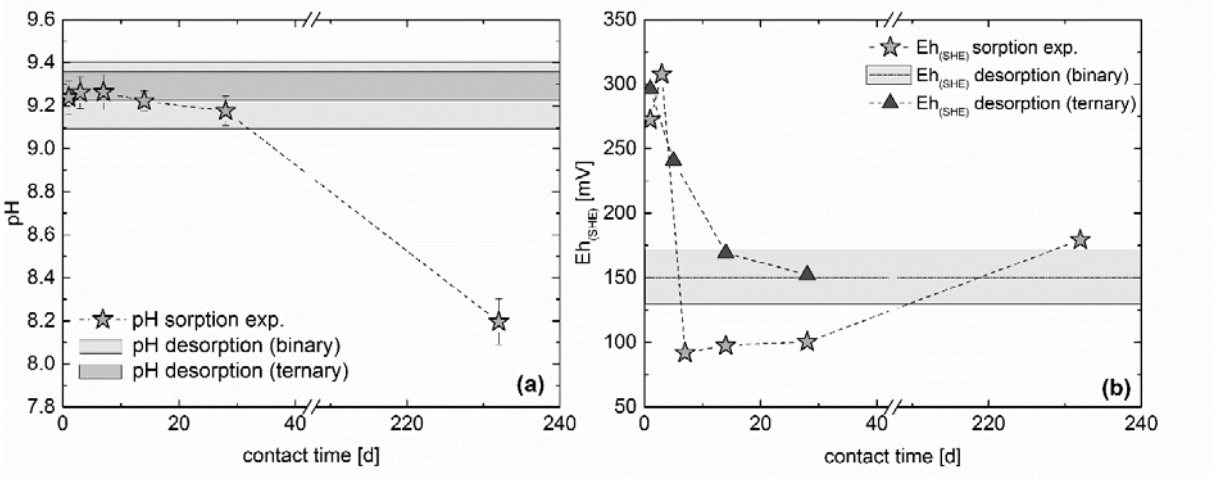

Figure 4: *(a) pH evolution for the sorption experiments (symbols), desorption in the binary system (light grey area) and desorption in the ternary system (dark grey area), respectively. (b) Eh_{SHE} evolution for the sorption (symbols) binary (grey area) and ternary desorption (symbols) experiments, respectively.*

^{99}Tc speciation

The dominant ^{99}Tc species is TcO_4^- over the entire pH and Eh_{SHE} region of interest. ^{99}Tc predominance and speciation diagram can be found in Figure 5 which shows that there is no relevant species except TcO_4^- under the experimental conditions prevailing. Reduction of Tc(VII) (TcO_4^-) to Tc(IV) followed by precipitation of $TcO_2 \cdot 1.6\ H_2O_{(s)}$ is unlikely given the distance to the 50/50 borderline where both species are present in equal amounts.

^{233}U speciation

The predominance diagram for ^{233}U shows two relevant species within the region of interest (Figure 6). In case of pH values below 9, the negatively single charged $(UO_2)_2CO_3(OH)_3^-$ complex is dominant. At the highest pH values of 9.3, relevant for most of the samples, the negatively single charged $UO_2(OH)_3^-$ dominates. The speciation diagram for ^{233}U reveals two additional relevant species (Figure 6). The calcium containing complexes $CaUO_2(CO_3)_3^{2-}$ and $Ca_2UO_2(CO_3)_3$,aq have to be taken into account additionally since they have been shown to be of importance under near-neutral pH conditions and in presence of Ca^{2+} in aqueous environments (Bernhard et al., 2001). Equilibrium constants for these complexes are currently not implemented in the NEA database used and have been added using the thermodynamic constants from (Endrizzi & Rao, 2014). At pH 9.3 slightly more than 50% of the uranium is bound in the Ca-containing complexes, separated in 22% and 30% for the negatively double charged $CaUO_2(CO_3)_3^{2-}$ and the neutral complex $Ca_2UO_2(CO_3)_{3,aq}$, respectively. The maximum concentration of these complexes coincides with the pH value of all samples except the long-term sorption sample series. At the lower limit of the pH region, the ratio decreases to 6% and 9% in case of the negatively double charged and the neutral complex, respectively. All described complexes contain uranium in the oxidation state +VI and reduction to U(IV) is thermodynamically not expected. Moreover, it has been shown that the Ca-UO_2-CO_3 complexes are very stable towards reduction (Brooks et al., 2003).

^{237}Np speciation

The predominance diagram for ^{237}Np shows only the pentavalent species, NpO_2^+ (Figure 7, left) under the experimental conditions. Lowest Eh_{SHE} values are close (< 50mV) to the transition borderline from Np(V) to Np(IV) but still in the stability field of Np(V). Np speciation shows NpO_2^+ in a ratio of 95% at pH 8.2 and still 67% at pH 9.3 with $NpO_2CO_3^-$ as the second dominating species (Figure 7, right).

^{242}Pu speciation

The predominance diagram for ^{242}Pu can be found in Figure 8 (left). A Pu(IV) stock solution was used in the experiments and the dominant complex $Pu(OH)_4$ does not show a change of the oxidation state under the conditions prevailing. Due to the distance to the Pu/IV)/Pu(III) borderline, reduction is not expected. Calculation of the speciation under the given conditions show that the $Pu(OH)_4$ neutral complex is the only relevant one in the system (Figure 8, right).

^{243}Am speciation

The predominance diagram for ^{243}Am (Figure 9, left) shows two relevant species, namely $AmCO_3^+$ at pH values below 8.5 and $Am(OH)_2^+$ at pH values above pH 8.5. At low pH values a third complex ($AmOH^{2+}$) gains minor importance (~15%) as can be seen in the speciation diagram in Figure 9 (right). Precipitation or a change of the oxidation state is in case of ^{243}Am not expected.

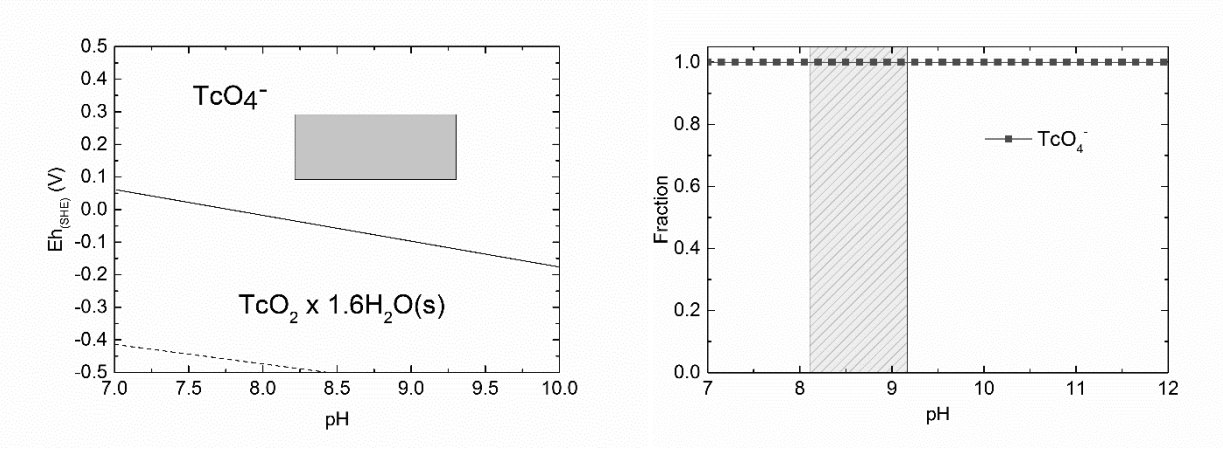

Figure 5: *(left) Predominance diagram for ^{99}Tc under the given conditions. The region of interest is marked with the light grey area and (right) thermodynamic speciation calculation.*

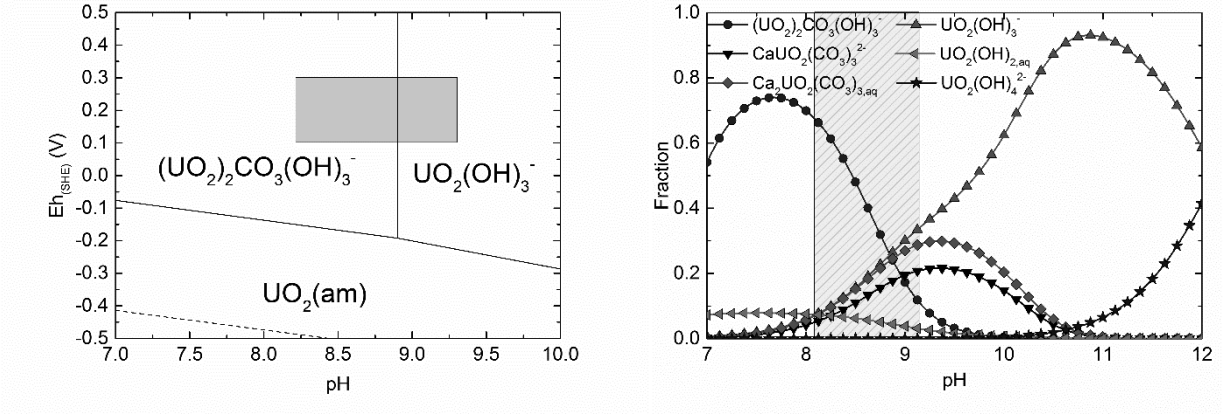

Figure 6*: (left) Predominance diagram for ^{233}U under the given conditions. The region of interest is marked with the light grey area and (right) thermodynamic speciation calculation. There is no change in the oxidation state but it is obvious that calcium complexes which are not shown in the predominance diagram cannot be neglected.*

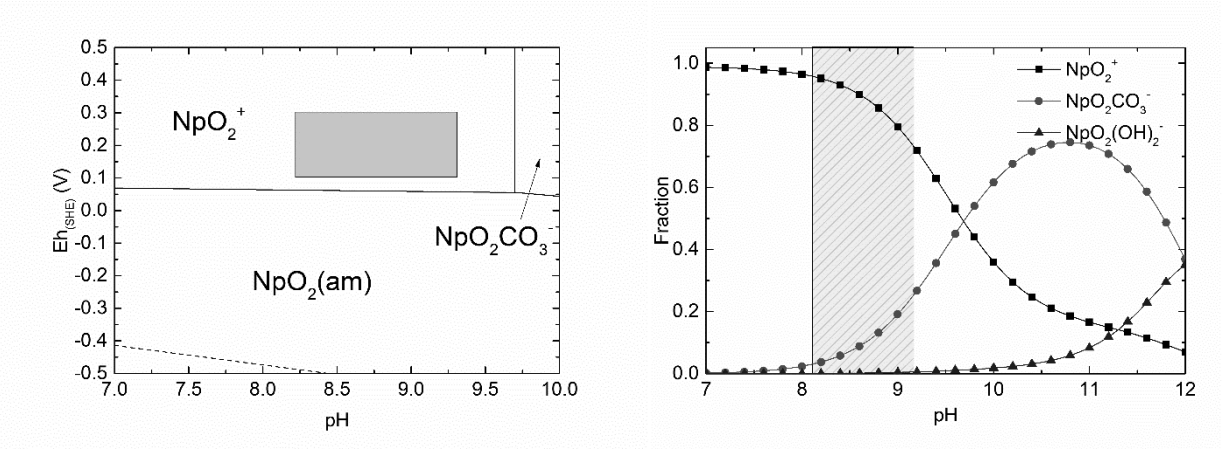

Figure 7: *(left) Predominance diagram for ^{237}Np under the given conditions. The region of interest is marked with the light grey area and (right) thermodynamic speciation calculation.*

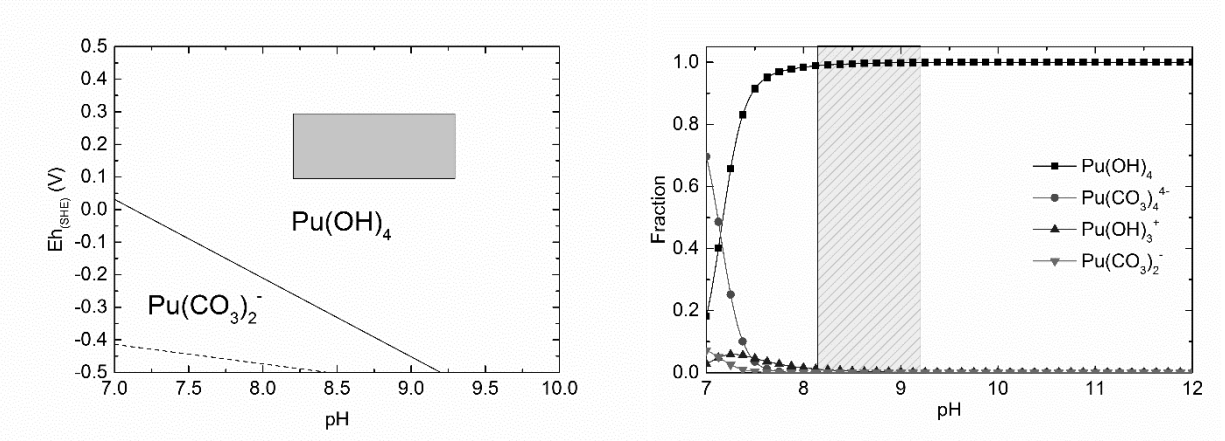

Figure 8*: (left) Predominance diagram for ^{242}Pu under the given conditions. The region of interest is marked with the light grey area and (right) thermodynamic speciation calculation.*

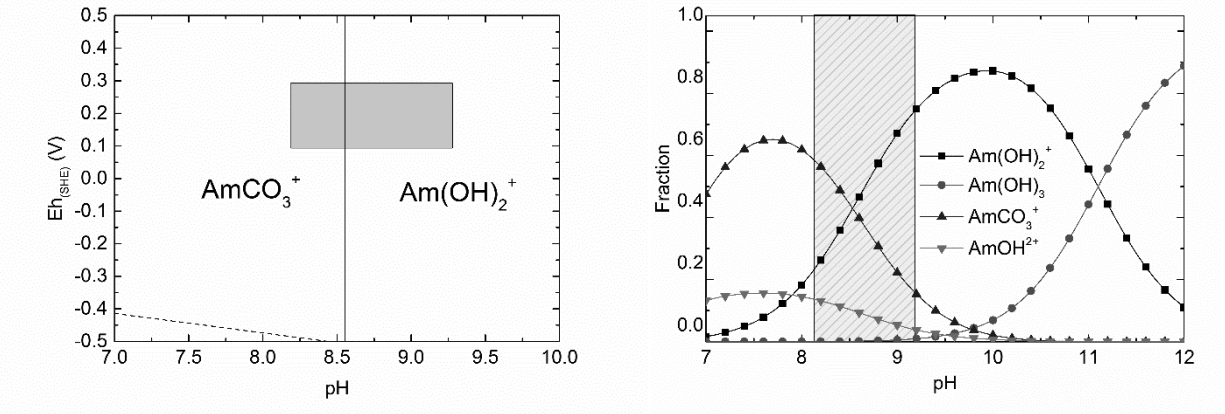

Figure 9*: (left) Predominance diagram for ^{243}Am under the given conditions. The region of interest is marked with the light grey area and (right) thermodynamic speciation calculation.*

RN sorption kinetics

^{99}Tc(VII), ^{233}U(VI) and ^{237}Np(V)

The results for the ^{99}Tc(VII) sorption kinetics are shown in Figure 10a for both the single RN experiments and the RN cocktail experiments. Less than 10% sorption was observed for the cocktail samples after 28 d contact. The same is true for the single RN samples except the values after 28 d, which is around 17%. For the long-term sample after 232 d both the single RN experiments yielded values of 60% and ~45% for the RN cocktail samples, respectively. Regarding the thermodynamic modelling, a reduction of Tc(VII) to Tc(IV) is rather unlikely since the measured redox potentials are more than 200 mV above the 50/50% borderline for Tc(VII)/Tc(IV) reduction. The removal process leading to the decrease in aqueous ^{99}Tc(VII) concentration is most probably a surface-induced redox transformation of ^{99}Tc(VII) to ^{99}Tc(IV). It is well known that a dramatic change in the sorption properties is accompanied with the reduction process (Huber, et al., 2011). While Tc(VII) behaves like a conservative tracer and is therefore not interacting with the FG surface, Tc(IV) shows a very strong sorption behavior. Thus, it seems likely that during the experimental duration a coupled process of reduction and subsequent sorption occurred (sorptive reduction). As potential redox partner Fe(II) might be responsible which is found in the Grimsel FG material as verified by XRF measurements (2.7 wt-% FeO). A similar behavior of 99Tc sorptive reduction in the same system has been observed e.g. by (Huber, et al., 2011; Huber et al., 2015; Bouby, et al., 2011). Regarding thermodynamic simulation results, no reduction should be expected based on the measured pH-Eh range. This is apparently in agreement with measurements for short contact times. For longer contact times, however, calculations and experiment differ. One has to state clearly that the determination of the redox potential in natural systems is associated with very high uncertainties due to local redox disequilibrium as discussed for example (Grenthe, et al., 1992; Geckeis et al., 2013). A study by (Marsac, et al., 2015; Miller et al., 2000) investigated Np(V) interaction with illite and found that although the measured redox potential measured in solution would predict Np(V), the reduced Np(IV) species was detected on the illite surface. This observation was explained by the occurrence of a very stable Np(IV) surface complex. A similar behavior for Tc(VII) surface reduction was just recently reported by (Huber, et al., 2017; Lagaly & van Olphen, 1978). Another possible explanation would be that the redox potential measured in solution with a redox electrode can be different to the redox potential prevailing at the solid-liquid interface and that it is reducing enough to build up Np(IV) surface species.

Sorption kinetics for ^{233}U(VI) are shown in Figure 10b. Only values for the cocktail samples are shown since no single RN experiment has been conducted for ^{233}U(VI). A maximum of ~40% sorption was observed which was obtained already after 14 d contact time. Afterwards only a very small increase could be observed until 232 d (~2%). This might be interpreted as a faster initial sorption followed by a very slow sorption reaction. Regarding the thermodynamic modelling a reduction of U(VI) to U(IV) as shown for ^{99}Tc is rather unlikely since the measured redox potentials are more than 100 mV above the 50/50% borderline for U(VI)/U(IV) reduction. It seems more reasonable to assume the sorption of U(VI) species. It has been shown that the $CaUO_2CO_3$ species is rather weakly sorbing and thus also very stable against reduction when assuming a sorptive reduction process. This would be in line with the results observed.

Both single RN and cocktail experiments have been conducted for ^{237}Np(V). Results are depicted in Figure 10c. The results indicate the absence of an equilibrium state within the experimental duration of 232 d. There is a steady increase in sorption for ^{237}Np(V) up to ~90% after 232 d contact time. No difference is observable between the cocktail and the single RN samples indicating the absence of any competition effects. Since the pentavalent Np is known to sorb rather weakly the removal process might again be explained by a sorptive reduction process to Np(IV) at the surface of the FG material. This seems to be corroborated by thermodynamic considerations which predict Np(IV) species at around 60 mV in the pH range 8 to 10. Given the uncertainties of the $Eh_{(SHE)}$ measurements as noted above, the measured values are relatively close to the Np(V)/Np(IV) borderline. A transformation of Np(V) to Np(IV) and a subsequent sorption to the FG material can therefore be hypothesized as Np removal process.

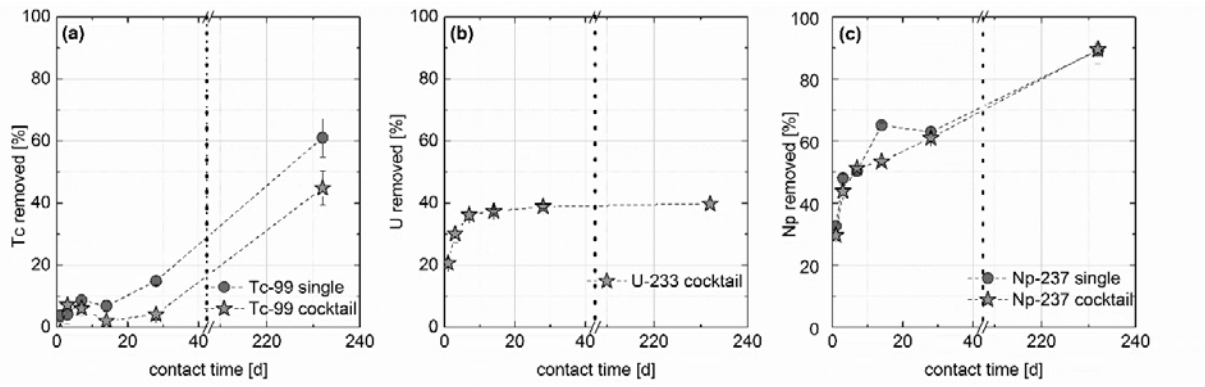

***Figure 10**: Results of (a) ^{99}Tc, (b) ^{233}U and (c) ^{237}Np batch sorption kinetic experiments.*

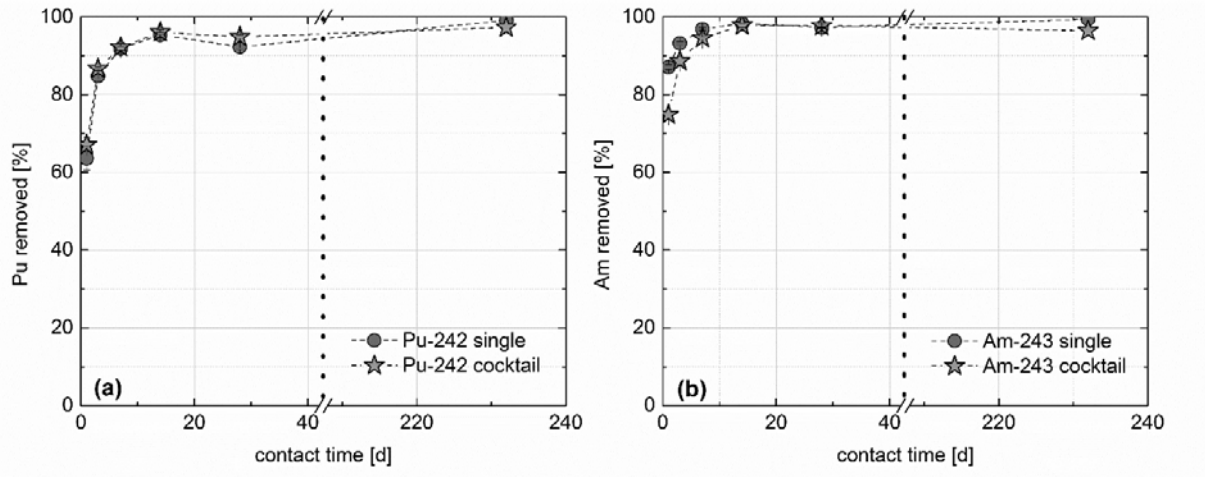

***Figure 11:** Results of ^{242}Pu (a) and ^{243}Am (b) batch kinetic sorption experiments.*

^{242}Pu(IV) and ^{243}Am(III)

With respect to ^{99}Tc, ^{233}U and ^{237}Np, ^{242}Pu(IV) shows a much faster sorption reaction since more than 80% is already sorbed after 3 d contact time as can be seen in Figure 11. The high degree of sorption was expected since the tri- and tetravalent RNs are known to sorb very strongly onto various mineral phases (Geckeis et al., 2013). The sorption increases to more than 90% after 7 d to 14 d possibly reaching already a steady state equilibrium process. After 232 d contact time, the sorption is even slightly higher at around 98%. This increase between 28 d and 232 d might indicate a very slow sorption reaction step. Again, no difference was observed between single RN experiments and cocktail experiments, respectively.

A very similar sorption behavior was found for ^{243}Am(III) compared to ^{242}Pu(IV). After 7 to 14 d, the sorption is > 95% reaching a plateau which can be interpreted as an equilibrium state. No difference is found between single RN experiments and cocktail experiments. A summary of the sorption values and associated distribution coefficients are listed in Table 6. The possibility of colloidal species has not been ruled out by centrifugation during sampling. Therefore, Kd values are minimum values. Regarding the maximum sorption values of up to 99%, only 1% of the total activity is left in the supernatant and either dissolved or sorbed on a colloidal phase. Considering the extreme that the remaining RN fraction is quantitatively colloid associated will have a great impact on the distribution coefficients. Assuming that the maximum distribution between mineral sorbed and colloid sorbed RN is 100:1 and that is valid for all radionuclides, only a minor effect on the distribution coefficients is expected in case of ^{99}Tc, ^{233}U and ^{237}Np. The distribution coefficients on FG are direct input data for the performance assessment models and play a key role with respect to the level of the concentration plateau in long-term tailings of the ^{242}Pu and ^{243}Am breakthrough curves in the field migration experiments, see Section 3.2.4.

Table 6: *Maximum sorption values and distribution coefficients of the RN sorption samples. Duplicates have been prepared and a value for each sample is given*

	Max. sorption [%]	**$K_{d\ min}$ [L/kg]**	**$K_{d\ max}$ [L/kg]**
^{242}Pu(IV)			
Single RN exp.	99	487	727
Cocktail exp.	98	122	322
^{243}Am(III)			
Single RN exp.	99	183	253
Cocktail exp.	96	71	171
^{233}U(VI)			
Cocktail exp.	40	3.6	3.8
^{237}Np(V)			
Single RN exp.	89	32	81
Cocktail exp.	90	38	60
^{99}Tc(VII)			
Single RN exp.	60	6.8	11.6
Cocktail exp.	45	3.7	5.8

Sorption data treatment

Using an exponential growth equation (Equation 1) sorption rates k [1/t] were fitted to the experimental datasets.

$$y = A_1 \cdot e^{\frac{x}{t_1}} + y_0 \quad with\ k = \frac{1}{t_1} \qquad 1$$

where y_0 is the radionuclide fraction in equilibrium that was removed by sorption.

The fitting results of the sorption data are given in Table 7. Sorption rates are given as negative values because the data is fitted over the radionuclide concentrations which are dissolved in solution. Therefore, the concentration will decrease with increasing sorption and negative rates are needed to describe this decline. These rates are needed as input parameters in numerical codes for performance assessment calculations like e.g. COFRAME (Reiche, et al., 2016). The fastest rates were found for Pu with values of ~-0.52 to -0.54 [1/d]. Am and U show very similar rates of -0.37 to -0.45 [1/d] (^{243}Am(III)) and -0.38 [1/d] (^{233}U(IV)). Although the rates for ^{243}Am(III) and ^{233}U(IV) are very similar the amount of sorbed species is totally different for these two radionuclides. That is, because the sorption rate is not sensitive to the final amount sorbed on the FG but to the gradient of the sorption data. Rates of around one order of magnitude lower were found in case of Np yielding values of -0.027 to -0.037 [1/d]. For ^{99}Tc(VII), the fitting routine was not successful due to the very low amount of ^{99}Tc(VII) sorbed within the first month of the experiments which can be seen as induction time for the higher sorption values that occurred after 232 days sorption.

RN desorption kinetics in the binary system

Subsequent to the sorption studies, desorption experiments were conducted to examine a possible sorption reversibility as function of the overall RN - FG contact time. The desorption data is presented in the following way: (i) the amount sorbed after the selected contact time is set to 100%, (ii) the amount desorbed after each desorption step is plotted as cumulative concentration as a function of time.

^{99}Tc(VII), ^{233}U(VI) and ^{237}Np(V)

Desorption kinetics for ^{99}Tc(VII) are depicted in Figure 12. As in all sorption samples contacted for < 28 days, the fraction of sorbed Tc is rather low, the desorption data are not considered reliable and highly affected by uncertainties. A reasonable trend of desorption rates with increasing contact time is therefore hard to be derived. For long contact periods (232 d), however, it is evident that the dissociation of Tc from the FG to solution is slow. In contrast to ^{99}Tc(VII), data for ^{233}U(VI) show a clearer trend between the sorption time and the reversibility. For short contact time samples coinciding desorption rate curves are obtained. Uranium desorbs, however, not completely until ~400 days, where only about 70% are removed from the FG surface. Uranium desorption rates decrease significantly after a contact time of 168 d and only 30% of uranium could be desorbed after 232 days sorption. This result highlights that the previous sorption time has a direct influence on the desorbable amount. A possible explanation for this observation might be found in a coupled sorption reduction transformation over time. That is, ^{233}U was sorbed initially as hexavalent ^{233}U on the FG material and was reduced to U(IV) by e.g. Fe(II) during the course of the experiment especially for the long-term samples. Since ^{233}U(IV) is showing a stronger sorption behavior as ^{233}U(VI), the total desorption and the desorption rate is expected to be less which is in line to the results described above. If a change of the uranium oxidation state can be neglected, the lower total desorption in the 232 d sorption sample can be explained by alteration of the mineral surfaces. Thereby part of the radionuclides are incorporated in the mineral matrix.

***Table 7**: Radionuclide sorption rates fitted to the batch sorption experiment results.*

	Rate [1/d]	**Error [±]**	**R2 [-]**
^{242}Pu(IV)			
Single RN exp.	-0.52	0.15	0.948
Cocktail exp.	-0.54	0.1	0.976
^{243}Am(III)			
Single RN exp.	-0.37	0.088	0.962
Cocktail exp.	-0.45	0.059	0.934
^{233}U(VI)			
Cocktail exp.	-0.38	0.053	0.98
^{237}Np(V)			
Single RN exp.	-0.037	0.017	0.84
Cocktail exp.	-0.027	0.011	0.9
^{99}Tc(VII)			
Single RN exp.		No fitting possible	
Cocktail exp.		No fitting possible	

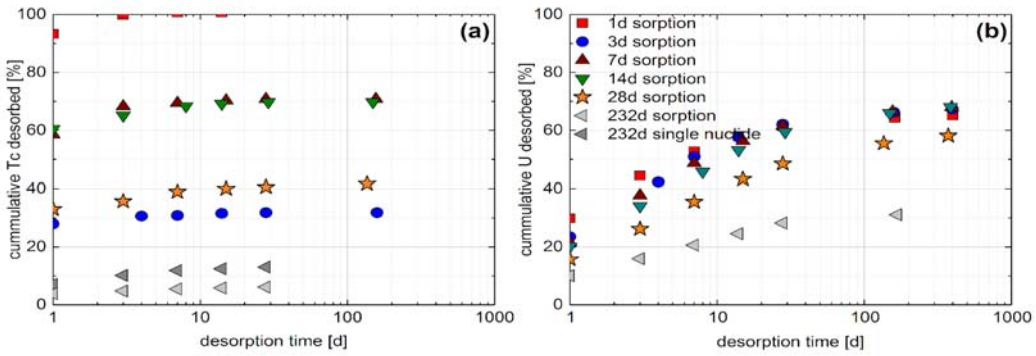

***Figure 12:** Results of (a) ^{99}Tc and (b) ^{233}U batch kinetic desorption experiments.*

An even clearer correlation between the previous sorption time and desorption rates is found for ^{237}Np(V) as shown in Figure 13. The longer the sorption time, the slower the desorption. The maximum desorption increases from ~30% after 1 d desorption up to ~68% after 399 d desorption for the 1 d sorption sample. For the 232 d sorption samples, the desorption values increase only from below 10% after 1 d up to a maximum of only ~20% after 168 d desorption. Moreover, the desorption kinetics slow down between 28 d and 168 d desorption time indicating near equilibrium conditions. Regarding short sorption times until 28 days, slightly higher desorption values (~5 to 10%) were observed for the cocktail samples compared to the single RN samples. A very similar explanation for the correlation between the sorption time and the Np desorption behavior is postulated as above for Tc. Np(V) was reduced to Np(IV) during the sorption experiments and removed via sorption to the FG material. The increasing amount of stronger sorbing Np(IV) for longer contact times during the sorption experiments is directly visible in the decreasing amount of desorbed Np for the longer contact times of the sorption samples within the desorption experiments.

Distribution coefficients have been calculated after each desorption time step of the 232 days sorption samples. These samples have been chosen because lowest recoveries have been observed in comparison to shorter sorption times and consequently highest K_d values. Distribution coefficients during desorption are in case of ^{99}Tc with values of 460±340 L/kg (Single RN) and 1060±610 L/kg (RN cocktail) up to two orders of magnitude increased, supporting the theory of a surface induced reduction to Tc(IV). Distribution coefficients are in case of ^{233}U with a value of 97±26 L/kg and ^{237}Np with values of 150±56 L/kg (Single RN) and 240±100 L/kg (RN cocktail) also increased. The maximal difference of only one order of magnitude is closer to the sorption derived distribution coefficients. Comparison to the distribution coefficients during sorption and desorption supports the theory of surface induced reduction in particular in regard of the ^{99}Tc sorption reversibility.

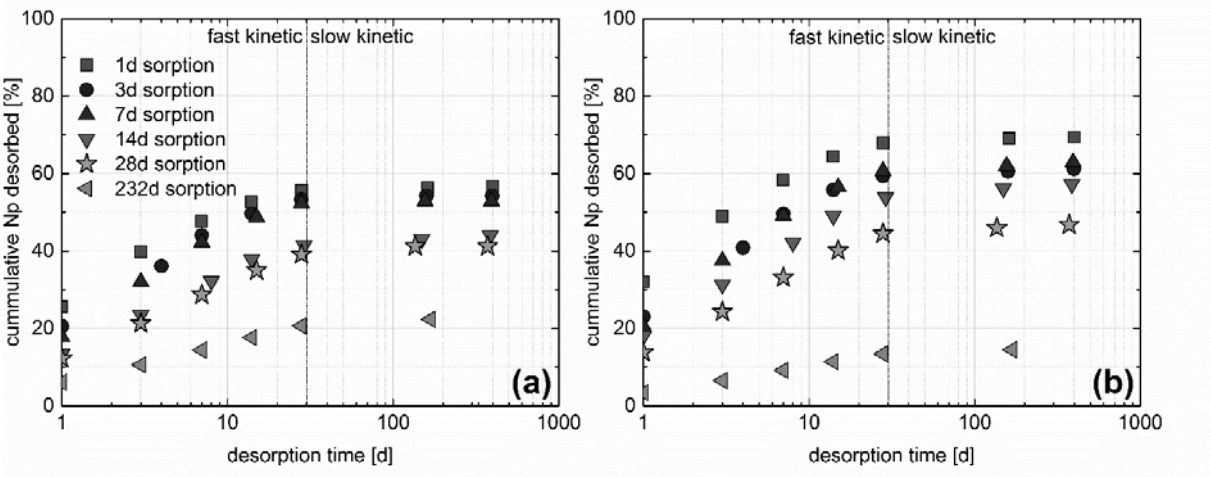

Figure 13: *Results of (a) ^{237}Np single radionuclide and (b) ^{237}Np cocktail kinetic desorption experiments, respectively.*

^{242}Pu(IV) and ^{243}Am(III)

The results of the desorption experiments for both ^{242}Pu(IV) and ^{243}Am(III) show a very similar trend (Figure 14). Both radionuclides are strongly and fast sorbing in the sorption experiments. Desorption increases from ~1% after 1 d desorption time to a maximum of ~15% (or even less) after 232 d desorption time. No clear dependence of desorption extent and rate on the contact time was observed. A very slow desorption kinetic might be seen in case of the single RN experiments especially for Pu. Even slower kinetics were observed for the cocktail experiment samples for Pu and Am single RN experiments. Unfortunately, no results for ^{243}Am cocktail sample series have been obtained due to very little amount of desorption lying below the detection limit of the ICP-MS, which is given with 0.3 ng/L (Table 8). Distribution coefficients have been calculated after each desorption time step of the 232 days sorption samples. These samples have been chosen because lowest desorption has been observed in comparison to shorter sorption times, except in case of the ^{242}Pu cocktail sample whereat all desorption samples are close together (Figure 14b). Average distribution coefficients of 670±300 and

810±450 L/kg have been obtained for the single nuclide and the radionuclide cocktail samples of ^{242}Pu, respectively. These values match with the distribution coefficients that have been determined during the sorption experiment (Table 6). An average distribution coefficient of 2700±1150 L/kg is determined in case of the ^{243}Am single nuclide desorption samples. This value is one order of magnitude above the distribution coefficient that has been observed during the sorption experiment. The difference of the Kd -values indicates the possibility of a colloidal species in the sorption samples and therefore under-determined distribution coefficients. Higher Kd values during desorption can also be explained by an alteration process, which immobilized part of the sorbed RNs by incorporation into the FG matrix. This effect was not observed in case of the ^{242}Pu samples and is therefore less probable. To conclude, both radionuclides show only very weak desorption in the range of the Kd values that have been observed during the sorption experiment.

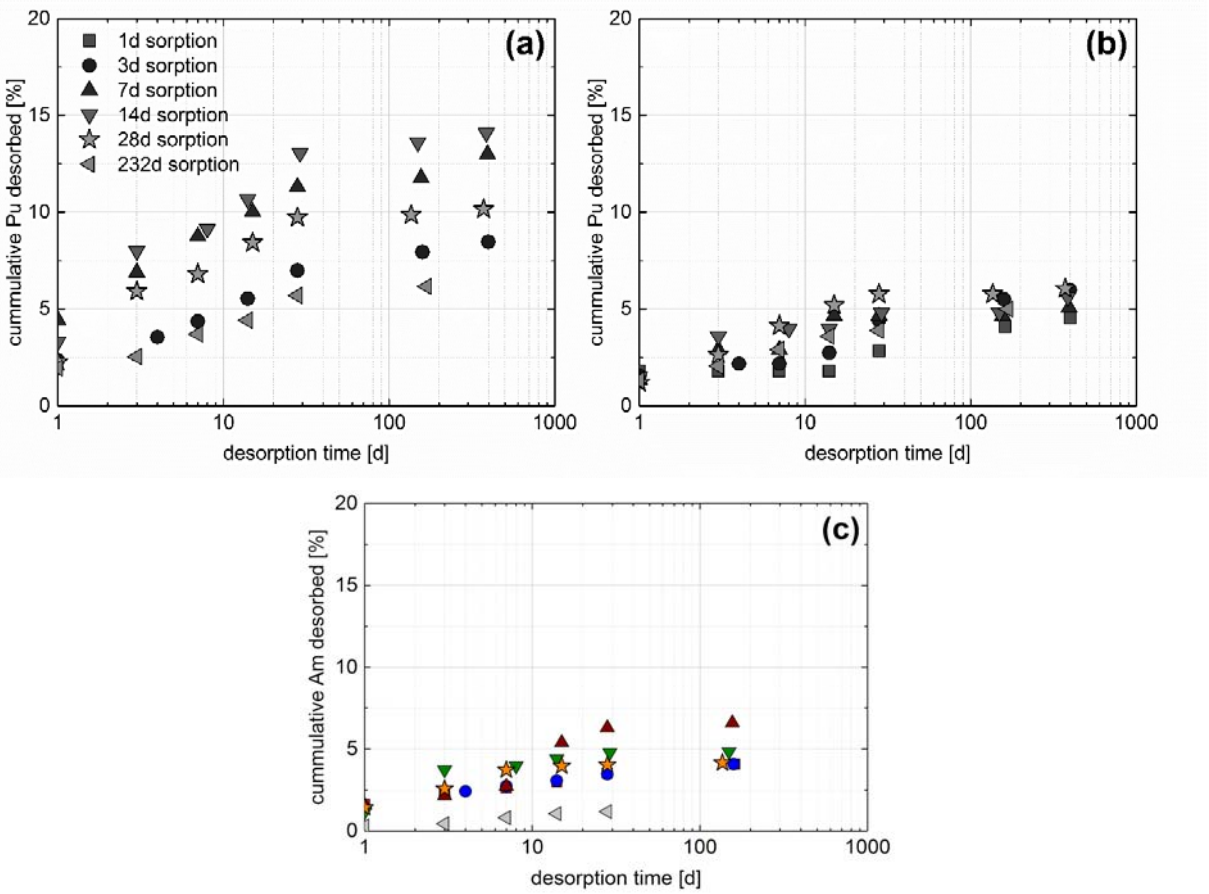

Figure 14: *Results of (a) ^{242}Pu single radionuclide, (b) ^{242}Pu cocktail and (c) ^{243}Am single radionuclide kinetic desorption experiments, respectively. The legend in (a) is valid for all diagrams*

Therefore, experiments adding montmorillonite colloids as concurrence ligand to the RN containing FG material samples were conducted to investigate if the desorption could be enhanced. Sorption time dependence during the desorption process has not been observed.

Desorption data was fitted using an exponential decay equation (Equation 2):

$$y = A_1 \cdot e^{-\frac{x}{t_1}} + y_0 \quad with\ k = \frac{1}{t_2} \qquad 2$$

Fitting the desorption data with Equation 2 was not successful for all radionuclides. Especially data of the redox-sensitive nuclides neptunium and uranium were not described satisfactorily. Therefore, a two-rate fit (Equation 3) was applied for these radionuclides because desorption of two oxidation states (e. g. Np(V) and Np(IV) in parallel cannot be neglected in case of the redox-sensitive radionuclides. Desorption of different surface associated species as shown in the speciation

diagram of uranium (Figure 6) that show different desorption behavior have to be taken into account and lead to a two-site desorption kinetic:

$$y = A_1 \cdot e^{-\frac{x}{t_3}} + A_2 \cdot e^{-\frac{x}{t_4}} + \ y_0 \ \ with\, k_1 = \frac{1}{t_3}\ and\ k_2 = \frac{1}{t_4} \qquad 3$$

Table 8: *Overview of the fitted desorption rates and measured radionuclide recoveries. Recovery denotes the radionuclide fraction found in solution after the desired contact time of desorption*

		Single nuclide samples				**RN cocktail samples**			
		1-rate fit	2-rate fit			1-rate fit	2-rate fit		
Sorp-tion time [d]	Desorption time [d]	k [1/a]	k_1 [1/a]	k_2 [1/a]	Recovery [%]	k [1/a]	k_1 [1/a]	k_2 [1/a]	Recovery [%]
					^{237}Np				
1	399	147 ± 24.2	409 ± 23.4	48 ± 3.5	57	150 ± 25.7	424 ± 28.0	47 ± 4.0	70
3	397	96 ± 12.9	479 ± 117.3	57 ± 7.8	55	95 ± 13.0	446 ± 115.0	56 ± 9.2	61
7	393	100 ± 89.2	296 ± 24.3	47 ± 3.4	53	93 ± 12.8	254 ± 24.0	38 ± 4.1	63
14	386	66 ± 10.7	351 ± 74.7	39 ± 4.6	44	68 ± 11.8	336 ± 57.4	36 ± 4.1	57
28	372	58± 10	323 ± 29.7	33 ± 1.9	42	67 ±10.0	319 ± 47.8	37 ± 3.4	46
232	168	50 ± 8.7	331 ± 35.5	29 ± 1.8	22	81 ± 11.8	273 ± 13.3	29 ± 0.8	15
					^{233}U				
1	399					132 ± 28.6	403 ± 51.8	33 ± 6.3	65
3	397					76 ± 12.9	301 ± 60.8	30 ± 7.0	67
7	393					69 ± 14.2	250 ± 31.0	23 ± 3.3	58
14	386	no single nuclide samples for U-233				47 ± 9.8	275 ± 61.5	21 ± 4.1	68
28	372					37 ± 8.2	260 ± 69.2	19 ± 3.7	58
232	168					52 ± 11.9	376 ± 52.4	25.4 ± 2.6	0.3
					^{99}Tc				
232	168	163 ± 41.9	380 ± 61.2	18.9 ± 8.0	14	217 ± 62.2	654 ± 128.3	32 ± 10.3	6.5
					^{242}Pu				
1	399	41 ± 16.2	622 ± 148.3	14 ± 3.1	13	9 ± 4.1		5 ± 2.2	5
3	397	27 ± 5.2	664 ± 297.3	20 ± 2.6	9	15 ± 3.4	13 ± 3.0	168167 ± 0	6
7	393	51 ± 14.1	351 ± 131.5	23 ± 7.8	13	57 ± 13.6	386 ± 530	39 ± 27.2	5
14	386	48 ± 11.0	253 ± 116.5	21 ± 9.3	14	52 ± 18.8	196 ± 53.3	1 ± 2.7	6
28	372	65 ± 12.4	227 ± 115.0	28 ± 13.7	10	58 ± 5.3	159 ± 81.7	41 ± 11.8	6
232	168	38 ± 7.8	1024 ± 1101.4	27 ± 4.5	6	32 ± 7.7	195 ± 86.4	12 ± 5.7	5
					^{243}Am				
1	399	36 ± 11.6	494 ± 73.9	15 ± 1.6	4				
3	397	39 ± 10.8	308 ± 57.8	11 ± 2.3	4				
7	393	32 ± 4.6			7				
14	386	100 ± 27.0	175± 44.1	3 ± 3.1	5	below ICP-MS detection limit			
28	372	113 ± 11.6	138 ± 11.6	3 ± 3.0	4				
232	168	34 ± 5.3	75 ± 37.9	9 ± 11.8	1				

RN desorption kinetics in the ternary system

Due to the strong binding and the slow release of the tri- and tetravalent actinides ^{242}Pu(IV) and ^{243}Am(III), a competing surface has been added to the system in order to force and to quantify the release rates of the RN from the FG. Single nuclide samples of ^{242}Pu(IV) and ^{243}Am(III) as well as the RN-cocktail samples have been included in this experiment. Therefore, the supernatant of each sample was exchanged after a total run-time of 400 days (sorption and desorption in the binary system) by a 35.9 mg/L Ni-labelled montmorillonite colloid containing suspension in GGW (Figure 3). ^{99}Tc and ^{237}Np single nuclide samples have not been included in this study because of difficulties in the quantification of the desorbed concentration due to low sorption values (^{99}Tc) or because a significant amount already desorbed in the binary system (^{237}Np). Nevertheless, both radionuclides are part of the radionuclide cocktail samples. After each desorption time step two samples were taken and the remaining supernatant was exchanged against fresh Ni-montmorillonite containing GGW. One sample was measured after centrifugation (18.000 rpm, 1h) and the remaining sample was measured without further treatment to differentiate between colloid bound and dissolved fractions. Collected kinetic data will be used to improve the input parameters of the transport code COFRAME (Reiche, et al., 2016).

^{99}Tc(VII), ^{233}U(VI) and ^{237}Np(V)

Desorption data for ^{99}Tc in the ternary system is depicted in Figure 15a. As explained in Chapter 3 desorption data values hold a high uncertainty. This results in recoveries above 100% that have been found in part of the shorter sorption time samples ($\leq$ 28 d). Samples with a sorption time of 232 d deliver once again the only reliable data and show an increase of the desorbed fraction from 6% in the binary to 40% in the ternary system for the latest sampling, respectively. Desorption equilibrium in the binary system was established within the first days of desorption. A fast kinetic was found but in case of the ternary system equilibrium is not reached within 211 days of desorption. Therefore, the desorption rate is only preliminary and smaller in comparison to the binary case although the 6-fold amount of Tc was desorbed from the FG. Analysis of ultra-centrifuged sample settlements show that 91% of the desorbed Tc is associated to montmorillonite colloids with only 9% being free in solution. This can be interpreted as a hint for the surface reduction process from weak sorbing Tc(VII) to strong sorbing Tc(IV), already mentioned before. In the ternary system Tc(IV) desorbs from the FG to attach selectively to the higher charged montmorillonite colloids.

Desorption data for ^{233}U in the ternary system is depicted in Figure 15b. Uranium desorption in the ternary system shows only minor differences in comparison to the latest values in the binary case. An additional fraction of 2% for the short time sorption samples going up with increasing sorption time to 9% for 232 d sorption in relation to the initial sorbed amount was remobilized. The last desorption value after 211 days desorption is set as equilibrium although there is still a small increase and desorption rates are derived in the range of 21 ± 5 1/a for all samples. These values are smaller compared to the desorption in the binary system. A sorption time dependence is not detectable. Under the assumption of a combined sorption and partial surface reduction process from U(VI) to U(IV) and the remobilization of the weaker sorbed U(VI) in the binary desorption experiments mainly U(IV) should be on the FG at the beginning of the ternary desorption. Analysis of the centrifuged samples showed that 76 ± 10% of the desorbed U is Ni-montmorillonite colloid associated while 24 ± 10% are free in solution. The relatively high diluted ratio is a hint for the presence of U(VI) in solution as one would expect U(IV) as sorbed species. Nevertheless, an analysis of this issue is due to very low concentrations ($< 1 \cdot 10^{-10}$ M in solution) not possible.

Desorption data for ^{237}Np in the ternary system is depicted in Figure 15c. The behavior of ^{237}Np is very similar to ^{233}U. A small additional fraction of 3% to 8% in relation to the values in the binary system, which is increasing with higher initial sorption time is released during desorption in the ternary system. The last desorption value after 211 days desorption is set as equilibrium value and desorption rates are derived in the range of 32 ± 7 1/a for all samples which is significantly lower compared to the rates in the binary system. Analysis of the centrifuged samples showed that 60 ± 12% of the desorbed Np is Ni-montmorillonite colloid associated while 40 ± 12% free in solution. The relatively high dilution ratio is a hint for the presence of Np(V) in solution as one would expect Np in the oxidation state +IV as sorbed species. As in the case of U further analysis of this issue is due to very low concentrations ($< 1 \cdot 10^{-10}$ M in solution) not possible.

^{242}Pu(IV) and ^{243}Am(III)

The results of ^{242}Pu and ^{243}Am desorption experiments are depicted in Figure 16 and results are given in Table 9. Both Pu and Am samples show significant desorption triggered by the addition of a sorption surface and the tendency of both radionuclides to sorb on the Ni-montmorillonite particles. The three- to five-fold Pu fraction is released from the FG during desorption in the ternary system in comparison to the binary system for both cocktail and single nuclide experiments. This is an average increase of the recovery from 5% after desorption without, to 25% in the presence of montmorillonite particles for the cocktail experiments and from 11% to 31% in case of the single nuclide experiments, respectively. Desorption is not sorption time dependent and desorption rates are with an average value of 40 ± 9 a^{-1} (cocktail samples) and 52 ± 30 a^{-1} (single nuclide samples) very close to the average value found in the binary system. Analysis of the centrifuged samples found that ≥97% of the released Pu is colloid associated. In case of the Am single nuclide sample series, the reversible bound fraction increased from 4 ± 3% to 12 ± 4% by the addition of Ni-montmorillonite particles. The desorption rate is in the ternary system with a mean value of 23 ± 6 a^{-1} even lower in comparison to desorption rates in the binary system with a mean value of 59 ± 12 a^{-1}. Centrifugation of the samples found that > 99% of the released Am is colloid associated.

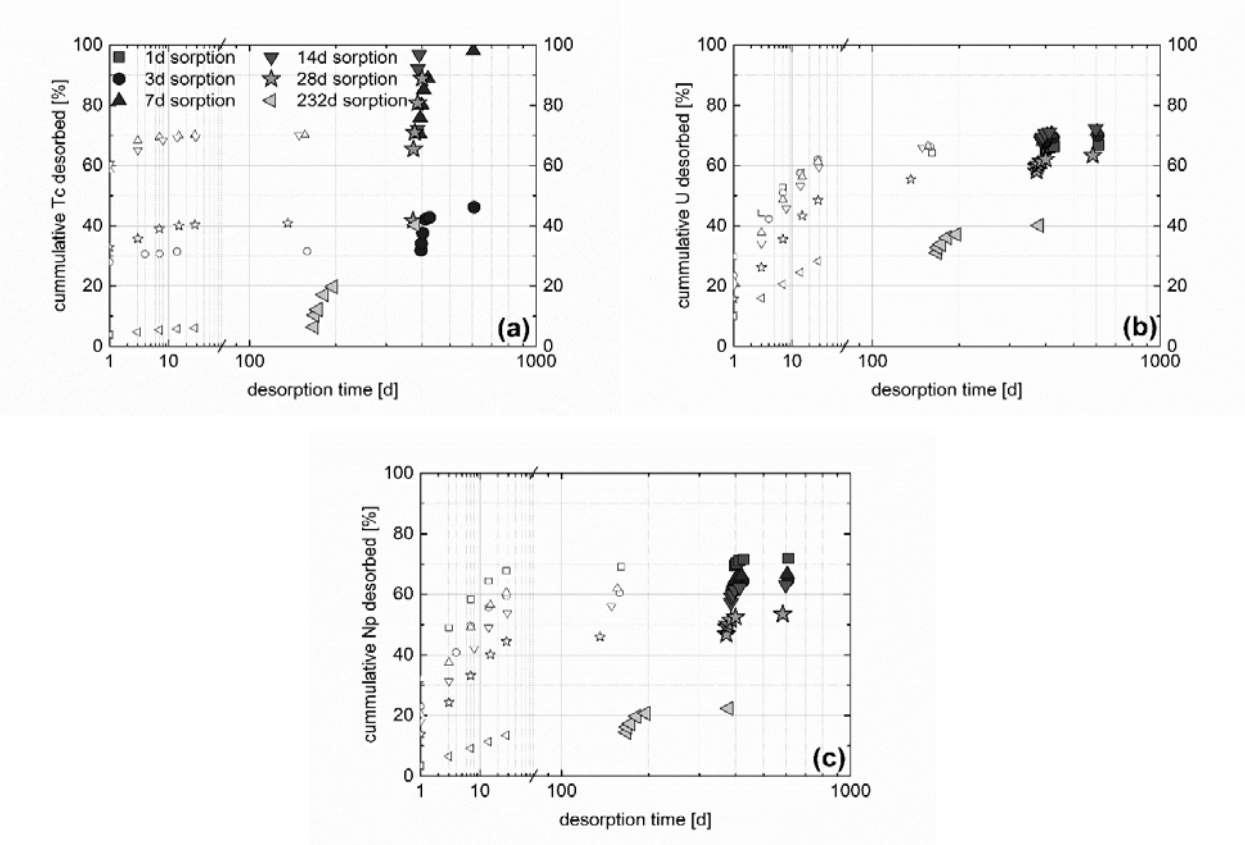

***Figure 15**: Results of ^{99}Tc (a), ^{233}U (b) and ^{237}Np (c) desorption experiments of the radionuclide cocktail sample series. A combination of the desorption in the binary (open symbols) and the ternary system (filled symbols) over the desorption time only. The legend in (a) is valid for all diagrams.*

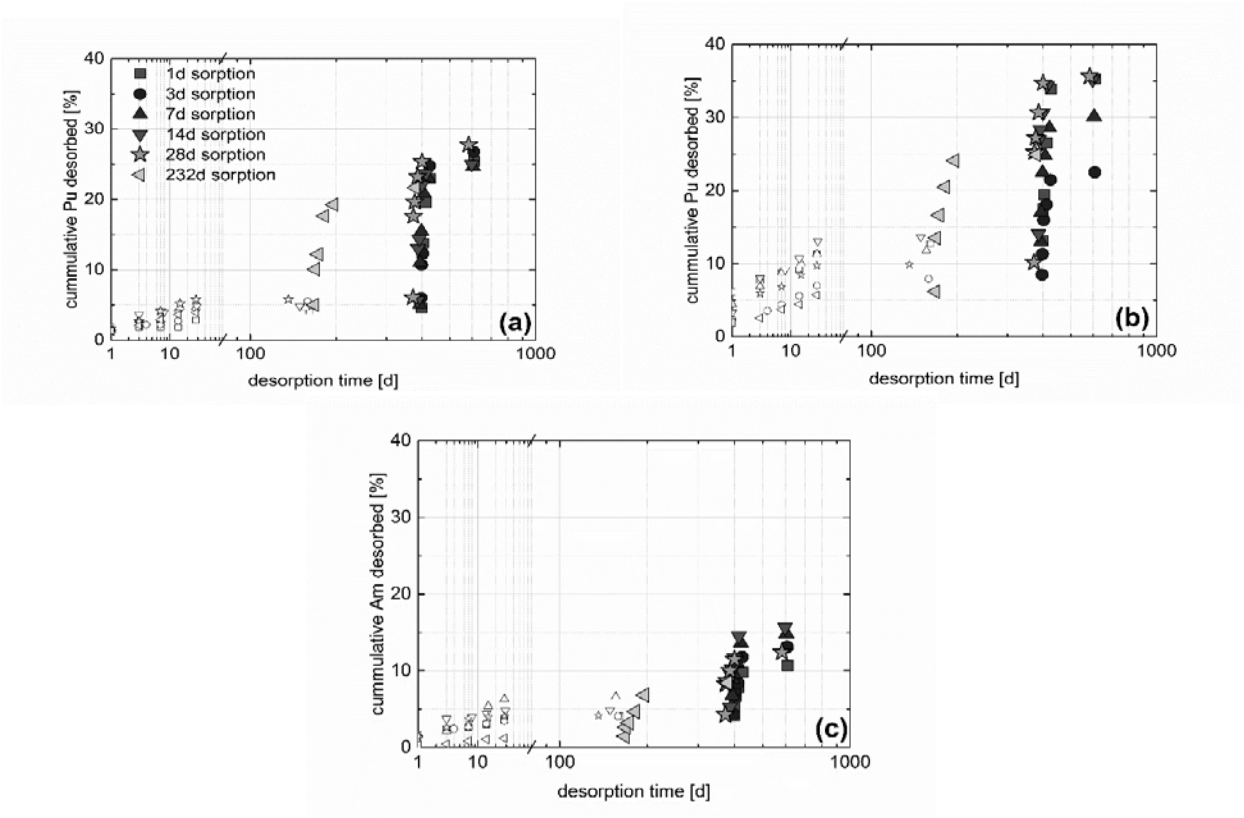

***Figure 16**: Results of ^{242}Pu (cocktail (a) and single nuclide (b)) and ^{243}Am (single nuclide (c)) desorption experiments. A combination of the desorption in the binary (open symbols) and the ternary system (filled symbols) over the desorption time only. The description in (a) is valid for all diagrams.*

***Table 9**: Results of ^{242}Pu (cocktail (a) and single nuclide (b)) and ^{243}Am (single nuclide (c)) desorption experiments. A combination of the desorption in the binary (open symbols) and the ternary system (filled symbols) over the desorption time only. The description in (a) is valid for all diagrams.*

Sorption time	Desorption time, binary	Rate, binary k [1/a]	Recovery [%]	Desorption time, ternary [d]	Rate, ternary k [1/a]	Recovery [%]
			^{99}Tc, cocktail experiments			
1 d	399	-	102%	211 d	-	109%
3 d	397	-	32%	211 d	-	46%
7 d	393	-	70%	211 d	-	98%
14 d	386	-	72%	211 d	-	141%
28 d	372	-	42%	211 d	-	125%
232 d	168	217 ± 62	6%	211 d	6.5 ± 1	40%
			^{233}U, cocktail experiments			
1 d	399	132 ± 29	65%	211 d	17 ± 2	67%
3 d	397	76 ± 13	67%	211 d	22 ± 3	70%
7 d	393	69 ± 14	68%	211 d	27 ± 6	71%
14 d	386	47 ± 10	68%	211 d	20 ± 4	72%
28 d	372	37 ± 8	58%	211 d	21 ± 6	63%
232 d	168	52 ± 12	31%	211 d	16 ± 3	40%
			^{237}Np, cocktail experiments			
1 d	399	150 ± 26	69%	211 d	27 ± 4	72%
3 d	397	96 ± 13	61%	211 d	35 ± 6	65%
7 d	393	95 ± 13	63%	211 d	39 ± 9	67%
14 d	386	68 ± 12	57%	211 d	33 ± 7	63%

Sorption time	Desorption time, binary	Rate, binary k [1/a]	Recovery [%]	Desorption time, ternary [d]	Rate, ternary k [1/a]	Recovery [%]
28 d	372	69 ±10	47%	211 d	33 ± 12	54%
232 d	168	48 ± 7	14%	211 d	24 ± 4	22%
		^{242}Pu, cocktail experiments				
1 d	399	9 ± 4	5%	211 d	31 ± 9	25%
3 d	397	15 ± 3	6%	211 d	34 ± 7	27%
7 d	393	57 ± 14	5%	211 d	45 ± 9	25%
14 d	386	52 ± 19	6%	211 d	43 ± 12	25%
28 d	372	65 ± 6	6%	211 d	53 ± 27	28%
232 d	168	32 ± 8	5%	211 d	33 ± 7	22%
		^{242}Pu, single nuclide experiments				
1 d	399	41 ± 16	13%	211 d	26 ± 4	35%
3 d	397	27 ± 5	8%	211 d	37 ± 7	23%
7 d	393	51 ± 14	13%	211 d	36 ± 8	30%
14 d	386	48 ± 11	14%	211 d	85 ± 51	35%
28 d	372	65 ± 12	10%	211 d	84 ± 47	36%
232 d	168	38 ± 8	6%	211 d	44 ± 14	25%
		^{243}Am, single nuclide experiments				
1 d	399	36 ± 12	4%	211 d	23 ± 3	11%
3 d	397	39 ± 11	4%	211 d	19 ± 5	13%
7 d	393	32 ± 5	7%	211 d	21 ± 4	15%
14 d	386	101 ± 27	5%	211 d	25 ± 9	16%
28 d	372	113 ± 12	4%	211 d	32 ± 14	12%
232 d	168	34 ± 5	1%	211 d	17 ± 2	8%

2.1.2 LIT mock-up: RN release, resin selection and overcoring test

2.1.2.1 Mock-up status

Bentonite erosion studies have been conducted in an artificial fracture set-up to simulate the intrusion of dilute glacial melt water in a repository. Natural Febex bentonite or a mixture with synthetic montmorillonite and GGW were used for this type of experiments to keep it close to the expected scenario in LIT.

The artificial fracture set-up consists of an acrylic glass housing that is built up by three parts, namely a lower and an upper plate and a cylindrical spacer that is placed inside the arrangement (Figure 18). A ring shaped compacted bentonite sample with inner diameter of 40 mm, outer diameter of 80 mm and 25 mm in height is located in the middle of the setup and the spacer is placed in the center of this ring to avoid any kind of swelling towards the center of the setup. The parts of the housing around the bentonite ring are not in contact. Thereby a slit with an aperture of 1 mm height and 180 mm in diameter is formed that mimics a parallel-plate synthetic fracture around the bentonite source and allows the granitic groundwater to reach the bentonite. Natural Grimsel groundwater is pumped through the synthetic fracture with constant flow rate of 50 µL/min. Modelling the flow velocity at the water-bentonite interface from the given volume flux with COMSOL Multiphysics yields a maximum velocity of $1.2 \cdot 10^{-5}$ m/s and a maximum shear stress of $3.3 \cdot 10^{-5}$ Pa. The flow velocity distribution within the 1 mm fracture set-up at the initial stage before the bentonite extrudes into the fracture is shown in Figure 19. The shear stress for instance determines if particles are removed from the gel-water interface in advection controlled systems (Neretnieks, et al., 2009).The dimensions of the compacted bentonite ring are identical to the long-term in-situ test (LIT) which is running since May, 2014 within the CFM project located at GTS. Four of these experiments are located at INE. Two are still running, one under ambient conditions and the other one is located in an Ar glove box. The experiment

under anoxic conditions has a slightly different bentonite composition (following the idea of LIT with addition of Zn-labelled synthetic montmorillonite) and holds three of the LIT radionuclide cocktail vials.

Over the course of the experimental duration after an initial swelling phase the release of Tc-99, U-233 and Np-237 as well as the conservative tracer Amino-G could be monitored in the outflow samples (Figure 17). Integrating the fluorescence detection of Amino-G over the first 315 days revealed a recovery of 12.2 mg with a monitored average flow velocity of 44µL/min. Taking into account the average initial mass of 8.55 mg per vial (see chapter 2.2.2.2) the estimated recovery is in the range of 48%. For the radioisotopes monitored with SF-ICP-MS recoveries of ^{99}Tc 108 ± 11%, 233U 0.8 ± 0.1% and ^{237}Np 1.3 ± 0.2% after 315 days could be determined. Here, one has clearly to state that the later described measurements via AMS revealed that the measured mass-99 recovery might be highly overestimated due to potential isobaric (^{99}Ru) and neighboring ($^{98/100}$Mo) interferences in the SF-ICP-MS measurements. Interestingly, the observed plateau value of ^{237}Np for the diffusion controlled release in the range of 6.7 ± 0.9 10-12 mol/L. This can be compared to a radial or planar diffusion model to investigate the release process and clearly linked to the redox state (Np(IV) or NP(V)) prevailing in the mock-up test (see chapter 3.3.2).

The last phase of LIT was the overcoring and the retrieval of the radionuclide holding bentonite packer system. Thereby a large diameter over core containing the bentonite source as well as the near-field observation boreholes was planned to extract the complete LIT experiment and the direct contact area with the MI shear zone. It was mandatory that the bentonite source and the extruded bentonite in the fractured near field remained as intact as possible during the overcoring process. Therefore, a supporting feasibility study to find a suitable way to conserve the sample during overcoring was established. To preserve the extrusion of the bentonite into the shear zone and directly measure the extrusion distance the conceptual idea was to use a resin directly injected into the water conducting feature. Therefore, a laboratory bentonite erosion experiment with identical dimensions and composition to LIT (excluding radionuclides) was used to identify the optimum overcoring procedure.

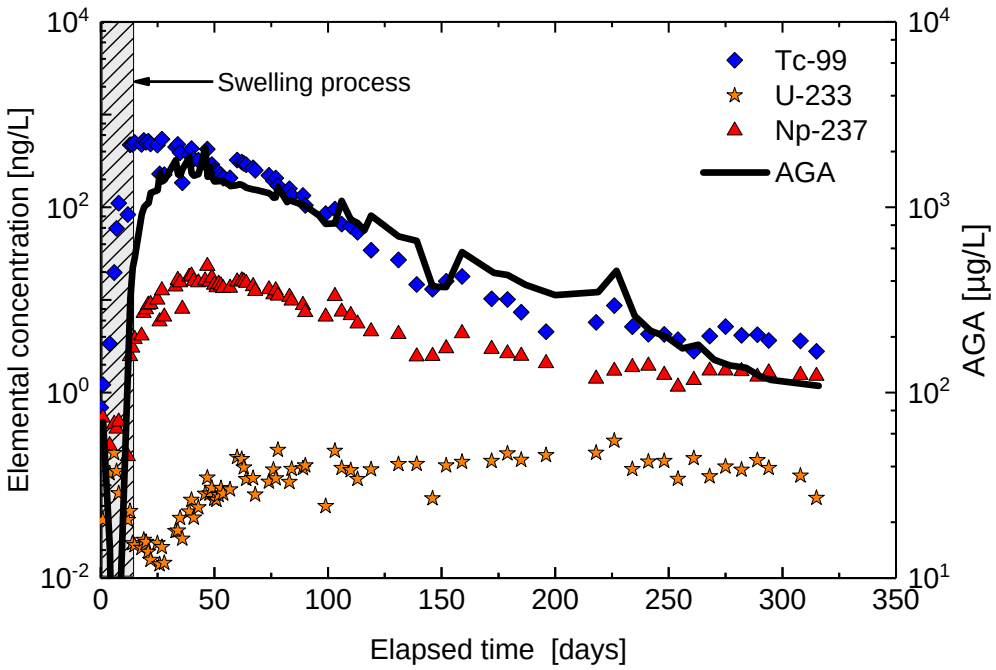

Figure 17: *Release of Tc-99, U-233 and Np-237 and the conservative tracer Amino-G (AGA) in the Mock-up experiment under Argon atmosphere.*

2.1.2.2 Resin selection

Resin impregnation test on fracture filling material (FFM)

Three possible resins have been pre-selected for the feasibility test of LIT overcoring, namely, LR white (Sigma-Aldrich Inc.), Sika-52 (Sikadur-52 Injection, Sika AG) and Araldite 2020 (Huntsman International LLC). First experiments were carried out on natural fracture filling material (FFM) from GTS in the grain size of 1 - 2 mm to select the best-suited resin prior to impregnation of the mock-up experiments due to the limited number of mock-up tests. Resin hardening was tested at 4 °C, 12 °C and 22 °C and in contact with Grimsel FFM. Constant temperature was ensured by resin curing in contact with a water bath. Most resins are not compatible to moisture and samples should be dried prior to impregnation, which is not possible in the shear zone around LIT. Therefore, water saturated FFM with a water content of 10.5 ± 2 % H_2O was used as well as oven-dried FFM at 60 °C, in order to simulate extreme cases. In addition, water saturated FFM was once washed with methanol to eliminate part of the water, which is a procedure that was applicable for LIT overcoring. Each sample contained ~ 6 g of water saturated FFM in the size range of 1-2 mm and the material was contacted with 5 mL of the respective resin. After addition of the resin, the samples rested 18 hours for curing.

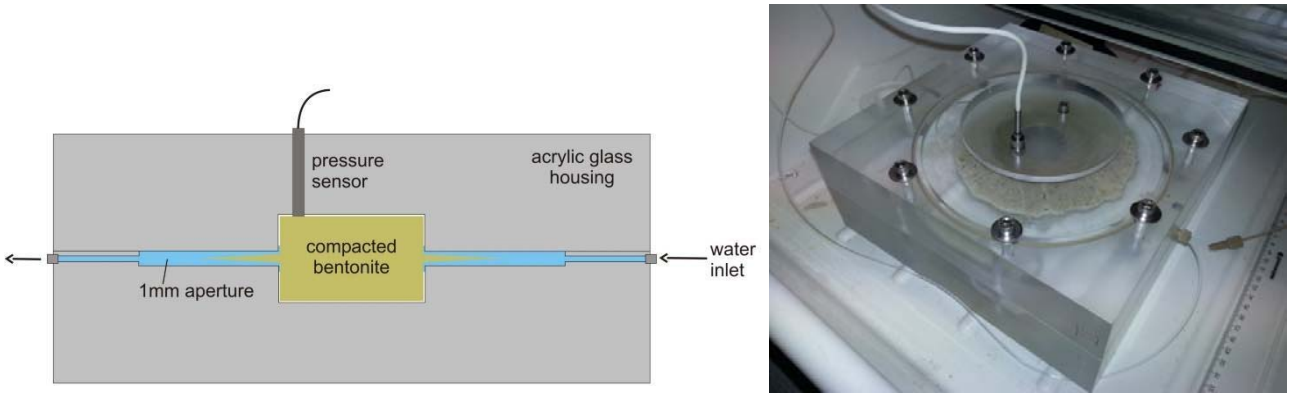

Figure 18: *(left) Schematic arrangement of the bentonite erosion experiment and (right) bentonite erosion experiment set-up as installed in the lab. Pressure monitoring sensor on top (white cable).*

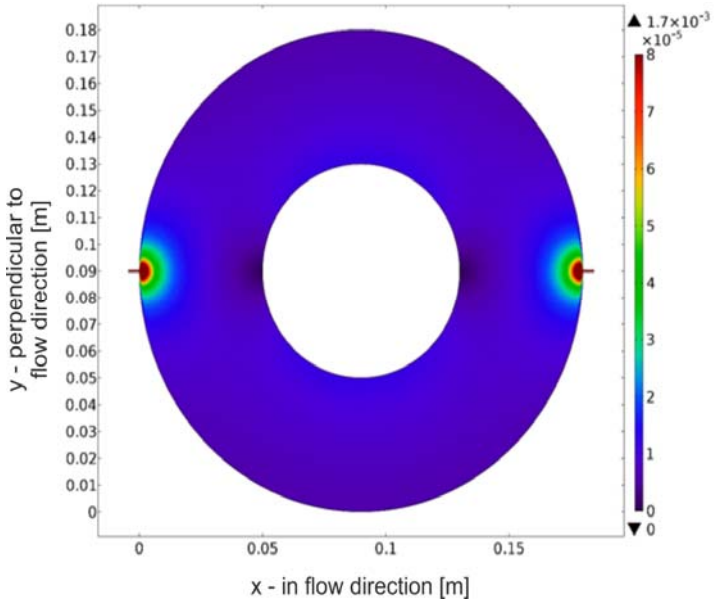

***Figure 19**: Flow velocity distribution in the 1mm artificial fracture erosion experiments calculated with COMSOL Multiphysics for the initial condition before swelling into the fracture*

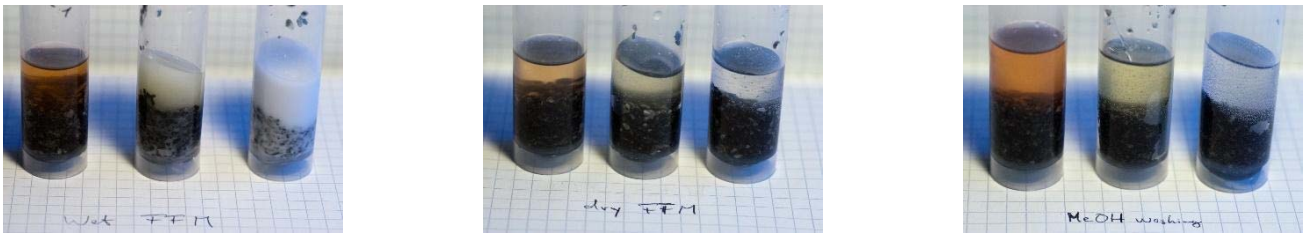

Wet FFM | Dry FFM (60 °C | MeOH washed FFM

***Figure 20**: FFM after different pre-treatment and in contact with LR white, Sika-52 and Araldite resin (from left to right, respectively) after hardening at 12 °C.*

LR white resin did not cure properly in any test case although it was strictly prepared according to the instruction manual. It only showed partial hardening in some cases but did not harden at all in the majority of cases. The only observation was a color change from light yellow to brown. LR white samples can be found in Figure 20 (left sample in each picture).

Sika-52 and Araldite resin cured properly in all test cases. In contact with water saturated FFM, the resin turned cloudy, which was not the case when the FFM was dried or washed with methanol. All Sika-52 and Araldite samples resulted in well-stabilized FFM. Phase separation in form of air or water inclusions were not visible. LR white is not suitable but hardening of Sika-52 and Araldite was complete at all tested temperatures. Therefore, LR white was not part of the following tests.

- FFM impregnation after washing with GGW/methanol mixtures

In order to test the water compatibility of the resins Sika-52 and Araldite 2020, a series of curing experiments with varying water content was performed. Therefore, dry FFM (1-2 mm, 5g) was in contact with four different GGW/methanol (5 mL) mixtures for several hours; 90% MeOH, 80% MeOH, 70% MeOH and 50% MeOH.

The GGW/methanol mixture was discarded and exchanged against 5 mL resin. Curing took place in a water bath at 12 °C.

The washing mixture was removed carefully but a small portion stayed attached to the FFM. However, phase separation was not observed in any case after curing. Up to the 80%-MeOH mixture Sika-52 samples remained clear but a higher water content caused cloudy samples (Figure 21). In case of Araldite even washing with only 70%-MeOH gave a clear cured result indicating that it is more compatible to moisture then Sika-52 resin.

The above-mentioned samples were taken out of the sample container and cut to investigate the interface between resin and FFM and to evaluate differences in the degree of fixation. All samples were cut on a low speed saw with a water-cooled, diamond-coated blade. **Araldite 2020** samples showed strong connection between FFM and the resin. All samples remained intact during cutting. Phase separation or liquid inclusions are not visible. Cut surfaces are smooth**. Sika-52** samples showed strong connection between FFM and the resin. All samples despite one remained intact during cutting. Again, phase separation or liquid inclusions are not visible and cut surfaces are smooth. In case of one sample (80/20 % MeOH) a crack appeared during cutting and the sample broke shortly after cutting. An upper and a lower part could be divided easily and the connection within this sample seemed to be weaker. There was no hint for the disintegration of this sample.

- Febex bentonite impregnation after swelling in contact with GGW and washing with methanol/GGW mixtures

Compacted Febex bentonite with a dry density of 1.65 g/cm3 was broken into bigger pieces (1-2 g per piece). 1-2 pieces with a weight of 2 g were used to simulate impregnation of the bentonite swelling zone. In a first step, the bentonite was contacted with GGW. One series was contacted with 1 mL GGW to investigate partly saturated samples and another series was contacted with 5 mL GGW to investigate fully saturated bentonite samples. In a second step remaining water was discarded and the samples are washed with MeOH or a 80/20% MeOH/GGW mixture in order to decrease the water content. One additional sample was used without washing. The experimental procedure is illustrated in Figure 22 and 23 and the sample list is given in Table 10.

Cured samples showed good connection to the top layer of the bentonite sample. As the curing process started immediately after addition of the resin, it did not penetrate into the bentonite sample. Only the top layer was preserved. These samples were not cut because the resin was on top of the bentonite. Cutting with a water cooled saw at the interface between bentonite and resin would have led to washing out of the bentonite.

As a result Araldite 2020 resin was selected as the most promising resin for impregnation of the LIT bentonite source and gel layer as the compatibility to water is slightly higher in comparison to Sika-52 resin.

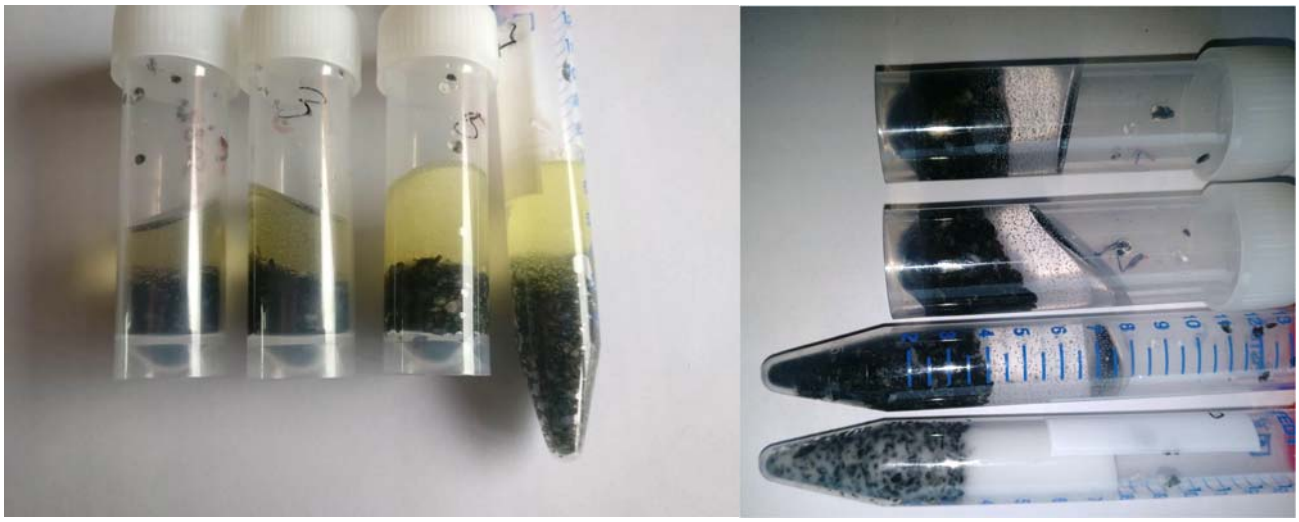

Figure 21*: FFM Resin impregnation after washing with 90/10, 80/20, 70/30, 50/50% MeOH/GGW mixture (from left to right). Sika-52 samples are shown in the left and Araldite samples in the right picture*

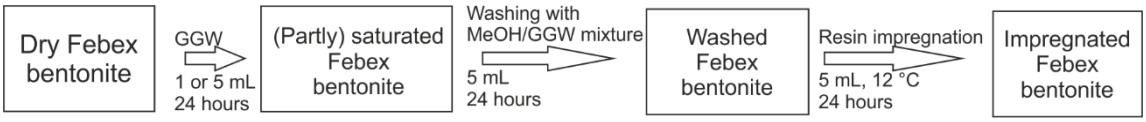

***Figure 22**: Experimental procedure for Febex bentonite impregnation*

***Table 10**: Sample list and details for Febex bentonite impregnation.*

#	GGW volume [mL]	Washing with (5 mL)	Resin
1	5	MeOH	Sika-52
2			Araldite
3		80/20 % MEOH/GGW	Sika-52
4			Araldite
5		No washing	Sika-52
6			Araldite
7		MeOH	Sika-52
8			Araldite
9	1	80/20 % MEOH/GGW	Sika-52
10			Araldite
11		No washing	Sika-52
12			Araldite

***Figure 23**: Araldite impregnated Febex samples; #2, 4, 6, 8, 10, 12 from left to right*

2.1.2.3 Mock-up test overcoring

Before overcoring of LIT the feasibility of the procedure was tested on one of the mock-up experiments described in Chapter 2.1.2.1. The test cell was modified by three boreholes on the upper part of the cell in a distance of roughly 4-5 cm from the bentonite source (Figure 24). These drill holes represent the LIT near-field monitoring holes, which were used during LIT overcoring for resin injection. By adding these boreholes to the mock-up, GGW flow through the test cell was still feasible at any time. Resin injection was simulated over the nearfield boreholes and under comparable conditions to LIT, in order to investigate the stability of the bentonite gel layer during the procedure. One concern before the test was the loss of bentonite material due to high resin flow rates during injection.

LIT mock-up overcoring test was performed in four steps: (1) Realization of basic parameters comparable to LIT, particularly in regard of rock temperature and fracture orientation, (2) EtOH injection into the fracture, (3) One-step resin injection and cold curing at 15 °C and (4) Overcoring of the bentonite sample in the workshop at the Grimsel Test Site.To (1): The rock temperature at GTS is at approximately 15 °C and the dipping angle of the MI shear zone is around 70°. In order to realize these parameters, the resin injection test was performed in a tempered water bath with the correct fracture orientation (Figure 25). Roughly, 40 to 50 % of the cell was in contact with the water bath.

To (2): EtOH was injected into the fracture in order to decrease the amount of water around the bentonite sample. GGW flow through the cell was not switched off and remained constant at approx. 50 µL/min while the cell was still in horizontal orientation. The free fracture volume was calculated to ~16 mL. A dye (bromothymol blue) was added to visualize the exchange of water for EtOH and later EtOH for resin. Bromothymol blue shows orange/red colors in EtOH and changes to blue in contact with the resin. 35 mL of colored EtOH have been injected over the observation boreholes. The flow was adjusted to 1 mL/min for each injection point. Injection was only successful over two out of three injection ports as one point was blocked.

To (3): Araldite 2020 resin was injected over the two remaining injection ports. A total of 46 mL has been injected at 0.5 mL/min. The low injection rate was chosen to protect the gel layer. Resin was stored in the tempered water bath to slow down the curing process. Curing of the resin was performed at 15 °C in the tempered water bath for 14 hours. The interface between the resin and the colored EtOH turned blue. Mixing of the phases has not been observed. The result of this resin injection is shown in Figure 26. The bentonite gel layer remained intact and no material was lost during washing and injection. However, the bentonite source was not completely surrounded by resin and the top part was not sealed. Therefore, the missing resin was injected directly in the open area. As the resin injection lines were sealed with resin at this point, a new hole was drilled in the cell and the resin was injected with a syringe. The final impregnated sample is shown in the right picture of Figure 26.

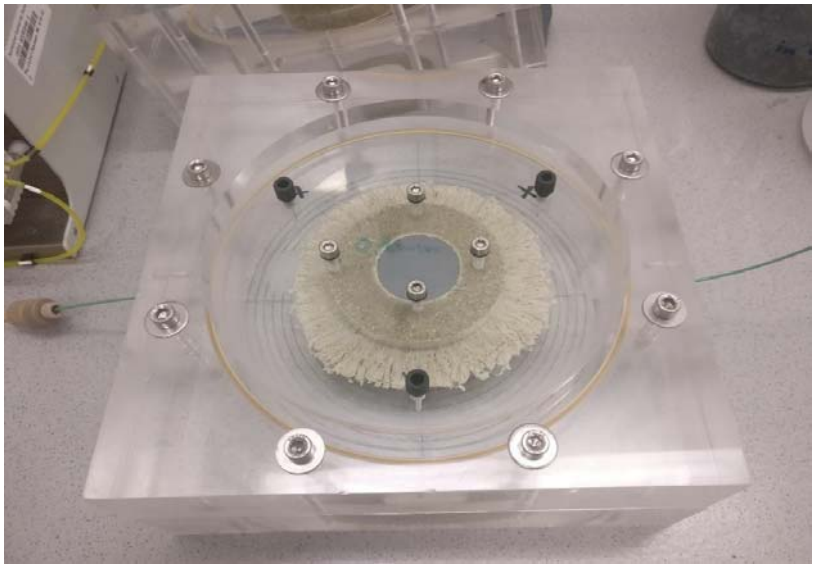

***Figure 24**: Bentonite erosion experiment used for LIT mock-up overcoring*

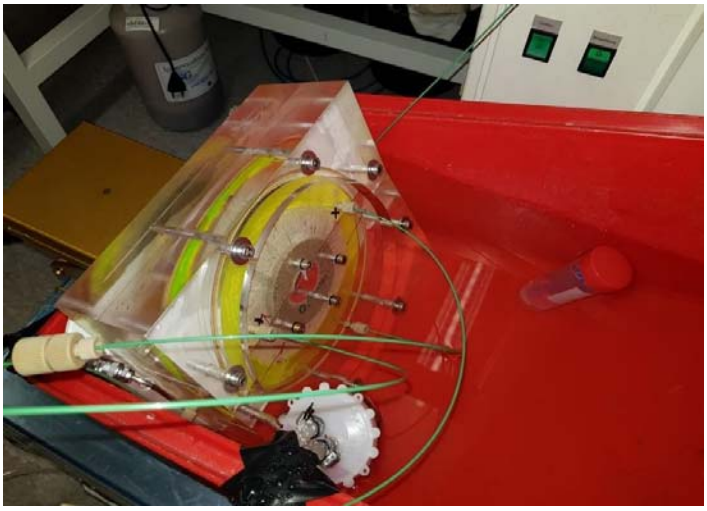

***Figure 25**: Test cell orientation in a tempered water bath during resin injection and curing*

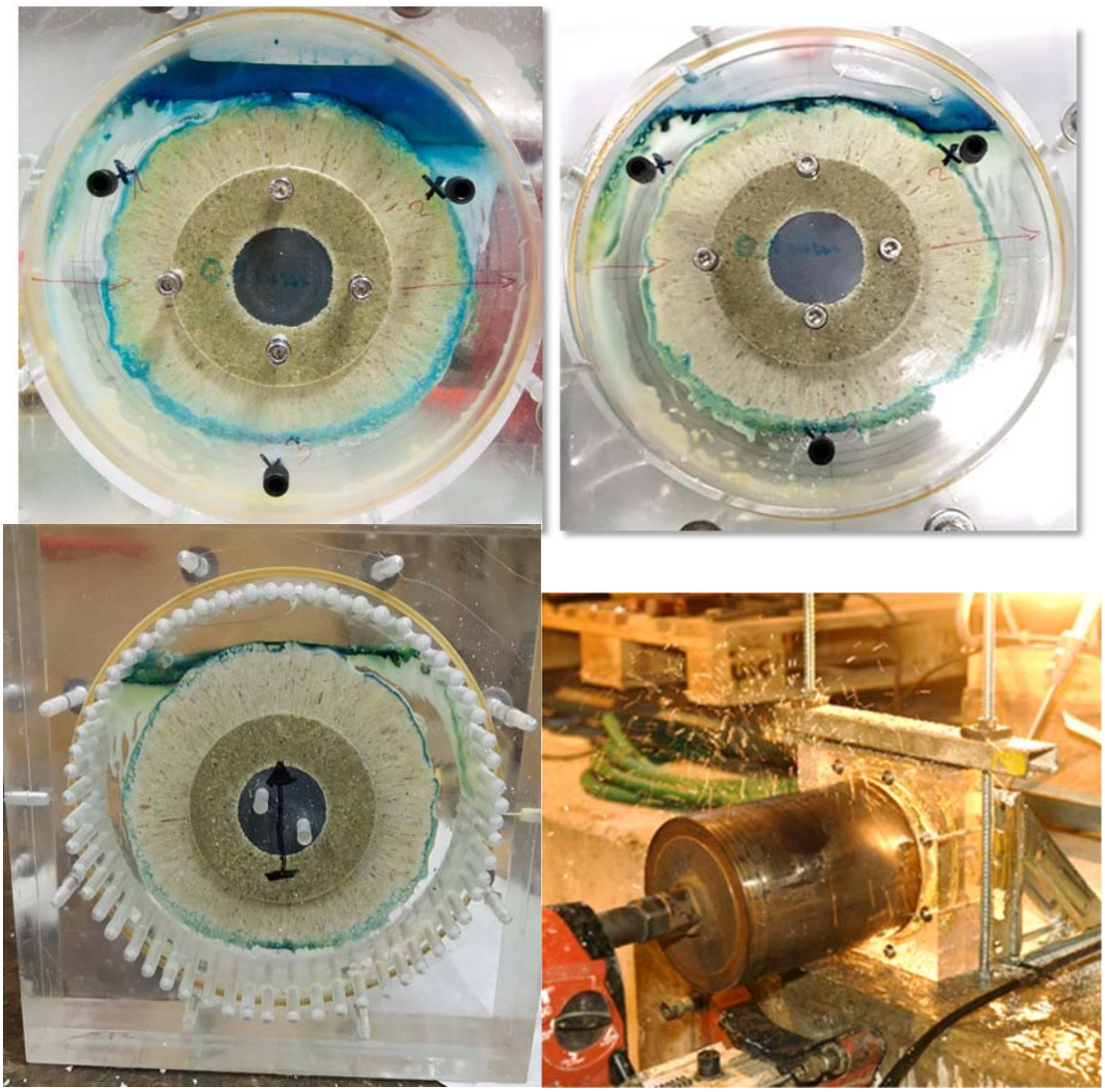

***Figure 26**: LIT mock-up after first (upper left) and second (upper right) resin injection. The blue color indicates regions with higher EtOH ratios. Prepa-ration for the overcoring (lower left) and water pressure during mack-up test overcoring (lower right).*

To (4): The impregnated mock-up experiment was transferred to GTS to simulate the overcoring process and to test the sample stability during the overcoring process. First overcoring tests on the acrylic glass set-up showed that the core drill crown is not designed for this material due to the smooth, polished surface. First drill results were poor as the acrylic glass began to melt in contact with the core drill crown. In order to weaken the acrylic glass and to offer the core drill crown some roughness, small holes were drilled at the contact area between the mock-up housing and the core drill crown (Figure 26, lower left). Core drilling was successful after modification of the set-up. It has to be mentioned that the drilling was performed with water-cooling (see Figure 26, lower right). Due to the water pressure used a wash out effect was initiated and this resulted in almost a complete loss of the bentonite gel layer during the drilling process. However, the resin surrounding the bentonite gel layer outer surface remained intact and would at least provide an information of the maximum bentonite swelling distance into the fracture. The reasoning for the wash out can be found in the rather poor connection between the resin and the smooth surface of the acrylic glass. An additional explanation might be the observed swelling pressure release taking place as soon as the crown cuts through the upper part of the acrylic glass set-up. Thereby the artificial fracture aperture increased. The hardened resin lost connection to the acrylic glass and drilling fluid could reach and wash out the gel layer.

The results show how important it is to protect the gel layer from the drilling fluid during the overcoring process. Due to the rough granodiorite surface in the LIT shear zone, connection between the fracture surface and the resin is supposed to

be much stronger and water intrusion between the surfaces expected to be unlikely. Furthermore, the LIT core should preserve the bentonite swelling pressure during drilling as the core also holds the near-field monitoring boreholes and the packer systems are still intact during overcoring.

2.2 Field experiments

2.2.1 AMS analysis of samples from the CFM 13-05 in situ radionuclide tracer test

GGW samples from the in-situ radionuclide tracer test CFM run 13-05 were selected for AMS analysis of the actinide tracers. The chosen samples were collected along a time interval from 0.01-660 days from the starting of the experiment. Sample preparation has been described previously, as well as the measurements carried out according to the multi-actinide analysis with AMS at the Vienna Environmental Research Accelerator (VERA) of the University of Vienna (Vienna, Austria) (Quinto et al., 2015). In this way, concentration of the tracers ^{233}U, ^{237}Np, ^{242}Pu and ^{243}Am (Figure 27-30) were determined over five orders of magnitude. The lowest levels were observed for all the actinide tracers in the sample collected at Pinkel surface packer in December 2014 (Pinkel-12-14) and were equal to 0.31±0.11 ppq, 0.43±0.05 ppq, 0.137±0.003 ppq and 0.025±0.002 ppq for ^{233}U, ^{237}Np, ^{242}Pu and ^{243}Am, respectively (Quinto, et al., 2017). The maximum concentration was determined in correspondence to the peak of the breakthrough curves of the actinide tracers in different samples taken at the collection point of the dipole of run 13-05 and were equal to 537±197 ppq for ^{233}U at 2 days from the starting of the experiment in sample CFM-13-29 (Figure 27), 5058±612 ppq for ^{237}Np at 3 days in sample CFM-13-31 (Figure 28) and 14896±163 ppq and 2102±195 ppq for ^{242}Pu and ^{243}Am, respectively, at 1.5 days in sample CFM-13-27 (Figure 29 and 30) (Quinto, et al., 2017).

Unexpected signal of ^{233}U, ^{237}Np, ^{242}Pu and ^{243}Am in the first five samples CFM-13-1 to CFM-13-10 before the peak arrival of the injected actinide tracers (Figure 27-30) were observed and could be explained as a background level coming from the previous in situ tracers experiments[2]. To this purpose, as described in (Quinto, et al., 2017), we have carried out further AMS analysis looking for the only two actinide tracers exclusively injected in CRR Run 2 and not employed in CFM Run 13-05 nor in other in situ radionuclide tracer tests, namely ^{241}Am and ^{244}Pu. In selected samples of CFM run 13-05 we have determined with AMS low but significant levels of ^{241}Am and ^{244}Pu. We could rule out that such ^{241}Am and ^{244}Pu signals would represent isotopic impurities in the actinide cocktail and in the ^{239}Pu and ^{248}Cm solutions used as internal tracers. This has proven that the levels of ^{241}Am and ^{244}Pu were inherent to the samples and therefore originate from the CRR test carried out in 2002 (Quinto, et al., 2017).

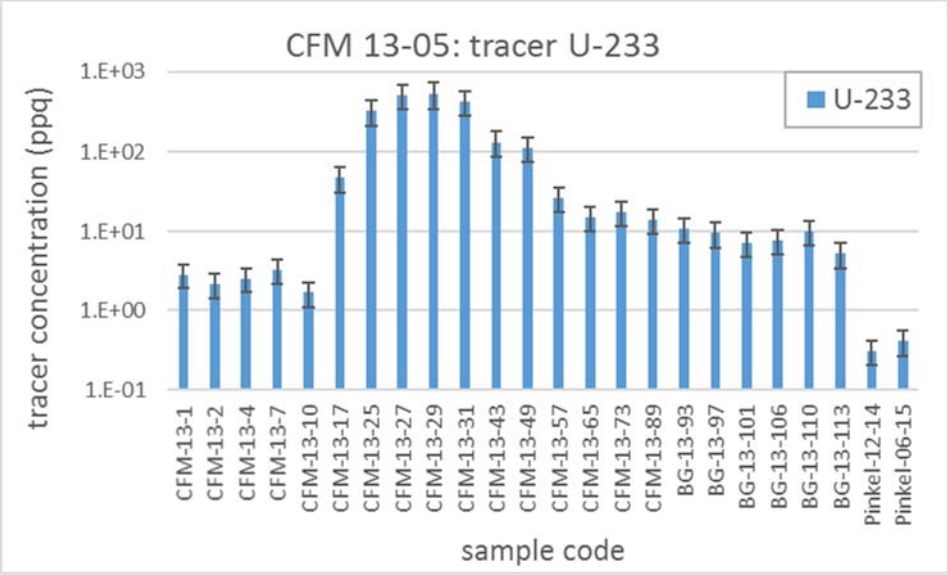

***Figure 27**: ^{233}U concentration (ppq) determined with AMS in chosen samples of the CFM run 13-05.*

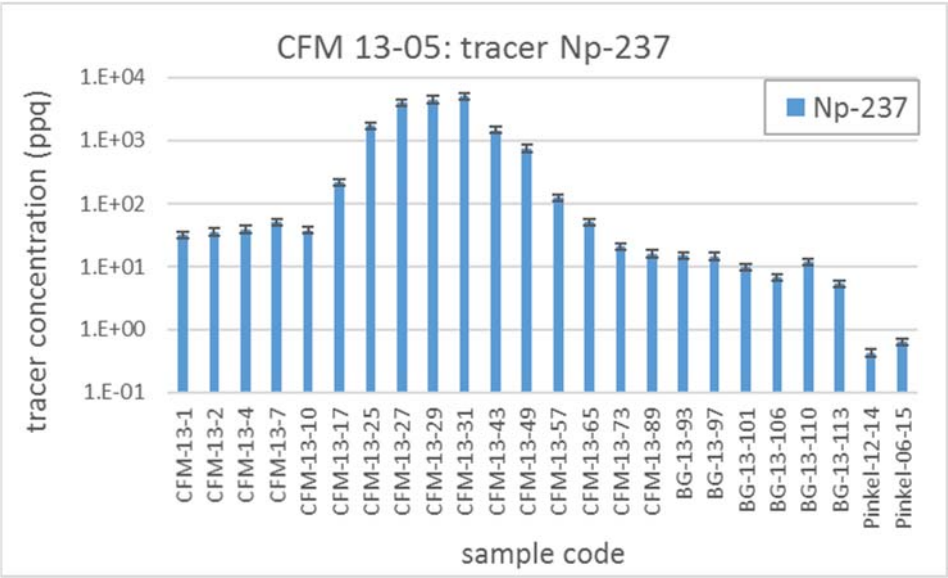

***Figure 28**: ^{237}Np concentration (ppq) determined with AMS in chosen samples of the CFM run 13-05.*

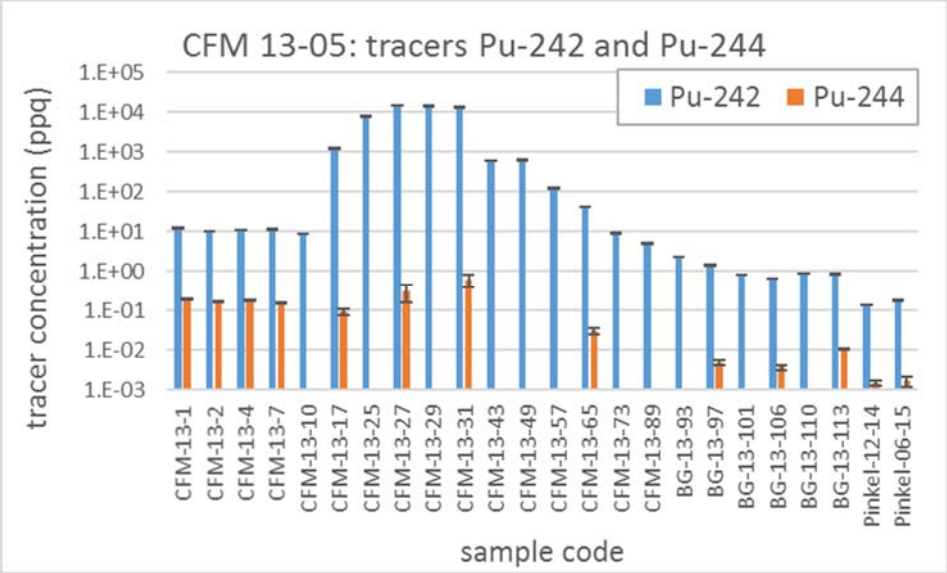

***Figure 29**: ^{242}Pu and ^{244}Pu concentration (ppq) determined with AMS in chosen samples of the CFM run 13-05.*

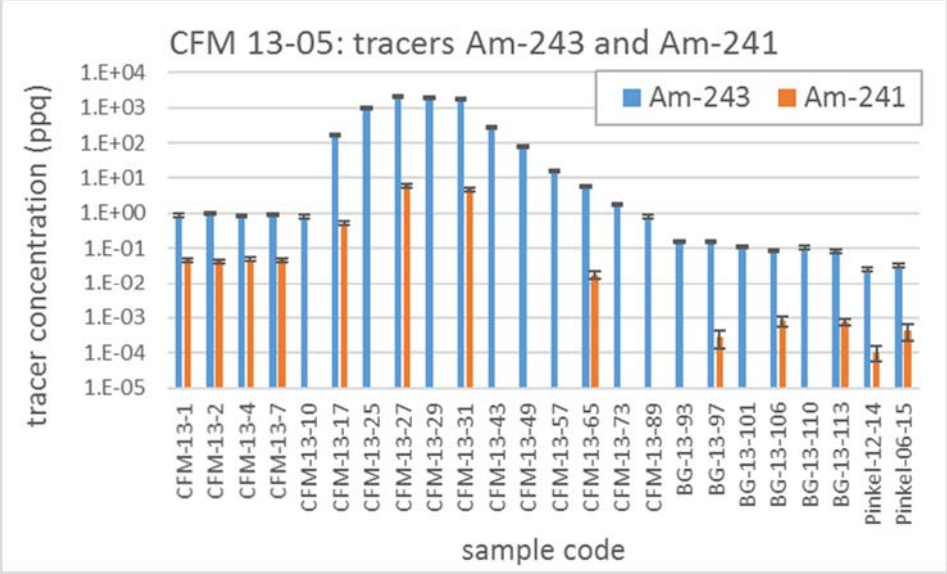

***Figure 30**: ^{243}Am and ^{241}Am concentration (ppq) determined with AMS in chosen samples of the CFM run 13-05.*

The shape of the breakthrough curves of the actinide tracers gave indication of their preferential migration mechanism. While the concentrations of ^{237}Np, ^{242}Pu, and ^{243}Am (Figure 28, 29 and 30) in the samples after the peaks were significantly lower than those determined before the arrival of the injected cocktail, the levels of ^{233}U after the peak were higher than those preceding it. These different trends could reflect a preferential stripping of Pu and Am from the fracture via binding to bentonite colloids, while Np(V) and U(VI) preferentially exist as dissolved species. The shape of the breakthrough curve of Np could be interpreted as an indication of a partial reduction and adsorption/precipitation of Np(IV) in the shear zone, which also might be partially desorbed by bentonite colloids. With the extreme sensitivity of AMS, we have investigated the long-term release and retention of the actinides up to 8 months in the tailing of the breakthrough curve of CFM 13-05 as well as in samples collected up to 22 months after at the "Pinkel" surface packer. Furthermore, the detection ^{241}Am and ^{244}Pu injected within the previous in situ test CRR Run 2 has proven the release from the fracture of actinide tracers employed up to 13 years before. This finding gives strong indications for the reversible and kinetically controlled interaction of actinides with fracture filling material and demonstrates the strong analytical capabilities of AMS for allowing the long-term in situ studies over a time span of more than a decade (Quinto, et al., 2017).

2.2.2 REMO tests

The aim of these tests was to determine the ability to re-mobilize colloids that have been "filtered" in the geosphere from the Tracer Test Run 13-05. (Ryan & Elimelech, 1996) discussed a variety of colloid mobilization processes including changes in water chemistry (e.g. acid injection) and shear strains induced by hydraulic water pulses. The water geochemistry in the shear zone is typically stable so the focus here is on flow rates or the treatment with an additional surface (bentonite colloid suspension) to change the sorption equilibrium established and remobilize nanoparticles and/or associated radionuclides. This chapter is only a summary of the key activities performed in the years 2016 and 2017 within the CFM project. A detailed summary can be found in the NAGRA reports NAB 16-63[2] and NAB 18-30[3].

During the tracer test of Run 13-05 in the monitoring period until 10.12.2015 4.1% ^{237}Np, 25.4% ^{243}Am, 28.7% ^{242}Pu, 15.2% ^{233}U and 35-37% of the injected colloids (mixture of Ni-montmorillonite and Febex bentonite derived colloids) were recovered, whereas 92.6% of the conservative tracer Amino-G were retrieved.

After the tracer test Run 13-05 the following tests have been performed that might have affected colloid stability and retained radionuclides in the region of CRR dipole D-1 prior to the REMO tests:

- Dewatering tests with open boreholes and pulse tests for permeability determination, which are documented in detail in Nagra Aktennotiz AN 14-116 (10 – 30 January 2014)
- LIT emplacement (NTB 15-03) (Schlickenrieder, et al., 2017)
- Tracer Test Run 15-01, documented in Nagra Aktennotiz AN 15-529 (09.10.2015)

The strongest influence on the near field could be expected during the "dewatering" of the shear zone by opening surface packers and borehole intervals as part of the preparation for the LIT emplacement. In order to minimize the flow from CFM 06.002, surface packers Roof-N, Roof-S, Kalotte and Floor C were opened together with the shear zone intervals of the monitoring boreholes (CFM 11.001, CFM 11.002 and CFM 11.003) around CFM 06.002. This resulted in a significant pressure drop in the shear zone around the tunnel. In addition, further disturbance occurred from pulse tests performed before/after the dewatering test, to check whether there was any change in hydraulic properties. However, it is rather unlikely that the two short pulse withdrawal tests performed in BOMI 87.010-i2 with a withdrawal of 100 ml over about a minute and induced pressure changes of 3.43 and 3.97 kPa have resulted in any significant mobilization of colloids, but it has to be considered in any interpretation of later data.

The proposed colloid remobilization tests had some limitations concerning the design, which were (a) a controlled method with sufficient flow rate to mobilize colloids, (b) the possibility to sample and monitor via LIBD the test before and afterwards, (c) an appropriate radioprotection (GTS BAG license) and (d) most importantly a minimal interference with the LIT test.

REMO 1: The remobilization test setup was installed in CRR 99.002-i2 including turbidity meter, a s-curve LIBD and an optimal LIBD system. Colloid background monitoring was performed with a flow rate of 5 ml/min prior to the start of the mobilization tests. For the stimulation two different flow rates were chosen, the first stimulation was initiated on the 26.04.2016 at 7:30 a.m. with a flow rate of 58 ml/min and a duration of 5 min leading to an overall pressure drop of 63 kPa in CRR 99.002-i2. Only a minor change in colloid concentration was seen in the turbidity and LIBD data.

---

[2] Blechschmidt, Lanyon, Kontar, Rösli, Schlickenrieder (2017): GTS Phase VI – CFM Phase 3: Field Activities January to December 2016. Nagra Arbeitsbericht NAB 16-63, Wettingen (CH), pp. 55.

[3] Blechschmidt, Schneeberger, Lanyon, Rösli, Kontar (2018): GTS Phase VI – CFM Phase 3: Field Activities January to December 2017 Data Report. Nagra Arbeitsbericht NAB 18-30, Wettingen (CH), pp. 66

***Table 11**: Selected list of samples taken from CRR 99.002-i2*[4]

Sample	Date	Start sampling time	End sampling time	Volume [ml]	Vial number
REMO-CRR99.02-1	25.04.2016	10:54	14:14	1000	1
REMO-CRR99.02-2	25.04.2016	14:15	17:35	1000	2
REMO-CRR99.02-3	25.04.2016	17:36	20:56	1000	3
REMO-CRR99.02-4	25.04.2016	20:58	00:18	1000	4
REMO-CRR99.02-5	26.04.2016	00:19	03:39	1000	5
REMO-CRR99.02-6	26.04.2016	03:40	07:00	1000	6
REMO-CRR99.02-7	26.04.2016	07:01	07:32	~150	7
REMO-CRR99.02-8*	26.04.2016	07:33	07:40		8
REMO-CRR99.02-9	26.04.2016	07:41	08:41		9
REMO-CRR99.02-10	26.04.2016	08:42	09:42	300	10
REMO-CRR99.02-11	26.04.2016	09:43	10:44	300	11
REMO-CRR99.02-12	26.04.2016	10:45	11:45	300	12
REMO-CRR99.02-12A**	26.04.2016	11:00	11:05	~1000mL	12A

Samples REMO-CRR99.02-13 to REMO-CRR99.02-30 (4.4.2016 21:20h) are not listed in the table.

**First stimulation pulse. Maximum water outflow from the pressure line collected into the automatic sampler bottle number 8.*

***Second stimulation pulse. Maximum water outflow from the pressure line collected directly after the flow meter with a separate bottle 12A.*

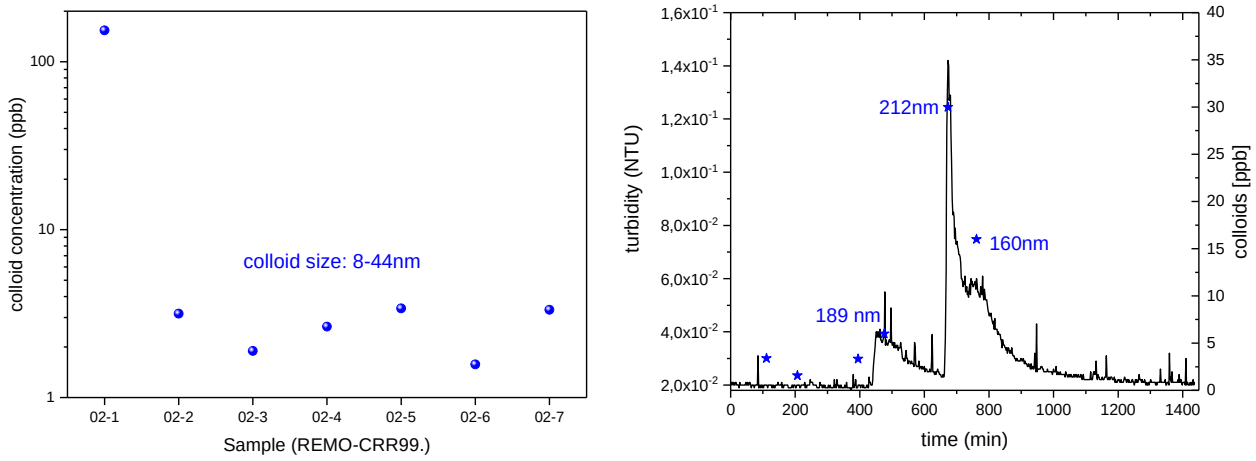

***Figure 31**: (left) colloid concentration (ppb) determined with LIBD before the start of the experiment showing the disturbance through the experimental setup reaching a plateau value, (right) In-line colloid monitoring through turbidity measurements (NTU) and direct measurements using in-line LIBD. Samples 02-5 to 02-7 also shown for comparison.*

The second hydraulic stimulation performed on the same day starting at 11:00 a.m. with 5 min duration and a maximum flow rate of 192 ml/min lead to a pressure drop of 239 kPa in borehole CRR 99.002-i2. During the testing campaign, samples were continuously taken from both CFM 11.002-i2 and CRR 99.002-i2. A two-circuit LIBD measured colloid content at both of these intervals for three days. Samples collected from the two intervals were sent to KIT for analysis. The turbidity meter (TIN-Turb) shows a concentration peak of 0.14 NTU (background 0.02 NTU) in the second hydraulic stimulation and a smaller peak with 0.04 NTU units in the 1st stimulation.

As visible from the data shown in Figure 31 (left) after connection of all the tubing for the REMO 1 test significant colloids/nanoparticles mobilized artificially were detectable in sample 2-1, but levelled off in the course of the background measurements to values around 2-3 ppb with an average size around 8-44 nm. It has to be mentioned here that measured

[4] Blechschmidt, Lanyon, Kontar, Rösli, Schlickenrieder (2017): GTS Phase VI – CFM Phase 3: Field Activities January to December 2016. Nagra Arbeitsbericht NAB 16-63, Wettingen (CH), pp. 55.

sizes below 20 nm are below the calibration of the LIBD and are interpolated. Starting the hydraulic stimulations, the concentration rises in the first stimulation pulse to approx. 6 ppb and in the second stimulation pulse up to ~30ppb, levelling thereafter off. During the pulse experiments the average size detected significantly increase to values around 189nm (1st stimulation) and 212nm (2nd stimulation). By simply looking to the average sizes mobilized this demonstrates clearly that the hydraulic perturbation mobilized a different colloid/nanoparticle population than seen in the background measurements.

The LIBD was installed near the LIT monitoring boreholes and connected to the flow control cabinet to measure colloids at the constant rate of 0.02 ml/min from interval CFM 11.002-i2 (circuit 1) to further investigate if the REMO-1 test has any influence on the LIT experiment. Here, no significant changes could be monitored.

REMO 2: The conceptual idea of this test was the injection of a high concentration colloid suspension as competing surface in the CRR dipole. Radionuclides remaining from Tracer Test Run 13-05 on the fracture wall should be released via desorption to the colloids or attached “old” colloids mobilized through the suspension. The experiment was carried out as a "pump and treat" or "push/pull" type test in CRR 99.002-i2. Colloids were injected at a rate of 25 mL/min followed by a shut-in period without flow before extraction took place at 25 mL/min. Pinkel outflow was not changed during the whole experiment. The LIBD monitoring was connected to the outflow line from the Pinkel surface packer. Injection and extraction were observed by monitoring fluorescence, turbidity and mean size and concentration of the suspension (PCS). The set-up of the experiment including the calibration of the on-site equipment is described in detail in NAB 18-30. In brief, the test was started on 9 May 2017 by injecting 2.80 L colloid suspension into CRR 99.002-i2. The colloid suspension consisted of 273 mg/L Na-Febex bentonite colloids and Ni/Zn-montmorillonite colloids 9.46 mg/L (Ni), 9.10 mg/L (Zn) as well as 0.89 mg/L Amino-G acid as conservative tracer.

From the onsite measurement of the injection phase the Eh and turbidity measurements correlated well with an increase in the Eh measurements from -273 mV to about -36 mV and a decrease after 38 minutes to values of -120 mV at the end of the injection. A similar behavior could be observed for the turbidity that initially increased from 0.09 to 31.6 NTU and decreased after 38 minutes to 3.3 NTU. This observation is in accordance to the suspension preparation, which was conducted under oxidizing conditions in KIT-INE labs. During the extraction phase, the Eh measurements decreased from 3 mV to about -336 mV. The turbidity values initially rose to 17.6 NTU and after 4 minutes decreased with a similar shape as the Eh measurements to 0.5 NTU.

An estimated colloid recovery of only 10.7% with 9.2% recovery could be estimated during the push/pull experiment showing the movement of the colloid plume after the shut-in phase towards the tunnel surface. Therefore, the consortium decided to stop the pull phase (see Figure 32) and the tracer was monitored in the Pinkel surface packer (see Figure 33).

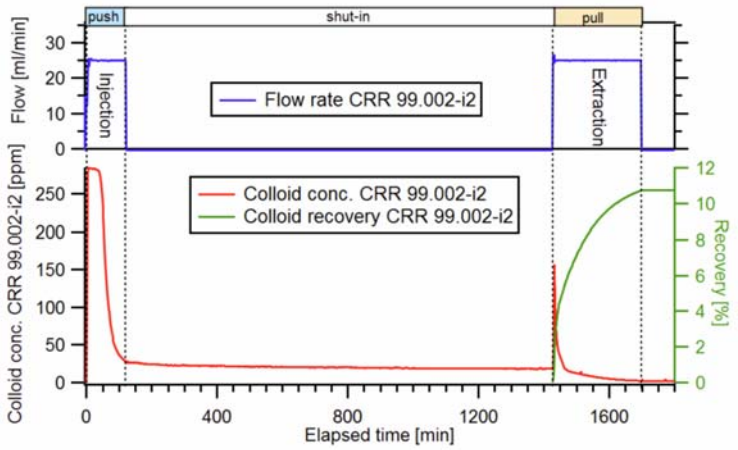

***Figure 32**: Colloid concentration (ppm) and calculated recovery during the push/pull experiment in observation borehole CRR 99.002-i2.*

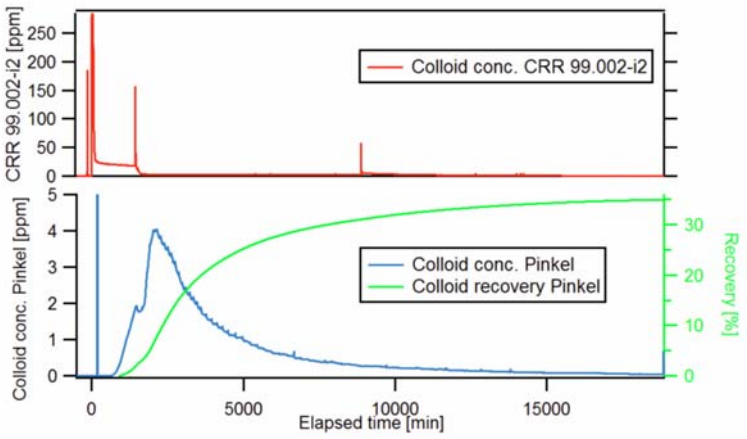

***Figure 33**: Colloid concentration (ppm) and calculated recovery during monitored at the Pinkel surface packer during the REMO 2 experiment with the comparison of the colloid detection of the push/pull experiment in observation borehole CRR 99.002-i2.*

The monitoring until the 10.05.2017 at 10:04h revealed a total Amino-G recovery of 48.4% with a colloid recovery slightly lower at 45.4%, respectively, in the Pinkel surface packer.

2.2.1.1 AMS analysis

The remobilization tests (REMO 1 and REMO 2) were performed without introducing actinide tracers with the intent to remobilize the fraction of actinide tracers introduced in previous in situ tests in the dipole of CFM run 13-05 that had not yet been recovered. In REMO 1 a hydraulic stimulation with reversal of flow direction with respect to that of CFM run 13-05 was carried out. The maximum flow rate was equal to ~192 mL/min (see above). In REMO 2 the injection of Grimsel groundwater containing clay colloids (~ 292 mg/L), with 25 mL/min flow rate to desorb retained actinide tracers from previous experiments was employed. The sample preparation and measurements were performed according to the multi-actinide analysis with AMS at VERA (Quinto et al., 2015). Interestingly, the highest concentration of the tracers 233U and 237Np was measured in sample 2-1 before the start of the REMO 1 hydraulic stimulation (see Figure 34 & 35). The colloid associated Am-243 and Pu-242 (not presented) show exactly the same trend giving a further hint, that the minor colloid fraction mobilized is not from the CFM run 13-05 experiment. Here, further evaluation of the data and equipment used is needed to clearly rule out the potential contamination through old tubings or dead volumes in the circuit. Anyhow, a simple correlation to the colloids/nanoparticles released for Americium and Plutonium cannot be drawn and for Uranium and Neptunium it was not expected.

Interestingly, merging the data of the Amino-G breakthrough curve together with the AMS results for the different tracers the general shape of the BTC is also seen in the AMS data (see Figure 36). However, for the trivalent Am-243 (not expected to have any redox reactions) in addition to desorption kinetics the peak maximum of Amino-G coincides with the AMS determined maximum concentration. A similar trend is seen for Pu-242, which has been added in Run 13-05 as Pu(III) and by readjusting the pH quantitatively transferred to Pu(IV) and is initially associated to colloids. Taking the slope analysis of the Amino-G BTC a tracer first arrival around 892min could be estimated providing the minimum contact time of the tracer cocktail with the fracture surface, while the peak maximum is around 2170min given an average time of contact. Looking at the Np-237 and U-233 data the maximum is clearly shifted towards longer times; namely sample #55 taken after 4368min. Here, during colloid injection beside providing an additional sorption surface also the redox conditions were significantly changed from -273 mV before the start of the injection to about -36 mV. This might be a reasoning for the difference in remobilization behavior as the significant retention observed in Run 13-05 for Np(V) and U(VI) is expected due to fracture surface induced reduction. Desorption rates documented for Pu and Am are around 1E-3 h^{-1} (Huber et al, 2015) with a remaining fraction of Pu-242 and Am-243 in the fracture after Run 13-05 of 30-35% and 21-22%, respectively. For Np and U the retention was significantly higher and only approx. 4% and 15%, respectively, could be recovered.

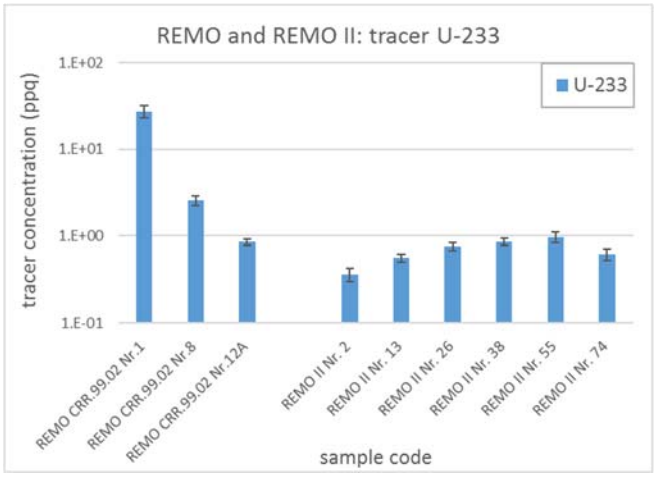

Figure 34: *^{233}U concentration (ppq) determined with AMS in chosen samples of the REMO and REMO II tests.*

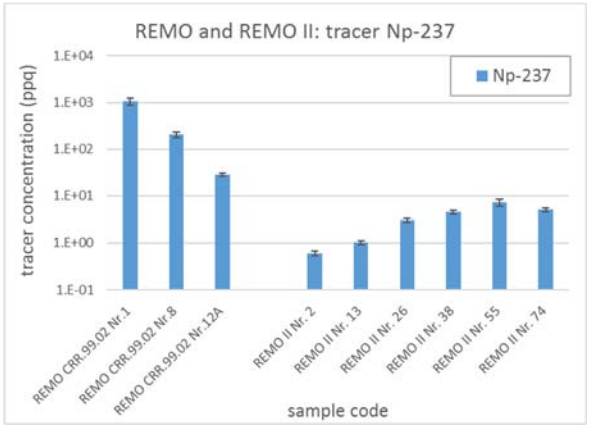

Figure 35: *^{237}Np concentration (ppq) determined with AMS in chosen samples of the REMO and REMO II tests.*

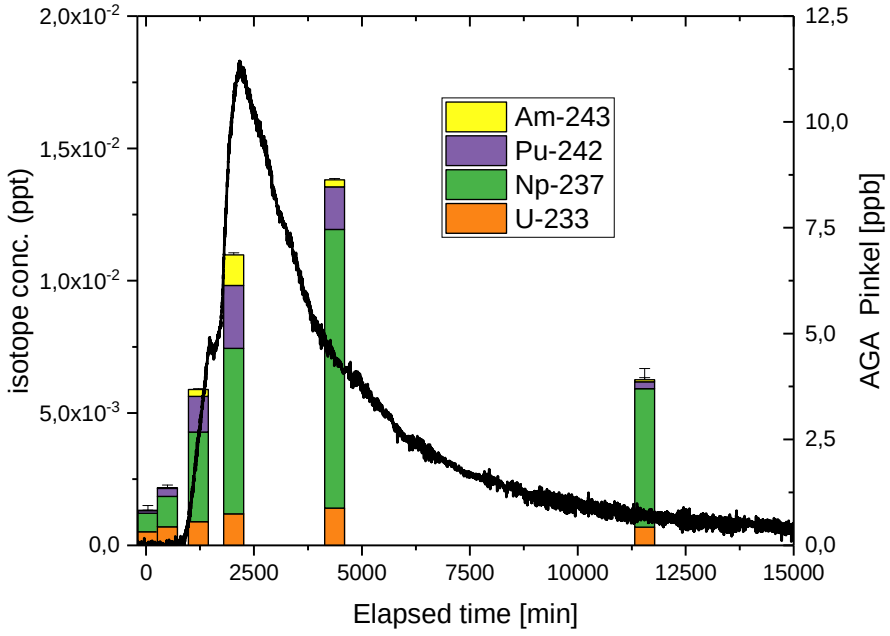

Figure 36: *Actinide concentrations (ppt) in comparison to the conservative data monitored at the Pinkel surface packer of REMO 2.*

2.2.2 Long-term In-situ test

The CFM project investigates in general the formation and migration of bentonite derived colloids in natural fractured rocks and colloid facilitated transport of radionuclides in this system. A series of hydraulic and tracer tests including well-defined bentonite colloids, conservative and radionuclide tracers in a natural fracture at GTS have been performed in the past. The next step included the implementation of a radionuclide tracer containing compacted bentonite colloid source in the water-bearing feature for better understanding of the real in-situ processes in a bentonite-based engineered barrier. The Long-term In-situ Test (LIT) included in-situ bentonite swelling, erosion and the transport of the eroded material under advection dominated conditions.

2.2.2.1 Experimental Layout

LIT is located in the radiation-controlled zone at GTS (see Figure 37 for the general setup). The borehole CFM 06.002 was chosen for the emplacement of the bentonite source with a diameter of 96 mm intersecting the migration shear zone at a depth of approximately 6.75 ± 0.05 m from the tunnel wall. It is surrounded by three 56 mm monitoring boreholes (CFM 11.001, CFM11.002 and CFM11.003) which are located in parallel to CFM 06.002 at a distance of only 40 mm and used for observation and sampling in the near field. Each monitoring borehole is equipped with a 54 mm triple packer system including two hydro-mechanical packers of 0.2 m sealing length and one hydraulic packer of 1 m length close to the tunnel wall. The migration shear-zone intersects the boreholes between the hydro-mechanical packers. Beside the PEEK lines stainless steel lines are integrated in each packer system for pressure monitoring and the option of resin injection which is needed to stabilize the radioactive bentonite source in the last phase of the experiment just before overcoring. An additional option for sampling can be found at the Pinkel surface packer in a distance of 6.08 m from the source located at the tunnel wall within the mega-packer system. The analytical program for these samples is limited in comparison to the near-field samples as dilution is due to the long distance much higher. A scheme of the experimental layout is depicted in Figure 38.

The source emplacement borehole CFM06.002 is instrumented with a triple packer system and includes two hydro-mechanical packers of 0.27 m sealing length and one hydraulic packer of 1 m length located at the borehole mouth. The system was designed to facilitate emplacement, monitoring and subsequent overcoring of the radionuclide labelled bentonite source. Several stainless-steel lines are located within the packer for water extraction and pressure monitoring. Therefore, two total pressure cells are installed at each end of the source interval. The interval consists of a carbon steel mandrel (ST52) of 44 mm diameter and 400 mm length to hold a total of 16 bentonite rings, each with 25 mm thickness. Sinter filters are placed between the sample and the respective packer. The total length of this interval from sealing element to sealing element is 520 mm (see Figure 39).

Pre-tests showed that the observation borehole CFM 11.002 features the best connection to CFM 06.002 and is therefore used for near-field monitoring and sampling during the early phase of the experiment. Low extraction rates of only 0.02 mL per minute are applied in order the keep the flow regime around the bentonite source undisturbed. The outflow is either channeled through the geochemistry cabinet for online monitoring or sampled in a fraction collector within an Ar glovebox for later analysis with an automatic valve shifting between the two lines. Samples are transferred to KIT and undergo an extensive analytical routine including the samples pH, Eh_{SHE}, fluorescence dye concentration analysis, elemental composition (IC, ICP-MS), radiochemical composition (LSC, Gamma, SF-ICP-MS and AMS) as well as size and concentration of the colloidal fraction (LIBD, s-curve LIBD).

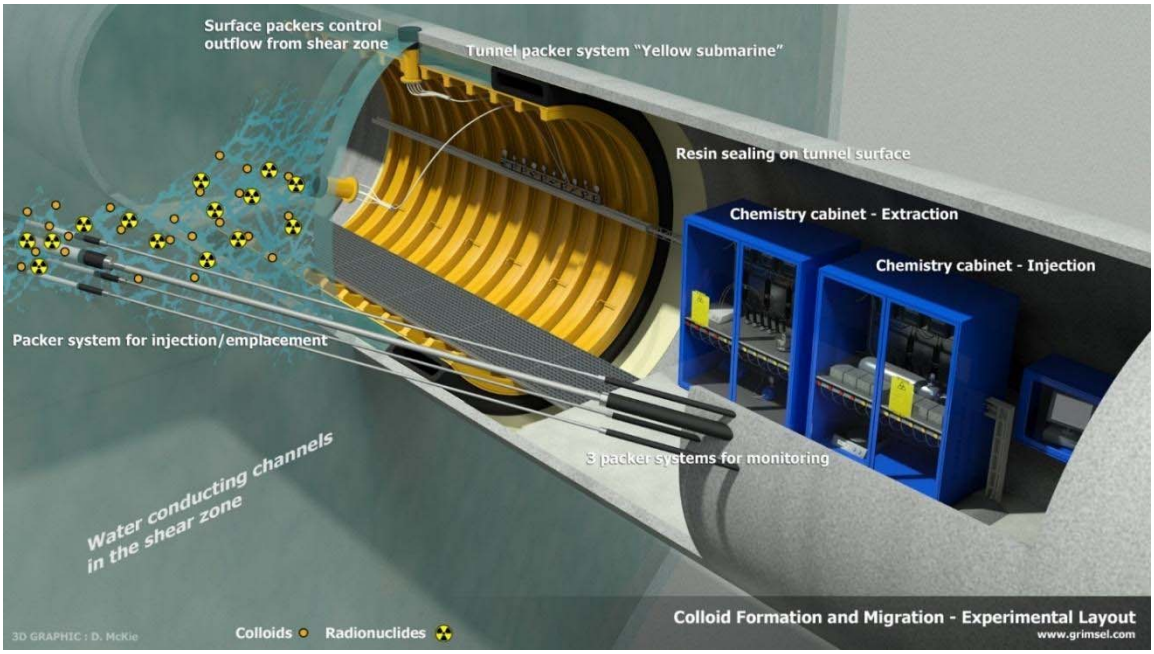

Figure 37: *LIT experimental layout (www.grimsel.com). LIT enables bentonite erosion and colloid generation directly from compacted bentonite and can be seen as enhancement in comparison to past experiments that focused on injection of colloid suspensions under realistic flow conditions.*

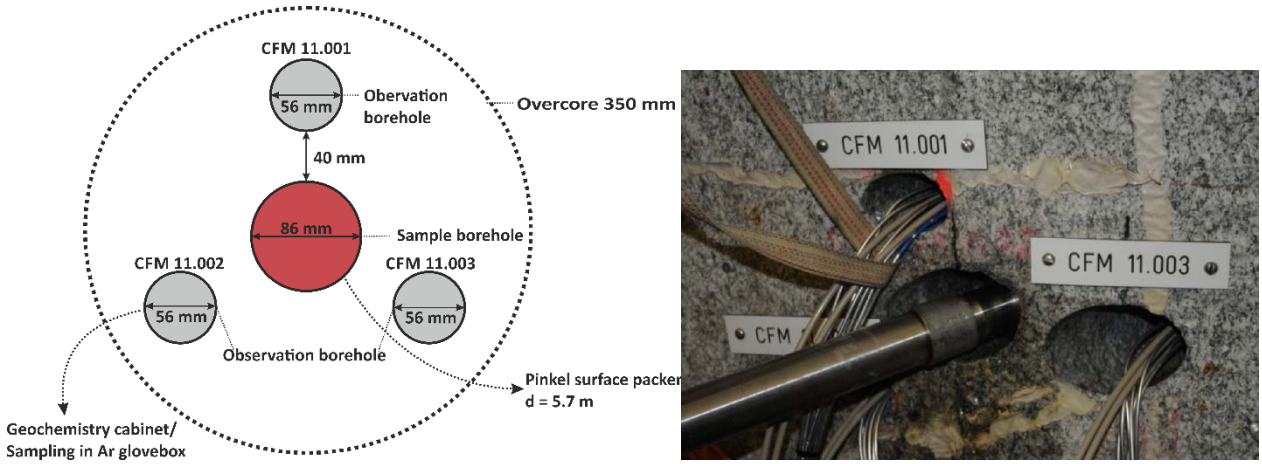

Figure 38: *Arrangement of the boreholes relevant for LIT. A schematic overview (left) and a picture of the installation site during the experiment (right). The bentonite source is located in the central borehole and the surrounding boreholes (CFM 11.00X) are used for near-field observation and resin-injection prior overcoring of the bentonite source.*

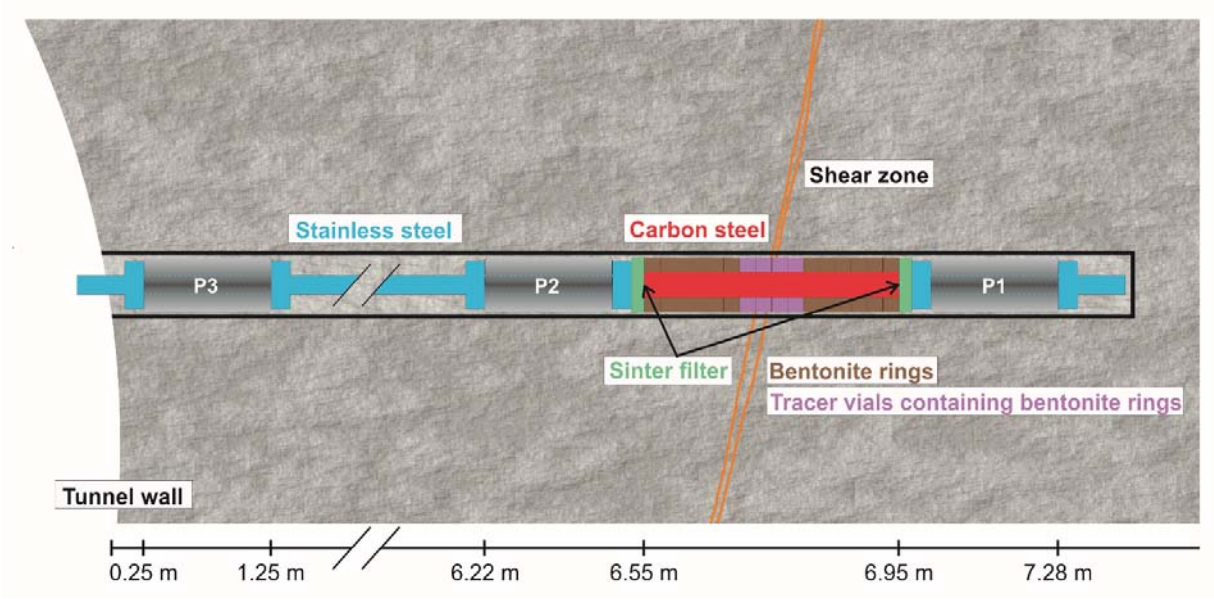

Figure 39: *Conceptual design of the emplacement packer system and location in the borehole CFM 06.002 (NAB 14-092). Observation boreholes are not shown. The source is sealed with two hydro-mechanical packers (P1 and P2) and the hydraulic packer (P3) is located close to the tunnel wall. Drawing not to scale.*

2.2.2.2 Bentonite sample and tracer composition

The bentonite source within LIT consists of 16 compacted bentonite rings with a compaction density of 1600 kg/m^3 which are stacked on the mandrel of the packer system. Combination of the bentonite rings results in a 400 mm high bentonite rod with an inner diameter of 43 mm and an outer diameter of 83 mm. A total of 2613.6 g bentonite composed of 2549.9 g natural Febex bentonite and 63.7 g synthetic Zn-labeled montmorillonite is emplaced in the migration shear zone. The fact that the contact area between bentonite source and migration shear zone is located in the region of the four central sample rings is the reason for special interest and deviating sample composition in the middle of the sample. The midst sample rings contain not only pure Febex bentonite but an admixture of 10% synthetic Zn-montmorillonite. Holes have been drilled laterally in the Zn-montmorillonite containing bentonite rings to host the tracer containing glass vials. A total of sixteen vials are implemented, 4 in each Zn-labeled bentonite ring. The caps of the glass vials have been removed prior mounting to facilitate contact between the tracer and the surrounding bentonite and the vials were emplaced with the open side pointing to the inside of the bentonite ring. Under the high swelling pressure, the vials are in addition supposed to break and release the radionuclide tracer uniformly as a type of point source.

The tracer inside the glass vials is composed of a radionuclide containing bentonite paste and Amino-G (Sigma Aldrich, order no. 14,664-7, Monopotassium-7-amino-1,3-naphthalenedisulfonate hydrate) as conservative fluorescence tracer. A mixture of natural Febex bentonite in the grain size < 63 µm and synthetic Ni-labeled montmorillonite (Reinholdt et al., 2013) was used in equal ratios (50% each). A 5g/L suspension of the mixture was prepared with synthetic Febex porewater according to table 13 of (Fernandez et al., 2004), resulting in an ionic strength of 0.9 M and a pH value of 7.49 in excellent agreement with the pH value of 7.44 documented in (Fernandez et al., 2004). The porewater was prepared by adding the following amounts of salt for one-liter total volume: 22.7907g NaCl, 12.0618g $CaCl_2$*2H_2O, 4.1894g $MgSO_4$*7H_2O, 16.2606g $MgCl_2$*6H_2O and 0.2231g KCl.

The bentonite suspension was first equilibrated with the strongly sorbing radionuclide tracers ^{241}Am(III), ^{137}Cs(I) and ^{242}Pu. Pu was added in the trivalent oxidation state after electrochemical reduction. The suspension was equilibrated for 26 hours and the solid phase was separated by centrifugation at 2.800 g for 60 min. The centrifugate was stored in a fume cupboard to remove remaining water. Then, the bentonite paste was transferred in an Ar glovebox and the weakly sorbing radionuclides ^{99}Tc(VII), ^{75}Se(VI), ^{45}Ca(II), ^{233}U(VI) and ^{237}Np(V) were added. The resulting mixture with 5g/5mL was homogenized using a spatula. Afterwards the glass vials (VWR International, product number 548-0347, 7,8 mm outer diameter,

35 mm height, shortened to 10 mm) were filled by average with 8.55 ± 0.10 mg Amino-G powder per vial and 222 mg of the radionuclide containing bentonite slurry respectively by using a syringe (5 mL, Luer solo, B. Braun, order no. 4606051V). The glass vials were closed with a plastic lid and transported confined to GTS. A total of 19 glass tracer vials were prepared, 16 of them for the LIT experiment and the remaining vials for the laboratory mock-up test. The activities of all of the emplaced radionuclides are under the licensed limits (Table 12).

Gamma spectroscopy and high resolution ICP-MS were applied for radiochemical characterization of the samples. Gamma spectroscopy focused on the quantification of ^{75}Se, ^{137}Cs and ^{241}Am. None of the before mentioned radionuclides were found as all samples were below the detection limit. SF-ICP-MS was applied for all radionuclides within LIT. Due to the detection of the atomic mass several isobaric interferences are possible and have to be taken into account.

2.2.2.3 Background monitoring

The installed monitoring system includes beside the Ar glovebox with the fraction collector, a flow control and a geochemistry cabinet. All components were installed before the start of LIT to monitor the chemical parameter changes in the nearfield monitoring intervals within CFM 11.001, CFM 11.002 and CFM 11.003. Switching from one observation borehole to another is possible by a valve. Due to the possible geochemical perturbation of the extracted water by the direct contact with the probes under the established low flow rates an electrical valve is programmed to switch between water sampling and online monitoring to bypass the geochemistry cabinet while sampling with an extra time programmed to flush the tubing dead volumes. The geochemistry cabinet is equipped with a turbidity meter, a fluorimeter, pH, EC and Eh_{SHE} probes (Figure 40). Data measured in the geochemistry cabinet shows periodic disturbances which are caused by the stagnant phase in the probes during the sampling intervals mentioned above.

2.2.2.4 LIT online monitoring

Swelling pressure evolution

Four total pressure sensors are implemented in the source packer system to measure the swelling pressure evolution of the expanding bentonite source when contacted with the groundwater. Swelling pressure evolution is shown in Figure 41. Two sensors are installed on the lower interface between the packer and the bentonite source (TP_3 and TP_4) and two on the upper interface (TP_1 and TP_2). Pressure rises immediately after the installation of the packer system and reaches steady state on all pressure sensors within 20 days. Values of 900 ± 100 kPa are obtained on both sensors at the lower end of the sample and are stable over the total experimental time. Both pressure sensors measure very comparable values indicating homogeneous swelling in this region. Higher swelling pressure in the order of 1.4 (TP_2) to 1.9 MPa (TP_1) is obtained on the upper side of the packer. Both installed pressure sensors give different values indicating inhomogeneous swelling or some kind of sealing, preventing compensation of the swelling pressure between the sensors. The values remain constant until a pressure release occurred at TP_1 after 520 days. Thereby part of the pressure is released and a new equilibrium is established within 25 days at 1.5 MPa. Total pressure on TP_2 remains constant during the drop on TP_1. Total pressure values rise during the remaining LIT-run-time but stay below the pressure values before the drop at TP_1. Concerning the dry density of the bentonite source, which is 1.65 g/cm3, one would expect much higher swelling pressure in the order of 5.0 to 6.5 MPa (Agus & Schanz, 2008). Swelling pressure in LIT is significantly lower in comparison to the laboratory experiments as the bentonite source has some space to expand before it reaches the wall of the borehole and additional space as it may intrude into the fractured system. A metal sleeve had to be installed around the bentonite sample during installation for radiation security reasons and was pulled backwards when the sample was in place. The removal of the sleeve led to a gap between the sample and the tunnel wall of approximately 2-3 mm. The bentonite sample will expand to the tunnel wall when contacted with GGW taking an additional volume of 16 to 21% in comparison to the sample volume. Thereby, the effective dry density is decreasing to only 1.37 to 1.45 g/cm3. Swelling pressure of 900 to 1100 kPa which is lying in between the experimental values is expected for this density region, according to (Agus & Schanz, 2008). The additional volume in the borehole was not compensated by using a bentonite sample with a higher degree of compaction to match repository conditions. This may limit the comparability of bentonite erosion and colloid generation within LIT to

a HLRW repository. The addition of the synthetic Zn-montmorillonite in this experiment may also have an effect but cannot be evaluated as there is no data to compare the swelling properties of the synthetic montmorillonite and the Febex bentonite.

Table 12: *Within LIT emplaced activity and license limits.*

Nuclide	Total activity in LIT (16 vials) [Bq]	Max. activity based on license [Bq]
45Ca	7.10 · 105	1.0 · 106
75Se	4.78 · 104	1.0 · 106
99Tc	5.40 · 103	1.0 · 104
137Cs	4.39 · 103	1.1 · 105
233U	7.10 · 102	1.0 · 103
237Np	1.07 · 103	1.5 · 103
241Am	8.81 · 102	8.5 · 103
242Pu	2.13 · 102	3.0 · 102

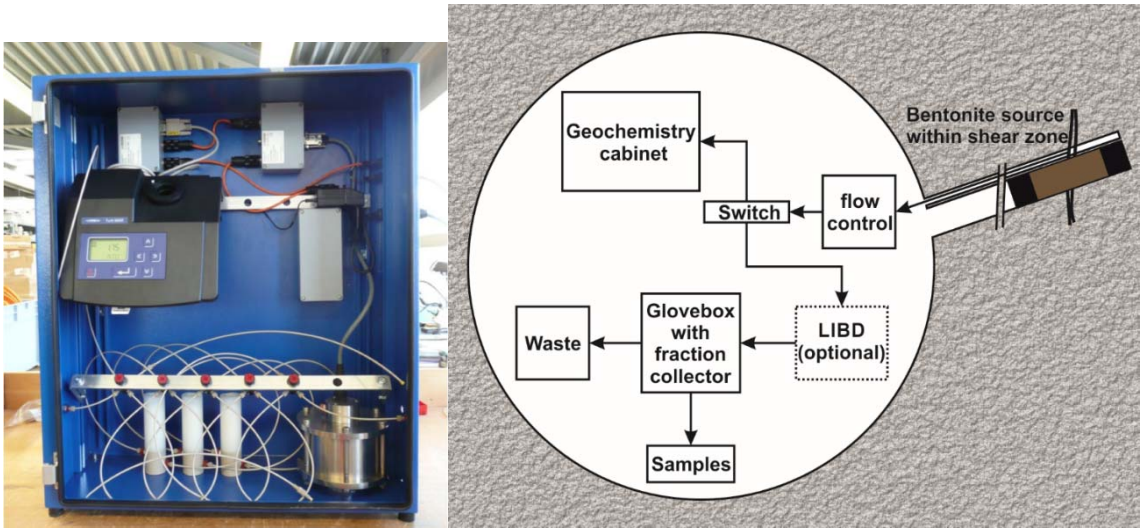

Figure 40: *Photograph of the geochemistry cabinet at GTS (left) and schematic overview of the surface equipment setup for nearfield monitoring and sample collection (right).*

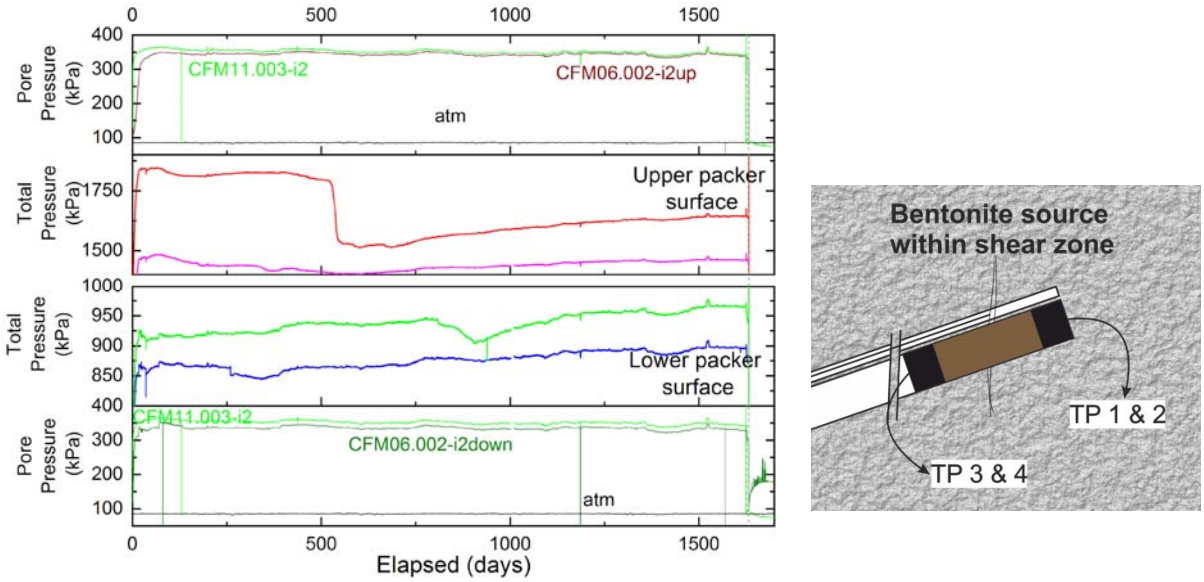

Figure 41: *Swelling pressure evolution within the LIT bentonite source.*

Hydro-geochemical monitoring – pH, Eh_{SHE}, conductivity and conservative tracer evolution

Near-field monitoring changed several times during LIT. The initial extraction started from CFM11.002 at a rate of 20 µL/min was increased to 50 µL/min after ~750 days. In the following, extraction was changed to CFM11.003 but extraction rate did not change (Figure 42).

pH is measured in the near-field of the bentonite source (CFM11.002/003) as well as at the Pinkel outflow within the surface packer system. Both data is shown in Figure 43. Especially the data obtained from the near-field shows periodic disturbances due to the before mentioned valve switch between monitoring and sampling.

After implementation of the bentonite source, pH drops in the near-field from 9.6 to 9.1 ± 0.1 within 50 days and stays stable for 370 days. This is followed by a continuous increase to a maximum value of 10.1 ± 0.1 after 680 days. The steady increase in the second year of the experiment doesn't give true values but can be seen as alteration process of the pH electrode. The electrode was replaced after 690 days and pH is once again stable at 9.0 ± 0.1. The pH drop around 690 days refers to the replacement of the electrode. PH values rise again after 1200 days which can be explained by the same effect. The sink around 95 days can be explained by a longer period without flow through the geochemistry cabinet as it was bypassed for several days to facilitate continuous sampling during the first LIBD on-site campaign. The same effect is observed for $Eh_{SHE,}$ electrical conductivity and fluorescence monitoring. In addition to the near-field pH values observed from CFM11.002/003 water samples are also collected at the Pinkel extraction point which is located at the tunnel wall. Samples from this spot show higher pH values around 9.4 ± 0.2 for the first year of LIT. A pH drop occurs at a run-time of 200 days and is caused by a power breakdown in the facility. New calibration of the pH probe after 310 days explains slightly lower values for the following data. The pH probe was replaced after 580 days as the former installed probe suffered from alteration. This is shown by the drift of 1.5 pH units in 100 days and the noisy signal prior replacement.

The redox potential is shown in Figure 43 and was also measured on both sampling spots giving very different results. Reducing values are measured on the Pinkel extraction point with the exception of one drastic increase 300 days after the start of LIT which is caused by recalibration of the Eh probe. All values are however, in the range of -240 ± 60 mV and close to literature data (Möri et al., 2003). Considerably higher redox potentials have been measured in the near field of the bentonite source, which can be explained by interaction with the bentonite sample, for instance dissolution of accessory

phases or mixing with the bentonite porewater. After an initial drop from 220 mV down to 160 mV followed by the by-passed period without flow in the geochemistry cabinet, a first plateau is obtained for a short period of 50 days at a redox potential of -50 mV. Afterwards Eh_{SHE} increases to a second plateau which lasts for 450 days at a redox potential of 130 mV. Increase of extraction rate after 750 days leads to a drop in Eh_{SHE} towards the values measured at Pinkel. This process indicates that the amount of extractable groundwater in contact with LIT is limited and therefore more fresh groundwater without contact to the bentonite source is extracted. The change of the near-field extraction borehole after 900 days leads to slowly increasing Eh_{SHE} values. A plateau is reached after 1050 days at ~+200 mV. Differences between the extraction points are caused by the interaction of the bentonite source with the surrounding groundwater. Due to the distance from the source to the Pinkel extraction point and the expected dilution on that migration pathway, the effect is only visible for the near-field monitoring.

Electrical conductivity at the Pinkel extraction point is quite stable at 60 ± 10 µS/cm for the first 300 days, showing only one re-calibration induced step 300 days after the start of LIT and slightly decreased values around 50 ± 10 µS/cm for the remaining run-time (Figure 43). Values before and after this event are very stable. In contrast, the near field data shows a breakthrough curve that reaches a maximum of 170 µS/cm after 30 days and slowly levels off during the remaining run-time. Equilibrium is not reached before changing the extraction rate and values are still above the GGW background. Higher extraction rate and subsequent change of the monitoring borehole lead to major disturbances and conductivity is not stable for the remaining experimental time. Initially increased values can be explained by the dissolution of accessory phases within the bentonite sample. Readily soluble phases like halite are responsible for the early maximum and the dissolution of hardly soluble phases like gypsum and the bentonite itself are responsible for the long tailing. The early maximum and the constant decrease of the values indicate stable contact between the bentonite source and the surrounding groundwater without serious disturbances by e.g. the release of air from the cavities within the bentonite source which may result in air bubbles around the sample and partly separation of the swelling bentonite from the groundwater or the spontaneous release of those air bubbles.

Additional prove for good contact between the bentonite source and the groundwater can be found in the fluorescence signal of the conservative tracer, Amino G (Figure 42 & 43). Concentrations start rising around 20 days after emplacement and reach a maximum after 600 days. The detected tracer sums up to a released fraction of 3.7% of the total tracer mass. The sharp peak around 200 days run-time is again caused by the power failure at GTS. The rate change from 20 to 50 µL/min leads to ~60% lower tracer concentrations. This is an additional hint for a limitation of the extractable contact water. Extraction increase leads to dilution again indicating a higher proportion of fresh groundwater extraction.

2.2.2.5 LIT sample analysis

Samples have been taken regularly from the near-field observation boreholes CFM11.002/003 as well as from the Pinkel extraction point. The effluent from CFM11.002/003 was collected under anoxic conditions in 15 mL septum sample vials until October, 2015 and in 40 mL septum vials afterwards at a flow rate of 20-50 µL/min, respectively. All pierced sample caps have been replaced against fresh ones prior to the transfer out of the argon glovebox and the transport from GTS to the INE laboratory to ensure anoxic conditions during transport. No samples from CFM11.002 were collected within the first 100 days due to a software malfunction. In addition, large volume samples (1 L) have been collected with an autosampler (6712FR, Teledyne Isco Inc.) in parallel at the Pinkel extraction point at a flow rate of 20 mL/min under ambient conditions. Samples have been collected regularly. Sample batches were transferred to the INE laboratories for further analysis twice a year. A total of 98 samples from the near-field and 40 samples from the Pinkel extraction point have been received within the first two years of LIT. Due to the fact that samples from the Pinkel extraction point were highly diluted and didn't show observable interaction with LIT within the online monitoring, analysis focused mainly on the near-field samples.

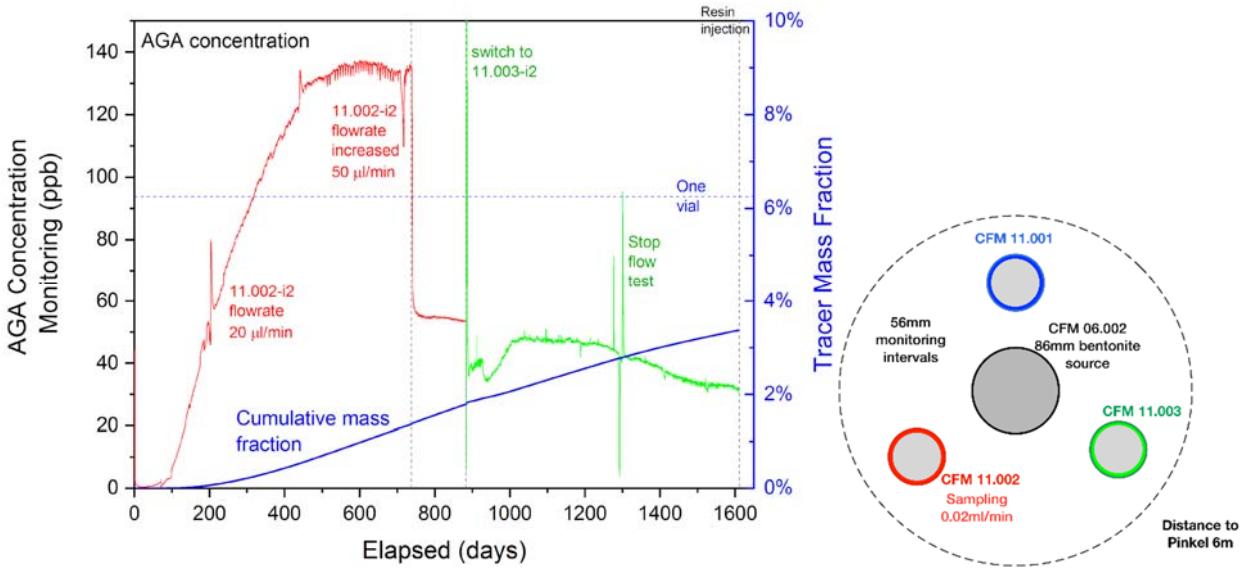

Figure 42: *Amino G concentration as a function of sampling flow velocity and extraction point as indicated by the color-coding. Cumulative extracted Amino-G mass is summed up from all monitoring boreholes .*

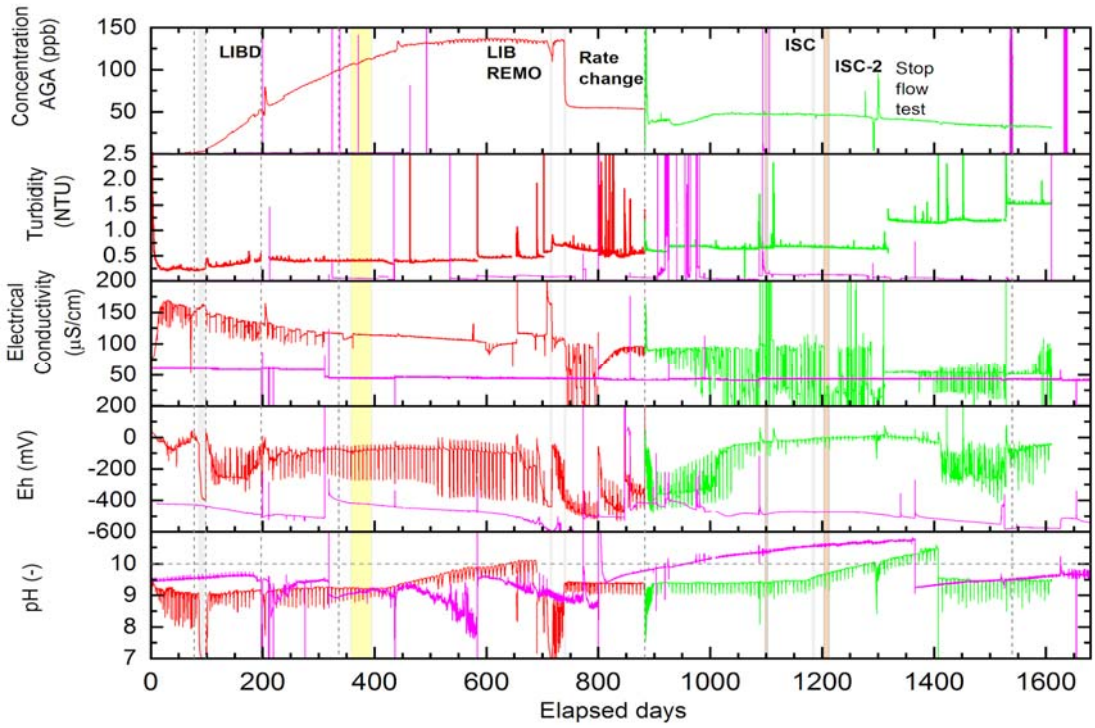

Figure 43: *LIT - Geochemical evolution, data from Pinkel is colored in magenta. The color code of the near-field monitoring boreholes is shown in the borehole scheme.*

Hydro-geochemical monitoring – pH, Eh_{SHE} and conservative tracer evolution

pH of the CFM11.002/003 samples is depicted in Figure 44. Stable pH of 9.1 ± 0.1 ((n=214), mean: 8.93 ± 0.39, min: 6.04, median: 9.04, max.: 9.74). over three years of the experiment is very comparable to online data from GTS and indicates successful isolation of the samples from the atmosphere during the transport. The later sample batches show a pH shift to lower values, indicating insufficient isolation from the atmosphere and carbonization during transport. Samples from the Pinkel extraction point have in contrast to the near-field samples been sampled and transported under oxic conditions. This

results in a pH drift due to carbonization towards neutral values around 7.6 ± 0.3. The concentration of the conservative tracer has been determined over the fluorescence signal (Figure 44). Values are again in-line with the online evolution described previously. Monitoring of redox potentials in the laboratory was not possible for the 15 mL samples as the volume is not sufficient for a reliable measurement and the risk of leakage of the electrolyte within the electrode should be avoided. Therefore, the redox potential was only measured in case of the 40 mL samples and is with an Eh_{SHE}-value of 152 ± 32 mV (n=5) comparable to the online monitored data.

Elemental characterization

Elemental composition of the cationic components was determined by ICP-MS and ion chromatography was applied for determination of the anion concentrations. ICP-MS measurements focused basically on the bentonite source forming main elements Zn, Mg, Al, and Ni as well as on elements connected with the dissolution of accessory minerals like Na in the case of halite and Ca in the context of gypsum. An overview on the remaining elements was achieved by the semi-quantitative TotalQuant method. Evolution of selected elements with the respective background value are presented in Figure 45. Increased concentrations in comparison to the GGW background have been measured for the bentonite source forming elements Mg, Al and Zn. One event is remarkable. The concentrations are very stable until some fluctuations occur at a run-time around 510 days. It goes along with the previously described pressure drop. Slightly higher concentrations for a short period and subsequent lowest values under these conditions in the case of Al (180 µg/L before and 86 µg/L after the event) and even values below the detection limit in case of Zn indicate an initial release of bentonite particles during the pressure drop and afterwards potentially less connection between the bentonite source and the surrounding water. The effect of this event is in case of the Mg concentration not as pronounced as for Al and Zn and its concentration is in regard to the elemental composition of the source disproportionately high. An explanation can be found in the bentonite porewater and the Febex interlayer composition. A continuous cation exchange reaction is the dominating process. Mg evolution before the pressure drop is linearly decreasing from initially ~500 µg/L to 230 µg/L after 500 days and even lower values after changing the extraction rate and the extraction borehole, indicating that it is not only related to the Al concentration that remained stable during that time. It is rather a dilution process of the bentonite porewater until it is removed from the system.

Divalent cation concentration is very important as one of the controlling factors for bentonite erosion as e.g. increased concentrations limit the stability of the bentonite colloids. Calcium concentrations above the GGW background concentrations are observed for the first year of LIT and decrease steadily until a plateau below the background value is reached after ~400 days. The dissolution of gypsum, which can be found with a fraction of 0.14% in natural Febex bentonite, is the main Ca source in the system. It is remarkable that although the dissolution of gypsum releases the same amount of calcium and sulfate the elemental concentrations do not match. The sulfate concentration is always ~50 µM above the calcium concentration and in contrast to calcium never reaches values below the background. This observation can simply be explained by cation exchange of Ca against Na and Mg within the bentonite interlayer.

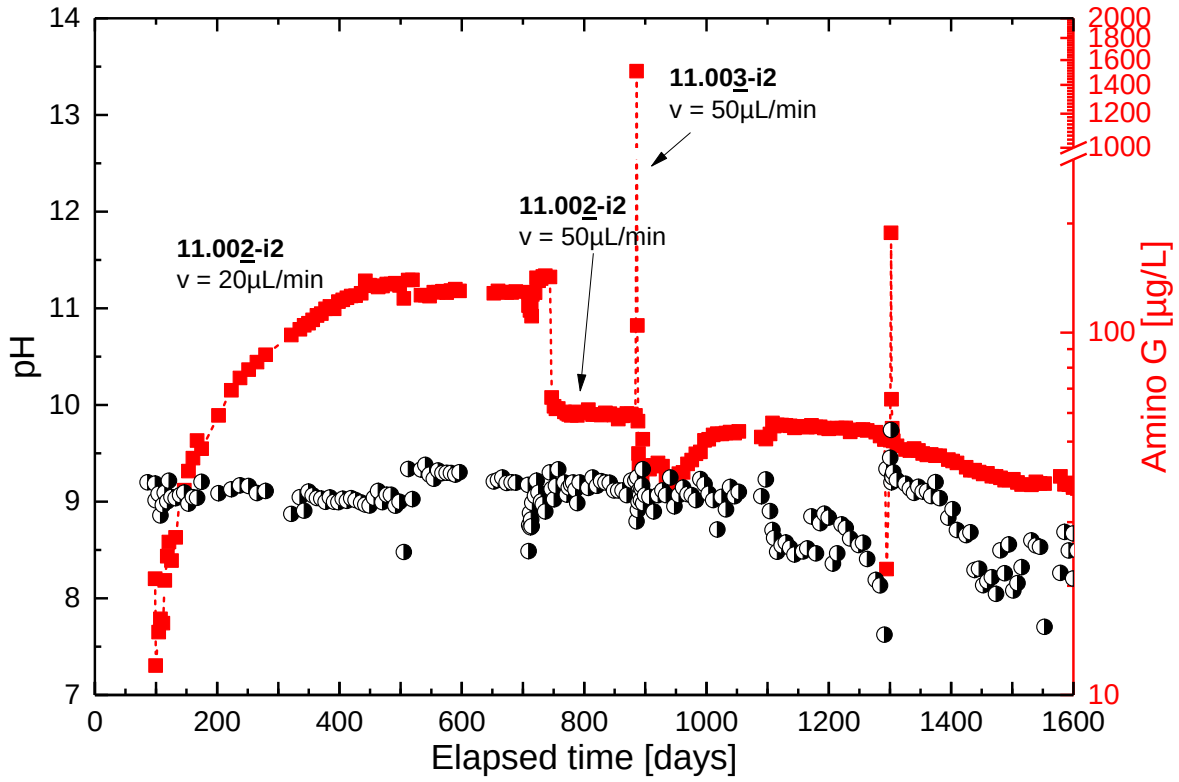

Figure 44: *pH and conservative tracer evolution.*

Concerning the different experimental phases that have been observed and described within the bentonite erosion laboratory experiment a clear separation of the postulated phases cannot be made. Phase I (washing) is located in the period without sampling (< 100 days). According to the evolution of the calcium concentration, Phase II (dissolution of accessories) should last until ~400-500 days as Ca concentrations drop below the background value (Figure 45) and phase III (bentonite erosion) should follow up. Al concentrations are actual rising for a short period around 470 days but this is due to the before mentioned disturbance by the pressure drop an unreliable prediction.

Increased Zn concentrations as tracers for colloid release are detected from an experimental run-time of 100 days onwards. Samples taken before 100 days show strongly decreased concentrations. These samples have been taken continuously without stop for geochemical monitoring during the first LIBD on-site campaign. The firstly decreased concentrations can be explained by a disequilibrium within the system due to a moderate change of the volumetric outflow from 20 µL/min to 50 µL/min. Equilibrium recovered within 14 days and concentration plateau at 14.5 µg/L formed for Zn. Concentrations show some scatter in the course of the experiment and mean concentrations slightly decrease to reach values of roughly 10 µg/L at a run-time of 500 days. Samples taken after the pressure drop only contain measureable amounts of Zn and Ni in some exceptional cases. In most samples the concentrations are below the detection limit of ICP-MS (< 5 ppt) supporting the theory that the incident that caused the pressure drop and limited Al concentrations also limited zinc concentrations and indicates that this element is linked over a colloidal fraction. Changing the extraction rate and subsequent the extraction borehole leads to increased Zn concentrations.

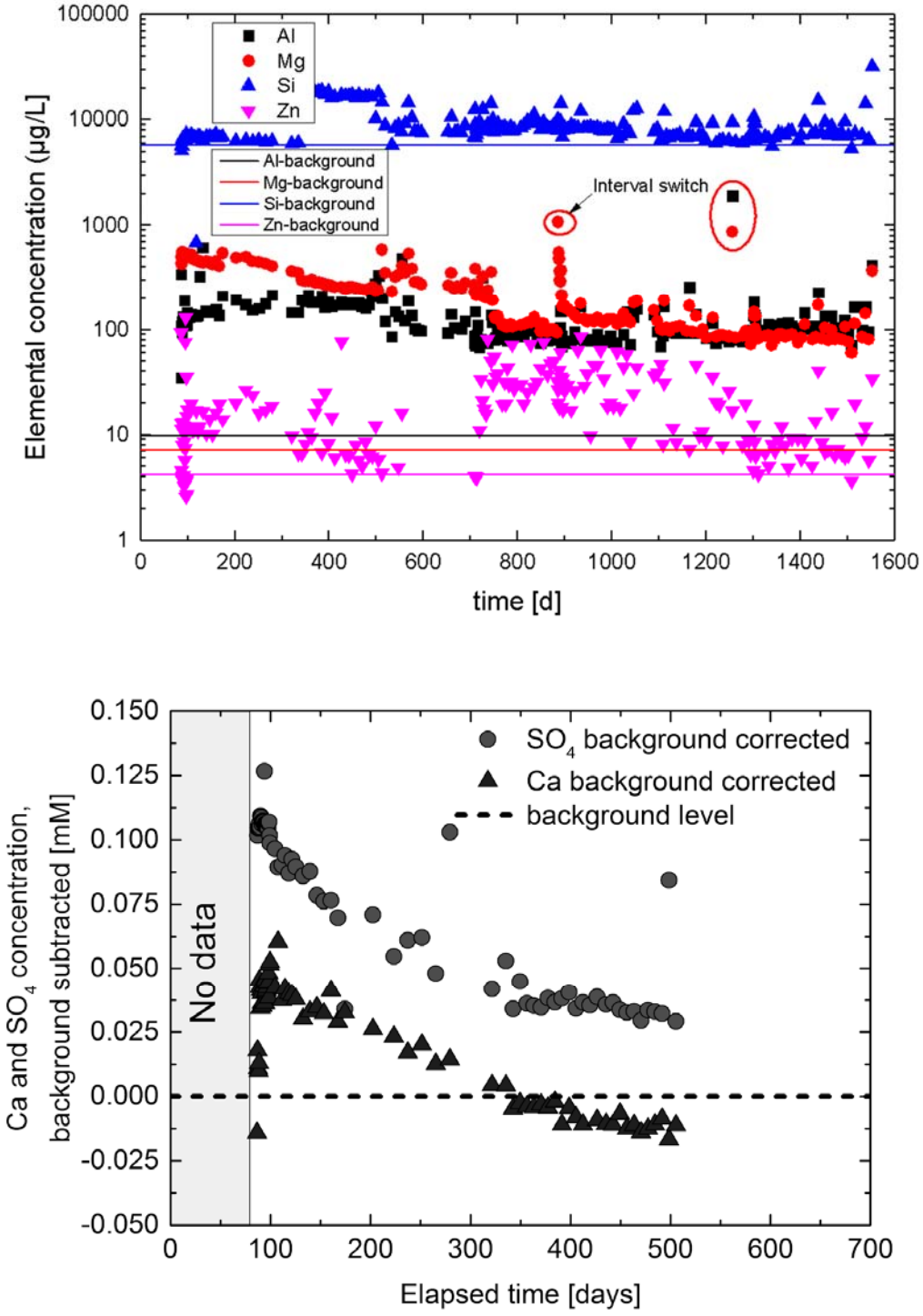

Figure 45: *(top) Magnesium, aluminum and zinc evolution in comparison to the respective background value of Pinkel and (bottom) calcium and sulfate molar concentrations. The respective background concentrations (0.09 mM Ca and 0.06 mM SO_4 from Pinkel, n=21) are subtracted to compare the molar ratios regarding the dissolution of gypsum.*

Colloid characterization

Colloid concentrations and mean particle sizes are determined by LIBD with optical data acquisition and the results can be found in Figure 46. Linear dependence between particle density and size is based on the method. The increase in particle

mean sizes and concentrations coincides with the drop of the Ca concentration below the detection limit (Figure 46, bottom). Based on the structural formula of the Febex bentonite, the elemental mass fractions of the main elements are calculated. The same is done for the admixture with the synthetic Zn-montmorillonite, which is in contact with the shear zone and the synthetic Ni-montmorillonite in the tracer containing glass vials (Table 13). These values are used to calculate colloid concentrations based on the ICP-MS data and under the assumption that the total Zn, Al and Ni concentration is colloid bound and originating from the midst bentonite rings or the tracer vials, respectively. Concerning the before mentioned elemental concentrations, maximum colloid concentrations of 1.4 mg/L and 1.7 mg/L are calculated from the zinc and aluminum concentrations, respectively. Ni concentrations can be applied to calculate the concentration of a released Ni-colloid fraction. Average Ni colloid concentrations are calculated to 15 µg/L. A cross-link to the total colloid concentration is not possible because the Ni-colloids originate from a montmorillonite paste within the tracer vials and not from a dry compacted bentonite sample. Colloid release in both cases will differ.

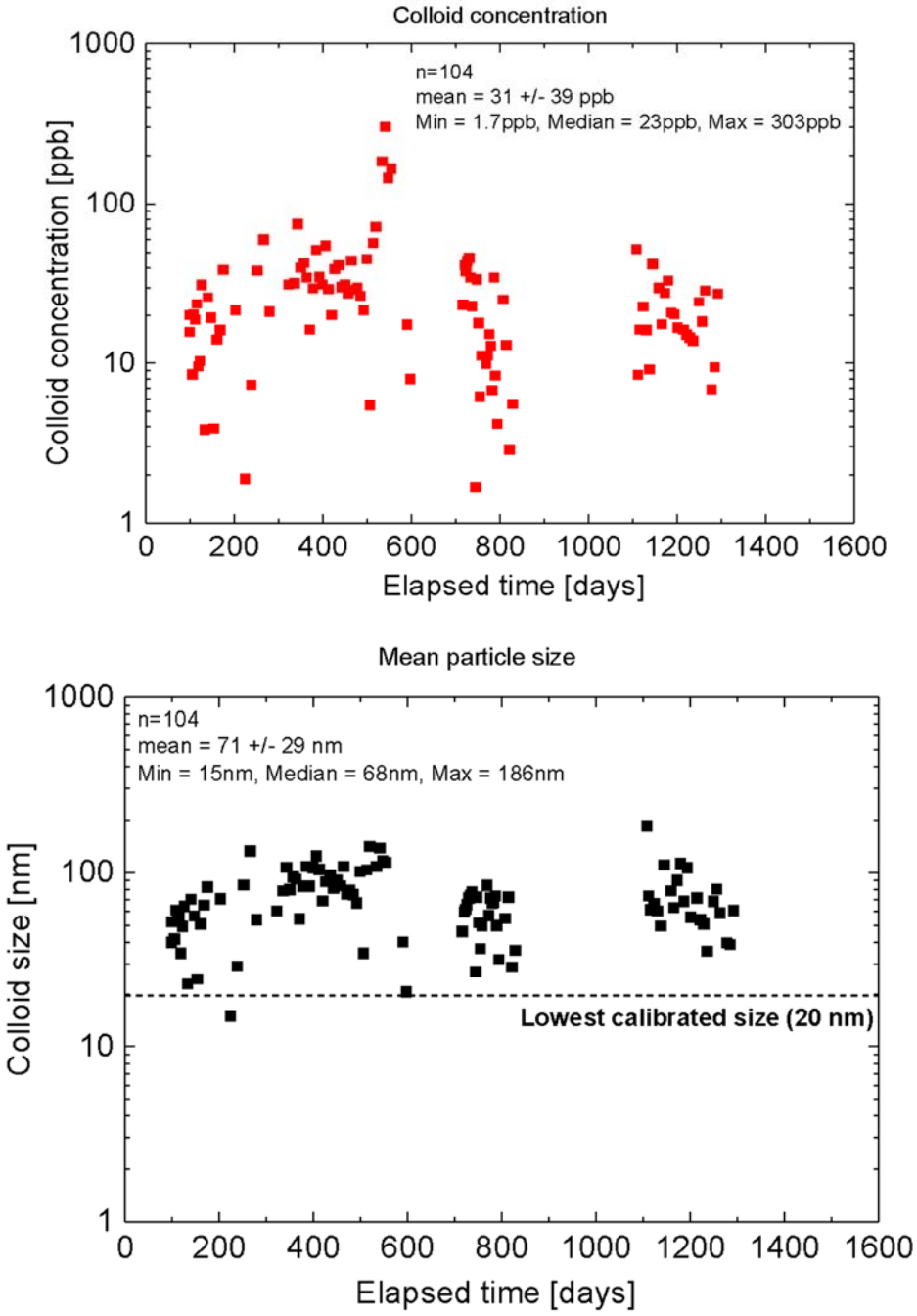

Figure 46: *(top) Colloid concentrations and (bottom) mean sizes derived by LIBD with optical data acquisition.*

Table 13: *Elemental composition of the bentonite rings emplaced within LIT.*

Element	Febex bentonite [weight-%]	Febex/Zn-Mnt admixture [weight-%]	Ni-montmorillonite [weight-%]
Fraction of total sample mass	76%	24%	only in glass vials
Si	29.1%	29.2%	29.5%
Al	10.1%	10.3%	11.6%
Mg	3.4%	3.1%	---
Zn	---	0.7%	---
Ni	---	---	6.0%
Fe	3.6%	3.2%	---

These results are in disagreement with the LIBD measurements, where colloid concentrations of 31 ± 39 ppb have been detected. Taking into account that 10.3% and 0.7% of the Zn-montmorillonite doped Febex bentonite consist of aluminum and zinc, respectively, the determined elemental mass concentrations measured by ICP-MS gives up to 50-fold higher concentrations. Therefore, it was questionable if the total Al, Zn and Ni concentrations found were colloid associated or free in solution because dissolution of the bentonite cannot be excluded under GGW pH conditions. To clarify the discrepancy between ICP-MS and LIBD data, part of the samples have been ultra-centrifuged at 90,000 rpm (694,000 g) for one hour to distinguish between particulate bound and dissolved concentrations. Following ICP-MS measurements no significant difference between centrifuged and untreated samples could be detected indicating only a minor colloidal fraction in the samples. The colloidal fraction consists due to LIBD measurements of less than 3% of the total Al and even less for the Mg concentration which is in the range of the analytical uncertainty of ICP-MS and confirms the LIBD results to be true.

Radiochemical characterization

The radionuclides introduced for the LIT experiment can be divided in fission and activation products (^{45}Ca, ^{75}Se, ^{99}Tc and ^{137}Cs) and actinides (^{233}U, ^{237}Np, ^{241}Am and ^{242}Pu). All fission products or rather elements at the mass respective channel have been detected during the SF-ICP-MS measurements. Selenium and cesium can be excluded in combination with the results obtained by gamma-spectroscopy as both radionuclides were below the detection limit of 0.03 Bq/mL. Calcium was not expected in the effluent as it was supposed to take part in the cation exchange process and should be immobilized in the bentonite interlayer. Because of the short half-life of ^{45}Ca in combination with the allowed activity limit within LIT, only a very small amount of $2.4 \cdot 10^{-11}$ mol (710 kBq) were added to the tracer vials. If part of the Ca was in the effluent, it would not be detectable by (SF-)ICP-MS being far below the detection limit of this technique and furthermore impossible due to the isobaric scandium-45 interference that is part of GGW in much higher concentration. Nevertheless, trace amounts of ^{45}Ca would have been detectable in the radiochemical analysis (liquid scintillation counting, LSC), which was not the case. Calcium has a short half-life of only 162.2 days. 97% of the initial mass are already decayed within the first 3 years and later detection will be challenging. Detected concentrations of nucleon number 99 are rising in parallel with the conservative tracer (Figure 47) but level off earlier after 300 days to reach values close to the detection limit after 600 days. Due to isobaric interferences, the signal cannot be assigned to a release of ^{99}Tc. To answer this question, additional AMS studies have been performed.

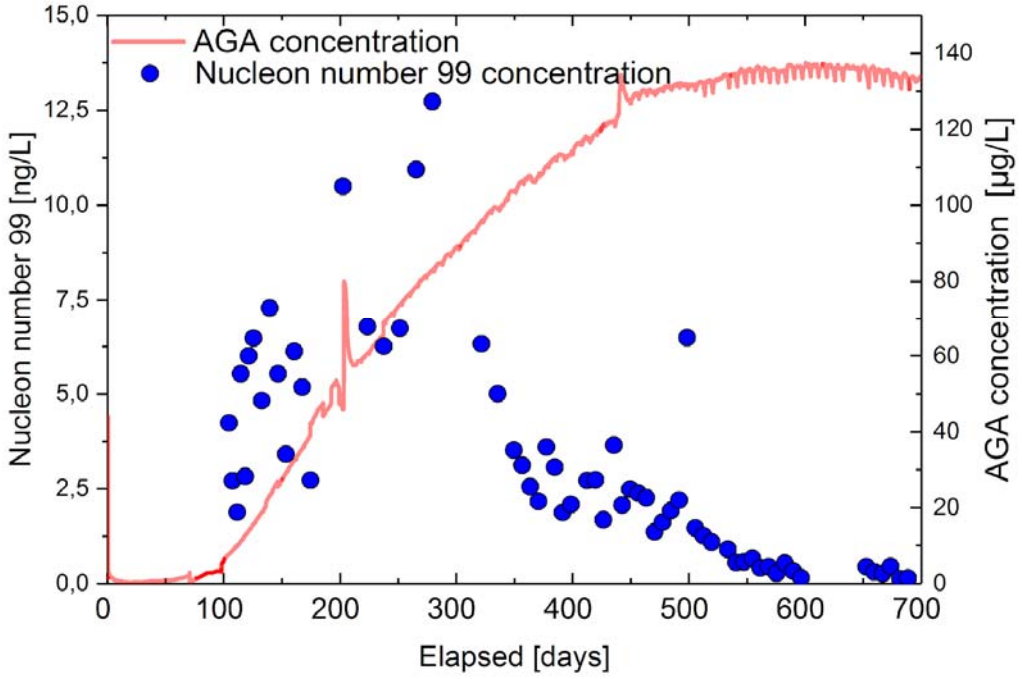

Figure 47: *Nucleon number 99 release from LIT sampled from GTS borehole CFM11.002.*

The concentration of ^{99}Tc was determined in seven LIT samples with a novel analytical approach employing AMS with a Gas Filled Analyzing Magnet System (GAMS) at the 14 MV Tandem AMS facility of the Maier-Leibnitz Laboratorium (MLL) of the Technical University of Munich (TUM, Garching, Germany) (Quinto, et al., 2019). The samples were collected within a time interval of 129−877 days from the starting of the experiment and were named LIT 14-35, -44, -52, -54, -84, -102, and -141. Because of experimental requirements, the samples had a limited size, and aliquots of 1.7 or 8 mL were dedicated to ^{99}Tc analysis, according to the available volume. Sample preparation has been described in Quinto et al., 2019[3]. Briefly, the samples were poured into Duran evaporation vessels to which 3 or 4 mg of ^{93}Nb from a Niobium ICP standard solution (Certified Reference Material, NH_4NbF_6 in H_2O, Certipur) was added. The solution obtained in this way was evaporated to dryness on a hot plate at 80 °C. The hot plate temperature was then increased stepwise up to 395 °C and left at such a temperature for 1 h to obtain the sample in a matrix of Nb oxide. The whole material was then thoroughly pressed into Cu sample holders suited to be used with the Cs-sputter negative ion source of the AMS at MLL. AMS measurements were carried out according to the procedure described in (Quinto, et al., 2019) and (Koll, et al., 2019) and profited especially of the use of the GAMS magnet filled with nitrogen gas. In the GAMS, ^{99}Tc (Z = 43) and ^{99}Ru (Z = 44) can be separated spatially in the x-direction on the basis of their different nuclear charge, since the trajectory of ^{99}Tc has a larger radius than ^{99}Ru that can be already partially stopped by the aperture in front of the detector and, in this way, suppressed by ~4 orders of magnitude before the particles enter the detector (Quinto, et al., 2019; Koll, et al., 2019).

Figure 48 shows that, among the LIT groundwater samples, sample LIT 14-102 presented the lowest ^{99}Tc level equal to ~1.3 ppq, while the highest level of ^{99}Tc was determined in correspondence of sample LIT 14-44 with ~192 ppq. It is important to note that the obtained data demonstrated that ^{99}Tc concentrations at ppq levels can be quantified in groundwater. This qualifies AMS-GAMS as an extremely sensitive analytical method for studying ^{99}Tc migration over a long-term period under in situ conditions (Quinto, et al., 2019).

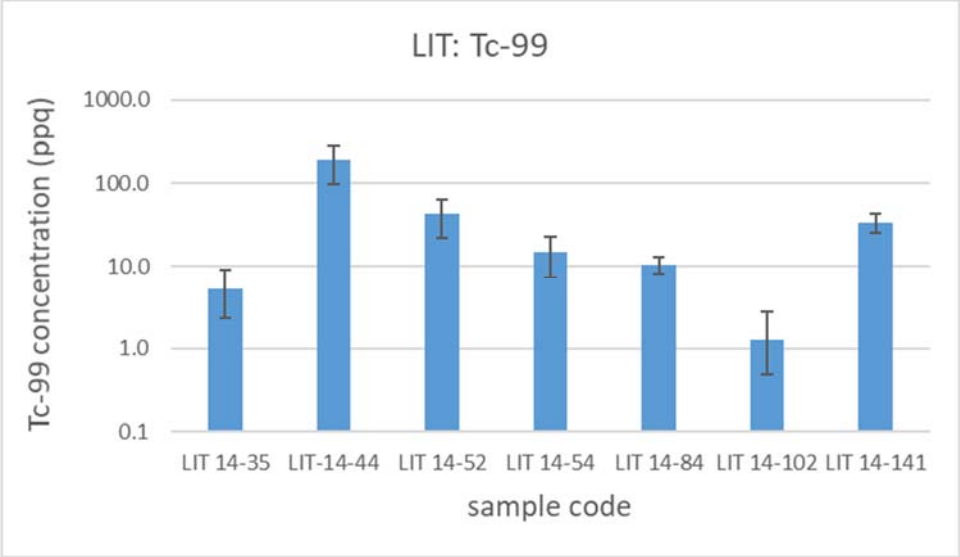

Figure 48: *^{99}Tc concentration (ppq) determined with AMS in chosen samples of LIT.*

2.2.3 Reaction of MI shear zone on ISC activities: LIBD versus hydraulic results

In order to use geothermal energy for the production of electricity, especially in the crystalline basement in Switzerland, stimulation experiments of the rock mass in order to develop a heat exchanger are required. To improve the geomechanical process understanding of permeability creation and induced seismicity, a scientific group of the Eidgenössische Technische Hochschule Zürich (ETH Zürich) performed stimulation experiments in the URL Grimsel between February and May 2017. Those experiments, which are part of the **I**n-situ **S**timulation and **C**irculation (ISC) project, where located near the MI shear zone. Since this shear zone is the respective shear zone of the LIT experiment, monitoring measurements by the staff of KIT-INE were necessary. Using Laser-Induced Breakdown Detection (LIBD) and several additional monitoring measurements, e.g. turbidity and pressure measurements, possible influences from the actions of ISC on the LIT experiment could be able to be observed.

Monitoring strategy & results

LIBD was utilized to monitor possible reactions of the ISC on the MI shear zone. In order to monitor continuously the colloid concentration and size the s-curve and the MOB-2 LIBD systems worked in parallel. Due to the fast measurement intervals of the MOB-2 system, this system was used to determine the average size and concentration of the colloids within short time intervals (between 5 and 15 min). The s-curve LIBD system, however, was set to a constant energy value, here 380 µJ, to investigate possible colloid concentration changes, via BDP fluctuations.

The first monitoring session covered the period from February 8th to February 15th. During this time, the group of the ETH Zürich performed stimulation experiments on preexisting fractures (transmissivities ranges from 1E-6 to 1E-10 m²/s). The stimulation of one fracture should be accomplished in one day and consists of three stimulation cycle procedures. Cycle procedure 1, with two sub cycles (1.1 and 1.2), was a pressure-controlled test phase, while cycle procedure 2 and 3 were flow rate controlled test phases. The duration of the cycles was between 40 and 70 min with a stepwise increase in applied pressure or flow rate, followed by a shut-in and a venting phase. The pressure-controlled test phase served to capture the initial breakdown of the transmissivity, and the flow-rate controlled test phase was used to increase the extent of the stimulation away from the injection hole (Source: internal report).

The monitoring using the MOB-2 system shows that to every time the colloid concentration and the average colloid size were below the detection and size limit of the device. The average breakdown probability at the highest calibrated voltage, which is 203 mV, was 32 %, which is too low to determine concentration and size. Therefore, in the following only the

measurement results of the s-curve LIBD system in monitoring mode are presented. Figure 48 present the monitoring results for each stimulation day. The cycle, the shut-in and the venting phases are highlighted and numbered. Next to the LIBD results, the turbidity, the pressure progress at the Pinkel and at the observation boreholes CFM11 and CFM0601 are shown over time. Since the BDP of the LIBD is a statistic value, rational time periods need to be set. From the 8th to the 10th of February a mean BDP was determined over a time period of 15 min and from the 13th to the 15th the frequency was increased to a mean BDP every 5 min.

Comparing the pressure progress over time at the three locations, a noticeable pressure increase during stimulation cycle procedure 2 is observable, with an increase of 1–2 kPa. This directly shows that the Grimsel fracture system is hydraulically well connected. Due to the stimulation the pressure increased with each stimulation day (8th to the 10th and 13th to 15th) and recovered to its initial value over the weekend (11th and 12th of February). The LIBD signal and the turbidity however remained unaffected and do not follow the pressure progress, except for the 15th of February. During the cycle procedure 2 on the 15th of February a contemporaneous increase in BDP with an increase in pressure could be observed. This however was not able to measure with the MOB-2 LIBD. The higher mean BDP values on the 14th and 15th of February were a cause of a slightly higher energy of the LIBD system (≈ 385 µJ) and therefore negligible.

Since the fluctuations and the colloid concentrations are that low, significant influences from the stimulation of preexisting fractures on the LIT experiment can be excluded.

The second monitoring session covered the period from the May 15th to May 18th. The stimulation experiments during this time aimed in creating new fractures due to hydraulic fracturing. A test protocol in 5 phases was considered: Phase 1 – Pulse test; Phase 2 – Formation breakdown; Phase 3 – Fracture propagation; Phase 4 – Pulse test; and Phase 5 – Final cycle (Source: internal report).

In May the hydraulic fracturing in the frame of ISC was conducted one week after the experiments of REMO-II, where a colloid and solute tracer pulse were injected to the MI shear zone (Chapter 2.2.1.). Since the tailing of this colloid pulse was longer as first expected, the signal of this tailing was still significantly higher as the background and persists during the planned monitoring week during the hydraulic fracturing of ISC. The mean BDP on the 15th of May was with an energy of 380 µJ 100 %. Decreasing the energy to 220 µJ the BDP decreased from 66 % on the 15th of May to 34 % on the 18th of May. Therefore, no comparability between the monitoring session in February and in May was given. The hydraulic data (data not shown) was comparable with the monitoring session in May and the overall pressure increased within the week around 3 kPa in total. However, since the turbidity (Turb_OBS, data not shown) remained unaffected and since the background of the LIBD signal was significantly increased by REMO-II, it is not possible to give a clear assessment on the impact of ISC on LIT

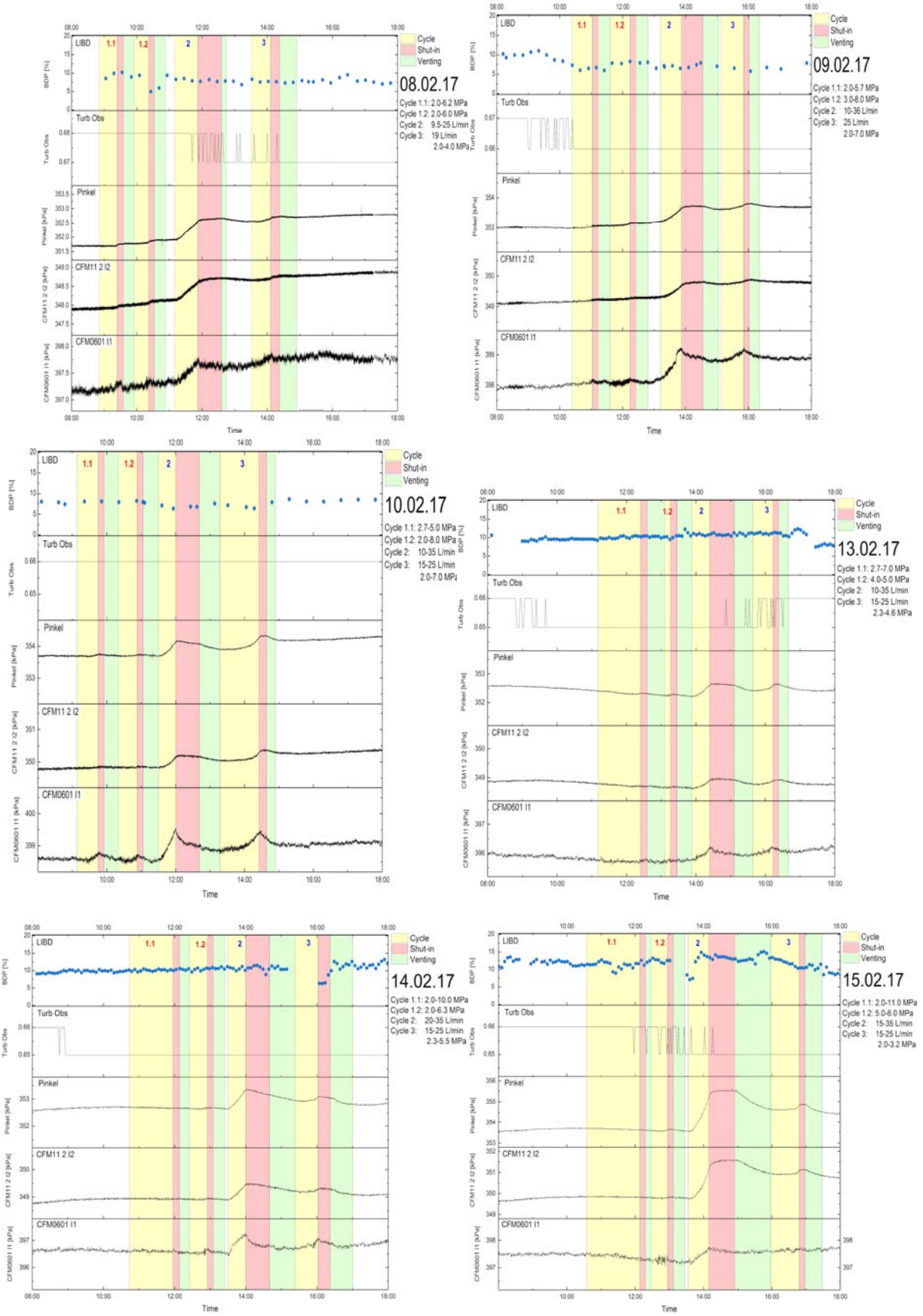

Figure 49: *Monitoring data by LIBD and pressure heads (08.02.2017, 09.02.2017, 10.02.2017, 13.02.2017, 14.02.2017 & 15.02.2017); respective date is indicated in the figure*

3. Modelling

The objectives of modelling within Kollorado-e^2 project are focused on various aspects. Thermodynamic benchmark calculations are performed in order to better understand the speciation of homologues and radionuclides under the field conditions at GTS, which has strong impact on their mobility in the emplaced bentonite and the Grimsel shear zone. Modelling of the flow field and the transport of ideal tracers aims at understanding the flow conditions in differently altered natural fractures and the comparison of experimental data under different hydraulic condition to µCT based models. Focus was especially lead on the effect of geometry simplifications compared to the real tracer migration experiments. Further, it contributes to a better understanding on the interaction of the flow field (fracture surface roughness and correlation length) with a compacted bentonite and corresponding erosion of the bentonite. Moreover, the application of transport models including kinetically-controlled processes to describe the interaction between radionuclides, colloids and sediment matrix as well as redox reactions of homologues and radionuclides with changes in their chemical properties yields in understanding the impact of the different processes on the shape of the break-through curves and on the recovery of the radionuclide tracers. It is here also used to design new field experiments in order to clarify and support model assumptions like a two-site desorption mechanism or the reduction of U(VI) and Np(V) during transport through the shear zone. The simulation of the radionuclide diffusion in the bentonite gives evidence on the expected radionuclide release from the bentonite during LIT and also contributes to some aspects of the analysis of the overcored material from LIT. Finally, the model calculations contribute to the qualification of the codes and sets the basis for calculations with regard to the long-term safety of deep geological repositories.

3.1 Thermodynamic benchmark calculations

In order to describe the transport and retardation effects of the radionuclides, particularly in the evolving geochemical conditions of the LIT their speciation needs to be known, cf. section 2.2.2. This is especially important for the redox state but also for the properties and charge of the major dissolved species, which strongly impacts the sorption behavior on the bentonite buffer/colloids and the fracture filling material as well as the maximum solubility of each element. For example, model calculations for radionuclide diffusion in the bentonite source of the LIT indicate that the tri- and tetravalent elements are expected to be rather immobile and not being released from the source within the 4.5 years duration of the experiment, whereas higher oxidized forms of technetium, uranium or neptunium, if present, are likely in large quantities released (see section 3.3).

An earlier thermodynamic benchmark for radionuclide speciation at the GTS was performed in 2000 (Bruno, et al., 2000). Since then updates affecting radionuclide speciation calculations have been reported in the literature which are mainly related to new thermodynamic data, more detailed knowledge on ground- and pore- water compositions and redox conditions for the scenario of interest. Particularly the conditions at the interface between bentonite and crystalline rock have been included into the new benchmark.

3.1.1 Benchmark description

An Excel table describing the modelling task for all involved partners and formalized tables for documentation of applied thermodynamic data and calculation results were distributed to the participants of the benchmark. The task was formulated as follows.

Speciation calculations shall be performed for five chemical solutions: (i) bentonite porewater, reducing, reducing (BPWR), (ii) bentonite porewater, oxidizing (BPWO), (iii) Grimsel groundwater (GGW), (iv) a 10/90 mixture of reducing bentonite porewater and GGW (MWR) and (v) a 10/90 mixture of oxidizing bentonite porewater and GGW (MWO).

Please use the reference data for bentonite waters and Grimsel groundwater as compiled in Table 14.

The chemical speciation of the following elements shall be considered in the benchmark calculations: Ca, Se, Tc, U, Th, Np, Am, Pu.

- Please calculate the chemical composition, Eh and pH value (i) for a mixture of 10% reducing bentonite porewater and 90 % Grimsel groundwater, and (ii) for a mixture of 10% oxidizing bentonite porewater and 90 % Grimsel groundwater. Please use these mixtures in the following speciation calculations.
- Speciation calculations 1: Please calculate the speciation for each element in all five solutions with the initial concentrations given in Table 15
- Speciation calculations 2: Please calculate the maximum dissolved element concentration and the speciation in all five solutions assuming an appropriate solid phase for each element.
- Please create ph-Eh diagrams for the elements Se, Tc, U, Np and Pu for all five solutions with the element concentrations given in Table 15
- Please provide the thermodynamic data of relevant complexes (contribution of more than 1 percent in at least one of your calculations) and solids and information about data uncertainties for the considered elements in the data sheets.
- Please fill in your calculation results and uncertainties in the result sheets.

Please provide additionally a word document with a brief summary of the calculations you did, the codes and thermodynamic database you used, necessary further information and comments/remarks, e.g. on specific problems or changes you needed to make.

Partners from UJV (Czech Republic), JAEA/NUMO (Japan), RWM/AMEC (UK) KAERI (Korea) and GRS and KIT (Germany) participated in the benchmark. In 2018 a workshop was performed to discuss the results and identify any shortcomings. Based on the results from the workshop several issues were identified, where further information was needed. Therefore, GRS and KIT developed a short questionnaire to receive as complete as possible information on:

- ionic strength correction equation or formalism,
- thermodynamic data and uncertainties,
- any modifications used for the reference water (e.g. charge balance and ions used),
- a short description of the strategy
  - to select the solid phase used (explanation for example why fresh or aged species have been used; “please consider that the duration of the LIT experiment is now about 4 years”
  - for considered or excluded aqueous species
  - use of deviating stability constants to the NEA-TDB or “national database” …
  - additional explanations like expert judgement, conservatism, etc.

A detailed evaluation of all calculation results and answers to the questionnaire has so far been performed only for the partners GRS and KIT-INE and is published in (Montoya, et al., 2020, to be submitted). Here, in section 3.1.2 only some key results are summarized. For the final evaluation of the results of all partners an additional meeting is planned, and a publication is foreseen in 2020.

Both, GRS and KIT used PHREEQC v.3.3 geochemical program (Parkhurst & Appelo, 2013) for the calculations and PhreePlot v.11, (2017 release, (Kinniburgh & Cooper, 2011) to generate the Pourbaix diagrams. GRS used the database adapted from PSI/Nagra thermodynamic database (Thoenen, et al., 2014) and modified for the application in the WEIMAR project (Noseck, et al., 2018). KIT used the database Thermochimie (Giffaut, et al., 2014).

Table 14: *Log p_{CO2}, pH-value, Eh-value and concentration of dissolved elements in [M] in bentonite porewaters (Fernandez et al., 2004) and Grimsel groundwater (Duro, et al., 2006).*

	BPWR	**BPWO**	**GGW**
Log pCO_2	3.5		-
pH	7.44		9.6
Eh(SHE. mV)	-200	100	-220
Na [M]	3.3E-01		6.9E-04
K [M]	2.6E-03		5.0E-06
Mg [M]	8.1E-02		6.2E-07
Ca [M]	6.8E-02		1.4E-04
Al [M]	-		2.63E-06
Fe [M]	2.0E-09	1.0E-09	3.0E-09
Mn [M]	-		5.0E-09
Sr [M]	6.10E-04		2.0E-06
Cl [M]	4.20E-01		1.6E-04
HCO_3 [M]	3.10E-04		4.5E-04
Si [M]	1.80E-04		2.5E-04
SO_4 [M]	1.90E-02		6.1E-05
F [M]	-		3.6E-04
Br [M]	-		3.8E-07

Table 15: *Reference concentrations for the elements considered in the benchmark*

Element	**Ref. concentration [mol/l]**	**Element**	**Ref. concentration [mol/l]**
Se	$1 \cdot 10^{-5}$	Np	$9 \cdot 10^{-8}$
Tc	$1 \cdot 10^{-8}$	Am	$4 \cdot 10^{-10}$
U	$4 \cdot 10^{-10}$	Pu	$2 \cdot 10^{-9}$
Th	$5 \cdot 10^{-9}$		

3.1.2 Benchmark results

In the first step the composition of the mixing waters was calculated. After charge balancing of the waters the pH values were predicted by allowing their values to vary under the electrical neutrality constraint. With respect to the Eh-value of the waters different approaches were used and the results are shown in Table 16. For GRS the redox potentials of the resulting mixtures were predicted by allowing their values to vary under the constraint of there being a constant number of redox electrons. KIT applied Eh values similar to the ones proposed for reducing and oxidizing bentonite porewater to the mixed waters. This results in more reducing conditions in MWR (Eh_{SHE} = -303 mV) and MWO (Eh_{SHE} = -148 mV), for the calculations from GRS compared to the respective values of Eh_{SHE} = -220 mV and Eh_{SHE} = +100 mV for the calculations from KIT. All element concentrations are similar or differ only slightly.

Table 16:P*H-value, Eh-value and concentration of dissolved elements in [M] in reducing and oxidizing mixed waters as calculated by GRS and KIT.*

	GRS		**KIT**	
	MWR	MWO	MWR	MWO
pH	9.06		8.97	

Eh(SHE. mV)	-303	-148	-220	100
Na [M]	3.39E-02		3.46E-02	
K [M]	2.65E-04		2.72E-04	
Mg [M]	8.10E-03		8.34E-03	
Ca [M]	6.93E-03		7.13E-03	
Al [M]	2.37E-06		2.37E-06	
Fe [M]	2.91E-09	2.80E-09	2.91E-09	2.80E-09
Mn [M]	4.50E-09		4.50E-09	
Sr [M]	6.28E-05		6.28E-05	
Cl [M]	5.95E-02		4.34E-02	
HCO_3 [M]	4.35E-04		4.37E-04	
Si [M]	2.43E-04		2.44E-04	
SO_4 [M]	1.96E-03		2.01E-03	
F [M]	3.24E-04		3.24E-04	
Br [M]	3.42E-07		3.42E-07	

Selenium

For Se as a redox-sensitive element the speciation is strongly affected by the Eh and pH value. The thermodynamic data for the species relevant in the investigated systems are rather similar for both databases (Table 17). For the systems BPW and GGW Se(s) has been selected as concentration determining solid phase by GRS and KIT, see Table 18. The slightly higher concentrations for GRS in BPWR and GGW are due to the formation of polyselenides, which have not been considered by KIT. Differences in MWR and MWO are due to the higher Eh values of the mixed waters and thereby caused different solubility determining solid phases. in case of KIT (see above). These aspects are discussed in detail in (Montoya, et al., 2020, to be submitted).

Technetium

For Tc very similar results are yielded by GRS and KIT, see Table 19, which is well explained by the very similar thermodynamic data in both databases (Table 20). Moreover, in all cases TcO_2:1.6H_2O(s) is the solubility limiting solid phase. Under reducing conditions in BPWR, GGW and MWR the calculated maximum concentration is around $4 \cdot 10^{-9}$ mol/l and the speciation is dominated by the Tc(IV) species $TcO(OH)_2$. For BPWO the concentrations are around $1.75 \cdot 10^{-3}$ mol/l and the system is dominated by the heptavalent TcO_4^- species. The only difference between GRS and KIT is observed for MWO, where the system is in case of KIT dominated by Tc(VII) and no solubility determining mineral phase could be determined due to the much higher Eh-value in this system, see above.

Uranium

The chemistry of uranium is complex and its speciation in aqueous solutions has been extensively investigated. The thermodynamic databases applied by GRS and KIT are very similar with respect to the key uranium species in the systems considered here, cf. Table 22. Consequently, there are no significant differences in the calculated maximum concentrations of GRS and KIT, see Table 21.

In a pH range from 7.2 to 10.8, i.e. in all considered systems, ternary calcium uranyl carbonate complexes dominate the speciation. This is also indicated in the Pourbaix diagram in Figure 50, where the left figure shows the large range of $CaUO_2(CO_3)_3^{-2}$. complex, whereas in calculations from JAERI, where this complex has not been considered, uranyl carbonate and hydroxo complexes are dominating

The benchmark exercise has also contributed to the identification of a shortcoming in the PSI/Nagra TDB. As already discussed in the report (Thoenen, et al., 2014) the stability constant ($\log\beta = 29.22 \pm 0.25$) for $Ca_2UO_2(CO_3)_3$ was identified to be too low and therefore GRS checked available literature and finally decided to use the value of ($\log\beta = 30.6 \pm 0.09$) which was derived from a recent review (Richter, et al., 2015) and is recommended in the German database THEREDA (Moog, et al., 2015). Using this value, the benchmark results are much better comparable. Details can be found in (Montoya, et al., 2020, to be submitted).

Thorium

Thorium(IV) is the only stable oxidation state under aqueous conditions, therefore no difference in speciation for reduced and oxidized waters (BPWR/BPWO and MWR/MWO) occur, Table 23. The stability constants for the complexes are very similar in both databases, see Table 24. However, a difference regards the solubility determining solid phase. Both, GRS and KIT selected an amorphous ThO2 mineral phase but GRS performed calculations for a fresh and an aged species, whereas KIT used the solubility product for an averaged value not distinguishing between a fresh and aged solid. This is directly reflected in the Th maximum concentrations, decreasing in the order fresh – averaged - aged. With respect to the LIT experiment, which has been performed over a time frame of 4.5 years it was recommended in (Montoya, et al., 2020, to be submitted) to use the data for the aged species, which was derived from studies where the systems were equilibrated for more than 70 days.

Neptunium

For neptunium again the calculated maximum concentrations in the range of $1 \cdot 10^{-9}$ to $2 \cdot 10^{-9}$ mol/l agree very well for GRS and KIT for nearly all of the systems (Table 25). This is again due to very similar thermodynamic data for the key species in both databases (Table 26). $Np(OH)_4$ is the predominant species in nearly all of the systems. One exception is the more oxidizing BPWO, where Np(V) species become relevant. The higher concentration in case of GRS can be explained by the formation of the strong $NpO_2SiO(OH)_3$ complex, which is not included in the Thermochimie database used by KIT, see discussions in (Montoya, et al., 2020, to be submitted). In the case of KIT Np(V) species are also relevant in MWO due to the much higher Eh value in this system compared to GRS.

Americium

Am(III) is the only stable oxidation state under the evolving conditions of the LIT experiment consequently, differences due to redox reactions are not relevant. For americium similar maximum concentrations have been determined by GRS and KIT, with always slightly higher values calculated by GRS, see Table 27. The main reason for that is the higher value allocated to the stability constant of the $AmOSi(OH)_3^{2+}$ complex by GRS ($\log\beta = -1.71 \pm 0.4$) compared to ($\log\beta = 2.31 \pm 0.13$) applied by KIT (Table 28). An additional small contribution results from the slightly higher value for the stability constant of $Am(CO_3)_2^-$ in the database applied by GRS. The origin of the data and reasons for differences are further discussed in (Montoya, et al., 2020, to be submitted).

Plutonium

Pu is mainly present in the oxidation states (+III) and (+IV) under the conditions of the systems considered here. Both, GRS and KIT considered the solid PuO_2(am) in all systems as the solubility limiting phases. However, the maximum Pu concentrations are always more than a factor 6 higher in the calculations from KIT, see Tab. 30. The main reason for this difference is the large difference in the solubility products applied by GRS ($\log K = -2.33 \pm 0.52$) and by KIT-INE ($\log K = -0.80$), cf. Tab. 31. The value for a much lower solubility used by GRS was selected for the PSI/Nagra database and is based on NEA TDB (Guillaumont, 2003). The origin and differences to the value included in Thermochimie is discussed in (Montoya et al. 2019). The difference in plutonium maximum concentrations is less than expected, because of the con-

sideration of the strong ternary complexes $PuSiO(OH)_3^{2+}$ and $Pu(CO_3)(OH)_3$ as supplemental data in the PSI/Nagra database. Both complexes have not been included in ThermoChimie database. Particularly the latter complex dominates the speciation in solution in the BPWO, GGW, MWR and MWO systems in GRS calculations.

Table 17: *Maximum concentration and dominating species calculated for selenium.*

	BPWR		**BPWO**		**GGW**		**MWR**		**MWO**	
	GRS	KIT	GRS	KIT	GRS	KIT	GRS	KIT	GRS	KIT
SLP	Se(cr)	Se(s)	Se(cr)	Se(s)	Se(cr)	Se(s)	$FeSe_2$	Se(s)	$FeSe_2$	$Ca(SeO_3)$: H_2O(s)
Setot [M]	1.0E-08	5.6E-09	3.1E-09	1.7E-08	2.2E-09	1.7E-10	1.7E-08	8.7E-10	2.0E-07	3.7E-04
HSe-	90	100	<1	<1	11	100	100	99	<1	<1
Se_4^{-2}	8	n.c	<1	<1	73	n.c.	<1	n.c.	98	n.c.
Se_3^{-2}	2	n.c	<1	<1	16	n.c.	<1	n.c.	2	n.c.
$H(SeO_3)$-	<1	<1	78	70	<1	<1	<1	<1	<1	11
SeO_3^{-2}	<1	<1	22	30	<1	<1	<1	1	<1	89

n.c. = not applied in calculation

Table 18: *Relevant stability constants logβ and solubility products logK for selenium contained in the databases of GRS and KIT.*

Species	**GRS**	**KIT**
$9\ H^+ + 8\ e^- - 4\ H_2O + SeO_4^{-2} = HSe^-$	81.60	81.57
$2\ H^+ + 2\ e^- - H_2O + SeO_4^{-2} = SeO_3^{-2}$	28.05	28.04
$H^+ + SeO_3^{-2} = HSeO_3^-$	8.36	8.36
$-3H^+ - 4e^- + 3HSe^- = Se_3^{-2}$	5.24	– b
$-4\ H^+ - 6\ e^- + 4\ HSe^- = Se_4^{-2}$	13.38	– b
$FeSe_2(cr) = 2\ HSe^- - 2\ H^+ - 2\ e^- + Fe^{+2}$	-17.13 c	-17.13
$Se(s) = HSe^- - H^+ - 2\ e^-$	-7.60	-7.62
$Fe1.0_4Se(beta) = 1.04Fe^{+2} - H^+ + 0.080e^- + HSe^-$	Not in DB	-3.40
$Ca(SeO_3):H_2O = Ca^{+2} + SeO_3^{-2} + H_2O$	-6.40	-6.4

Table 19: *Maximum concentration and dominating species calculated for technetium.*

	BPWR		**BPWO**		**GGW**		**MWR**		**MWO**	
	GRS	KIT	GRS	KIT	GRS	KIT	GRS	KIT	GRS	KIT
SLP	TcO_2:1.6H_2O(s) / TcO_2:1.63H_2O(s)									
Tctot [M]	4.1E-09	4.0E-09	1.7E-03	1.8E-03	4.2E-09	4.3E-09	4.1E-09	4.1-09	4.9E-09	n.s.l.
$TcO(OH)_2$	99	99	<1	<1	94	88	98	15	81	13
$(TcO)(OH)_3^-$	<1	<1	<1	<1	5	12	2	<1	1	<1
TcO_4^-	<1	<1	100	100	<1	<1	<1	84	17	86

**n.s.l. = no solubility limiting phase*

Table 20: *Relevant stability constants logβ and solubility products logK for technetium contained in the databases of GRS and KIT.*

Species	**GRS**	**KIT**
$TcO(OH)_2$	master species	master species
$TcO(OH)_2 + H_2O - H^+ = TcO(OH)_3^-$	-10.9	-10.8
$TcO(OH)_2 + CO_3^{-2} + 2\ H^+ - H_2O = TcCO_3(OH)_2$	19.30	19.26

$TcO(OH)_2 + H^+ + CO_3^{-2} = TcCO_3(OH)_3^-$	-11.00	-10.96
$TcO(OH)_2 + H_2O - H^+ - 3\ e^- = TcO_4^-$	-29.40	-29.43
$TcO_2\_1.6H_2O(s) = TcO(OH)_2 + 0.6\ H_2O$	-8.4	-8.4

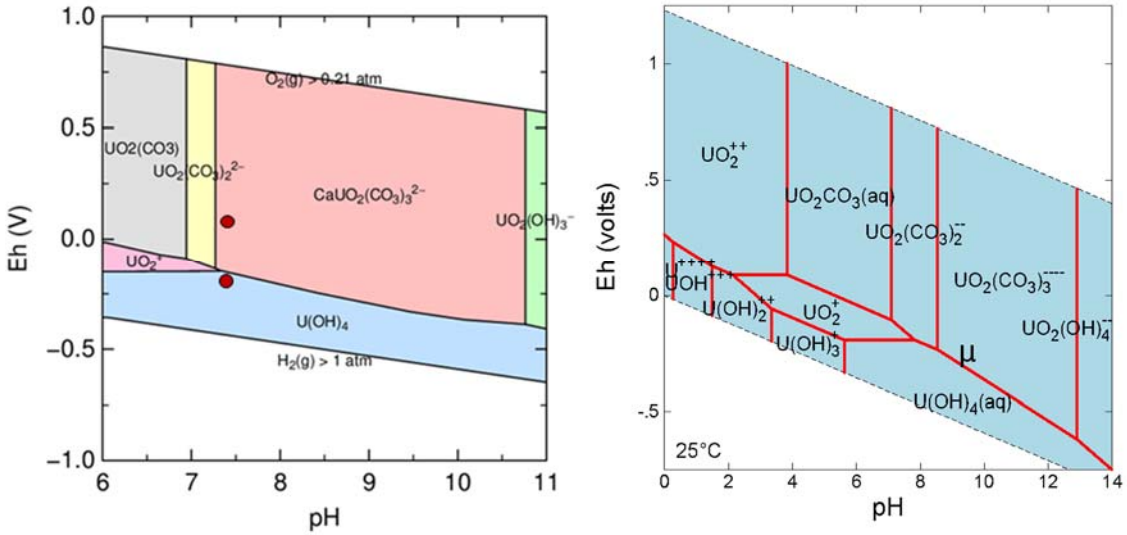

Figure 50: *PH-Eh diagram calculated with (KIT-INE, left) and without (JAERI, right) consideration of ternary calcium UO_2 carbonate complexes for GGW; [U] = $4 \cdot 10^{-10}$ mol/l*

Table 21: *Maximum concentration and dominating species calculated for uranium with modified value for the $Ca_2UO_2(CO_3)_3$ complex for GRS.*

	BPWR		**BPWO**		**GGW**		**MWR**		**MWO**	
	GRS	KIT	GRS	KIT	GRS	KIT	GRS	KIT	GRS	KIT
SLP	UO_2 (am.hyd)	$UO_2 \cdot 2H_2O$ (am)	Uranophane		Uranophane		Uranophane		Uranophane	
U_{tot} [M]	3.8E-08	3.5E-08	8.2E-07	7.3E-07	3.4E-08	3.5E-08	2.6E-07	3.5E-07	2.4E-07	2.1E-07
$U(OH)_4$	8	9	<1	<1	<1	<1	4	<1	<1	<1
$UCO_3(OH)_3^-$	7	n.d.	<1	n.d.	<1	n.d.	5	n.d.	<1	n.d.
UO_2^+	1	<1	<1	<1	<1	<1	<1	<1	<1	<1
$UO_2(CO_3)_3^{-4}$	<1	<1	<1	<1	5	5	<1	<1	<1	<1
$Ca_2UO_2(CO_3)_3$	79	80	94	89	18	21	66	80	72	80
$CaUO_2(CO_3)_3^{-2}$	5	9	5	10	75	72	23	20	25	20
$MgUO_2(CO_3)_3^{-2}$	<1	n.d.	<1	n.d.	<1	n.d.	2	n.d.	3	n.d.

n.d. = not included in database

Table 22: *Relevant stability constants* logβ *and solubility products* logK *for uranium contained in the databases of GRS and KIT.*

Species	**GRS**	**KIT**
$UO_2^{+2} + 3H_2O = UO_2(OH)_3^- + 3H^+$	-20.25	-20.25
$UO_2^{+2} + 2H_2O = UO_2(OH)_2^{+} 2H^+$	-12.15	
$3UO_2^{+2} + 5H_2O = (UO_2)_3(OH)_5^+ + 5H^+$	-15.55	-15.55
$3UO_2^{+2} + 7H_2O = (UO_2)_3(OH)_7^{-+} 7H^+$	-32.2	-32.2
$4UO_2^{+2} + 7H_2O = (UO_2)_4(OH)_7^+ + 7H^+$	-21.9	-21.9
$UO_2^{+2} + 2CO_3^{-2} = UO_2(CO_3)_2^{-2}$	16.61	16.61

$UO_2^{+2} + 3CO_3^{-2} = UO_2(CO_3)_3^{-4}$	21.84	21.84
$2UO_2^{+2} + CO_3^{-2} + 3H_2O = (UO_2)_2(CO_3)(OH)_3^- + 3H^+$	-0.86	-0.86
$2Ca^{+2} + 3CO_3^{-2} + UO_2^{+2} = Ca_2UO_2(CO_3)_3$	29.22 (30.6)	30.7
$Ca^{+2} + UO_2^{+2} + 3CO_3^{-2} = CaUO_2(CO_3)_3^{-2}$	27.18	27.18
$Mg^{+2} + UO_2^{+2} + 3\ CO_3^{-2} = MgUO_2(CO_3)_3^{-2}$	26.11	
$U^{+4} + 3H_2O = U(OH)_3^+ + 3H^+$	-4.70	-4.70
$U^{+4} + 4H_2O = U(OH)_4 + 4H^+$	-10.0	-10.0
$U^{+4} + CO_3^{-2} + 3\ H_2O - 3\ H^+ = UCO_3(OH)_3^-$	4.0	
$4H^+ + UO_2^{+2} + 2e^- = U^{+4} + 2H_2O$	9.04	9.04
$UO_2^{+2} + e^- = UO_2^+$	1.484	
Uranophane: $Ca(H_3O)_2(UO_2)_2(SiO_4)_2{:}3H_2O = Ca^{+2} + 2\ UO_2^{+2} + 2\ Si(OH)_4 + 5\ H_2O - 6H^+$	9.42	9.42
$UO_2{:}2H_2O(am) = U^{+4} - 4\ H^+ + 4\ H_2O$	Not in DB	1.5
$UO_2(am) = U^{+4} - 4\ H^+ + 2\ H_2O$	1.5	Not in DB

Table 23: *Maximum concentration and dominating species calculated for thorium.*

	BPWR/BPWO			**GGW**			**MWR/MWO**		
	GRS		KIT	GRS		KIT	GRS		KIT
SLP	ThO_2,ag	ThO_2,fr	ThO_2,am	ThO_2,ag	ThO_2,fr	ThO_2,am	ThO_2,ag	ThO_2,fr	ThO_2,am
Th_{tot} [M]	1.69E-09	1.1E-08	1.4E-09	2.4E-09	1.5E-08	1.5E-08	2.2E-09	1.5E-08	1.4E-08
$Th(OH)_4$	69	69	59	52	52	53	58	58	53
$Th(OH)_3^+$	n.d.	n.d.	8	n.d.	n.d.	<1	n.d.	n.d.	<1
$Th(OH)_2(CO_3)$	1	1	1	<1	<1	<1	<1	<1	<1
$Th(OH)_3(CO_3)^-$	28	28	30	45	45	44	39	39	44
$Th(OH)_2(CO_3)_2^{-2}$	1	1	2	3	3	3	3	3	3

n.d. = not included in database

Table 24: *Relevant stability constants* logβ *and solubility products* logK *for thorium contained in the databases of GRS and KIT.*

Species	**GRS**	**KIT**
$Th^{+4} - 3\ H^+ + 3\ H_2O = Th(OH)_3^+$	Not in DB	-11
$Th^{+4} + 4\ H_2O - 4\ H^+ = Th(OH)_4$	-17.4	-17.4
$Th^{+4} - 2\ H^+ + CO_3^{-2} + 2\ H_2O = Th(OH)_2(CO_3)$	2.51	2.5
$Th^{+4} + 2\ CO_3^{-2} + 2\ H_2O - 2\ H^+ = Th(CO_3)_2(OH)_2^{-2}$	8.81	8.8
$Th^{+4} - 3\ H^+ + CO_3^{-2} + 3\ H_2O = Th(OH)_3(CO_3)^-$	-3.69	-3.7
$Th^{+4} + CO_3^{-2} + 4\ H_2O - 4\ H^+ = ThCO_3(OH)_4^{-2}$	-15.6	-15.6
ThO_2(am,fresh) = $Th^{+4} + 2\ H_2O - 4\ H^+$	9.3	8.9
ThO_2(am,aged) = $Th^{+4} + 2\ H_2O - 4\ H^+$	8.5	

Table 25: *Maximum concentration and dominating species calculated for neptunium.*

	BPWR		**BPWO**		**GGW**		**MWR**		**MWO**	
	GRS	KIT	GRS	KIT	GRS	KIT	GRS	KIT	GRS	KIT
SLP	NpO_2(am.hyd) / $NpO_2{\cdot}2H_2O$(am)									
Np_{tot} [M]	9.9E-10	1.0E-9	6.7E-09	1.9E-09	1.0E-09	1.0E-09	9.9E-10	1.0E-09	1.0E-09	2.5E-09
$Np(OH)_4$	98	97	14	52	100	98	100	98	99	40

$Np(OH)_3^+$	2	2	<1	1	<1	<1	<1	<1	<1	<1
$Np(CO_3)(OH)_3^-$	<1	1	<1	<1	<1	2	<1	2	<1	1
NpO_2^+	<1	<1	13	44	<1	<1	<1	<1	<1	30
NpO_2Cl	n.d.	1	n.d.	1	n.d.	<1	n.d.	<1	n.d.	<1
$NpO_2(CO_3)^-$	<1	<1	<1	1	<1	<1	<1	<1	<1	29
$NpO_2SiO(OH)_3$	<1	<1	73	n.d.	<1	n.d.	<1	n.d.	1	n.d.

n.d. = not included in database

Table 26: *Relevant stability constants* logβ *and solubility products* logK *for neptunium contained in the databases of GRS and KIT.*

Species	**GRS**	**KIT**
$Np^{+4} + 3\ H_2O - 3\ H^+ = Np(OH)_3^+$	-2.8	-2.8
$Np^{+4} + 4\ H_2O - 4\ H^+ = Np(OH)_4$	-8.3	-8.3
$Np^{+4} + 2\ CO_3^{-2} + 2\ H_2O - 2\ H^+ = Np(CO_3)_2(OH)_2^{-2}$	Not in DB	15.17
$Np^{+4} + CO_3^{-2} + 3H_2O - 3H^+ = NpCO_3(OH)_3^-$	2.0 7	3.82
$Np^{+4} - 4\ H^+ + CO_3^{-2} + 4\ H_2O = Np(OH)_4(CO_3)^{-2}$	Not in DB	-6.83
$NpO_2^{+2} + e^- = NpO_2^+$	19.59	19.59
$NpO_2 + H_2O - H^+ = NpO_2OH$	-11.3	
$NpO_2^+ + Cl^- = NpO_2Cl$	Not in DB	-0.93
$NpO_2^+ + SiO(OH)_3^- = NpO_2SiO(OH)_3$	7.0	
$NpO_2{:}2H_2O(am) = NpO_2^+ + 4H_2O - 4H^+$	Not in DB	-0.7
NpO_2 (am, hyd) $= Np_4^+ + 2H_2O - 4H^+$	-0.7	Not in DB
$NpO_2OH(am, fr) = NpO_2^+ + H_2O - H^+$	5.3	

Table 27: *Maximum concentration and dominating species calculated for americium.*

	BPWR/BPWO		**GGW**		**MWR/MWO**	
	GRS	KIT	GRS	KIT	GRS	KIT
SLP	$AmOHCO_3$ (am.hyd)	$Am(CO_3)(OH)$ (am)	$Am(OH)_3$ (am)	$Am(OH)_3$ (am)	$AmOHCO_3$ (am.hyd)	$Am(CO_3)(OH)$ (am)
Am_{tot} [M]	4.0E-05	2.4E-05	8.7E-08	5.0E-08	6.8E-07	3.1E-07
Am^{+3}	4	18	<1	<1	<1	<1
$Am(OH)_2^+$	<1	<1	<1	<1	1	3
$Am(OH)^{+2}$	2	5	19	33	9	18
$Am(OH)_3$	<1	<1	<1	1	<1	<1
$Am(CO_3)^+$	8	10	10	13	10	21
$Am(CO_3)_2^-$	<1	<1	50	43	10	12
$Am(SO_4)^+$	1	3	<1	<1	<1	<1
$AmCl^{+2}$	<1	1	<1	<1	<1	<1
$AmOSi(OH)_3^{+2}$	83	61	20	9	70	46

Table 28: *Relevant stability constants* logβ *and solubility products* logK *for americium contained in the databases of GRS and KIT.*

Species	**GRS**	**KIT**
$Am^{+3} + H_2O - H^+ = AmOH^{+2}$	-7.2	-7.2
$Am^{+3} + 2\ H_2O - 2\ H^+ = Am(OH)_2^+$	-15.1	-15.1
$Am^{+3} + 3\ H_2O - 3\ H^+ = Am(OH)_3$	-26.2	-26.2
$Am^{+3} + CO_3^{-2} = AmCO_3^+$	8	7.9
$Am^{+3} + 2\ CO_3^{-2} = Am(CO_3)_2^-$	12.9	12.6
$Am^{+3} + Si(OH)_4 - H^+ = AmSiO(OH)_3^{+2}$	-1.71	-2.31
$Am^{+3} + SO_4^{-2} = AmSO_4^+$	3.3	3.45
$Am^{+3} + Cl^- = AmCl^{+2}$	0.24	0.24
$AmCO_3OH(am) = Am^{+3} + CO_3^{-2} + H_2O - H^+$	-6.2	-6.2

$AmCO_3OH(cr) = Am^{+3} + CO_3^{-2} + H_2O - H^+$	-8.4 *	
$Am(OH)_3(am) = Am^{+3} + 3\ H_2O - 3\ H^+$	16.9	16.9

** $AmOHCO_3 : 0.5H_2O(cr)$*

Table 29: *Maximum concentration and dominating species calculated for plutonium.*

	BPWR		**BPWO**		**GGW**		**MWR**		**MWO**	
	GRS	KIT	GRS	KIT	GRS	KIT	GRS	KIT	GRS	KIT
SLP					PuO_2(hyd.ag) / $Pu(OH)_4$(am)					
Pu_{tot} [M]	4.3E-09	2.9E-8	3.9E-11	5.4E-10	8.2E-11	5.0E-10	6.8E-11	5.0E-10	6.5E-11	5.0E-10
Pu^{+3}	3	39	<1	<1	<1	<1	<1	<1	<1	<1
$Pu(OH)^{+2}$	3	22	<1	<1	<1	<1	<1	<1	<1	<1
$Pu(CO_3)^+$	6	12	<1	<1	<1	<1	<1	<1	<1	<1
$Pu(SO_4)^+$	4	22	<1	<1	<1	<1	<1	<1	<1	<1
$Pu(SO_4)_2^-$	<1	3	<1	<1	<1	<1	<1	<1	<1	<1
$PuCl^{+2}$	6	n.d.	<1	n.d.	<1	n.d.	<1	n.d.	<1	n.d.
$PuSiO(OH)_3^{+2}$	77	n.d.	<1	n.d.	<1	n.d.	3	n.d.	<1	n.d.
$Pu(OH)_4$	<1	2	6	92	3	92	3	100	4	100
$Pu(OH)_3^+$	<1	8	<1	8	<1	8	<1	<1	<1	<1
$Pu(CO_3)(OH)_3^-$	<1	n.d.	94	n.d.	97	n.d.	91	n.d.	96	n.d.

n.d. = not included in database

Table 30: *Relevant stability constants* logβ *and solubility products* logK_s *for plutonium contained in the databases of GRS and KIT.*

Species	**GRS**	**KIT**
$Pu^{+4} + e^- = Pu^{+3}$	17.69	
$Pu^{+3} - H^+ + H_2O = PuOH^{+2}$	-6.9	-6.9
$Pu^{+3} + CO_3^{-2} = PuCO_3^+$	8	7.64
$Pu^{+3} + 2\ CO_3^{-2} = Pu(CO_3)_2^-$	12.9	12.54
$Pu^{+3} + SO_4^{-2} = PuSO_4^+$	3.9	3.91
$Pu^{+3} + SO_4^{-2} = Pu(SO_4)_2^-$	5.7	5.7
$Pu^{+3} + Cl^- = PuCl^{+2}$	1.2	
$Pu^{+3} + Si(OH)_4 - H^+ = PuSiO(OH)_3^{+2}$	-1.71	
$Pu^{+4} + 4\ H_2O - 4\ H^+ = Pu(OH)_4$	-9.3	-8.5
$Pu^{+4} + CO_3^{-2} + 3\ H_2O - 3\ H^+ = Pu(CO_3)_2(OH)_2^{-2}$	6.0	
$Pu^{+4} + 2\ CO_3^{-2} + 2\ H_2O - 2\ H^+ = Pu(CO_3)_2(OH)_2^{-2}$	Not in DB	16.76
$PuO_2(hyd,ag) = Pu^{+4} - 4\ H^+ + 4\ H_2O$	-2.33	
$Pu(OH)_4(am) = Pu^{+4} - 4\ H^+ + 4\ H_2O$		-0.80

3.1.3 Benchmark conclusions and outlook

Thermodynamic benchmark calculations have been performed to determine the aqueous speciation of seven radionuclides mainly including actinides and fission products (i.e. ^{75}Se(VI), ^{99}Tc(VII),^{233}U(VI), ^{237}Np(V), ^{241}Am(III), Th(IV) and ^{242}Pu(IV)) in different water compositions representing the geochemical evolution through the in-situ experiment LIT at GTS. By comparison of the results obtained by the modelling groups from GRS and KIT key geochemical parameters affecting radionuclide transport could be identified.

Since publication of a previous modelling exercise (Bruno, et al., 2000) thermodynamic databases have been further developed and harmonized, particularly within the NEA TDB project, where both databases applied here are based on. Particularly, the existence of new species like ternary silica actinide complexes, ternary uranyl carbonate complexes or iron selenides have been proofed and included, impacting for example the speciation and solubility of uranium, americium or selenium in the systems investigated here.

The model comparison also showed the relevance of expert judgement in modelling decisions. The characteristics of solid phases, especially the selection of a crystalline, aged or fresh mineral phase directly impacts the solubility. For ThO_2, as an example, it is recommended to use the value for the aged phase considering the 4.5 years duration of the LIT experiment. In a similar way, the inclusion/exclusion of mobile species leads to an increase/decrease of the solubility like for the polyselenides in case of selenium. A further aspect regards differences in the conceptual models, e.g. for the mixing of bentonite and Grimsel water. Here the different assumptions used by GRS and KIT causes very different Eh values for the mixed waters and impacts maximum concentrations of redox sensitive species like selenium or technetium. All these modelling decisions need to be transparent and well justified.

In general, the calculations of both modelling groups agree well and differences in results could always be traced back to slight differences in data or in modelling assumptions as described above. This enhances confidence and represents a sound basis for a planned second part of the modelling exercise, which will emphasize on ion exchange and surface complexation processes on key mineral phases in the bentonite and the minerals of the shear zone / crystalline rock at GTS.

The evaluation of the whole benchmark including the results obtained by other partners from the CFM project is still on the way and will be published soon. For the second part of the benchmark it is planned to perform this exercise once again within participants from other countries in the CFM project.

Results from the benchmark calculations presented here may be verified by the currently started analysis of the over-cored material of the LIT, where it is amongst others intended to identify radionuclide redox states and mineral phases in the bentonite and the adjacent granite. This will be performed within the German follow-on project Kollorado-e3 and CFM project phase IV.

3.2 Transport calculations with COFRAME

Flow and transport calculations have been performed with the transport code COFRAME (Reiche, et al., 2016). A schematic view of the processes considered is shown in Figure 51.

This model represents a double porosity approach for fractured media including the process of matrix diffusion. Transport of colloids and radionuclides is considered in a fracture characterized by its aperture, extension and porosity. Perpendicular to the transport direction in the fracture matrix diffusion into the stagnant matrix porewater with a distinct penetration depth for the contaminants is considered. Sorption on the rock matrix is modelled by K_d-concept. For colloids no matrix diffusion is considered, since it is assumed that colloid size is too large to enter the pore space around the fracture. Colloid transport and interaction processes between colloids, contaminants / radionuclides and fracture surface are considered by kinetically controlled processes. The interaction processes regarded in COFRAME and its denotations are shown in Figure 52. These are in detail

- contaminant exchange between the fracture and the adjoining rock matrix due to molecular diffusion Q_{fp},
- sorption of contaminants within the rock matrix Q_{pr},
- sorption of contaminants onto the fracture surface Q_{fr},
- sorption of contaminants on mobile and immobile colloids Q_{frm} and Q_{fri},

- filtration and remobilization of colloids Q_c due to their interaction with the fracture surface as well as thereby induced filtration and remobilisation of contaminants adsorbed on colloids Q_{cr}.

Consistently the concentrations of the different components are denoted as

- dissolved mobile contaminants in the fracture with concentration C_{fr} [mol/m^3],
- dissolved mobile contaminants in the pore water of the rock matrix C_{pr} [mol/m^3],
- mobile contaminants adsorbed on mobile colloids C_{cr} [mol/m^3],
- immobile contaminants adsorbed on the fracture surface S_{fr} [mol/m^2],
- immobile contaminants adsorbed on rock matrix pore surfaces S_{pr} [mol/kg],
- immobile contaminants sorbed on filtered colloids S_{cr} [mol/m^2],
- mobile colloids C_c [mol/m^3],
- immobile colloids filtered on the fracture surface S_c [mol/m^2].

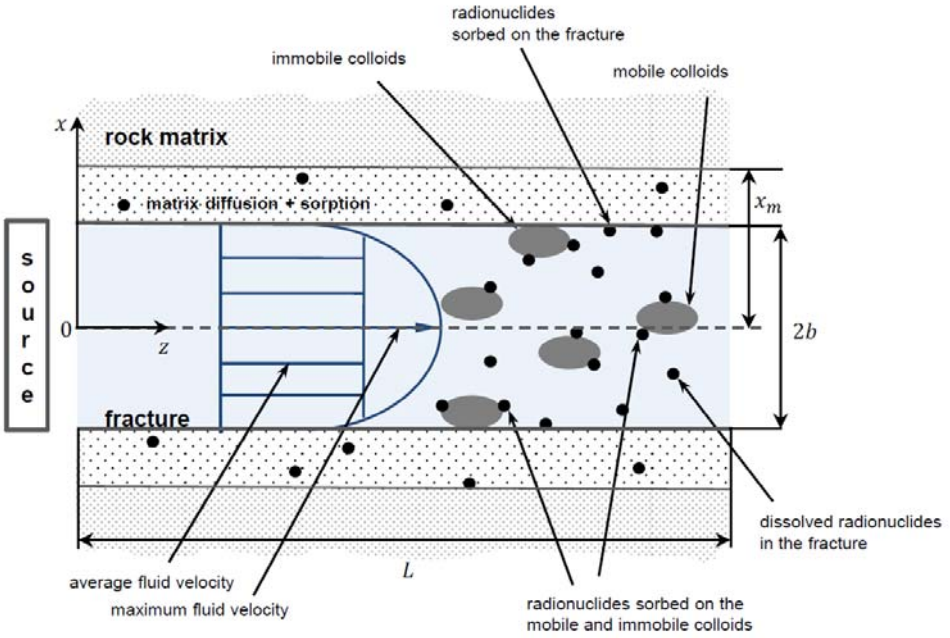

Figure 51: *Transport code COFRAME for colloid facilitated radionuclide transport in fractured media.*

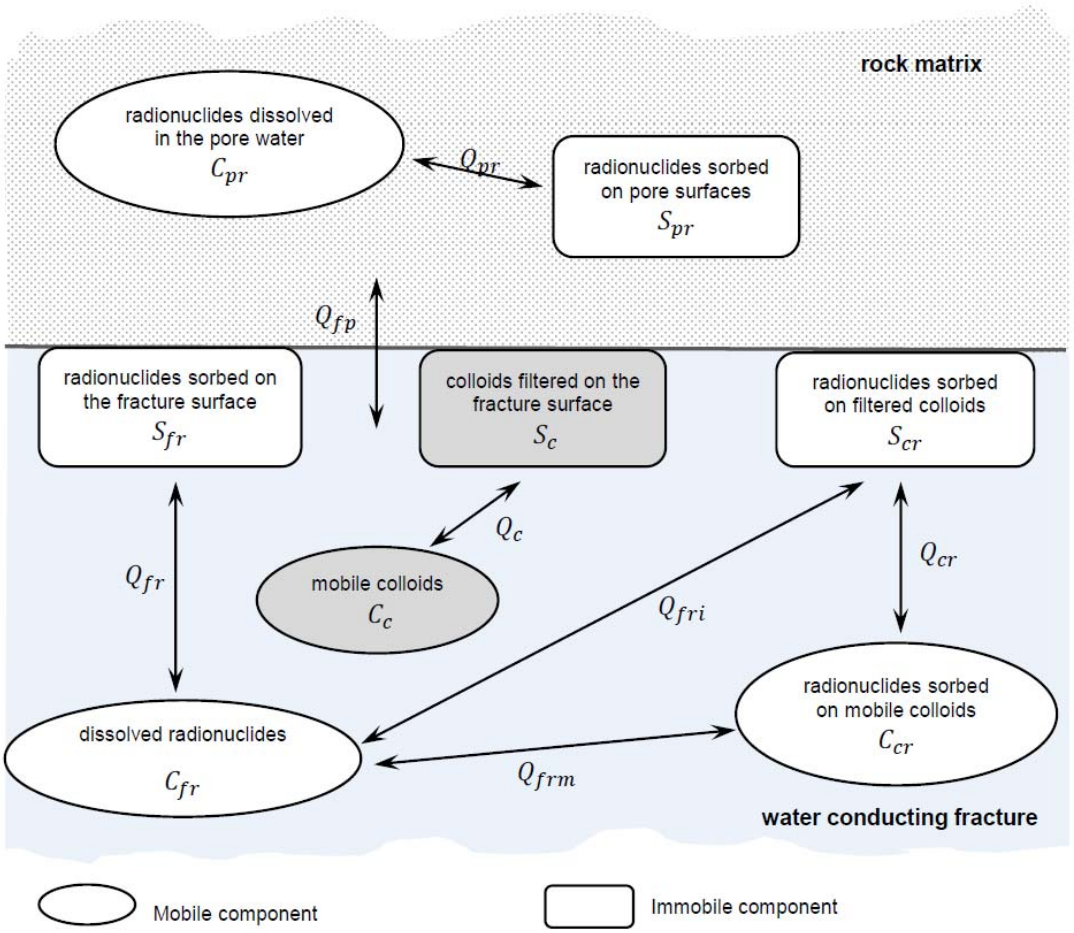

Figure 52: *Exchange processes between the components that represent radionuclides and colloids in the modelling system.*

The rate constants and the distribution coefficients for each interaction process are denoted by k and K, respectively with the index of the distinct interaction process. A more detailed description of the code and the equations for all interaction processes can be found in (Reiche, et al., 2016).

During the project phase of Kollorado-e^2 the focus on the field investigations within the CFM- project was on the LIT experiment. This experiment is described in detail in section 2.2.2. The spiked bentonite source was installed in borehole CFM 06.002 and tracer concentrations as well as other chemical parameters were detected and analyzed at the Pinkel and observation boreholes in few cm distance from CFM 06.002. This area is illustrated in Figure 53 and designated as dipole 1. However, several calculations with COFRAME have been performed for recent field tests, which were carried out between injection borehole BOMI 99.002 and extraction borehole BOMI 87.010, which is denoted in this chapter as dipole 2.

3.2.1 Screening calculations for radionuclide remobilization tests

As mentioned, one specific objective for the application of the COFRAME code is the prediction of field tracer tests in order to contribute to the design of the tests and to verify the assumption of the modelling approach.

The remobilization tests were planned to be performed in May 2017 at dipole 2, approximately four years after CFM RUN 13-05 has been carried out at the same dipole. The objective of this test was to investigate a potential remobilization of the radionuclides Am-243, Pu-242, Np-237 and U-233, which have been injected in CFM RUN 13-05 and were recovered by about 26 %, 32 %, 4 % and 15 %, respectively (Huber et al. 2016). Thus, a significant fraction of all four radionuclides is

still present in the dipole system, either sorbed on fracture filling material or sorbed on immobilized bentonite colloids. The idea of the remobilization test was to inject a defined pulse of Grimsel groundwater with a high amount of dissolved bentonite colloids. By injection of such a competitive sorbent it is expected that part of the radionuclides desorbs from the fracture filling material or the immobilized colloids and sorb to the injected, mobile bentonite colloids.

As discussed in Section 2.2.1 the REMO 2 Test has been changed in a way that the extraction was finally done at Pinkel extraction point. However, the predictive calculations were carried out for the originally planned test considering extraction at BOMI 87.010. Implications of the modified experimental conditions are discussed below.

In order to estimate, the expected amount of desorbing radionuclides and the expected radionuclide concentrations in solution model calculations with the transport code COFRAME were performed in advance to the remobilization test. Such calculations are also meant to optimize the experimental conditions, for example to use a bentonite colloid concentration high enough or a pulse duration long enough to receive a detectable radionuclide concentration.

The modelling approach consists of two parts and is restricted to Am-243 and Pu-242. For U-233 and Np-237 it is assumed that they have been reduced during the transport and subsequently sorbed to fracture filling material (see Section 3.2.5). Since during the REMO Test also oxygen was introduced, their remobilization might be caused by re-oxidation. For this process no data have been available so far. The first part of the modelling approach represents the simulation which was used to finally describe the colloid-facilitated transport of Am-243 and Pu-242 in CFM Run 13-05. In the second part of the calculation a pulse injection of bentonite colloids for a distinct time is simulated. The calculations are performed with the same parameters used for simulation of CFM RUN 13-05 as described in (Huber, et al., 2016). Due to the occurrence of numerical problems the calculations were restricted in the following way:

- The water flow conditions are considered constant over the whole calculation range, reflecting the experimental conditions of CFM RUN 13-05, namely a constant outflow of 5ml/min and a water inflow with a constant rate of 0.33 ml/min is used.
- The colloid pulse is injected 0.1 year after start of the experiment CFM RUN 13-05 (instead of 4 years). Since the long-term tailings for Am-243 and Pu-244 show a constant concentration plateau in the calculations for several years, it is assumed, that this is of limited influence.

Distribution coefficients as well as sorption and desorption rates between radionuclides, colloids and fracture filling material are available from the model calculations of recent field migration tests at GTS. For these interaction reactions all parameter values applied in CFM RUN 13-05 (Huber, et al., 2016) have been used in the simulation here.

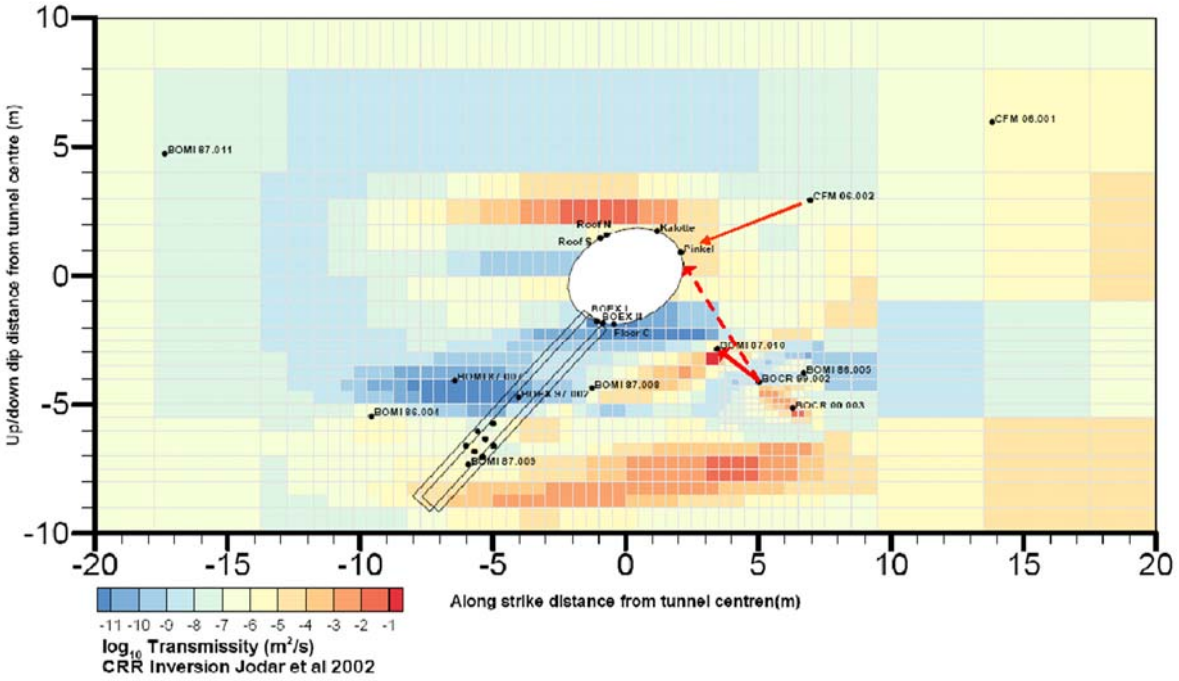

Figure 53: *Cross section of the shear zone with transmissivities and location of boreholes. The red arrows indicate the dipoles used for the field tests in the CFM project: dipole 1 with injection borehole CFM06.002 and outflow at tunnel surface Pinkel and dipole 2 located between BOCR 99.002 and BOMI 87.010. See text for more explanation.*

As mentioned above 0.1 year after the injection of the radionuclide/bentonite cocktail applied in CFM RUN 13-05 a second injection of a constant pulse of bentonite colloids is assumed. With respect to the injection two types of parameter variations are performed:

- Two different colloid concentrations of 1000 mg/l and 100 mg/l, respectively
- Two different durations of colloid inflow 5 days (120 hours) and 2.5 days (60 hours), respectively

The simulation results for the radionuclide concentrations expected at the extraction borehole (break through curves) are shown in Figure 54 to Figure 56. Please denote, in all figures the absolute concentration is given in mol/m^3.

As can be seen in Fig. 54 the first maximum of the breakthrough curves for Am-243 and Pu-244 is related to CFM RUN 13-05. It is determined by the colloid-bound fraction of both radionuclides, which travels as fast as the non-sorbing tracer (not shown). After about 10 days the curves for the colloid-bound fraction (C_{cr}) decrease by orders of magnitude, because the colloid concentration decreases accordingly. During the transport a large amount of both radionuclides desorb from the mobile colloids and become bound to the fracture filling material. Due to the desorption rate from the fracture filing material, some radionuclides become mobilized and transported again. This process leads to an increase of the free radionuclide concentration (C_{fr}) in solution, which reaches a plateau in the breakthrough curve after app. 20 days.

The bentonite pulse, which is injected after 36.5 days with a concentration of 1000 mg/l and a duration of 5 days leads to a sudden, strong increase in the concentration of the colloid-bound radionuclide fraction by orders of magnitude. In the simulations this peak is high enough to increase above the concentration plateau of the freely dissolved radionuclides and therewith leads to an increase of the total radionuclide concentrations by about one order of magnitude.

The observations for the calculations with a reduced duration of the injection pulse and with a reduced colloid concentration are qualitatively similar. However, the peak of the colloid-bound radionuclide fraction and therewith the peak for the total radionuclide concentration is less pronounced and leads to a slight increase only, for a colloid concentration of 100 mg/l.

Finally, the experiment REMO 2 has been performed with different parameters (see Section 2.2.1). The total bentonite colloid concentration was 292 mg/l, which is within the investigated range. The pulse duration was 40 minutes, which is a factor of 90 lower than 2.5 days, the lowest duration considered for modelling. Furthermore, the simulations considered extraction at borehole BOMI 87.010, whereas only experimental extraction data are available for the Pinkel surface packer. Since the AMS analyses and data evaluation is rather complex and time consuming, the data became available at the end of the project. Therefore, at this stage only a first comparison between experiment and modeling was done.

The breakthrough curve at the Pinkel showed a clear peak for Am-243 and Pu-242 coinciding with the peak of the colloids. Such a result is also obtained from the simulations for the breakthrough curve at borehole BOMI 87.010. The colloid curve is not explicitly shown, but the radionuclide peak is associated with the colloid peak (colloid bound fraction, Ccr in Figure 54 to Fig. 56). Concerning the absolute radionuclide concentrations, the simulated long-term plateau for the Pu-242 and Am-243 curves is in the range of 10^{-10} mol/m^3 for Pu-242 and $2 \cdot 10^{-11}$ mol/m^3 for Am-243 and the peak concentrations derived from the colloid pulse in the Remo test are about $3 \cdot 10^{-10}$ mol/m^3 for Pu-242 and 10^{-10} mol/m^3 for Am-243 (see Fig. 54) for a pulse injection of 100 mg/l for 5 days. The measured maximum concentrations for the signal of the Remo test are 10^{-11} mol/m^3 for Pu-242 and $5 \cdot 10^{-12}$ mol/m^3 for Am-243 are about a factor of 20 to 30 and the plateau concentrations are more than 2 orders of magnitude lower than the simulated concentrations. Three main reasons are likely responsible for this difference. Firstly, the concentrations are measured at Pinkel, where a higher dilution of the pulse occurs, and measured concentrations are always lower than at BOMI 87.010 for CFM RUN 13-05. Secondly, the experimental data for the long-term tailing indicated for CFM Run 12-02 and CFM RUN 13-05 a concentration plateau, which is more than one order of magnitude lower compared to the simulations with reference values (cf. Section 3.2.4 and (Huber, et al., 2016)). Thirdly, in between CFM RUN 13-05 and the test REMO 2 significant changes occurred in the shear zone due to installation of the LIT experiment. Finally, the duration and concentration of the pulse need to be adapted to the experimental values. All these aspects will be considered in follow-on simulations performed in near future.

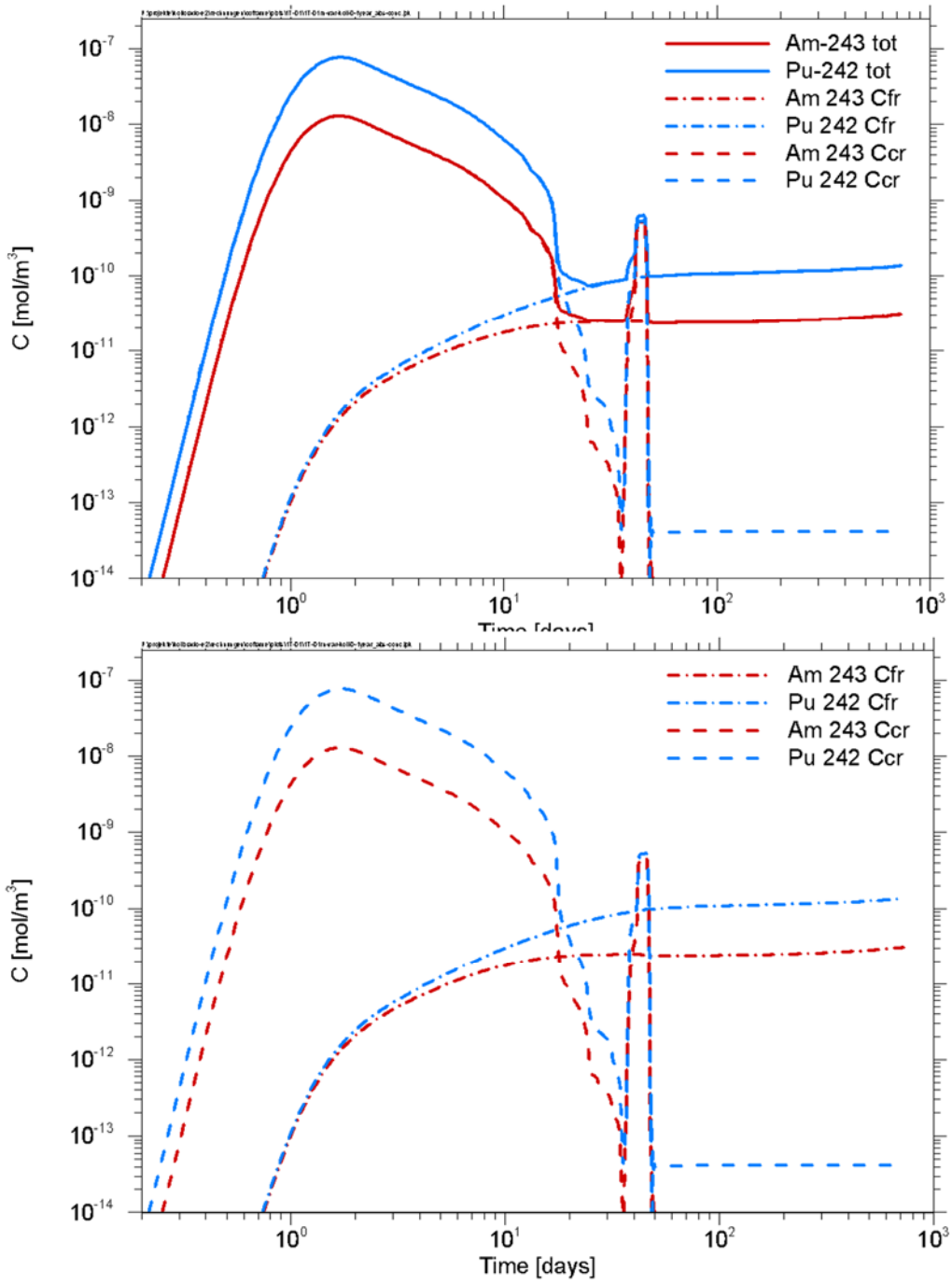

Figure 54: *Total concentration and concentration of the free (C_{fr}) and colloid-bound (C_{cr}) radionuclide fraction for Am-243 and Pu-242 applying a colloid concentration pulse with 1000 mg/l for 5 days (top). For better visibility the total concentration is not shown (bottom).*

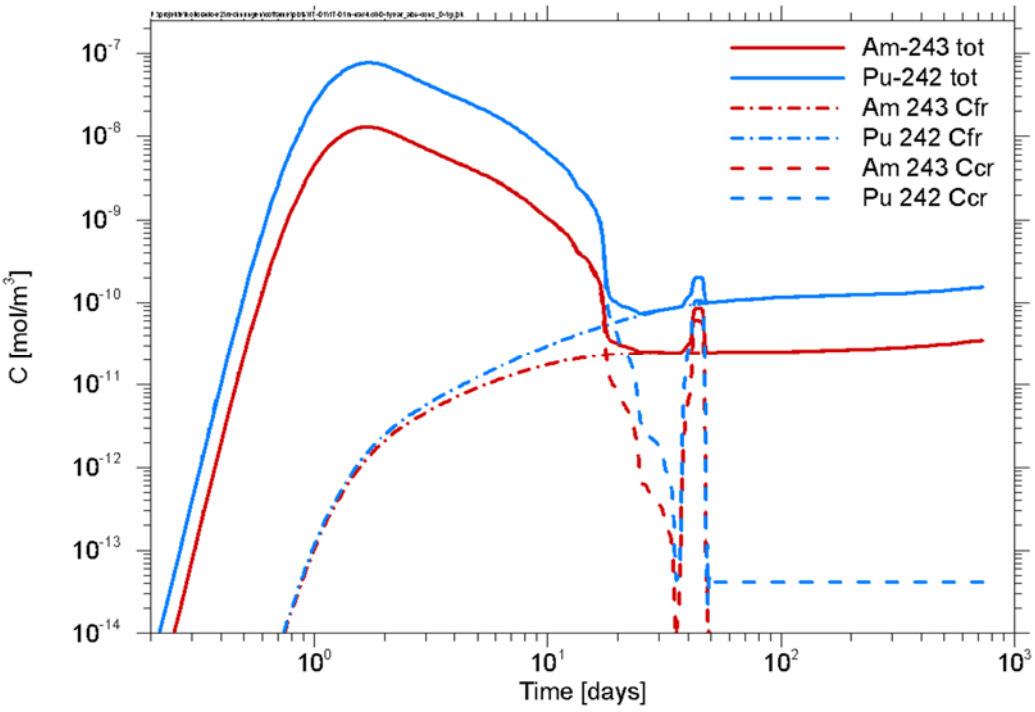

Figure 55: *Total concentration and concentration of the free (C_{fr}) and colloid-bound (C_{cr}) radionuclide fraction for Am-243 and Pu-242 applying a colloid concentration pulse with 100 mg/l for 5 days.*

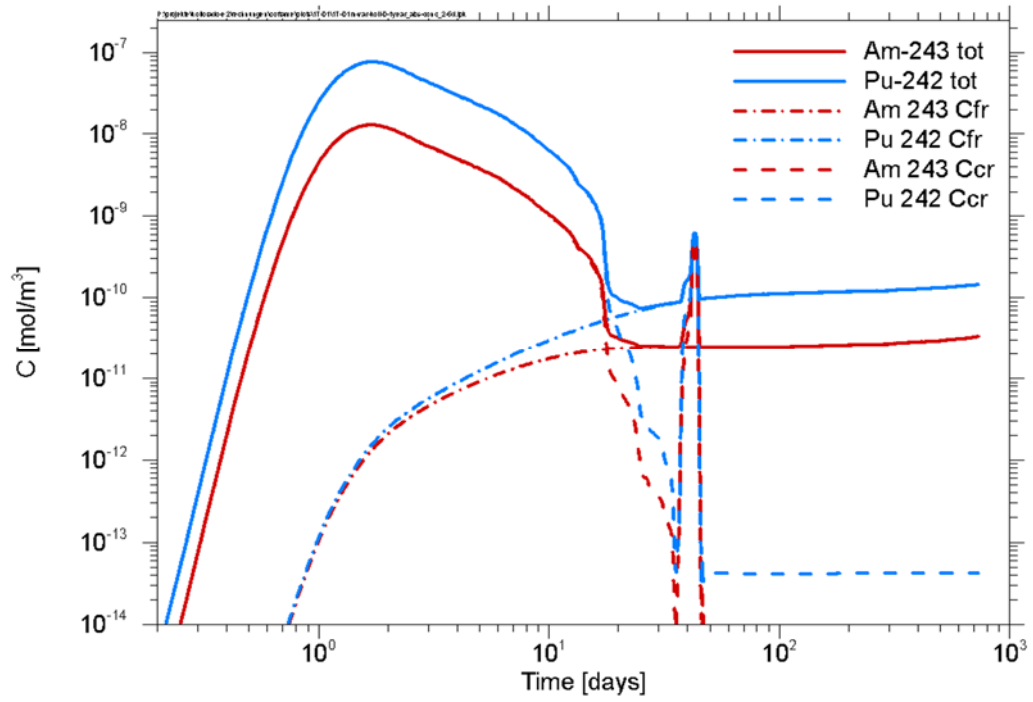

Figure 56: *Total concentration and concentration of the free (C_{fr}) and colloid-bound (C_{cr}) radionuclide fraction for Am-243 and Pu-242 applying a colloid concentration pulse with 1000 mg/l for 2.5 days.*

3.2.2 Screening calculations for a field experiment to further investigate the desorption mechanism

Background

As discussed in detail in (Huber, et al., 2016) and (Noseck, et al., 2016) a prominent decrease of the radionuclide desorption rate from the colloids (k_{fri}, k_{frm}) with increased travel time is observed for trivalent and tetravalent actinides in good agreement by the different transport codes RELAP, r^{3}t and COFRAME as illustrated in Figure 57.

Although there is a difference in the absolute values for the desorption rates, i.e. the tetravalent species desorb more slowly than the trivalent species in any given test, the similar slope for decrease of the desorption rate constants with residence time implies a similar time-scale dependence, see (Noseck, et al., 2016). Mechanistically, time-dependent rate constants for specific reactions are not supported by theory or literature data. However, a small number of different types of sorption sites with different corresponding desorption rates, could describe the observed time-dependent behavior. An interpretation of the recoveries obtained in the field tests with respect to a two-site desorption mechanism, i.e. a fast desorption from a weak site and a slower desorption from a strong sorption site, has been undertaken in (Huber, et al., 2016).

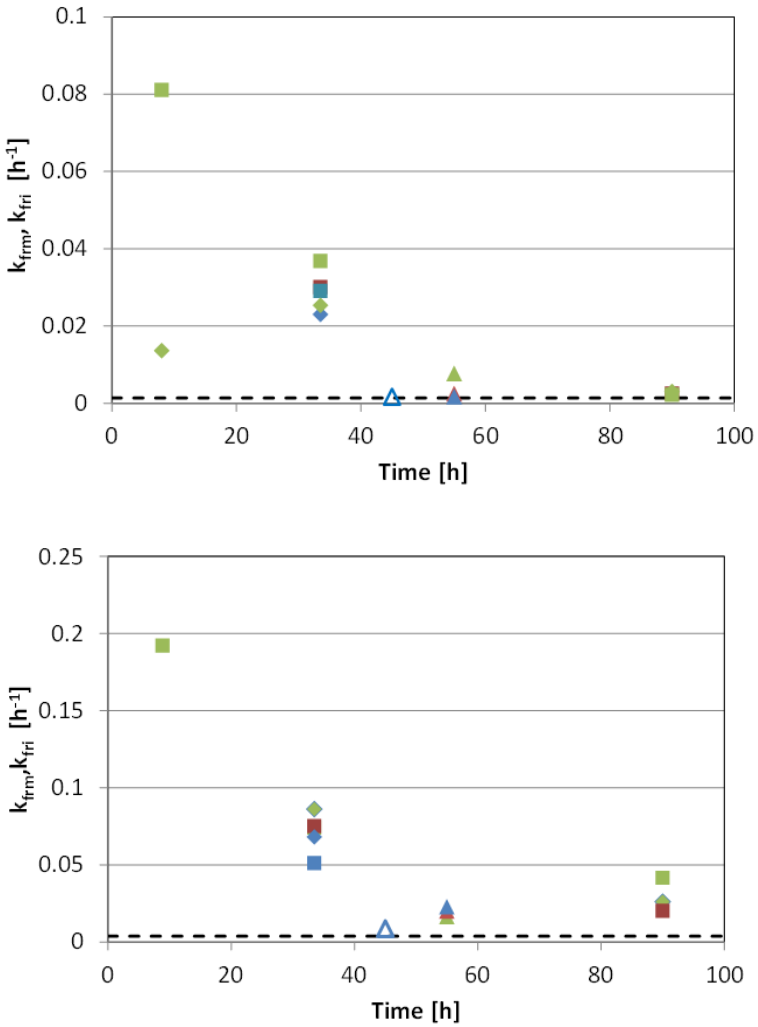

Figure 57: *Desorption rates of tetravalent Th (squares), Hf (rhomb) and Pu (triangles) – see top – and desorption rates of trivalent Eu (squares), Tb (rhomb) and Am (triangles) – see bottom – from colloids as a function of travel time as derived from model simulations with the codes RELAP (green), r^{3}t (red) and COFRAME (blue). The dotted black line indicates values determined in batch experiments.*

In order to further investigate this effect of two (or more) different sorption sites, an additional field experiment has been proposed in (Noseck, et al., 2016). The idea is to adsorb the target radionuclides/homologues onto the colloids as always done for the injection cocktails of the recent field migration tests, and then to perform large-scale desorption experiments using shear zone material in contact with this solution to remove homologues or radionuclides that are adsorbed to the weaker colloid sorption sites (with faster desorption kinetics). The remaining colloids and associated radionuclides could be used as part of an injection cocktail in the planned field tracer test. (Dittrich & Reimus, 2015; Dittrich & Reimus, 2016). Using a relatively short travel time for the field experiment, e.g. ten hours, where the observed desorption rates in the previous tracer tests have been rather high due to a strong impact of the weak sorption sites with faster desorption kinetics, should result in significantly lower desorption rates in this new experiment. This is exemplarily illustrated for the trivalent actinides in Figure 58.

Due to the elongation of the LIT experiment and the connected high analytical and logistical effort this type of experiments have not been performed in phase (III) of the CFM project, but there are still plans to carry out some field migration experiments to further investigate the idea of different sorption sites with different desorption kinetics in the next phase of CFM. Therefore, the results of the screening calculations are presented her.

It is intended to carry out further dipole field experiment at the dipole used in CFM Run 13-05. Therefore, screening calculations are performed for the conditions of this dipole.

Input data

Using the geometrical model parameters applied in CFM Run 13-05, denoted as CRR dipole, since it has been used for several dipole tests within the CRR project, an appropriate travel time in the range of 10 hours is estimated for an outflow rate of 24 ml/min. Figure 59 illustrates the outflow rates applied in the field experiments of the CFM dipole and the CRR dipole and the corresponding fluid travel times.

All transport parameters used for the predictive simulation of CFM Run 16-02 are compiled in Table 31. In general, these parameters are the same as used for the simulation of CFM-RUN 13-05 except the volume flow.

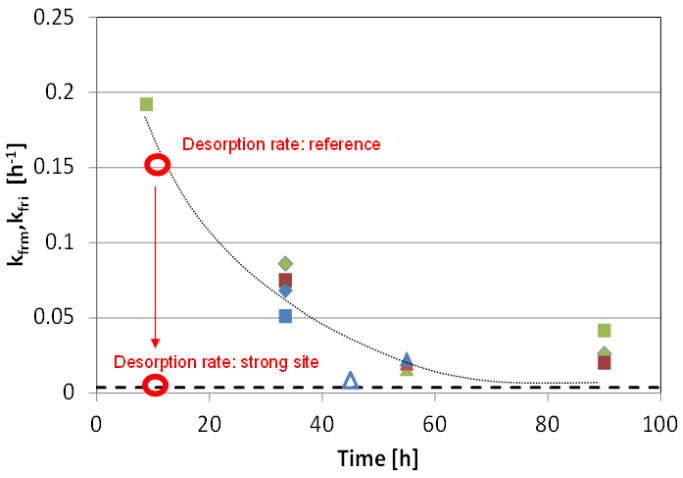

Figure 58: *Predicted difference in desorption rates of trivalent radionuclides from colloids between previous experiments (reference desorption rate) and the proposed new experiment (desorption rate: strong site) for an envisaged travel time of ten hours.*

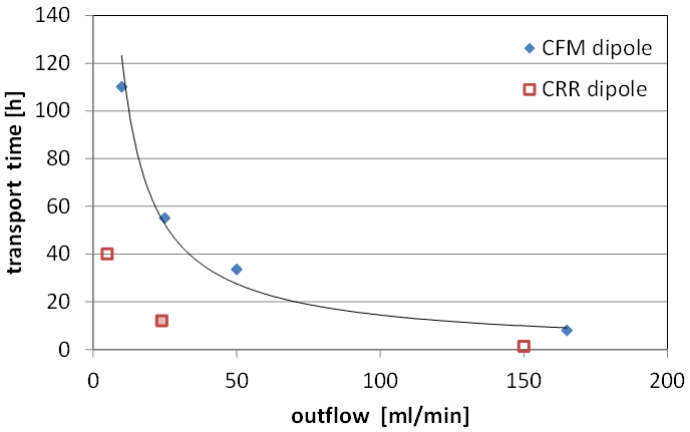

Figure 59 *Transport time vs. outflow rates for the field experiments in the CFM (blue rhombs) and CRR dipole (red open squares).*

Table 31: *Transport parameters used in the predictive simulations for CFM-RUN 16-02.*

Parameters	**Values**
Transport pathway length [m]	2.23
Cross section [m^2]	0.08229
Fracture aperture [m]	0.0022
Fracture porosity	1
Total trace length [m^{-1}]	23.7
Volume flow [ml/min]	24
Injection flow rate [ml/min]	0.77
Penetration depth [m]	0.02
Rock porosity [-]	0.05
Rock density [kg/m^3]	2670
Diffusion coefficient in rock matrix [m^2/a]	8·10-3
Diffusion coefficient in fracture [m^2/a]	0.03 (RN) / 0.003 (colloids)
Dispersion length [m]	0.1

The interaction parameters for the homologues or radionuclides have been derived from investigations to describe the observed recoveries of the tri- and tetravalent homologues and radionuclides in the different field tracer tests by a two-site sorption model with a weak sorption site 1 and a strong sorption site 2, see (Huber, et al., 2016).

These interaction parameters are compiled in Table 32. The colloid filtration rate has been set to 0.02 h^{-1} representing an upper value for most of the field experiments. An additional calculation was also performed with a filtration rate of 0.03 h^{-1} taking account of slightly higher filtration rates observed in CFM Run 13-05.

Firstly, a reference case is defined. The reference case represents a calculation for a typical field test for colloid-facilitated transport, i.e. the injection cocktail is equilibrated and injected into the dipole as it has been done in the previous dipole tests, e.g. CFM-RUN 10-01,12-02 and 13-05. The values derived in (Huber, et al., 2016) for the desorption rate from a weak sorption site 1, namely 0.15 h^{-1} for the trivalent and 0.05 h^{-1} for the tetravalent actinides, respectively, are used. For the short travel time of app. 10 hours it is expected that the breakthrough curve of the radionuclide is dominated by the desorption rate for site 1, which is also illustrated by Figure 60. Two reference calculations denoted as ref a and ref b are performed with different colloid filtration rates as discussed above.

In order to describe the conditions of the planned field experiment, where the injection cocktail is pre-conditioned in a way that injected colloid-bound fraction is represented by radionuclides sorbed to the strong sorption site, calculations applying desorption rates for the stronger sorption site 2 are performed. Due to the uncertainties in the desorption rate observed for the stronger sorption site 2 (see discussions in (Huber, et al., 2016), this rate is varied between 0.015 and 0.005 h^{-1} for the trivalent and 0.002 and 0.0002 h^{-1} for the tetravalent actinides. These calculations are denoted as case 1, 2 and 3. The interaction rates are summarized in Table 32.

Results for two step desorption

The resulting breakthrough curves for ref a and case 1 to 3 are shown for the trivalent actinide Am-243 and the tetravalent actinide Pu-242 in Figure 60 and Figure 61, respectively. In all calculations a non-sorbing tracer (denoted Aga) is considered, too. For all four calculation cases the curves for the non-sorbing tracer and the colloids are identical. The breakthrough curves for Am-243 and Pu-242 certainly depend on the desorption rates.

Table 32: *Interaction parameters for cases considered in the bounding calculations.*

Case	Filtration rate [h-1]	Desorption rate kfrm,fri, (III) [h-1]	Desorption rate kfrm,fri, (IV) [h-1]
1	0.02	0.005	0.0002
2		0.01	0.001
3		0.015	0.002
ref a		0.15	0.05
ref b	0.03	0.15	0.05

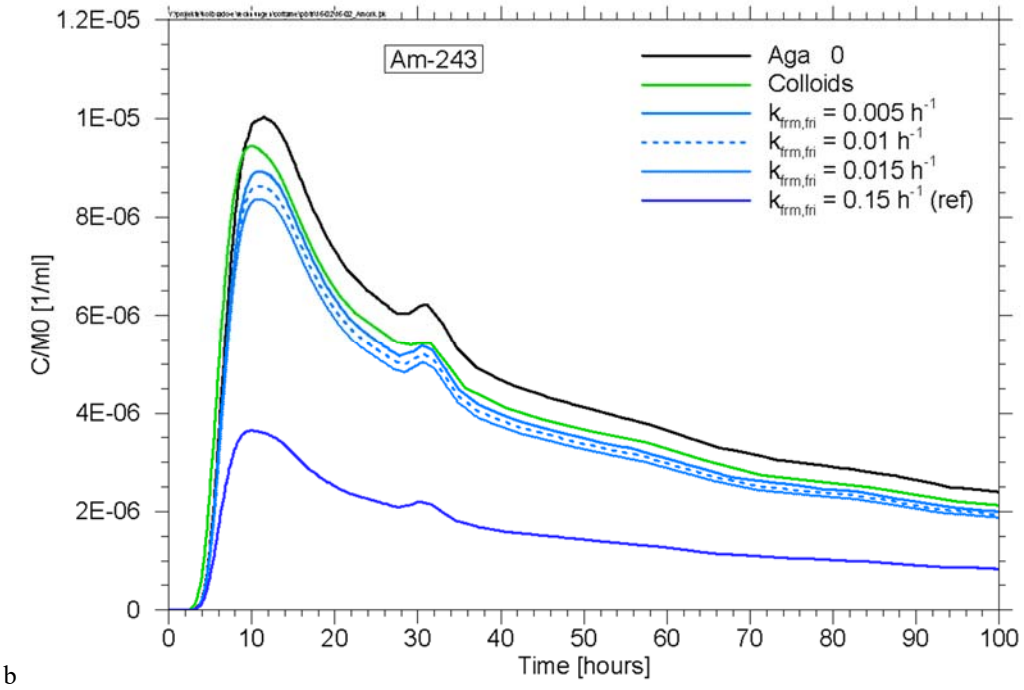

b

Figure 60 *Simulated breakthrough curves for Aga, colloids and Am-243 for case 1, 2, 3 and ref a.*

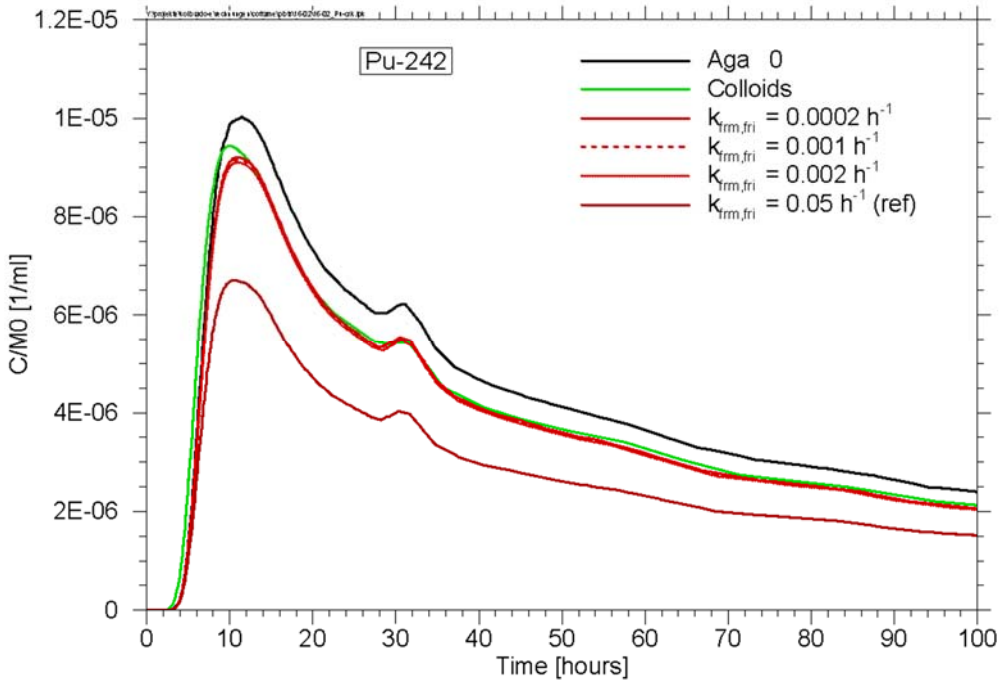

Figure 61 *Simulated breakthrough curves for non-sorbing tracer Aga, colloids and Pu-242 for case 1, 2, 3 and ref a.*

The maximum normalized concentrations and the recoveries for all calculation cases are compiled in Table 33. For Am-243 the peak concentration of the curve for the reference case is decreased by nearly a factor of 3 compared to the peak concentration of the colloids. The strongly reduced peak concentration is due to the application of a high desorption rate. Consequently, a large amount of Am-243 desorbs from the colloids and is retarded by the fracture filling material during transport. This results in a reduced recovery for Am-243 of only 37 % after 800 h model time. The application of a desorption rate for a strong sorption site results in an only slightly reduced peak maximum for Am-243 compared to the colloid curve. Due to the much lower desorption rate only a small amount of Am-243 desorbs from the colloids and is retarded by the fracture filling material, also visible in comparably high Am-243 recoveries between 84.2 and 79.3 % for calculation cases 1, 2 and 3.

The picture for Pu-242 is similar, with generally higher maximum concentrations and recoveries due to the lower desorption kinetics of tetravalent compared to trivalent actinides. For Pu-242 the breakthrough curves and the recoveries (between 85.3 and 86 %) are not distinguishable for calculation cases 1, 2 and 3. The calculation curve for the reference case shows a reduction of the peak maximum by one third and a reduction of the recovery by one fourth.

From the figures for both actinides it becomes obvious that a dipole experiment with a fluid travel time of 10 hours is suitable to show distinguishable breakthrough curves and recoveries for tri- and tetravalent actinides which are either injected as in previous field tests or preconditioned in a way that injected colloid-bound fraction is represented by radionuclides sorbed to the strong sorption site. The results of such an experiment can be a strong indication for the existence of a sorption model with different sorption sites.

On the other hand it shows that the impact of the desorption rates $k_{frm,fri}$ applied in case 1, 2 and 3 is low under these flow conditions. In other words, the uncertainty in the desorption rate for a slow desorption from a strong sorption site is of rather low influence and does not negatively impact an experiment under the proposed flow conditions. In the same way an increased colloid filtration rate of 0.03 h^{-1} (ref b) is expected to have only a low impact on the results.

3.2.3 Screening calculations for a field experiment on U and Np reduction

As described in section 3.2.5 there is strong evidence that mobile U(VI) and Np(V) become reduced and subsequently immobilized during transport through the shear zone. First order reaction rates for the reduction of both elements have been derived based on the decrease of recoveries with increased residence time, see section 3.2.5. The evaluation is based on two experiments with residence times (peak maximum of the breakthrough curve) of approx. 1.3 and 44 hours.

To confirm such a process, it is planned to perform an additional field experiment in dipole 2 at an intermediate residence time. To get an impression of the expected breakthrough curves and recoveries respective model calculations have been performed for residence times of 5, 10 and 15 hours applying a volume outflow for the dipole of 48, 24 and 16 ml/min. Except for the volume flow in the first and third simulation the same conditions and transport parameters as for the calculations described in Section 3.2.2 are applied here. The conceptual model and the reaction rates for the reduction of U(VI) and Np(V) to their reduced forms are taken from the evaluation in Section 3.2.5 and are listed in Table 34.

The results are exemplarily shown for an extraction rate of 24 ml/min in Figure 62.

The normalized maximum concentrations and recoveries for all calculations are listed in Table 34. In general, a residence time of 10 hours established by an extraction rate of app. 25 ml/h seems to be suitable for such a field experiment at dipole CRR 99.002-i2 – BOMI 87.010. The recoveries are well distinguishable from those obtained in CRR#32 and CFM RUN 13-05. This extraction rate would also enable a combined field experiment for the investigation of the desorption mechanism of Pu and Am and the reduction of U and Np.

Table 33: *Normalized maximum concentrations and recoveries for AGA, colloids, Am and Pu obtained in the different calculated cases.*

Case	Normalized maximum concentration [1/ml]				Recovery [%] (after 800 h)			
	AGA	Colloids	Am(III)	Pu(IV)	AGA	Colloids	Am(III)	Pu(IV)
1	10^{-5}	$9.4\cdot10^{-6}$	$8.9\cdot10^{-6}$	$9.2\cdot10^{-6}$	99.5	86.2	84.2	86
2			$8.6\cdot10^{-6}$	$9.15\cdot10^{-6}$			81.7	85.7
3			$8.4\cdot10^{-6}$	$9.1\cdot10^{-6}$			79.3	85.3
ref a			$3.6\cdot10^{-6}$	$6.7\cdot10^{-6}$			37	64.6
ref b		$8.8\cdot10^{-6}$	$3.4\cdot10^{-6}$	$6.3\cdot10^{-6}$		80.6	35	60.9

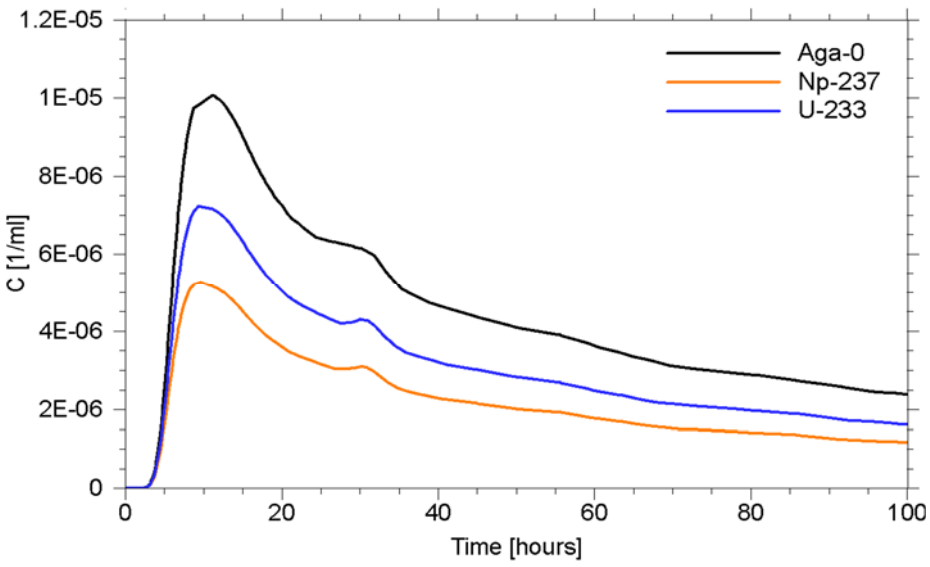

Figure 62 *Simulated breakthrough curves for non-sorbing tracer Aga, U-233 and Np-237 assuming a reduction and subsequent immobilization of U(VI) and Np(V). The reaction rates are taken from Tab. 36.*

Table 34: *Normalized maximum concentrations and recoveries for AGA, U and Np obtained in the screening calculations, reference case, peak residence time (RD) 5 h and 15h, respectively.*

	Normalized maximum concentrations			**Recovery [%] (after 400 h)**		
	AGA	U-233	Np-237	AGA	U-233	Np-237
Ref. case, RD = 10 h	10^{-5}	$7.2 \cdot 10^{-6}$	$5.3 \cdot 10^{-6}$	98	68	49
RD = 5 h	$5.7 \cdot 10^{-6}$	$4.9 \cdot 10^{-6}$	$4.1 \cdot 10^{-6}$	98	81	68
RD = 15 h	$1.4 \cdot 10^{-5}$	$8.5 \cdot 10^{-6}$	$5.3 \cdot 10^{-6}$	99	56	34

3.2.4 Simulation of long-term tailing in CFM RUN 13-05

As discussed in (Huber, et al., 2016) analysis of Pu and Am concentrations in the sub ppq range by AMS opens a new aspect for the investigation of the CFM field experiments. Such analyses have been performed amongst other radionuclides for Pu-242 and Am-243 by (Quinto et al., 2015) and (Quinto, et al., 2017) in samples from the field experiments CFM RUN 12-02 and CFM RUN 13-05, respectively. Data for both experiments for up to app. 230 days after injection of the cocktail are now available. An evaluation of the long-term behavior of both radionuclides in CFM RUN 12-02 was already performed in (Huber, et al., 2016). In this section additional calculations performed for CFM RUN 13-05 are reported.

As can be seen in Figure 63 the data for the long-term tailing of CFM RUN 12-05 and CFM RUN 13-05 in general show a similar picture with a plateau for Am-243 and Pu-242 in the same concentration range of 10^{-9} to 10^{-10} ml^{-1}. However, as indicated in the graph for CFM RUN 13-05 the AMS values represent the mass 243 and 242, respectively. It is obvious that in CFM RUN 13-05 – in contrast to CFM RUN 12-02 and to the model simulation – the measured concentration for mass 242 is higher than for mass 243. A second unexpected observation is an offset of both concentrations at the beginning of the experiment, where no radionuclides should occur. The observation has been thoroughly investigated in (Quinto, et al., 2017) and the evaluation gives evidence that the offset concentrations stem from an earlier experiment at that dipole, namely CRR #31, where Am-243 and Pu-242 have already been used as radiotracers. Therefore, the offset concentration and the concentrations in the long-term tailing are biased by residual concentrations of both radionuclides still present in the system.

Nevertheless, a transport simulation for CFM RUN 13-05 has been performed with COFRAME. Model calculations for CFM RUN 12-02 showed that particularly the sorption value K_{fr} for Am and Pu sorption on the fracture filling material has a strong impact on the plateau concentration in the long term (Huber et al. 2016). Therefore, calculations for two parameter sets of K_{fr} – the same, which have been used for CFM RUN 12-02 – are performed and the results are also shown in Figure 63. The solid lines show the calculations with best-estimate values derived from the experiments in binary systems for single radionuclides with Am and Pu and fracture filling material, namely K_{fr} = 2.85 m for Am (corresponding to K_{fr}^* = 0.22 m^3/kg) and K_{fr} = 7.5 m for Pu (corresponding to K_{fr}^* = 0.6 m^3/kg), cf. Section 2.1.1.4, Table 6. However, similarly, as for CFM RUN 12-02 the range of the plateau concentrations are best met with 10-fold higher distribution coefficients of K_{fr} = 28.5 m (corresponding to a distribution coefficient K_{fr}^* of 2.2 m^3/kg, for Am-243 and 75 m (corresponding to a distribution coefficient K_{fr}^* of 6 m^3/kg) for Pu-242, see (Huber, et al., 2016) and the discussion therein. As stated in Section 2.1.1.4 the Kd (K_{fr}^*)- values for Pu-242 and Am-243 measured in the binary system with FG are minimum values: Regarding the maximum sorption values of up to 99%, only 1% of the total activity is left in the supernatant and either dissolved or sorbed on a colloidal phase. Considering the extreme that the remaining RN fraction is quantitatively colloid associated could easily explain the 10-fold higher distribution coefficients on FG for both radionuclides. A further indication is the average distribution coefficient of 2700±1150 L/kg, which was determined for ^{243}Am in the single nuclide desorption experiments, which matches the assumed 10-fold higher distribution coefficient K_{fr}^* of 2.2 m^3/kg very well.

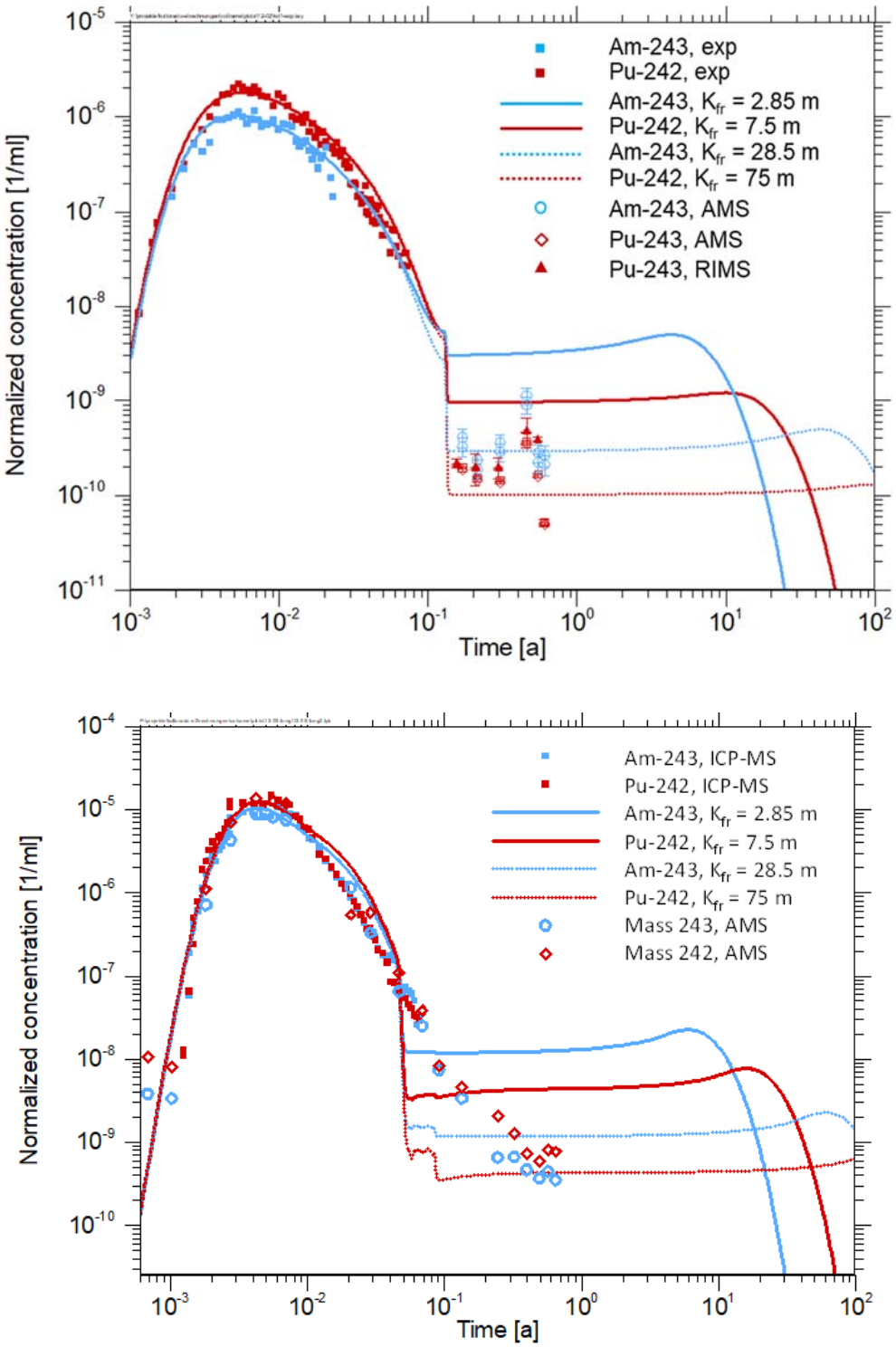

Figure 63 *Measured and simulated breakthrough curves with long-term tailings for Run 12-02 (top), Run 13-05 (bottom), for explanations see text.*

As discussed in Section 2.1.1.4 also new long-term desorption rate data for the binary system with FG are available now. The average values for Am-243 and Pu-242 are in the range of 20 to 60 a^{-1}. Additional calculations for CFM RUN 12-02 have been performed so far with ad-/desorption rates of 1000 a^{-1} and higher, oriented at the observed adsorption rates (see Section 2.1.1.4, which show only low impact on the breakthrough curves (not shown). For consideration of significantly lower desorption rates an independent adsorption and desorption rate need to be implemented into the transport code COFRAME, which is planned for the new project.

The simulation predicts the concentration for Pu-242 to be higher than for Am-243 but the experiment shows a converse concentration profile. The reason for this is very likely due to the traces of experiment CRR #31, since the offset concentration of Am-243 measured at the start of CFM RUN 13-05 was already higher than for Pu-242. Since the long-term tailing data in CFM RUN 13-05 are biased a more detailed evaluation is considered to be not meaningful.

However, few additional calculations have been performed to shed some light on the offset concentrations likely caused by field test CRR #31. The CRR#31 tracer test has been performed in January 2001, approximately 12 years before CFM RUN 13-05 was started. Model calculations describing the long-term migration of Am-243 and Pu-242 after the CRR#31 migration test have been performed for a time frame of 20 years. The injection of both radionuclides was reduced by the fraction of 34 and 20 % for Am-243 and Pu-242, which was recovered in CRR#31, probably as fraction bound to natural colloids, since no colloids have been introduced in CRR#31. Figure 64 shows breakthrough curves for Pu-242 and Am-243 considering as interaction process only sorption on fracture infill material with the K_{fr} values 7.5 m and 2.85 m, respectively. Considering the series of in situ tests performed at the GTS in the period between test CRR#31 and CFM 13-05 a total volume of 10^5 L as upper value of groundwater having passed the fracture during this time has been estimated in (Quinto, et al., 2017). This corresponds approximately to a flow rate of 15 ml/min in our model. The breakthrough curves were then simulated for low flow conditions of 15 and 10 ml/min. Due to the higher K_{fr} value the peak maximum for Pu-242 appears later than that for Am-243. Therefore, the Pu concentration exceeds the concentration of Am after a certain time. With a volume flow of 10 ml/min the range and the ratio of the concentrations of Am-243 and Pu-242 observed as offset concentrations in CFM-RUN 31-05 can be met.

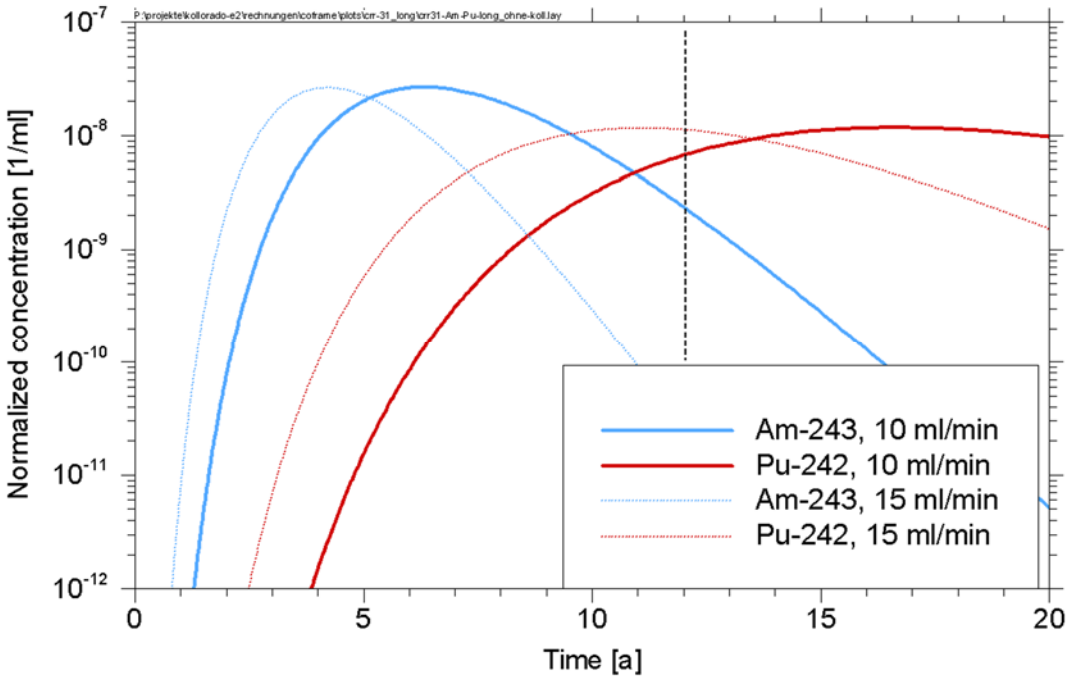

Figure 64 *Development of concentrations for Am-243 and Pu-242 after run CRR #31 in the very long term based on an exemplary model simulation, explanation see text.*

3.2.5 Simulation of redox reactions of Np and U

Field experiments have shown that the mobility of injected U(VI) and Np(V) depends on their residence time in the shear zone: The recoveries of both elements decrease with increasing residence time. As shown in Table 35 the recovery for U-233 decreases from 100 % in field test CRR #32 with a peak arrival time of 80 minutes to 15% in CFM RUN 13-05 with

a peak arrival time of 2640 minutes. In the same way the recovery of Np-237 decreases from 82 % to 4 %, cf. (Möri et al., 2003; Geckeis et al., 2004) and Nagra[5].

In their oxidized forms both elements are not, or only to a minor degree, associated with colloids, i.e. under these conditions the transport of both elements is not significantly impacted by colloids. One explanation is that a redox process is responsible for the different recoveries obtained in CRR RUN #32 and CFM RUN 13-05. Both radionuclides are injected in the oxidized form as U(VI) and Np(V), respectively. Under the undisturbed conditions of the Grimsel groundwater with very low redox potential $Eh_{(SHE)}$ = -220mV a reduction of both elements into the tetravalent state is possible, cf. discussions in (Huber et al., 2015). In the oxidized state uranium is expected to occur mainly in form of negatively charged calcium carbonato or hydroxo uranyl complexes at pH values around 9.6. For neptunium(V) the formation of anionic hydroxo-carbonate or neutral hydroxo-silicate complexes is also possible, see Section 3.1. Therefore, in the oxidized state they might be very mobile and travel as fast as the conservative tracer and the colloids. Contrary, in their reduced form both elements are expected to be rather immobile and strongly retarded by the fracture filling material

Conceptual ideas and input data

Based on these assumptions a concept for the treatment of the redox process in both transport experiments is developed. The reduction is modelled by first order reaction from the respective radionuclide in the oxidized form to the radionuclide in the reduced form. In the transport code COFRAME this is realized by implementing two "daughter radionuclides" for U-233 and Np-237 and applying a decay rate for the transfer from the oxidized form (mother nuclide) into the reduced form (daughter nuclide). The reaction rate can then be characterized by its "half-life", which is used as input parameter. For each form of the radionuclide different interaction data with the fracture filling material and with the colloids are applied. For the oxidized forms it is assumed that they behave like a non-sorbing tracer, namely all sorption values and interaction rates are set to zero. For simplification the initially colloid-bound fractions of 6 % and 1 % of U-233 and Np-237, respectively, is neglected. For the tetravalent reduced forms the properties, which have been assigned in CFM-RUN 13-05 for tetravalent plutonium, are applied here, i.e. strong sorption on fracture filling material and colloids and respective reaction rates. All relevant interaction parameters applied for the oxidized and reduced forms are compiled in Table 35.

The hydraulic data for the simulation of both experiments are listed in Table 36. For CFM RUN 13-05 the data applied in the calculations for the colloid-facilitated transport of Am and Pu in this field test (Huber, et al., 2016) have not been changed. The shear zone of the CFM experiment is considered in these calculations as an open fracture with an aperture of a few mm, here 2.2 mm is assumed. All information about the field experiments can be derived and are not described here[6]. The transport parameters are taken from these descriptions and cross sections were fitted to match the breakthrough curve of the conservative tracers iodide and AGA, respectively. For CFM RUN 13-05 the input function for the conservative tracer was available and the injection flow rates were adapted to the injected mass of the conservative tracer, M_0. For CRR #32 no input function is available and therefore a step function was used. Furthermore, a slightly higher dispersion length has been used for CFM RUN 13-05. This is connected with the general difficulty to describe the tailing of the breakthrough curves in this dipole. All curves show a very pronounced long-term tailing. For CFM RUN 13-05 a significant part of this tailing origins from the injection function, for CRR #32 this is not known.

The injected masses are as follows:

- CRR #32 I-131: $1.6 \cdot 10^{-8}$ mg, colloids: 220 mg, U-233: $2.02 \cdot 10^{-2}$ mg, Np-237: $2.58 \cdot 10^{-2}$ mg
- CFM RUN 13-05 AGA: 4.5 mg, colloids: 220 mg, 3 ($1.01 \cdot 10^{-6}$ mmol), Np-237: $9.69 \cdot 10^{-4}$ mg ($1.96 \cdot 10^{-5}$ mmol).

[5] *Nagra Aktentnotiz AN 13-617 (14. November 2013)*
[6] *Documented in Nagra Aktennotiz AN 12-302 (12. June 2012) and Nagra Aktentnotiz AN 13-617 (14. November 2013).*

The rates applied for the reduction of hexavalent U-233 and pentavalent Np-237 into their tetravalent forms – shown in Table 35 – have been determined in a way that they can properly describe the recoveries for both field tests, CRR#32 and CFM RUN 13-05. The rates are different for U-233 and Np-237, since the recovery of U-233 is always higher than for Np-237. The results for the experimentally determined and calculated recoveries are compiled in Table 37. The recoveries for Np-237 can be well described by a rate of 0.1 h^{-1}. For U-233 a rate of $5.32 \cdot 10^{-2}$ h^{-1} describes the recoveries fairly well. However, the quantitative uranium recovery in CRR #32 cannot be met with a single first order kinetic rate. The simulated curve results in a recovery of 87 %.

The breakthrough curves for CFM RUN 13-05 for the experiment and the simulation are shown in Figure 65 & 66. The simulation for non-sorbing tracer, U-233 and Np-237 fits the experimental curves rather well. The well-known injection function has also been applied for U-233 and Np-237 and seems to be mainly responsible for the strong tailing of the breakthrough curves.

Table 35: *Interaction data for uranium and neptunium in CRR RUN #32 and CFM RUN 13-05.*

	U(VI)	**Np(V)**	**U(IV) / Np(IV)**
Redox reaction			
"Half life" [a]	1.5E-3	7.59e-4	-
Reaction rate [h-1]	1.04E-1	5.27E-2	
Interaction of radionuclides with colloids			
Kfrm, fri [m^3/kg]	0.0	0.0	1600
Sorption rate [a-1]			15
Interaction of radionuclides with fracture			
Kfr* [m]	0.0	0.0	7.5
Kfr [m^3/kg]			0.6
Sorption rate [a-1]			45.0

Table 36: *Hydraulic data for CRR RUN #32 and CFM RUN 13-05.*

Parameter	**CRR RUN #32**	**CFM RUN 13-05**
Transport pathway length [m]	2.23	
cross section [m^2]	0.124	0.083
Fracture aperture [m]	0.0023	
Fracture porosity	1	
Total trace length [m-1]	23.53	
Volume flow [ml/min]	150	5
Penetration depth [m]	0.02	
Rock porosity [-]	0.05	
Rock density [kg/m^3]	2670	
Diffusion coefficient in rock matrix [m^2/a]	0.008	
Diffusion coefficient in fracture [m^2/a]	0.03 (RN) / 0.003 (colloids)	
Dispersion length [m]	0.1	0.2

Table 37: *Measured and calculated recoveries (after 800 h) for CRR RUN #32 and CFM RUN 13-05.*

	CRR RUN #32		**CFM RUN 13-05**	
	Experiment	**Model**	**Experiment**	**Model**
U-233	103 ± 5 %	87 %	15 %	16 %
Np-237	82 ± 4 %	80 %	4 %	4 %

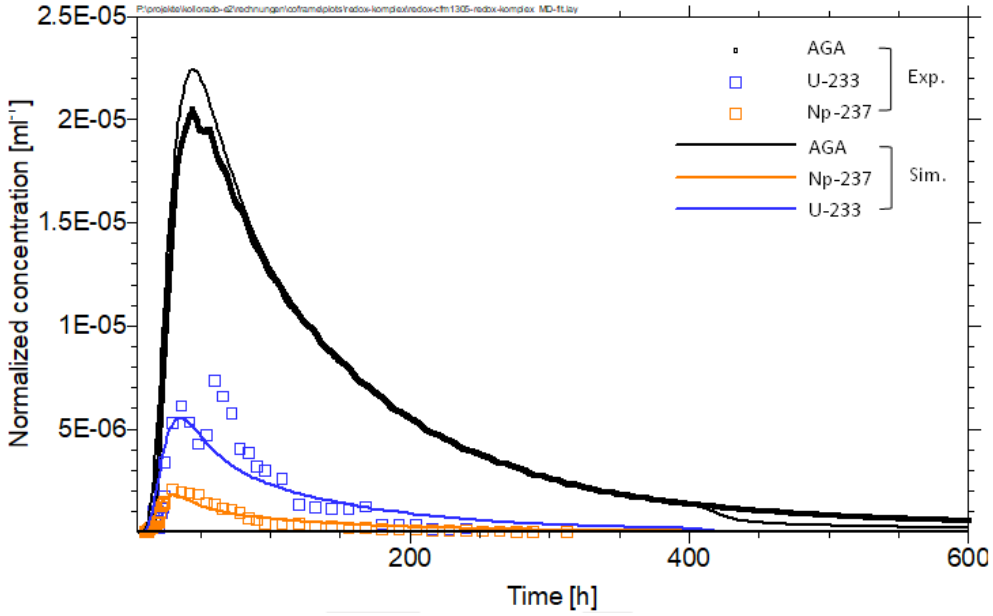

Figure 65 *Breakthrough curve for CFM RUN 13-05, linear scale: Experimental data and simulation results for non-sorbing tracer (AGA), U-233 and Np-237.*

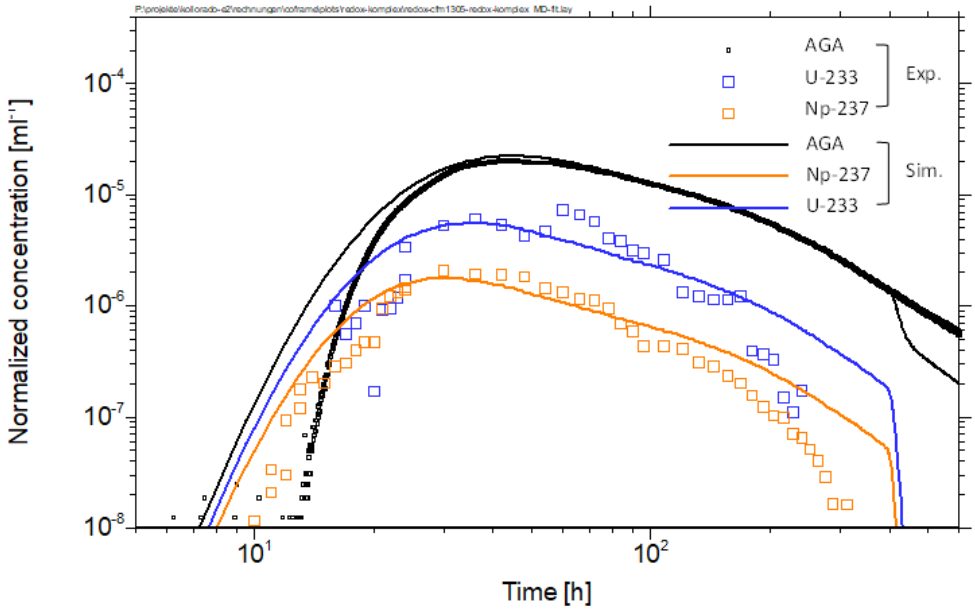

Figure 66 *Breakthrough curve for CFM RUN 13-05, log scale: Experimental data and simulation results for non-sorbing tracer (AGA), U-233 and Np-237.*

As already mentioned above the breakthrough curves in the dipole in CRR 99.002-i2 (injection borehole) and BOMI 87.010 (extraction borehole), which was used for both field tests, CRR #32 and CFM RUN 13-05, show significant tailings. It is

difficult to simulate such a tailing by a one-dimensional transport model, if the injection function is not known, which is the case for experiment CRR #32. An amount of 125 ml of the injection cocktail has been injected in the experiment. In a first step this is realized in the model by a rectangular input function. The resulting breakthrough curves are shown in Figure 67.

The concentration maximum of the breakthrough curve for the non-sorbing tracer I-131 is higher than that of the experimental curve and the pronounced tailing of the experimental curve is not met by the simulation. Furthermore, a similar difference between modelled and experimental curves is observed for U-233 and Np-237. The strong tailing of the experimental might be caused by different effects,

- a tailing in the input function,
- matrix diffusion, or
- a superposition of different transport pathways.

With respect to the impact of the input function Figure 68 exemplarily shows the breakthrough curves for an adapted simple two step injection function. An application of this injection function obviously can better describe the main peak and to some extent the tailing. However, there is no experimental evidence for the use of such an injection function.

It is also obvious that the maximum of the peak for the U-233 and Np-237 curves is strongly depleted compared to the non-sorbing tracer. Applying a first order reduction kinetics which meets the recoveries observed in the experiment, does not explain the strong tailing and strongly reduced peak compared to the iodine tracer to reach the recovery of the experimental curves as shown in Figure 68.

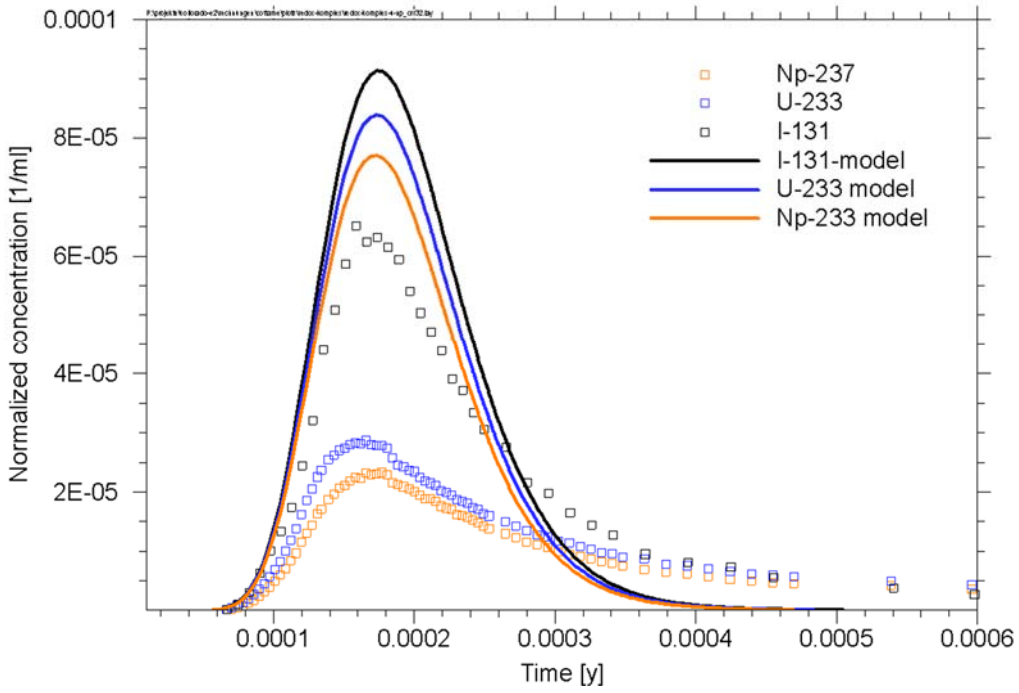

Figure 67 *Breakthrough curve for CRR #32: Experimental data and simulation results for non-sorbing tracer (I-131), U-233 and Np-237. Rectangular input function.*

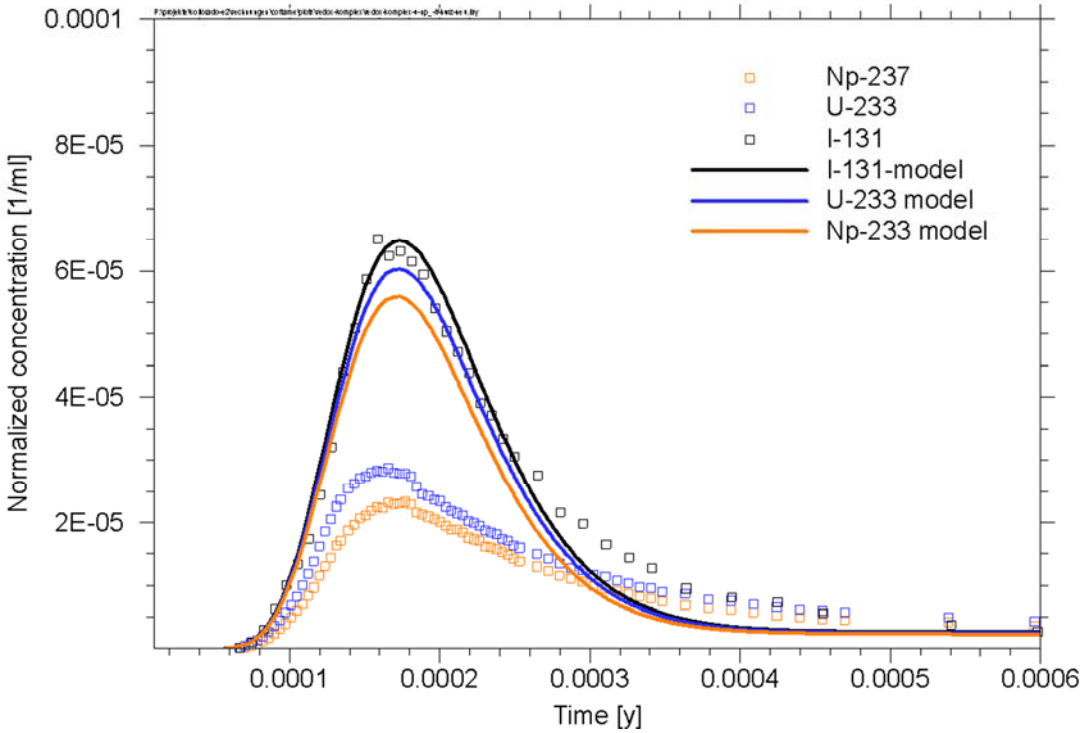

Figure 68 *Breakthrough curve for CRR #32: Experimental data and simulation results for non-sorbing tracer (I-131), U-233 and Np-237. Two step input function.*

Thus, an additional process/effect is needed to explain the depleted maxima and long-term tailing of the breakthrough curves for U-233 and Np-237. Another reason for the pronounced tailing might be the effect of matrix diffusion including sorption onto the mineral surfaces in the matrix. Some calculations have been performed to investigate, whether matrix diffusion might contribute to the pronounced tailing of the breakthrough curves in CRR #32, although it is discussed in (Hu & Möri, 2008), that the retention processes in the shear zone seem to be more complex as described by the simplified matrix diffusion approach used in COFRAME. For these calculations a rectangular injection function is applied. In order to derive an adequate description of the breakthrough curve of U-233 the porosity of the matrix and the diffusion coefficients need to be increased, the penetration depth decreased compared to the reference case, as listed in Table 39. There is also a need to address a weak sorption value for uranium in the matrix. With these parameters the breakthrough curve of uranium including the tailing is well described, see Figure 69.

Table 38: *Comparison of reference data for CRR #32 and data used to describe the tailing by matrix diffusion.*

Parameter	Unit	Reference value	MD value
Porosity		0.05	0.2
Penetration depth	m	0.02	0.009
Diffusion coefficient	m2/a	0.008	0.05
Sorption value	m3/kg	0.0	0.001
Spatial discretization	Number of blocks	8	8

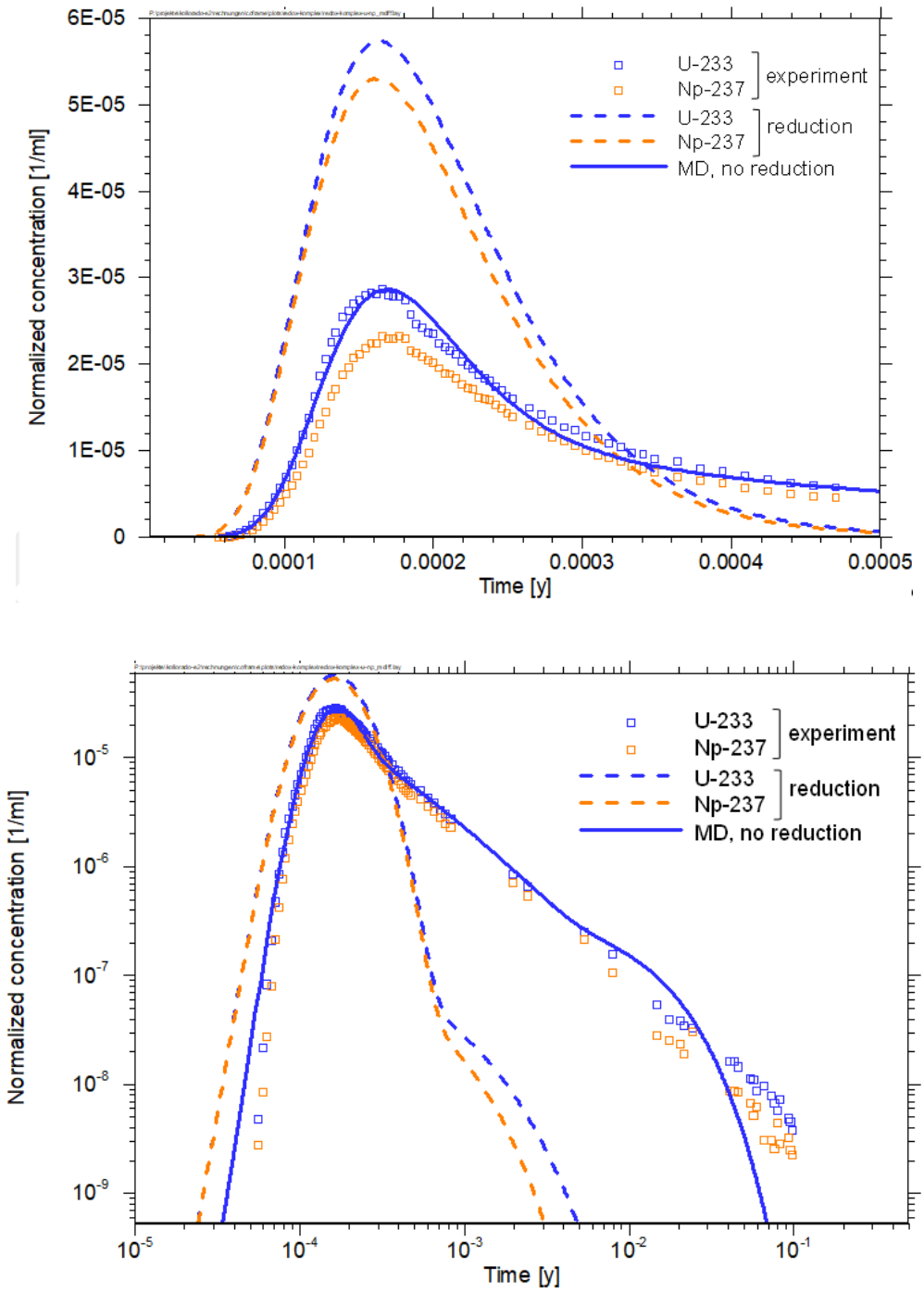

Figure 69 *Breakthrough curve for U-233 and Np-237, experimental data and model calculations; top: linear scale; bottom: log scale..*

However, the application of the matrix diffusion parameters to CFM RUN 13-05 show (Figure 70), that the obtained curves are not compatible with the experimentally obtained curve for the AGA tracer, i.e. matrix diffusion cannot explain the shape of all curves in both experiments consistently. Furthermore, for matrix diffusion the reduction kinetics of U(VI) and Np(V) would decrease the recovery of both radionuclides mainly at late times, i.e. the curve maximum would not be impacted. This is in contradiction with the experimental data, where the maximum of Np-237 is stronger depleted than U-233. However, a more thorough investigation of matrix diffusion will be performed, when data from overcoring of LIT are available.

Nevertheless, it is more likely that the transport does not occur via one single pathway, but the observed breakthrough curves are the result of a superposition of different (at least two) flow channels, as it was assumed, e.g. in (Kosakowski, 2004). This will also be further evaluated in the follow-on project.

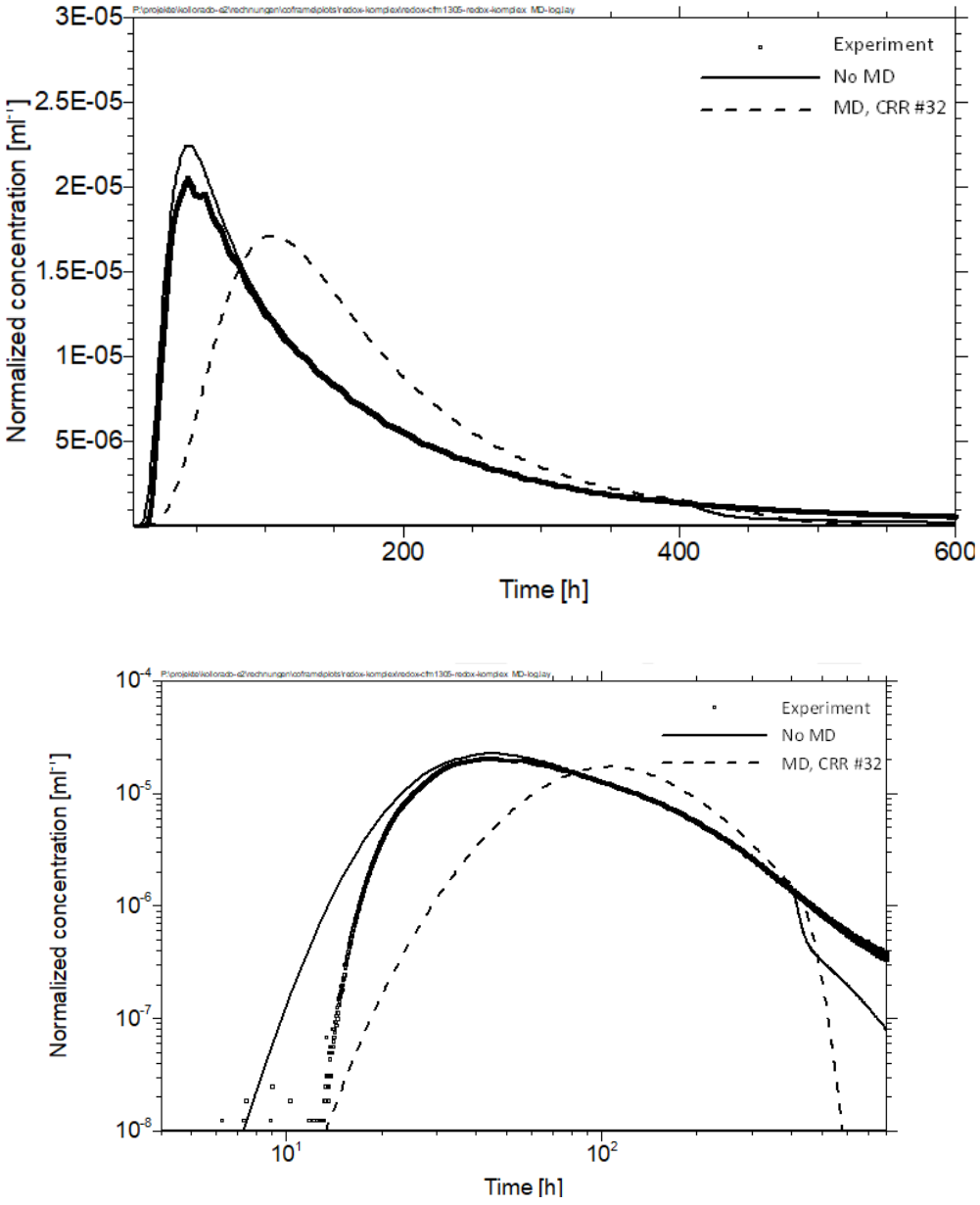

Figure 70 *Breakthrough curve for non-sorbing tracer AGA in CFM RUN 13-05: Experimental values and simulation results from fit (no matrix diffusion) and calculation with matrix diffusion parameters applied in CRR RUN #32 U-233, see text*

3.3 Simulation of radionuclide diffusion in the bentonite source of the LIT with CLAYPOS

One key experiment of the CFM project was the Long-term In-situ Test (LIT), where a radionuclide spiked bentonite source was emplaced in the shear zone at GTS and key hydraulic and hydrochemical parameters have been observed for the duration of the experiment (Rinderknecht, 2017). The experiment was started in May 2014 and was running until November 2018, all in all 4.5 years. In November 2018 the overcoring of the area around the bentonite source was started. One question concerns the mobility of the radionuclides in the bentonite. The calculations presented here are aiming to estimate either how RNs are distributed in the bentonite or whether significant amounts of radionuclides are expected to have been released from the bentonite.

3.3.1 Experimental set-up of bentonite source in LIT

A detailed description of the LIT experiment can be found in section 2.2.2[7]. The bentonite source within LIT consists of 16 compacted bentonite rings with a compaction density of 1600 kg/m^3, which are stacked on the mandrel of the packer system. Combination of the bentonite rings results in a 400 mm high bentonite rod with an inner diameter of 43 mm and an outer diameter of 83 mm. A total of 2613.6 g bentonite composed of 2549.9 g natural Febex bentonite and 63.7 g synthetic Zn-labeled montmorillonite is emplaced in the migration shear zone. A detailed description can be found in section 2.2.2.

A schematic sketch of one of the four midst rings of the LIT experiment is shown in Fig. 73. The status of the glass vials is uncertain. They might be broken due to the swelling pressure of the bentonite caused by water re-saturation. In this case RN diffusion will occur from the areas, where the vial wall is broken, into the bentonite ring. If the glass vial is not broken, RN diffusion will definitely occur from the open part of the vial in the inner part of the bentonite ring.

In order to get an estimate on radionuclide movement within the bentonite, screening calculations are performed. 1D diffusion models have been applied: a planar diffusion model and a radial diffusion model as also shown in Figure 71. Both types of models do not fully reflect the situation but give indications on expected travel distances in the bentonite during the LIT experiment. A further simplified assumption is a constant concentration in the vial. This is particularly not the case for mobile radionuclides and this assumption will be further refined in the next step.

3.3.2 Transport Code CLAYPOS

The module CLAYPOS belongs to the programme package RepoTREND, which is used for post-closure safety assessments of deep geological repositories for radioactive waste in Germany (Reiche, et al., 2016). CLAYPOS simulates one-dimensional radionuclide transport in low-permeable media either in cylindrical or in planar geometry (Rübel, et al., 2007). It considers linear sorption and radioactive decay in decay chains. For each time step the radioactive decay is calculated analytically for the dissolved / sorbed and the precipitated inventory and the diffusive transport of the radionuclides is solved numerically. An implicit solution algorithm is used with a fixed time step width given. That means that the variable parameters are inserted with their values at the end of the examined time step for higher stability of the algorithm, i.e. negative concentrations are automatically avoided. The time derivative is replaced by an upwind difference and the spatial derivative is replaced by the central difference between the segments (Rübel, et al., 2007). For the inner boundary condition two cases are distinguished. Supposing that the solubility limit has been reached (a), the boundary concentration is given, otherwise (b) a source is assumed. In order to represent also the gradient correctly at the inner and outer boundaries in the case of the stationary solution, the discretization raster is extended into the inner/outer area and the boundary condition is extrapolated. For the outer boundary condition of the radionuclide flux, the water volume flow in the aquifer is explicitly entered in the model. Since the volume flow in the aquifer can be very high and the impossibility to exactly specify the volume flow in every case, an excessively high water flow may be entered into the model to simulate a zero concentration boundary condition (Rübel, et al., 2007).

[7] *Documented in Nagra Aktennotiz AN 14-326 Long-term in-situ test (LIT): Bentonite source term packer system, surface equipment extension, QA and installation report (24. July 2014)*

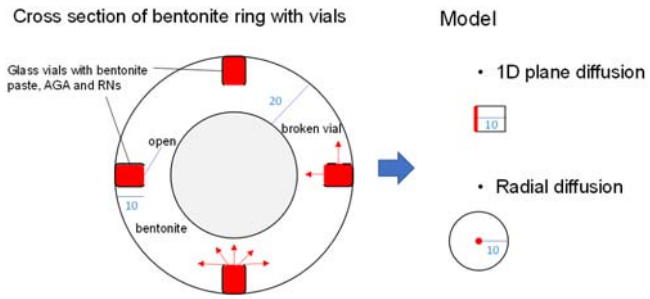

Figure 71 *Schematic cross section of a bentonite ring with radionuclide containing glass vials as used in the LIT experiment and the models applied for radionuclide diffusion.*

3.3.3 Diffusion and porosity in bentonite

Diffusion in compacted bentonite is a complex process, due to pore structure dependent types of water binding as illustrated in Figure 72. These are (i) the free bentonite porewater, (ii) interlayer water with water and cations between the TOT layers of montmorillonite, devoid of anions, and (iii) diffuse double layer water containing water, cations and anions; an excess of cations neutralizes the charge at the outer surface of the montmorillonite, e.g. (Appello, 2013).

The distribution of the water on the three different types of water or porosity strongly correlates with the degree of compaction, namely the dry density of the bentonite. In addition, the DDL water fraction is also affected by the ionic strength of the solution.

Neutral species and cations diffuse through all three types of water, i.e. the diffusion accessible porosity equals the total porosity. Anions are almost completely rejected from the interlayer pore space (Muurinen, 1994; Tournassat & Appelo, 2011; Van Loon, et al., 2007). The interparticle pore space, however, is partly accessible to anions, depending on the ionic strength of the porewater and compaction density (Van Loon, et al., 2007). At high ionic strength, the DDL pore space is largely suppressed and almost the total IP pore space is available for anions. At low ionic strength values, only a small part of the IP pore space is accessible to anions. Both is illustrated in Figure 73.

In (Van Loon, 2014) a procedure is described how to derive from diffusion in free pore space, on the surface (DDL) and in the interlayer an effective diffusion coefficient. For cations undergoing ion exchange this procedure is based on a correction for surface diffusion by a method developed by (Gimmi & Kosakowski, 2011). For anions ion exclusion is taken into account. Based on the composition and ionic strength of a typical porewater for MX-80 bentonite in the report from (Van Loon, 2014) reference effective diffusion coefficients for a total porosity of 36 % and upper values for a total porosity of 48 % are derived. The latter value is comparable to the expected total porosity in the LIT experiment; therefore, the corresponding effective diffusion coefficients are applied for the model calculations here.

3.3.4 Modelling data

The modelling data have been derived from the experimental description and from literature. For the models a transport length (or radius) of 0.01 m is assumed. At the outer boundary of the model a relatively high water flow of 1 m^3/a is used as boundary condition. For the radionuclide source (point source for radial diffusion) a constant concentration is assumed in the first step. The concentration is estimated from the radionuclide inventory in the bentonite sludge of a vial, the available fluid volume in the vial, the M/V ratio and the retardation factor applied for the bentonite.

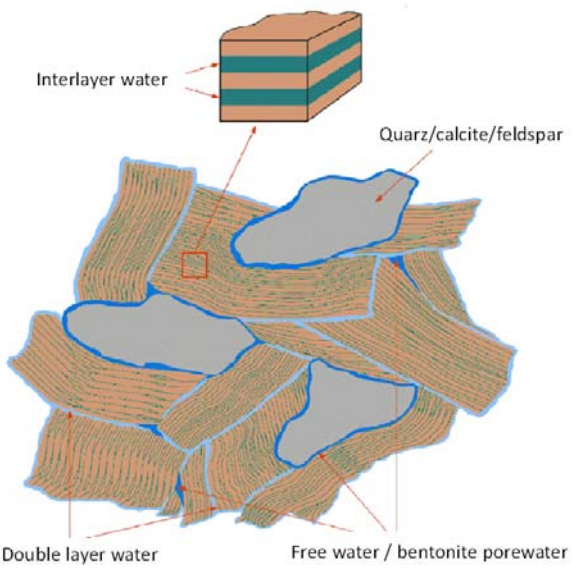

Figure 72 *Illustrations of the bentonite structure and porosity types (Appello, 2013).*

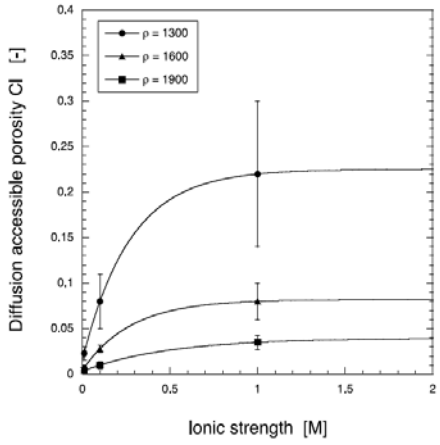

Figure 73: *Effect of ionic strength on the anion diffusion accessible porosity in bentonite compacted at different dry densities (Van Loon, et al., 2007).*

The retardation factor for each radionuclide i is calculated by

$$R_{f,i} = 1 + \frac{1-n}{n}\rho K_d.$$

Most K_d values have been taken from Bradbury & Baeyens, 2009. For U(VI) and Np(V) modified data based on Tachi 2014 have been used, see Table 39. The concentration in the fluid of the vial is then calculated – assuming sorption equilibrium – from the radionuclide inventory per vial, the fluid volume in the vial and the retardation factor in the vial by

$$c_{vial,i} = \frac{I_{vial,i}}{V_{l,vial}R_{fvial,i}}$$

For the radionuclide source a constant concentration is assumed. This is particularly not correct for very mobile elements, but in a first step applied to get an idea on the diffusion distance. Further calculations with limited inventory are planned. Diffusion is calculated over a time frame of 4.5 years according to the duration of the LIT. The transport code CLAYPOS has been used (Rübel et al., 2007).

Within the ring outside the vials the bentonite is higher compacted. Due to estimations in /RIN 17/ the bentonite dry density after water saturation is expected to be around 1350 to 1450 kg/m^3. In the calculations a bentonite dry density of 1435 kg/m^3 corresponding to a total porosity of 0.48 in the bentonite ring is assumed. From the calculated concentrations c_i in the bentonite porewater in the ring the radionuclide content $S_{b,i}$ in the bentonite is calculated via

$$S_{b,i} = c_i R_{f,i} \frac{V_l}{M_b}$$

The physical parameters for the bentonite are listed in Table 39 and the data used for calculating the radionuclide concentration in the source (porewater in glass vials) and retardation in the bentonite ring are listed in Table 40.

3.3.5 Results

Selected results for the spatial distribution of actinides and technetium are shown in Figure 74 to 76. The screening calculations indicate, that the actinides in the tetravalent state, Pu(IV), U(IV) and Np(IV) will be rather immobile showing steep decreasing spatial profiles in a distance of less than 0.001 m after 4.5 years duration of the LIT experiment. The radial diffusion, of course, always causes a lower concentration profile than the planar 1D diffusion. The spatial distributions calculated for trivalent Pu and Am, tetravalent Tc and hexavalent U show a concentration decrease of one order of magnitude at a travel length between 0.005 and 0.008 m, still less than 0.01 m. This suggests that, in case that no glass vial is broken, the actinides and Tc, if present in the reduced form, would have remained in the bentonite source.

The lower or non-sorbing elements with K_d-values below 1 m^3/kg, namely Cs and Ca, reach a steady state distribution in the bentonite model area of 0.01 m extension. The temporal distributions shown in Figure 78 suggest that these elements become released early reaching a steady state within a few months. The same is true for Np, Se and Tc, if they occur in their oxidized forms Np(V), Se(VI) and Tc(VII), see Figure 77. The strong decrease of the breakthrough curves for ^{45}Ca and ^{75}Se is due to radioactive decay.

Table 39: *Data applied for diffusion in bentonitediffusion.*

Parameter	Symbol	Value	Unit
Bentonite ring			
Transport length / radius	L	0.01	m
Bentonite mineral density	ρ_B	2760	Kg m^{-3}
Bentonite dry density		1435	Kg m^{-3}
Total bentonite porosity	n	0.48	-
Liquid / mass ratio	V_l/M_b	0.3333	l/kg
Glass vial			
Bentonite mass per vial	$M_{B,vial}$	0.111	g
Fluid volume per vial	$V_{l,vial}$	1.11E-4	l
Porosity	$\rho_{B,vial}$	0.734	-

Table 40: *Compilation of radionuclide data; K_d values are taken from (Bradbury & Bayens, 2010) if not marked otherwise; effective diffusion coefficients are taken from (Van Loon, 2014), see text.*

Radio-nuclide	Vial				Bentonite ring	
	Inventory $I_{vial,i}$ [mol]	$K_{d,i}$ [m^3/kg]	$R_{f,vial,i}$	Concentration $c_{vial,i}$ [mol/l]	$R_{f,i}$	Diffusion coeff. D_{eff} [m^2/s]
^{45}Ca	1.49E-12	0.0027	3.7	3.64E-09	9.1	2.8E-10
^{75}Se(IV)	7.41E-14	0	1	6.67E-10	1	1.8E-11
^{75}Se(-II)						4.4E-11
^{99}Tc(VII)	5.38E-09	0	1	9.70E-09	1	1.8E-11
^{99}Tc(IV)		5	63		14 951	1.8E-10
^{137}Cs	6.23E-13	0.032	33	1.70E-10	97	1.5E-09
^{233}U(VI)	5.34E-10	51	5001	9.62E-10	14 951	1.8E-10
^{233}U(IV)		293	293 001	1.64E-11	876 071	1.8E-10
^{237}Np(V)	1.08E-08	0.11	101	9.67E-07	300	1.8E-10
^{237}Np(IV)		375	375 001	2.60E-10	1 121 251	1.8E-10
^{241}Am	1.80E-12	9.5	9501	1.71E-12	28 406	1.8E-10
^{242}Pu(IV)	3.75E-10	3002	300 001	1.13E-11	879 001	1.8E-10
^{242}Pu(III)		9.5	9501	3.56E-10	28 406	1.8E-10

[1] *data modified from (Tachi, et al., 2014);* [2] *data estimated from U(IV) and Np(IV) values*

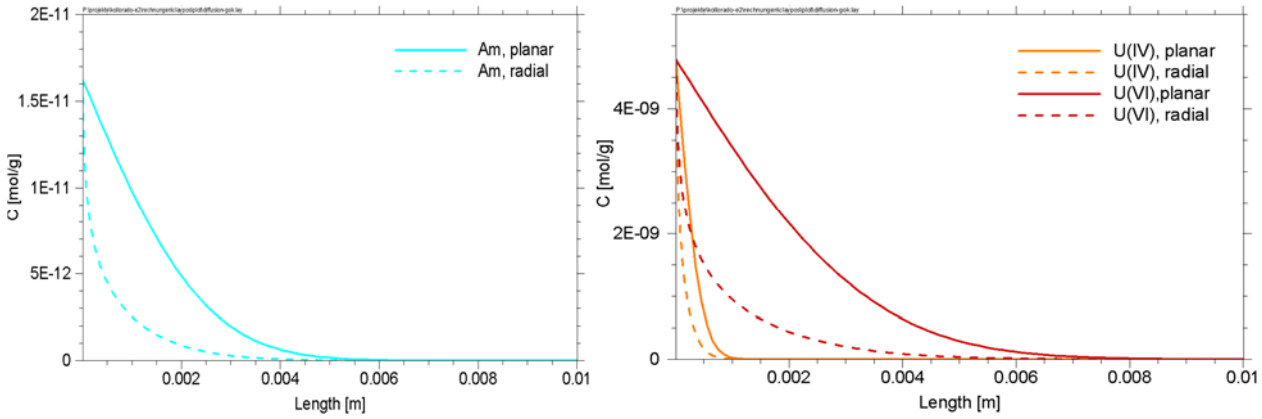

Figure 74: *Spatial distribution of Am (left) and U(VI) and U(IV) calculated for plane and radial diffusion after 4.5 years transport time.*

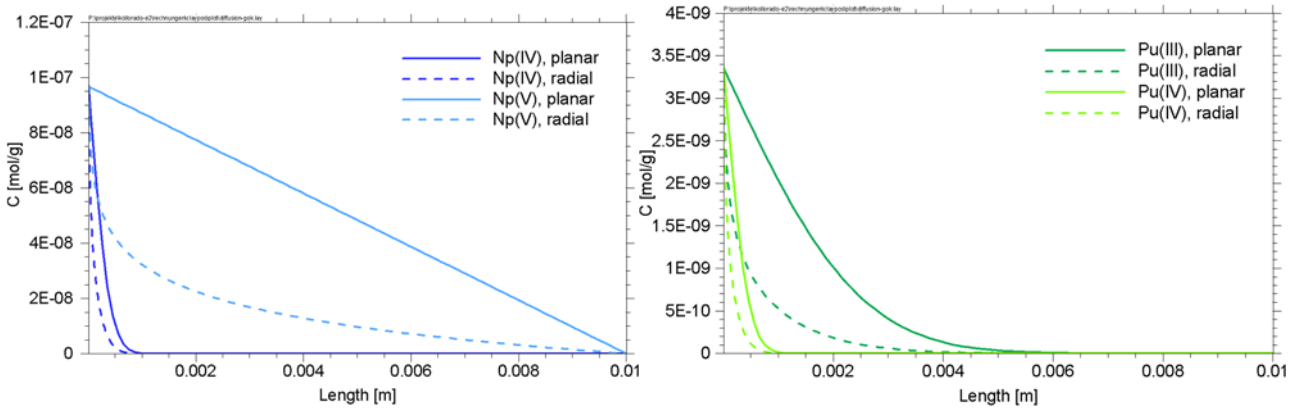

Figure 75: *Spatial distribution of Np(V) and Np(IV)(left) and Pu(IV) and Pu(III) calculated for plane and radial diffusion after 4.5 years transport time.*

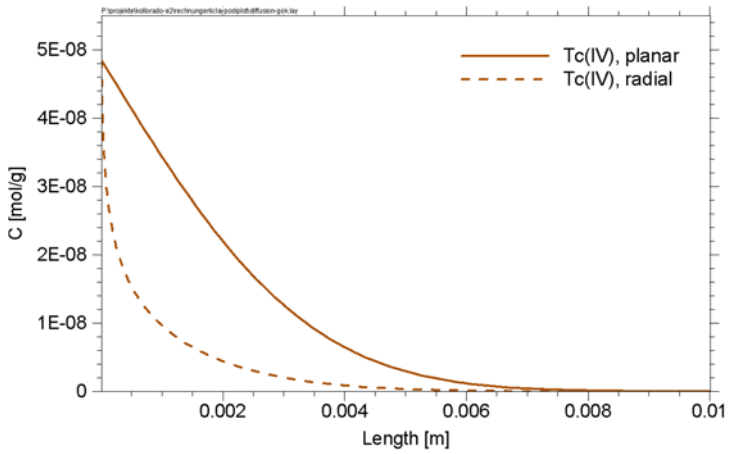

Figure 76: *Spatial distribution of Tc(IV) calculated for plane and radial diffusion after 4.5 years transport time.*

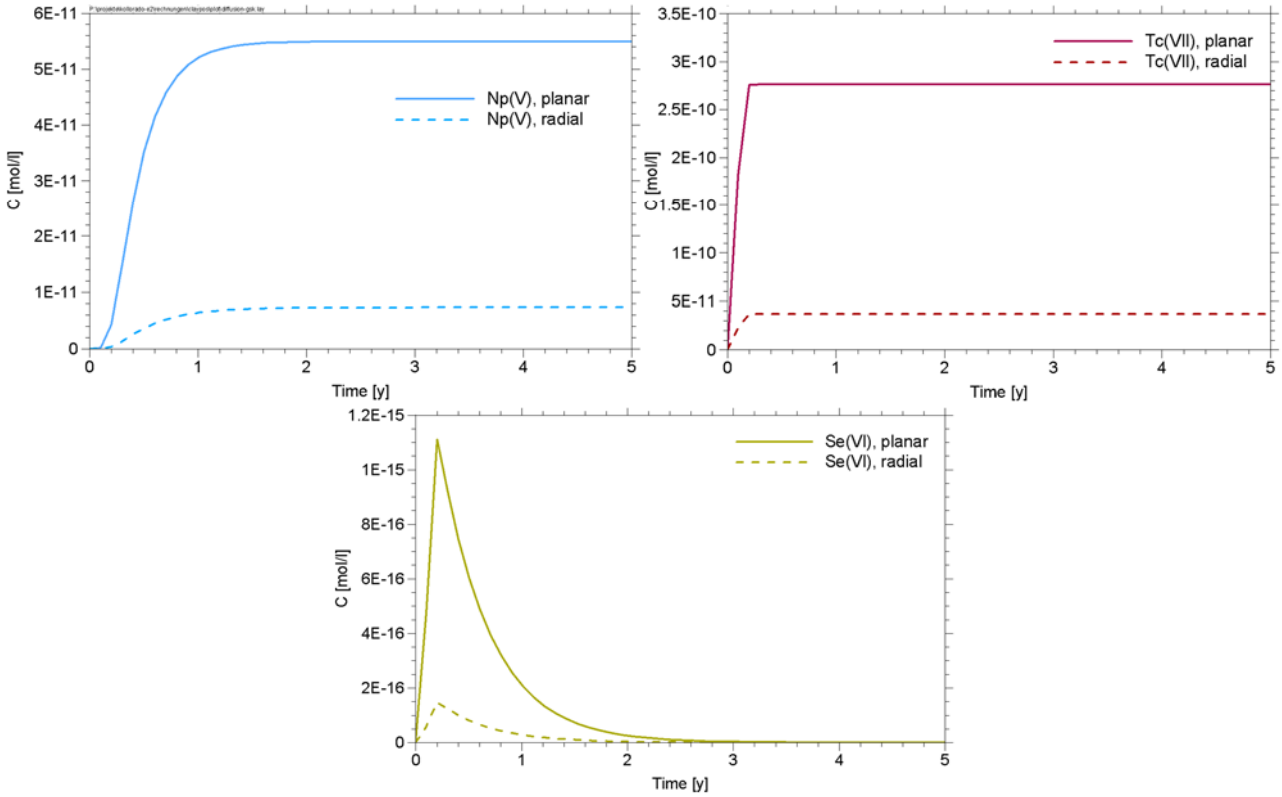

Figure 77: *Breakthrough curves for Np(V) (top), Tc(VII) (middle) and Se (VI) (bottom) calculated for plane and radial diffusion.*

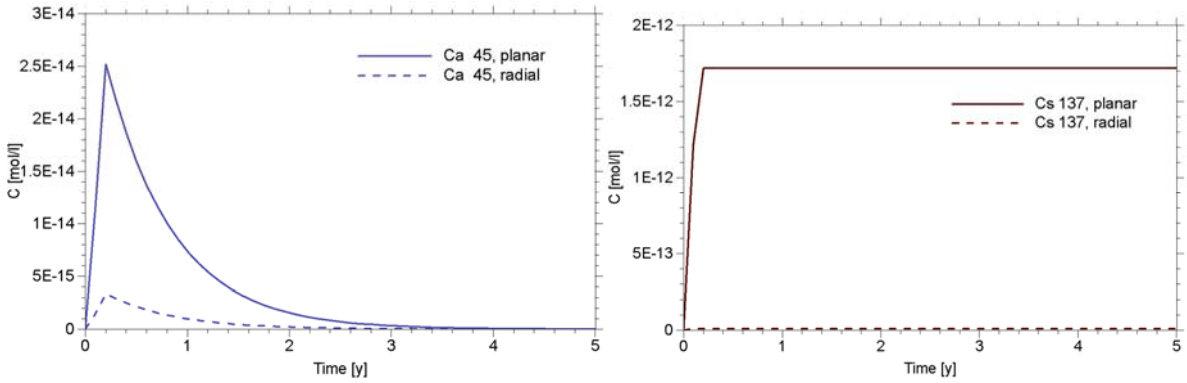

Figure 78: *Breakthrough curves for ^{137}Cs and ^{45}Ca (bottom) calculated for plane and radial diffusion.*

The results of the simulation can also be compared with results obtained in the Mock-up test (see Section 2.1.2). Although the experiment has been performed within a glove box, it is expected that the conditions in the Mock-up test are more oxidizing than in the LIT, since residual oxygen is contained in the system (bentonite rings and glass vials), flowing Grimsel groundwater is not as reducing based on Eh measurements as the original MI shear zone water sampled and there is no reducing capacity of the rock, which is simulated by a Plexiglas housing. Under such conditions it is expected that e.g. Np and Tc remains in their oxidizing states, namely as Np(V) and Tc(VII). Thus, the simulated breakthrough curves for both elements can be compared with the experimentally obtained breakthrough curves.

The simulation predicts a very early release of both elements from the bentonite within about one month for Tc-99 and about six months for Np-237. A rather early release within one month for Tc-99 and app. 2 months for Np-239 is indeed observed in the Mock-up experiment. Differences are likely due to simplifications in modelling, i.e. there is some uncertainty with respect to the arrival time of the maximum, since a concentration decrease in the long term has not yet been modelled so far, namely a constant radionuclide source in the bentonite is assumed, see above. A more realistic modelling of the source is expected to shift the maximum peaks of the simulated curves to earlier times.

For comparison of the concentrations it needs to be regarded that the model calculations have not been performed to explicitly describe the mock-up test but for the LIT experiment. This particularly concerns the water flow. For the modelling a relatively high flow of 1 m^3/y (as a conservative boundary condition) has been assumed, whereas in the mock-up test the water flow was adjusted to 50 µl/min corresponding to $2.63 \cdot 10^{-2}$ m^3/y (see Section 2.1.2). Consequently, the water flow and therewith the dilution of the radionuclide concentration is by a factor of 38 lower in the experiment. The maximum concentrations of the radionuclide release curves observed in the mock-up test are $8 \cdot 10^{-11}$ mol/l for Np-237 and $6 \cdot 10^{-9}$ mol/l for Tc-99. Considering a dilution increased by a factor of 38 it results in $2.2 \cdot 10^{-12}$ mol/l and $1.6 \cdot 10^{-10}$ mol/l for Np-237 and Tc-99, respectively. For Tc-99 this concentration is directly in the concentration range between the concentration curves calculated for radial and planar diffusion, respectively. For Np-237 this concentration is slightly below the calculated concentration for the radial diffusion. Although the diffusion calculations were not targeted to the Mock-up experiment, the agreement is rather well. In the follow-on project calculations directly adapted to the Mock-up experiment will be performed.

3.3.6 Conclusions on radionuclide diffusion

These calculations are meant as screening calculations in order to get an idea about the mobility of the radionuclides in the bentonite of the LIT experiment at GTS. The geometries have been kept simple as well as the assumption of a constant radionuclide source in the vials filled with bentonite sludge. The latter assumption is particularly not true for the mobile radionuclides. Some further calculations with refined assumption are planned for both, the mock-up experiment and the LIT experiment, as soon as spatial distribution results of radionuclides in the bentonite source become available. The complex diffusion in the bentonite, which occurs in the free porewater, the DDL layer and in the montmorillonite interlayers was treated as an effective diffusion process in the free pore space as usually done in performance assessment. Effective parameters derived by (Van Loon, 2014) have been applied here. The comparison with the Mock-up experiment indicates that this model describes the radionuclide diffusion in the bentonite rather well, at least for the oxidized forms of Tc-99 and Np-237.

3.4 The role of fracture geometry and orientation on transport properties and bentonite erosion[8]

The activities concerning the importance of natural heterogeneity (here surface roughness) focus on two aspects, (1) the implementation of natural fracture geometries in computational fluid dynamic models and comparison to real experiments and (2) the impact of the systematic variation of random aperture normal distributions and aperture correlation lengths on the bentonite erosion model initially computed for parallel plate geometry by (Moreno, et al., 2011).

In the first study very systematically the impact of fracture geometry in the x-y plane and aperture distribution on solute transport was investigated. Two differently altered, fractured, granitic drill cores were used for this study. By scanning the drill cores using μCT the internal structures of the fractures are accessible, showing the altered fracture to be more complex in geometry with a smaller mean aperture compared to the unaltered one. In contrast, the unaltered fracture showed to have a geometry with a minor number of asperity contacts and a larger mean aperture. The obtained μCT data served as input for 2.5-D flow and transport models of both fractures. Through three different injection and three different extraction points in the experimental setup for each fracture, different dipole flow field configuration could be established and experiments with the conservative tracer Amino-G were performed. The solute transport through both fractures could be qualitatively and partly quantitatively predicted based on the 2.5-D modeling approach. By comparing the experimental data from the altered and the unaltered fracture, the BTCs of the transport experiments through the altered fracture were less homogenous compared to the ones through the unaltered fracture, which confirmed the tomographic imaging. In the case of the altered fracture, there was good agreement between modelled and experimental BTCs. In conclusion, fluid flow through this fracture was overall dominated by the complex fracture geometry in the x-y plane, e.g. the high number of contact points and therefore channeling. This has been proven by performing stepwise model simplifications. The BTCs for the different experimental cases through the unaltered fracture showed less deviation but a wider spreading between each other. The large aperture might decrease the impact of fracture wall interaction and the fully open fracture might be the reason for the uniformity of the BTCs. The modelled BTCs showed to be more irregular compared to the experimental ones with an overestimation in the tailing region. Fluid flow in this fracture was majorly influenced by the aperture distribution and less by the fracture geometry in the x-y plane. By simplifying the models, it was qualitatively shown that the congruency of the modelled solute transport with the experimental data decreases. The decrease in complexity resulted in less pronounced and more even formed tailings of the derived BTCs without the occurrence of secondary peaks. It was obvious that the formation of these secondary peaks in the model BTCs was directly linked to the implemented aperture distribution. In conclusion, fluid flow and the mass transport in both fractures showed clear differences. The fracture geometry and the aperture distribution are needed to describe precisely fluid flow and mass transport to understand mechanisms prevailing in natural rough fractures. Which feature (asperity contacts or aperture distribution) dominates surely depends on the investigated fracture. Moreover, the importance of tomographic imaging for the generation of 3-D and 2-D numeric models could be highlighted. Despite the simplification from a fully 3-D to a 2.5-D model, the presented results provide a step forward in understanding and interpreting solute transport through natural single fractures and especially the tailing behavior.

In the second work the effect of fracture geometry on bentonite erosion for a generic repository site in crystalline host rock environment was investigated by means of 2d numerical simulations. Fracture geometry was varied systematically using random aperture normal distributions with a mean aperture of 1 mm and standard deviations between 0 and 0.7 mm, respectively. Moreover, two aperture correlation lengths (0.2 m and 2 m) were applied. Based on the synthetic fracture aperture fields generated, the cubic law in conjunction with the Darcy equation is used to simulate fracture flow fields for mean flow velocities in the fracture between $1x10^{-5}$ m/s and $1x10^{-7}$ m/s. These flow fields are used in a two-way coupling approach to bentonite erosion simulations. The results of the study clearly show the influence of variably fracture aperture on bentonite erosion behaviour and erosion rates (kg/a). Increasing fracture aperture standard deviation leads to increasing heterogeneous flow velocity distributions governing the erosion behavior and erosion rates. Calculated equilibrium erosion

[8] *The summary provided here is based on the publications: (1) Stoll, M., Huber, F.M., Trumm, M., Enzmann, F., Meinel, D., Wenka, A., Schill, E., Schäfer, T., 2019. Experimental and numerical investigations on the effect of fracture geometry and fracture aperture distribution on flow and solute transport in natural fractures. J. Contam. Hydrol. 221, 82-97. and (2) Huber, F.M., Leone, D., Trumm, M., Moreno, L., Neretnieks, I., Wenka, A., Schäfer, T., 2020 (in review). Impact of fracture geometry on bentonite erosion - a numerical study. Appl. Clay Sci.*

rates are in the range of ~0.25 kg/a down to ~0.014 kg/a. The highest erosion rate is calculated for the highest mean flow velocity in conjunction with the highest standard deviation. The effect of aperture heterogeneity diminishes for the lowest flow velocities.

In summary, the results show the effect of fracture heterogeneity on bentonite erosion, especially for high to medium mean flow velocities combined with high to medium fracture heterogeneity under the model boundary conditions and model capabilities and limitations considered. An increase of up to ~83 % in erosion rate compared to the constant aperture case highlights the need to consider fracture aperture heterogeneity and its effect on the bentonite erosion in the assessment of the safety and evolution of a high level nuclear waste repository.

4. Conclusions

Within the Kollorado-e^2 project the state of the art with respect to colloid formation, migration and interaction with radionuclides has been improved. Important experimental activities have been performed in the laboratory and the field accompanied by process modelling, which have increased the process understanding and substantiated the basis for modelling calculations in performance assessment.

The results of the project can be used in different ways in safety assessment and in a safety case: (i) as direct input parameters for the performance assessment codes, (ii) by improvement of the assessment basis due to increase of the process understanding, which is necessary for predictive calculations and up-scaling, and (iii) for demonstration issues as erosion behavior of a bentonite source and radionuclide mobility under near natural hydraulic conditions. Progress has been achieved on the following topics.

With respect to bentonite erosion and colloid formation at the bentonite / crystalline rock interface a feasibility study of structurally marked (Zn, Ni) montmorillonite for quantification of the erosion rates has been performed, and mock-up tests under the geometrical conditions of the LIT experiment to determine erosion rates of Febex bentonite. For the latter, Febex bentonite rings have been brought into contact with an artificial fracture of 1 mm aperture to yield a realistic colloid source term for the LIT. A key part of the investigations concerned the continuous observation of the LIT experiment. The long-term in-situ test (LIT) has been started in 2014 to investigate in situ colloid formation and mobilization of radionuclides from a radionuclide-labelled bentonite plug (NAGRA, 2016). During the KOLLORADO-e^2 project samples from observation boreholes and Pinkel have continuously been taken, analyzed and evaluated until the experiment has been stopped and overcored end of 2018. From LIBD analysis as well as from concentration profiles of Zn, Al and Mg measured in samples frequently taken from the observation boreholes in few cm distance of the LIT source bentonite release rates within the LIT experiment could be estimated. About 100 days after installation of the LIT source measurable concentrations of the respective elements could be detected and constant concentrations are reached after app. 200 days. From the long-term concentration profiles rather low erosion rates of 91 ± 30 g/m^2/a (normalized to the contact area) have been derived.

One essential factor for the evolving contact area and the extension of the swelling bentonite into the fracture – and therewith on the erosion process – is the geometry of the fracture at the bentonite fracture interface. Systematic model calculations have been performed to investigate the impact of the surface roughness of the fracture and the correlation length on the erosion rate (Huber, et al., 2020, in review). Model calculations show that flow channels and the surface forming at the contact zone is directly determining the concentration of the mobilized colloids and the geometry of the flow channel crucially impacts the mobility of the colloids and erosion rates in the fracture (Huber, et al., 2020, in review).

Concerning colloid stability and interaction with fracture surfaces the investigations focused on the colloid size and colloid density and its effect on the interaction process with fracture surfaces of different orientation. The investigations have shown that sedimentation can play a significant role even for carboxylated latex spheres in horizontally oriented fractures. Further studies focused on the effect of surface roughness of granodiorite from the Grimsel Test Site and horizontal / vertical fracture orientations in comparison to Plexiglas surfaces on the interaction energies of carboxylated latex particles. This experimental work has been successfully compared to 2D simulations with COMSOL Multiphysics® explaining the results observed (Stoll et al., 2016; Stoll, et al., 2017).

Thermodynamic benchmark calculations have been performed to better understand the speciation and therewith the transport and retardation effects of homologues and radionuclides under the evolving geochemical conditions in the field experiments at GTS, particularly the LIT. Especially, the conditions at the interface between bentonite and crystalline rock have become more important for the current experiments and been included into the new benchmark. By comparison of

the results obtained by two different modelling groups of the Kollorado-e^2 consortium key geochemical parameters affecting transport of the radionuclides Se, Tc, U, Np, Am, Th and Pu in this context could be identified. Since the publication of a previous modelling exercise (Bruno, et al., 2000) thermodynamic databases have been further developed and harmonized, particularly within the NEA TDB project, where both databases applied here are based on. Particularly, the existence of new species like ternary silica actinide complexes, ternary uranyl carbonate complexes or iron selenides have been proofed and included, impacting for example the speciation and solubility of uranium, americium or selenium in the systems investigated here. The model comparison also showed the relevance of expert judgement in modelling decisions. The characteristics of solid phases, especially the selection of a crystalline, aged or fresh mineral phase directly impacts the solubility. For ThO_2, as an example, it is recommended to use the value for the aged phase considering the 4.5 years duration of the LIT experiment. In a similar way, the inclusion/exclusion of mobile species leads to an increase/decrease of the solubility like for the poly-selenides in case of selenium. In general, the calculations of both modelling groups agree well and differences in results could always be traced back to slight differences in data or in modelling assumptions as described above.

One focus of the investigations in the KOLLORADO-e^2 project was still on the interaction of radionuclides, colloids and fracture filling material, particularly on determination of data for the radionuclide reversibility kinetics, which are necessary to simulate the field and laboratory experiments and are directly used in the transport codes. After evaluation of the RN reversibility of Febex clay mineral colloids in batch experiments by addition of (i) humic substance as competing ligand (Bouby, et al., 2011) and (ii) pre-conditioned granodiorite of different grain size (Huber, et al., 2011; Huber et al., 2015) a lack of data for sorption/desorption kinetics of ^{232}Th, ^{233}U, ^{237}Np, ^{242}Pu, ^{243}Am on the granodiorite or fracture filling material became visible. Therefore, in KOLLORADO-e^2 reversibility investigations for these radionuclides have been performed for the binary system radionuclide - fracture filling/fault gouge material with the addition of colloids to force desorption kinetics as a function of contact time. As a result, distribution coefficients for the five actinides on fault gauge material as well as kinetic parameters in the binary and ternary systems are available now. The batch experiments show that in case of Th(IV) as also for some redox sensitive radionuclides long-term kinetics of more than two years have to be taken into account which is supported by field experiments (Quinto, et al., 2017).

The application and further development of Accelerator Mass Spectroscopy (AMS, (Quinto et al., 2015) offered the opportunity to study the long-term mobility of radionuclides by sampling the tailing of the breakthrough curve over a period of six months and providing additional details on the sorption/desorption processes/kinetics of the fracture filling material. Further AMS data on the long-term tailing of CFM Run 13-05 have been collected and evaluated. It allowed to identify for the first time traces of radionuclides, which were injected in CRR tracer tests more than 12 years before CFM Run 13-05 in the same dipole. Although the data from CFM Run 13-05 are thus to some extent biased by the CRR experiment, calculations with COFRAME have been performed and indicated that the long-term concentration ranges for ^{243}Am and ^{242}Pu in CFM Run 13-05 can be met with the same parameters as used in CFM Run 12-02.

Further field experiments focused on the remobilization of radionuclides retained in the CFM Run 13-05 dipole test, called REMO tests. A “pump & treat” philosophy was used in Remo-1 mobilizing by flow reversal and two hydraulic pushes colloids and associated radionuclides from the injection borehole of tracer test CFM Run 13-05. Results show that only minor colloid concentrations in the ppb range were mobilized and the AMS studies in addition show, that especially in the first sample directly taken after the connection of the lines (so-called background sampling) before the actual Remo-1 test highest concentrations of actinides were detected. Remo-2 was designed initially as well as “pump & treat” test with the fast injection of a bentonite colloid plume and extraction after a certain shut-in phase. Due to the hydraulic restrictions to avoid an influence on the LIT experiment the injected colloidal plume could not be recovered in the pumping phase. Therefore, the colloid plume was monitored through the Pinkel surface packer and AMS samples taken show a direct correlation of tri- and tetravalent radionuclides with the colloid concentration, whereas Np and U concentration shows a delayed peak concentration. In summary, with all these investigations mentioned above in addition to the results from the field migration tests performed during the CFM project, now a good data tool on bentonite colloid filtration rates as well as interaction rates of radionuclides with colloids and fracture material exists.

One specific effect observed in the field tests CRR #32 and CFM-13-05 carried out in the same dipole with high and low fluid velocity, respectively, concerns the redox reaction of U and Np during transport through the shear zone. Both radionuclides initially added in their oxidized form (U(VI) and Np(V)) are not or only to a neglectable amount bound to colloids. Nevertheless, their recovery decreases significantly from the short transport time in CRR #32 to the long transport time in CFM Run 13-05. Simulations are performed in order to model their breakthrough curves in both experiments regarding a reduction of the mobile U(VI) and Np(V) into the rather immobile tetravalent forms. Reaction rates for both radionuclides have been derived and compared to laboratory determined values.

During the lifetime of the LIT experiment from May 2014 until November 2018 the analyses so far indicate that no or only very low concentrations of radionuclides have been released from the bentonite source. In order to understand the radionuclide mobility, one type of simulation addressed the diffusion of the radionuclides through the bentonite ring. The RN tracers had been injected in glass vials in the four inner rings of the bentonite source. Radial and planar diffusion calculations have been performed to estimate either how RNs are distributed in the bentonite or whether significant amounts of radionuclides are expected to have been released from the bentonite. The screening calculations indicate, that the actinides in the tetravalent state, Pu(IV), U(IV) and Np(IV) will be rather immobile showing steep decreasing spatial profiles in a distance of less than 0.001 m after 4.5 years duration of the LIT experiment. The spatial distributions calculated for trivalent Pu and Am, tetravalent Tc and hexavalent U show a concentration decrease of one order of magnitude at a travel length between 0.005 and 0.008 m, still less than 0.01 m. This suggests that, in case that no glass vial is broken, the actinides and Tc, if present in the reduced tetravalent or trivalent form, would have remained in the bentonite source. The lower or non-sorbing elements Cs and Ca, but also the oxidized forms Np(V), Se(VI) and Tc(VII) become released early reaching a steady state within a few months.

It is of high interest to proof these predictions during the overcoring of the LIT experiment. Although covered by several uncertainties, e.g. on the status of the glass vials, whether the PA model describing the diffusion and sorption process in the bentonite buffer is able to describe these processes in the bentonite source of LIT over a time frame of 4.5 years.

Further, the impact of fracture geometry and aperture distribution on fluid movement and on non-reactive solute transport has been investigated experimentally and numerically in single fractures. For this purpose, a hydrothermally altered and an unaltered granite drill core with axial fractures are investigated. Using three injection and three extraction locations at top and bottom of the fractured cores, different dipole flow fields were examined. Fluid flow and tracer transport were simulated using COMSOL Multiphysics® (Stoll, 2018). The fluid flow and the mass transport in both fractures showed clear differences. The fracture geometry and the aperture distribution are needed to describe precisely fluid flow and mass transport to understand mechanisms prevailing in natural rough fractures. Which feature (asperity contacts or aperture distribution) dominates depends on the investigated fracture. Moreover, the importance of tomographic imaging for the generation of 3-D and 2-D numeric models was shown. Despite the simplification from a fully 3-D to a 2.5-D model, the results provide a step forward in understanding and interpreting solute transport through natural single fractures.

Beside understanding of processes and application and qualification of models and databases some of the work performed within the KOLLORADO-e^2 project was dedicated to prepare or design field experiments. In this respect the mock-up tests have to be stressed, since they also served for a feasibility study aiming to find a suitable way to conserve the LIT sample during overcoring. Namely, the mock-up experimental set-up has been used to perform resin impregnation tests with subsequent investigation of the contact zones between resin and bentonite or fracture, respectively.

5. Outlook

The post-mortem analysis of the over-cored LIT experiment, which is currently under way within the CFM project, phase IV enables a thorough investigation of radionuclide transport in compacted bentonite under repository-like conditions. With respect to the injected tracers monovalent ^{137}Cs and trivalent ^{243}Am are not redox sensitive and are expected to be medium to strong sorbing. For all other injected radionuclides, namely ^{233}U, ^{237}Np, ^{242}Pu, and ^{99}Tc, their behavior is dependent on the redox state. ^{45}Ca and ^{75}Se will be decayed and no more detectable.

The analyses of the radionuclides and their distribution in the bentonite are of interest with regard to

- the identification of their redox state,
- the identification of potential secondary mineral phases, and
- the long-term reversibility of the sorption of radionuclides to clay minerals, and
- the evaluation of the applied diffusion/sorption model.

All observations can be compared to results from model calculations. Particularly, it shall be checked, whether the redox state and potentially observed secondary mineral phases are in accordance with the results from the thermodynamic benchmark calculations Furthermore, radionuclide distribution profiles in the bentonite will provide a validation tool for the applied diffusion model and show whether the assumption for the predictive calculations could be confirmed. Differences between the LIT in situ experiments and its mock-up could be (a) a slight misplacement of the radionuclide containing vials with respect to the shear zone in LIT already identified by CT analysis at EMPA or (b) the redox capacity of the MI shear zone being strongly different to the Plexiglas surface in the mock up. *Post mortem* analysis will be accompanied by updated simulations.

Other interesting aspects of the analyses of the over-cored LIT experiment concerns the distribution of the Ni- and Zn-montmorillonites, which have been used for the bentonite sludge in the glass vials, which might give information about differences in the erosion rates of these montmorillonites. Generally, the analysis of the shear zone and the penetration depth of the bentonite into the water-bearing fracture will contribute to a better understanding of the gel formation and erosion rates. Based on the existing thermodynamic benchmark calculations, which enhanced confidence In the thermodynamic databases, a second part of the modelling exercise is planned, which will emphasize on ion exchange and surface complexation processes on key mineral phases in the bentonite and the minerals of the shear zone / crystalline rock at GTS. This is of key interest to better understand the key geochemical reactions in the bentonite and at the interface bentonite / granite of the LIT.

Since several radionuclide and homologue tracer tests have been performed in the past at the LIT injection borehole, RN diffusion profiles in the shear zone are intended to be investigated as part of the analysis of the over-cored material. Such profiles will give more insight into the role of matrix diffusion processes and parameters might be derived by corresponding model simulations.

Within the CFM project a second in-situ bentonite erosion test (named i-BET) has started at the GTS. The motivation is based on the limited compaction density and bentonite source volume of the LIT experiment and the limited monitoring sensors for pressure and water saturation. Furthermore, Bara-Kade bentonite (MX-80) is used which is a reference bentonite material in Finland and Sweden instead of Febex bentonite. Here, no radionuclides are implemented. Within Kollorado-e^3 continuously samples are taken to quantify the bentonite erosion and monitor the contact water chemistry under possibly higher groundwater flow rates in a permeable fracture to force erosion under extreme conditions. Another aspect tackled is the gravity induced erosion, which can be monitored with a monitoring borehole emplaced directly below the compacted bentonite source.

Bentonites investigated show beside the major mineral component montmorillonite various amounts of accessory minerals. There is quite some controversy about the effect of these accessory minerals on the long-term stability and integrity of the engineered barrier (compacted bentonite). A focus of the studies planned in Kollorado-e^3 is also on the mechanical stabilization of the bentonite gel layer versus erosion considering low reactivity of some accessory minerals (quartz) and the effect on chemical stabilization via the provision of divalent cations (e.g. gypsum dissolution). In LIT we have observed a significant sulfate release over the complete experimental period. A side aspect of the LIT post mortem analysis and also the i-BET analysis will be the characterization of the microbial community in the vicinity of the bentonite buffer.

RN migration on the formation scale (large scale monitoring) is planned to be monitored by AMS measurements of groundwater outside of the MI shear zone. In cooperation with the Water-Rock Interaction Group of the University of Bern, based on these first results in 2018, a targeted sampling program of fissure waters with a significant amount of tritium and also old formation waters was planned and the first samples were already taken and measured (compare also LASMO project: http://www.grimsel.com/gts-phase-vi/lasmo/lasmo-introduction). These investigations are to be systematically supplemented (especially by the quantification of the inorganic (NTA / LIBD) and organic nanoparticulate content (LC-OCD-OND)) and can be used as a further indication of the expected mobility or retention of actinides in natural host rock formations, even if the migration path is of course inverse in this study.

With respect to colloid-facilitated radionuclide transport, several issues are of interest. Firstly, updated and more comprehensive model calculations are planned for the REMO 2 test, which address the real geometry and boundary conditions, as they have been applied in contrast to the original planning. This will be of interest with respect to the remobilization of colloids and to the radionuclide desorption and adsorption rates from immobile to mobile colloids. Regarding ^{233}U and ^{237}Np during the REMO 2 test injected oxygen might have induced their oxidation and subsequent re-mobilization. The simulation of the observed, in comparison to the colloid-bound ^{242}Pu and ^{243}Am slightly retarded breakthrough curves should allow the evaluation of reaction rates observed within the reversibility experiments on fault gauge minerals. Secondly, with respect to newly determined long-term desorption rates in the binary system of radionuclides with fault gauge material, their impact on the long-term tailing in CFM RUN 12-02 and 13-05 should be investigated. For consideration of significantly lower desorption rates an independent adsorption and desorption rate need to be implemented into the transport code COFRAME, which is currently planned.

Furthermore, selected laboratory experiments with drill core material are planned to be performed. The use of synthetic columns produced by 3d printing based on the measured surface structure and roughness allows the investigation of transport in constant geometries and under absence of chemical heterogeneity and matrix porosity.

And finally, after excavation and sealing of the LIT experiment, further radionuclide migration tests in the shear zone are contemplated. During this project phase, predictive calculations with COFRAME have been performed for a field migration experiment aiming to further investigate a postulated two-site desorption mechanism of colloid-bound radionuclides/elements, e.g. Am or Pu, during transport in the shear zone. It is recommended to combine such an experiment with the investigation of the postulated reduction of tetravalent Np and hexavalent uranium during the transport through the shear zone. As discussed in the report the fluid travel time for such an experiment should be in the range of ten hours. Beside the hitherto applied models for the simulation of such experiments also a multi-channel flow approach should be used.

Based on the development of German concepts for a potential disposal of high-level radioactive waste in crystalline formations it is planned to integrate all existing results and evaluate the impact of bentonite erosion and colloid-facilitated transport on the long-term safety by model simulations for appropriate scenarios.

6. References

Agus, S. & Schanz, T., 2008. A method for predicting swelling pressure of compacted bentonites. *Acta Geotechnica,* 3(2), pp. 125-137.

Alonso et al., 2006b. Role of inorganic colloids generated in a high-level deep geological repository in the migration of radionuclides: open questions.. *Journal of Iberian Geology,* 32(1), p. 79.

Alonso, U., Missana, T. & García-Gutiérrez, M., 2006a. Experimental Approach to Study the Colloid Generation from the Bentonite Barrier to Quantify the Source Term and to Assess its Relevance on the Radionuclide Migration. *MRS Proceedings,* p. 985.

Alonso, U., Missana, T. & García-Gutiérrez, M., 2007a. Experimental approach to study the bentonite colloid generation source term in different geochemical conditions. In: G. Buckau, B. Kienzler, L. Duro & V. Montoya, Hrsg. *2nd Annual Workshop Proceedings of the Integrated Project "Fundamental Processes of Radionuclide Migration" - 6th EC FP IP FUNMIG.* Stockholm: SKB, pp. 329-335.

Alonso, U. et al., 2004. μPIXE study on colloid heterogeneous retention due to colloid/rock electrostatic interactions.

Alonso, U. et al., 2007c. Colloid diffusion in crystalline rock: An experimental methodology to measure diffusion coefficients and evaluate colloid size dependence. *Earth and Planetary Science Letters,* 259(3-4), pp. 372-383.

Appello, C., 2013. *A Review of Porosity and Diffusion in Bentonite. POSIVA, Working Report 2013-29.* s.l.:s.n.

Apted et al., M., 2010. Buffer erosion–An overview of concepts and potential safety consequences. *SSM Report,* Band 31.

Baik, M., Cho, W. & Hahn, P., 2007. Erosion of bentonite particles at the in-terface of a compacted bentonite and a fractured granite. *Engineering Geology,* 91(2-4), pp. 229-239.

Bernhard et al., G., 2001. Uranyl (VI) carbonate complex formation: Validation of the Ca2UO2 (CO3) 3 (aq.) species. *Radiochimica Acta,* 89(8), pp. 511-518.

Birgersson, M. et al., 2009. *Bentonite erosion (Final report), SKB Technical Report TR-09-34.* s.l.:Clay Technology, AB.

BMU, F. M. f. t. E. N. C. a. N. S., Version of Sept. 30. 2010. *Safety Requirements Governing the Final Disposal of Heat-Generating Radioactive Waste.* s.l.:s.n.

Bouby, M., Finck, N. & Geckeis, H., 2012. Flow field-flow fractionation (FlFFF) coupled to sensitive detection techniques: a way to examine radionuclide interactions with nanoparticles. *Mineralogical Magazine,* 76(7), pp. 2709-2721.

Bouby, M. et al., 2011. Interaction of bentonite colloids with Cs, Eu, Th and U in presence of humic acid: A flow field-flow fractionation study. *Geochimica et Cosmochimica Acta,* 75(13), pp. 3866-3880.

Bowen, W. & Doneva, T., 2000. Atomic force microscopy studies of membranes: Effect of surface roughness on double-layer interactions and particle adhesion. *Journal of Colloid and Interface Science,* 229(2), pp. 544-549.

Bradbury, M. & Baeyens, B., 2009. Sorption modelling on illite. Part II: Actinide sorption and linear free energy relationships. *Geochimica Et Cosmochimica Acta,* 73(4), pp. 1004-1013.

Bradbury, M. & Baeyens, B., 2010. Comparison of the Reference Opalinus Clay and MX-80 Bentonite Sorption Data Bases used in the Entsorgungsnachweis with Sorption Data Bases Predicted from Sorption Measurements on Illite and Montmorillonite. PSI Bericht Nr. 10-09, ISSN 1019-0643.

Brooks et al., S., 2003. Inhihition of bacterial U(VI) reduction by calcium. *Environmental Science & Technology,* 37(9), pp. 1850-1858.

Bruno, J., Guimerà, J. & Rollin, C., 2000. Bruno J., D.L., Rollin C., Guimerà J.Prediction of the solubility and speciation of RN in Febex and Grimsel waters.

Buddemeier, R. & Hunt, J., 1988. Transport of colloidal contaminants in groundwater: radionuclid migration at the Nevada test site. *Appl. Geochem.,* Band 3, pp. 535-548.

Degueldre, C. & Benedicto, A., 2012. Colloid generation during water flow transients. *Applied Geochemistry,* 27(6), pp. 1220-1225.

Degueldre, C. et al., 1996. Colloid properties in granitic groundwater systems .2. Stability and transport study. *Applied Geochemistry,* 11(5), pp. 697-&.

Derjaguin, B. & Landau, L., 1941. Theory of the stability of strongly charged lyophobicsols and the adhesion of strongly charged particles in solutions of electrolytes. *Acta Physicochim. URSS,* Band 14.

Dittrich, T. & Reimus, P., 2015. Uranium transport in a crushed granodiorite: Experiments and reactive transport modeling. *J. Contam. Hydrol.,* Band 175, pp. 44-59.

Dittrich, T. & Reimus, P., 2016. Reactive transport of uranium in fractured crystalline rock: Upscaling in time and distance. *Journal of Environmental Management,* Band 165, pp. 124-132.

Duro, L. et al., 2006. Determination and assessment of the concentration limits to be used in SR-Can. Technical Report TR-06-32.

Endrizzi, F. & Rao, L., 2014. Chemical Speciation of Uranium(VI) in Marine Environments: Complexation of Calcium and Magnesium Ions with [(UO2)(CO3)3]4− and the Effect on the Extraction of Uranium from Seawater. *Chemistry – A European Journal,* 20(44), pp. 14499-14506.

Fernandez et al., A., 2004. Analysis of the porewater chemical composition of a Spanish compacted bentonite used in an engineered barrier. *Physics and Chemistry of the Earth,* 29(1), pp. 105-118.

Gallé, C., 2000. Gas breakthrough pressure in compacted Fo-Ca clay and interfacial gas overpressure in waste disposal context.. *Applied Clay Science,* Band 17, pp. 85-97.

Geckeis et al., H., 2004. Results of the Colloid and Radionuclide Retention experiment (CRR) at the Grimsel Test Site (GTS), Switzerland - Impact of reaction kinetics and speciation on radionuclide migration. *Radiochimica Acta,* 92(9-11), pp. 765-774.

Geckeis et al., H., 2013. Mineral-Water Interface Reactions of Actinides. *Chemical Reviews,* Band 113, p. 46.

Giffaut, E. et al., 2014. Andra thermodynamic database for performance assessment: ThermoChimie. *Applied Geochemistry,* Band 49, pp. 225-236.

Gimmi, T. & Kosakowski, G., 2011. How mobile are sorbed cations in clays and clay rocks?. *Environ. Sci. Technol.,* Band 45, pp. 1443-1449.

Grenthe, I. et al., 1992. Redox potentials and redox reactions in deep groundwater systems. *Chemical Geology,* 98(1-2), pp. 131-150.

Guillaumont, R., Mompean, F. & O.N.E. Agency, 2003. *Update on the Chemical Thermodynamics of Uranium, Neptunium, Plutonium, Americium and Technetium.* s.l.:Elsevier.

Huber et al., F., 2014. *Colloid/nanoparticle formation and mobility in the context of deep geological nuclear waste disposal (Project KOLLORADO-2) ; final report.* Karlsruhe: Karlsruhe Institute of Technology (KIT).

Huber et al., F., 2015. Radionuclide desorption kinetics on synthetic Zn/Ni-labeled montmorillonite nanoparticles. *Geochimica et Cosmochimica Acta,* 148(0), pp. 426-441.

Huber, F., Kunze, P., Geckeis, H. & Schäfer, T., 2011. Sorption reversibility kinetics in the ternary system radionuclide-bentonite colloids/nanoparticles-granite fracture filling material. *Applied Geochemistry,* 26(12), pp. 2226-2237.

Huber, F. et al., 2020, in review. Impact of fracture geometry on bentonite erosion - a numerical study. *Journal of Rock Mechanics and Mining Sciences.*

Huber, F., Noseck, U. & Schäfer, T., 2016. *Stability of compacted bentonite for radionuclide retardation – Experiments and modelling.* Karlsruhe: KIT.

Huber, F. et al., 2017. Tc interaction with crystalline rock from Aspo (Sweden): Effect of in-situ rock redox capacity. *Appl. Geochem.,* Band 80, pp. 90-101.

Hu, H.-Q. & Möri, A., 2008. Radionuclide transport in fractured granite interface zones. *Physics and Chemistry of the Earth, Parts A/B/C,* Band 33, pp. 1042-1049.

Jansson, M., 2009. *Bentonite erosion (Laboratory studies) SKB Technical Report TR-09-33.* s.l.:s.n.

Jasmund, K. & Lagaly, G. Hrsg., 1993. Tonminerale und Tone: Struktur, Eigenschaften, Anwendungen und Einsatz in Industrie und Umwelt. In: Darmstadt: Steinkopf, p. 490.

Johnson, P., Sun, N. & Elimelech, M., 1996. Colloid transport in geochemically heterogeneous porous media: Modeling and measurements. *Environmental Science & Technology,* 30(11), pp. 3284-3293.

Kersting et al., A., 1999. Migration of plutonium in ground water at the Nevada Test Site. *Nature,* Band 397, pp. 56-59.

Kim, M. et al., 2005. Interaction of actinides(III) with aluminosilicate colloids in "statu nascendi" Part III. Colloid formation from monosilanol and polysilanol. *Colloids and Surfaces A: Physicochemical and Engineering Aspects,* 254(1-3), pp. 137-145.

King, F. et al., 2010. *An update of the state-of-the-art report on the corrosion of copper under expected conditions in a deep geologic repository.* s.l.:SKB.

Kinniburgh, D. & Cooper, D., 2011. PhreePlot - Creating graphical output with PHREEQC User Manual. In: s.l.:s.n., p. 616.

Koll, D. et al., 2019. Recent developments for AMS at the Munich tandem accelerator. *Nuclear Instruments and Methods in Physics Research Section B: Beam Interactions with Materials and Atoms,* Band 438, pp. 180-183.

Kosakowski, G., 2004. Anomalous transport of colloids and solutesin ashear zone. *Journal of Contaminant Hydrology,* 72(1-4), pp. 23-46.

Kretzschmar, R., Holthoff, H. & Sticher, H., 1998. Influence of pH and humic acid on coagulation kinetics of kaolinite: a dynamic light scattering study. *J. Colloid and Interface Science,* Band 202, pp. 95-103.

Kretzschmar, R. & Schäfer, T., 2005. Metal retention and transport on colloidal particles in the environment. *Elements,* 1(4), pp. 205-210.

Kunze et al., P., 2008. The influence of colloid formation in a granite groundwater bentonite pore water mixing zone on radionuclide speciation. *Journal of Contaminant Hydrology,* Band 102, pp. 263-272.

Lagaly, G. & van Olphen, H., 1978. An Introduction to Clay Colloid Chemistry, 2nd Ed. John Wiley & Sons, New York, London, Sydney, Toronto 1977. 318 Seiten, Preis: £ 15.–, $ 25.–. *Berichte der Bunsengesellschaft für physikalische Chemie,* 82(2), pp. 236-237.

Liu, J. & Neretnieks, I., 2006. *Physical and chemical stability of the bentonite buffer. SKB Rapport R-06-103.* s.l.:Svens Kärnbränslehantering AB.

Liu, J. & Neretnieks, I., 2006. *Physical and chemical stability of the bentonite buffer. SKB Rapport R-06-103.* s.l.:Svensk Kärnbränslehantering AB.

Mahmood, A., Amirtharajah, T., Sturm, W. & Denett, K., 2001. A micromechanics approach for attachment and detachment of asymmetric colloidal particles. *Colloids and Surfaces A: Physicochemical and Engeneering Aspects,* Band 177, pp. 99-110.

Marsac, R. et al., 2015. Neptunium redox speciation at the illite surface. *Geochim. Cosmochim. Acta,* Band 152, pp. 39-51.

Meunier, A., 2005. Clays. In: Berlin, Heidelberg: Springer, p. 472.

Miller et al., W., 2000. *Geological Disposal of Radioactive Wastes and Natural Analogues.* s.l.:Elsevier Science.

Missana, T. & Adell, A., 2000. On the applicability of DLVO theory to the prediction of clay colloids stability. *J. Colloid Interface Sci.,* Band 230, pp. 150-156.

Missana, T., Alonso, T. & Turrero, M., 2003. Generation and stability of bentonite colloids at the bentonite/granite interface of a deep geological radioactive waste repository. *Journal of Contaminant Hydrology,* 61(1-4), pp. 17-31.

Missana, T., Alonso, U., Garcia-Gutierrez, M. & Mingarro, M., 2008. Role of bentonite colloids on europium and plutonium migration in a granite fracture. *Applied Geochemistry,* 23(6), pp. 1484-1497.

Montoya, V. et al., 2020, to be submitted. Radionuclide solubility and speciation calculations for the Long-term In-situ Test (LIT) at Grimsel Test Site (GTS, Switzerland). *Environ Sci Technol..*

Moreno, L., Liu, L. & Neretnieks, I., 2011. Erosion of sodium bentonite by flow and colloid diffusion. *Physics and Chemistry of the Earth, Parts A/B/C,* 36(17-18), pp. 1600-1006.

Moreno, L., Neretnieks, I. & Liu, L., 2010. *Moreno, L., Neretnieks, I., Liu, L.Modelling of erosion of bentonite gel by gel/sol flow. SKB Technical Report 06-103.* Stockholm, Sweden: Svensk Kärnbränslehantering AG.

Möri et al., A., 2003. The colloid and radionuclide retardation experiment at the Grimsel Test Site: influence of bentonite colloids on radionuclide migration in a fractured rock. *Colloids and Surfaces A: Physicochemical and Engineering Apects,* 217(1-3), pp. 33-47.

Muurinen, A., 1994. *Diffusion of anions and cations in compacted sodium bentonite. Pub. 168.* Finland: VTT, Finland.

NAGRA, 2016. *Grimsel Test Site Investigation Phase VI: Colloid Formation and Migration Project: Site instrumentation and initiation of the long-term in-situ test. Nagra Technical Report NTB 15-03.* Wettingen, Switzerland: Nagra.

NEA, 2013. *The Nature and Purpose of the Post-closure Safety Cases for Geological Repositories.* Paris: OECD Publishing.

Neretnieks, I., Liu, L. & Moreno, L., 2009. *Mechanisms and models for bentonite erosion, in Technical Report, SKB.* Stockholm: Svensk Kärnbränslehantering, Swedish Nuclear Fuel and Waste Management Co.

Neretnieks, I. & Moreno, L., 2018. Revisiting bentonite erosion understanding and modelling based on the BEL-BaR project findings. Technical Report TR-17-12. In: Stockholm, Schweden: SKB Svensk Kärnbränslehantering AG, p. 52 pp.

Noseck, U. et al., 2018. *Smart Kd-concept for long-term safety assessments. Extension towards more complex applications.* s.l.:Gesellschaft für Anlagen- und Reaktorsicherheit (GRS)gGmbH, FKZ 02 E 11102 (BMWi), GRS-500.

Noseck, U. et al., 2016. *Grimsel Test Site Investigation Phase VI. Colloid Formation and Migration Project: Modelling of tracer, colloid and radionuclide transport for dipole CFM 06.002 – Pinkel surface packer.*. s.l.:NAGRA Technical Report ntb 16-06.

Novich, B. & Ring, T., 1984. Colloid stability of clays using photon correlation spectroscopy. *Clays and Clay Minerals,* 32(5), pp. 400-406.

Parkhurst, D. & Appelo, C., 2013. Description of input and examples for PHREEQC version 3: A computer program for speciation, batch-reaction, one-dimensional transport, and inverse geochemical calculations. In: *U.S. Geological Survey Techniques and Methods, book 6, volume A43 of Modeling Techniques.* Denver, Colorado: U.S. Geological Survey.

Patelli, A. et al., 2006. Validation of the RBS analysis for colloid migration through a rough granite surface. *Nuclear Instruments & Methods in Physics Research Section B-Beam Interactions with Materials and Atoms,* Band 249, pp. 575-578.

POSIVA, 2012. *Safety case for the disposal of spent nuclear fuel at Olkilouto - Synthesis 2012.* Eurajoki, Finland: POSIVA Oy.

Pusch, R., 1983. *Stability of bentonite gels in crystalline rock - physical aspects, SKBF/KBS report TR 83-04, University of Luleå, SKB was formerly: SKBF/KBS; SKBF.* University of Luleå, SKB was formerly: SKBF/KBS; SKBF: Svensk Kärnbränsleförsörjning AB.

Push, R., 1983. *Stability of bentonite gels in crystalline rock - Physical aspects. TR 83-04.* Stockholm: SKB.

Quinto et al., F., 2015. Accelerator Mass Spectrometry of Actinides in Ground- and Seawater: An Innovative Method Allowing for the Simultaneous Analysis of U, Np, Pu, Am, and Cm Isotopes below ppq Levels. *Analytical Chemistry,* 87(11), pp. 5766-5773.

Quinto, F. et al., 2017. Multiactinide Analysis with Accelerator Mass Spectrometry for Ultratrace Determination in Small Samples: Application to an in Situ Radionuclide Tracer Test within the Colloid Formation and Migration Experiment at the Grimsel Test Site (Switzerland). *Anal Chem,* 89(13), pp. 7182-7189.

Quinto, F. et al., 2019. Ultratrace Determination of 99Tc in Small Natural Water Samples by Accelerator Mass Spectrometry with the Gas-Filled Analyzing Magnet System. *Anal Chem.*

Reiche, T., Noseck, U. & Schäfer, T., 2016. Migration of Contaminants in Fractured-Porous Media in the Presence of Colloids: Effects of Kinetic Interactions. *Transport in Porous Media,* 111(1), pp. 143-170.

Reinholdt et al., M., 2013. Hydrothermal Synthesis and Characterization of Ni-Al Montmorillonite-Like Phyllosilicates. *Nanomaterials,* 3(1), p. 48.

Rinderknecht, F., 2017. *Bentonite erosion and colloid mediated transport of radionuclides in advection controlled systems.* Karlsruhe: KIT.

Robinson, P. & Bath, A., 2011. *Workshop on copper corrosion and buffer erosion. Stockholm 15-17. September.* Stockholm: s.n.

Rübel, A., Becker, D.-A. & Fein, E., 2007. *Radionuclide transport modelling to assess the safety of repositories in clays, GRS-228.* Braunschweig: Gesellschaft für Anlagen und Reaktorsicherheit (GRS) mbH.

Ryan, J. & Elimelech, M., 1996. Colloid mobilization and transport in groundwater. *Colloids Surf. A,* Band 107, pp. 1-56.

Schäfer et al., T., 2012. Nanoparticles and their influence on radionuclide mobility in deep geological formations. *Applied Geochemistry,* 27(2), pp. 390-403.

Schäfer, T., 2010. *Colloid/ Nanoparticle formation and mobility in the context of deep geological nuclear waste disposal (Project KOLLORADO-1; Final report).* Karlsruhe: Forschungszentrum Karlsruhe in der Helmholtz-Gemeinschaft FZKA.

Schäfer, T., Geckeis, H., Bouby, M. & Fanghänel, T., 2004. U, Th, Eu and colloid mobility in a granite fracture under near-natural flow conditions. *Radiochimica Acta,* Band 92, pp. 731-737.

Schlickenrieder, Lanyon, Kontar & Blechschmidt, 2017. Grimsel Test Site Investigation Phase VI Colloid Formation and Migration Project: Site instrumentation and initiation of the long-term in-situ test. *NagraTechnical Report NTB 15-03,* p. 86.

Sellin, P. e. a., 2016. *Bentonite Erosion: effects on the Long term performance of the engineered Barrier and Radionuclide transport (BELBAR). Project final report..* s.l.:European Commission.

Sellin, P. & Leupin, O., 2013. The Use Of Clay As An Engineered Barrier In Radioactive Waste Management – A Review.. *Clays and Clay Minerals,* 61(6), pp. 477-498.

SKB, 2006a. *Buffer and backfill process report for the safety assessment SR-Can. Technical report TR-06-18.* Stockholm, Sweden.: Svensk Kärnbränslehantering AB.

SKB, 2006b. *Long-term safety for KBS-3 repositories at Forsmark and Laxemar - a first evaluation; Main report ofthe SR-Can project. SKB Technical report TR-06-09..* Stockholm, Sweden.: Svensk Kärnbränslehantering AB.

SKB, 2011. *Long-Term Safety for the Final Repository for Spent Nuclear Fuel at Forsmark. Main Report of the SR-Site Project. SKB Technical report TR-11-01.* s.l.:Svensk Kärnbränslehantering AB.

Smith et al., P., 2008. *CFM Phase I Modeling Report NAB 08-31.* Nagra, Wettingen (Switzerland): s.n.

Stoll et al., M., 2016. Impact of gravity, collector surface roughness and fracture orientation on colloid retention kinetics in an artificial fracture. *Journal of Colloid and Interface Science,* Band 475, pp. 171-183.

Stoll, M., 2018. *Colloid mobility controlling processes in single fractures: a bottom-up approach.* Jena: Faculty of Chemistry and Earth Sciences, Friedrich-Schiller-University Jena.

Stoll, M., Huber, F., Schill, E. & Schäfer, T., 2017. Parallel-plate fracture transport experiments of nanoparticulate illite in the ultra-trace concentration range investigated by Laser-Induced Breakdown Detection (LIBD). *Colloids and Surfaces A: Physico-chemical and Engineering Aspects,* Band 529, pp. 222-230.

Stumpf, S. et al., 2008. Immobilization of trivalent actinides by sorption onto quartz and incorporation into siliceous bulk: Investigations by TRLFS. *Journal of Colloid and Interface Science,* 318(1), pp. 5-14.

Taboada-Serrano, P., Vithayaveroj, V., Yiacoumi, S. & Tsouris, C., 2005. Surface charge heterogeneities measured by atomic force microscopy. *Environmental Science & Technology,* 39(17), pp. 6352-6360.

Tachi, Y., Ochs, M. & Suyama, T., 2014. Integrated sorption and diffusion model for ben-tonite. Part 1: clay water interaction and sorption modeling in dispersed systems. *J. Nucl. Sci. Technol.,* Band 51, pp. 1177-1190.

Thoenen, T., Hummel, W., Berner, U. & Curti, E., 2014. *The PSI/Nagra Chemical Thermodynamic Database 12/07, PSI Report 14-04.* s.l.:s.n.

Tournassat, C. & Appelo, C., 2011. Modelling approaches for anion-exclusion in compacted Na-bentonite. *Geochimica et Cosmochimica Acta,* 75(13), pp. 3698-3710.

Vakarelski, I., Ishimura, K. & Higashitani, K., 2000. Adhesion between silica particle and mica surfaces in water and electrolyte solutions. *Journal of Colloid and Interface Science,* 227(1), pp. 111-118.

Van Loon, L., 2014. Effective Diffusion Coefficients and Porosity Values for Argilla-ceous Rocks and Bentonite: Measured and Estimated Values for the Pro-visional Safety Analyses for SGT-E2. *Nagra Technical Report 12-03.*

Van Loon, L., Glaus, M. & Müller, W., 2007. Anion exclusion effects in compacted bentonites: Towards a better understanding of anion diffusion. *Appl. Geochem.,* Band 22, pp. 2536-2552.

Velegol, D. & Thwar, P., 2001. Analytical model for the effect of surface charge nonuniformity on colloidal interactions. *Langmuir,* 17(24), pp. 7687-7693.

Verwey, E. & Overbeek, J., 1948. *Theory of the stability of lyophobic colloids.* Asterdam: Elsevier.

Vilks, P., Miller, H. & Doern, D., 1991. Natural Colloids and Suspended Particles in the Whiteshell Research Area, Manitoba, Canada, and Their Potential Effect on Radiocolloid Formation. *Applied Geochemistry,* 6(5), pp. 565-574.

Wan et al., J., 2004. Colloid formation at waste plume fronts. *Environmental Science & Technology,* Band 38, pp. 6066-6073.

Yoshida, H., Takeuchi, M. & Metcalfe, R., 2005. Long-term stability of flow-path structure in crystalline rocks distributed in an orogenic belt. *Engineering Geology,* Band 78, p. 275.

Zänker et al., H., 2002. The colloid chemistry of acid rock drainage solution from an abandoned Zn-Pb-Ag mine. *Applied Geochemistry,* 17(5), pp. 633-648.

Zänker, H., Richter, W. & Hüttig, G., 2003. Scavenging and immobilization of trace contaminants by colloids in the waters of abandoned ore mines. *Colloids and Surfaces A: Physicochemical and Engineering Aspects,* 217(1-3), pp. 21-31.

KIT Scientific Working Papers
ISSN 2194-1629

www.kit.edu